

International Conference on Basic Sciences, Engineering and Technology

August 25-28, 2022

Istanbul/Turkey

EDITOR
DR.MEHMET OZASLAN

PROCEEDINGS BOOK

 **ISRES**
Publishing
ISBN: 978-605-73797-9-5

www.icbaset.net

INDEX

| | |
|--|-----|
| Data Analytic for Cyber Security: A Review of Current Framework Solutions, Challenges and Trends <i>Shereen KHAN, Tan Swee Leng OLIVIA, Nasreen KHAN, Ng Kok WHY, Tan Swee WEI</i> | 1 |
| On a Geometric Programming Approach to Profit Maximization: The Case of CES Technology <i>Vedran KOJIĆ</i> | 7 |
| De Novo Gold Nanoparticles Activate P53 by Inhibiting NF-Kb Signalling in Breast Cancer Cells <i>Muhammad SAFDAR, Mehmet OZASLAN</i> | 16 |
| Mineralogical and Elemental Characterization of Conventional Asphalt of Peruvian Roadways by X-Ray Diffraction and Energy Dispersive X-ray Fluorescence <i>Jenny Aleida MONTOYA-BURGA, Jorge Aurelio BRAVO-CABREJOS, Marlon Gastón FARFÁN-CÓRDOVA, María Luisa CERÓN-LOAYZA, Felipe Américo REYES-NAVARRO</i> | 22 |
| Development of Two-Dimensional Thermal Analysis Code for the Analysis of 3D Printed PLA Parts <i>Buryan APACOGU-TURAN, Kadir KIRKKOPRU</i> | 28 |
| Finite Element Method for Analysis of Off-Center Connected Continuous Beams <i>Albena DOICHEV</i> | 37 |
| Dynamic Control of Non-Linearly Tapering FGM Beams <i>Khalid EL HARTI, Rachid SAADANI, Miloud RAHMOUNE</i> | 46 |
| Moisture Absorption Behavior of CP5 Composite Materials Used in Industry <i>Băilă DIANA-IRINEL, Păcurar RĂZVAN, Păcurar ANCUȚA</i> | 55 |
| Smart Cities: Using GIS Technology in Urban Infrastructure Development at Migration Areas <i>Bushra ZALLOOM</i> | 64 |
| The Preparation of Montmorillonite/Carrageenan-Composite Hydrogel for Chromium (VI) Removal from Aqueous Solution <i>Gulen Oytun AKALIN</i> | 72 |
| Duty Cycle Detection Method for High Speed Input-Output Systems <i>Karen MELIKYAN</i> | 81 |
| Exploring the Risky Areas Due to Landslide Using Decision Tree Analysis: Case Study Tasmania, Australia <i>Mahyat SHAFAPOURTEHRAN</i> | 86 |
| Determination of Moisture Content and Morphological Characteristics of MDF Composite Materials Used For Industrial Products <i>Băilă Diana-IRINEL, Păcurar RĂZVAN, Păcurar ANCUȚA</i> | 102 |
| A Study on Wetlands of a Peruvian Bay Through the Hydrometer Method and X-Ray Diffraction <i>María Luisa CERÓN LOAYZA, Marlon Gastón FARFÁN-CÓRDOVA, Jenny Aleida MONTOYA BURGA Fanny MORI ESCOBAR, Felipe Américo REYES NAVARRO</i> | 109 |
| Content Management of Time Bank Credit Website for the Elderly in Malaysia <i>Tan Swee Leng OLIVIA, Ooi Shih YIN, Rossanne Gale VERGARA, Shereen KHAN, Nasreen KHAN</i> | 114 |
| Off-center Supported Beam with Additional Elastic Supports located at the Height of the Beam and Asymmetrical Cross Section <i>Albena DOICHEVA</i> | 120 |
| Estimation SNR of CCD camera for OD medium <i>Miranda KHAJISHVILI, Nugzar GOMIDZE, Jaba SHAINIDZE</i> | 130 |
| Extraction of Frequent Itemset Mining on Spark <i>Youssef FAKIR, Mohamed FAKIR, Rachid ELAYACHI</i> | 139 |

The Monte Carlo Solution of Nonlinear Problems in Engineering

A.S. RASULOV, G.M. RAIMOVA, D. HASANOVA.....146

The Eurasia Proceedings of Science, Technology, Engineering & Mathematics (EPSTEM), 2022

Volume 18, Pages 1-6

ICBASET 2022: International Conference on Basic Sciences, Engineering and Technology

Data Analytic for Cyber Security: A Review of Current Framework Solutions, Challenges and Trends

Shereen KHAN
Multimedia University

Tan Swee Leng OLIVIA
Multimedia University

Nasreen KHAN
Multimedia University

Ng Kok WHY
Multimedia University

Tan Swee WEI
Multimedia University

Abstract: In context of technology, cybersecurity has seen vital technological and operational developments in recent years, with information science at the forefront of the revolution. The key in creating a complicated and automatic security system is extracting network activity patterns or cybersecurity information insights and constructing an identical data-driven model. The applying of a spread of scientific methodology, machine learning techniques, processes, and systems; information science is to grasp and analyse actual occurrences with information. During this analysis, the researchers consider and in short justify cybersecurity information science, during which information is obtained from relevant cybersecurity sources as well as legislations and analytics are wont to supplement the most recent data-driven trends to supply more practical security solutions. The paradigm of cybersecurity information science, in distinction to standard cybersecurity computing techniques, permits for more practical and complex computing. Researchers check and highlight variety of connected analysis topics and future directions. Additionally, researchers propose a multi-layered framework for cybersecurity modelling. Overall the target is to target the connection of data-driven deciding framework model for safeguarding systems from cyber-attacks, instead of simply discussing cybersecurity information science and applicable approaches.

Keywords: Cyber security, cybercrime, data analytic, legislations

Introduction

Data analytics is a strategy for ensuring accurate data analysis, cleansing, altering, and modelling via the application of proper analysis. Data analysis aids in the discovery of important nuances and leads to a positive outcome. Cybercrime is now a factor in all projects, as part of Malaysia's National Policy on Industry 4.0, which aims to improve the country's industrial capacity by enacting appropriate legislation to combat the use of ICTs for illegal purposes. Assuming that the cybercrime data is thoroughly investigated, the outcome might be quickly concluded, allowing better judgments to be made about combating cybercriminals through appropriate laws. Cybercrime is sometimes confused with a presentation that focuses solely on computers and the internet. However, not all cybercrime is limited to computers and the internet; for example, the instance of Joseph Marie

- This is an Open Access article distributed under the terms of the Creative Commons Attribution-Noncommercial 4.0 Unported License, permitting all non-commercial use, distribution, and reproduction in any medium, provided the original work is properly cited.

- Selection and peer-review under responsibility of the Organizing Committee of the Conference

Jacquard and another common model would be dumpster diving , which is a tactic for recovering data that might be used to launch an attack on a computer network. Their presentation includes not just scanning the trash for valuables, but also getting access and a secret key written on scribbled notes (Lew, 2020).

Vizom is a popular video conferencing programme that is now important to companies and social life as a result of the coronavirus outbreak (Brewer, 2021). The danger with such attacks is that they can eventually lead to a cascade breakdown of interbank finance, perhaps sparking a bigger systemic liquidity crisis. In all of these circumstances, the companies' activities are so linked with those of other organisations in their respective countries that their collapse will certainly cause those other or connected businesses to fail as well. As a result, protecting such infrastructures, also known as key information infrastructures, is considered a national security concern.

Background of the study

Cyber-attacks are frequently in the news, posing a security risk to governments, sectors, and enterprises. Things might grow even worse with society's dependency on technology and the emergence of the internet of things. As seen by the devastating malware they employ to target enterprises, cyber thieves are becoming more intelligent and sophisticated.

This paper focuses on the current tend challenges of data analytic on cybersecurity in Malaysia and Malaysia is chosen to be the country for this research due to its strategic economic geographical location and Malaysia has been classified among the top ten nations with a strong commitment to cybersecurity in the International Telecommunications Union's Global Cybersecurity Index 2020 study (ITU). Malaysia faces many challenges in defending its cybersecurity domain. The information was gathered through interviews with experts in the field of cybersecurity. The findings indicated that in order to incorporate a cybersecurity aspect in the organisation, awareness and funding are critical. Due to the Prime Minister's digital economy blueprint, YAB Tan Sri Dato' Haji Mahiaddin container Haji Mohd, Yassin in 2021, a substantial increase in cyberisation would be 81 percent of Malaysians are now dynamic via web-based media in 2020, and 90 percent of government is now online (Mok, 2021). Simultaneously, concerns about cyber security approaches on advancement toward administrative arrangements command and updating outdated legislation are needed to provide robustness in combating cyber-attacks as Malaysia's cyberization progresses.

Literature Review

Industry 4.0 offers great benefits to businesses in terms of long-term viability. Internet of things, big data, supply chain, cloud computing, horizontal and vertical integration, autonomous robot, addictive manufacturing, cyber security, simulation, and augmented reality are the nine pillars in total. However, cyber security is the most significant problem in this digitalization era. The privacy and security of data will always be top security priorities for every firm.

All individuals, professionals, legislators, and, more broadly, all decision makers are concerned about cybersecurity. It has also become a big problem for societies that must protect itself against cyber-attacks using both preventative and reactive methods, which include a lot of monitoring, while still preserving their independence and avoiding widespread surveillance. Computer security, often known as cyber security or IT security, is the safeguarding of computer systems against harm to their hardware, software, or information, as well as disruption or misdirection of services they offer (Roca , 2019). Data integrity is a challenge in cyber security management. Due to the vast amount of information and data, securing data integrity in an IoT context has proven to be rather difficult. Data from many sources has a wide range of ideas and forms, making it challenging for analysts to combine it. Furthermore, a lack of monitoring and security against unauthorised modifications or alteration will result in undesirable data alterations. During peak hours, when enterprises may lack the internal competence and systems to manage and safeguard data, malicious data searchers are continually seeking for new methods to steal it (Campos et al., 2016).

Cybersecurity Data Analytic

The ultimate objective of cybersecurity data science is to use security data to make data-driven intelligent decisions for smart cybersecurity solutions. Cybersecurity data represents a partial paradigm change away from

old well-known security solutions like firewalls, user authentication and access control, encryption systems, and so on, which may or may not be successful in today's cyber business. The issues are that these are often handled statically by a few competent security analysts, with ad-hoc data management.

However, as the frequency of cybersecurity events in the various forms indicated above continues to rise, traditional solutions have proven ineffective in managing such cyber dangers. As a result, a large number of complex assaults are developed and disseminated swiftly throughout the Internet. Although several researchers use various data analysis and learning techniques to build cybersecurity models, as summarised in the section "Framework model in cybersecurity," a comprehensive security model based on the effective discovery of security insights and latest security patterns may be more useful. To overcome this problem, we need to create more flexible and efficient security systems that can respond to attacks and change security rules in a timely manner to mitigate them intelligently.

Table 1. Statistics on types of cybercrime in Malaysia 2022

| | January | February | March | April | May | June | July | August | September | October | November | December | Total |
|-----------------|---------|----------|-------|-------|-----|------|------|--------|-----------|---------|----------|----------|-------|
| Spam | 8 | 5 | 6 | 15 | 0 | 0 | 0 | 0 | 0 | 0 | 0 | 0 | 34 |
| Intrusion | 15 | 12 | 4 | 6 | 0 | 0 | 0 | 0 | 0 | 0 | 0 | 0 | 37 |
| Attemp | | | | | | | | | | | | | |
| Vulnerabilities | 6 | 3 | 3 | 4 | 0 | 0 | 0 | 0 | 0 | 0 | 0 | 0 | 16 |
| Report | | | | | | | | | | | | | |
| Malicious | 62 | 68 | 174 | 103 | 0 | 0 | 0 | 0 | 0 | 0 | 0 | 0 | 407 |
| Codes | | | | | | | | | | | | | |
| Content | 2 | 0 | 0 | 2 | 0 | 0 | 0 | 0 | 0 | 0 | 0 | 0 | 4 |
| Related | | | | | | | | | | | | | |
| Denial | of 0 | 2 | 1 | 1 | 0 | 0 | 0 | 0 | 0 | 0 | 0 | 0 | 4 |
| Service | | | | | | | | | | | | | |
| Intrusion | 68 | 54 | 50 | 74 | 0 | 0 | 0 | 0 | 0 | 0 | 0 | 0 | 246 |
| Fraud | 431 | 423 | 388 | 396 | 0 | 0 | 0 | 0 | 0 | 0 | 0 | 0 | 1638 |
| | 592 | 567 | 626 | 601 | 0 | 0 | 0 | 0 | 0 | 0 | 0 | 0 | 2386 |

Table 1, data indicates the statistic on types of cybercrimes in Malaysia 2022. In order to analyse the data coherently to reflect the accuracy, it is necessary to evaluate a large quantity of important cybersecurity data collected from many sources, such as network and system sources, and to identify insights or correct security policies in an automated way with little human interaction. Analyzing cybersecurity data and developing the necessary tools and methods to effectively guard against cybersecurity events entails more than a basic set of functional requirements and understanding of risks, threats, and vulnerabilities.

Proposed framework to safeguard data analytic for cybersecurity

As previously stated, cybersecurity data science is data-driven, employs machine learning techniques, attempts to quantify cyber risks, employs inferential techniques to analyse behavioural patterns, focuses on generating security response alerts, and ultimately seeks to optimise cybersecurity operations. As a result, the researchers briefly explain a layered data processing architecture that can be utilised to extract security insights from raw data and develop smart cybersecurity systems, such as dynamic policy rule-based access control or intrusion detection and prevention systems.

Collecting relevant cybersecurity data is a critical stage that serves as a link between cyber infrastructure security issues and data-driven solution processes in this methodology. As a result, the question is how to gather relevant and unique requirements data in order to construct data-driven security models. A strict framework, such as proposed policies and legislations, should play an essential role in safeguarding pure cybersecurity data for analysis.

This layer in this framework is responsible for finalising the resulting security model by including new intelligence as needed. This might be accomplished by additional processing in numerous modules, such as recency mining and security model updating, which is responsible for keeping the security model up-to-date for improved performance by extracting the most recent data-driven security patterns.

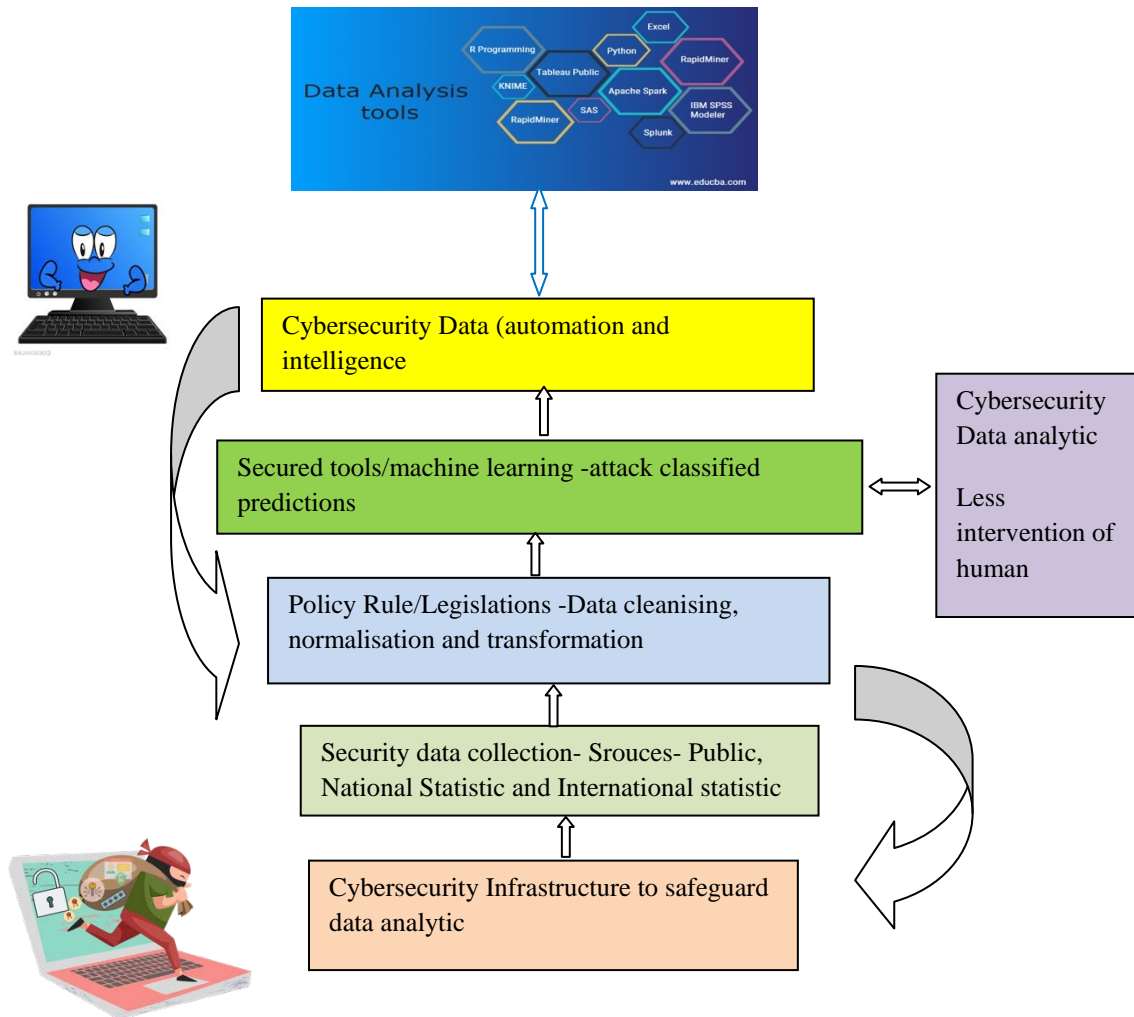


Figure 1. Cybersecurity layered data processing architecture framework

Results and Discussion

Data from computer networks, telecommunication networks, banking, healthcare, social media networks, bioinformatics, E-Commerce, surveillance, and other sources are some of the most common sources of big data transactions. The absence of security software that can be upgraded for protection is the next issue (Yaaqob et al., 2017). Due to a scarcity of equipment, tools, and systems, this is the case. An organization's software upgradeability is also expensive. On the one hand, most businesses are unable to organise unstructured data (Campos et al., 2016).

From the proposed framework in Fig.1, it is predicted that with this high level proposed data cleaning , normalisation and a comprehensive policy and legislation in place, the cybersecurity of Malaysia will be fully protected and moreover data-driven intelligent decision making in smart cybersecurity systems and services is what cybersecurity data science is all about.

Conclusion

Finally, the researchers have emphasised the current state of the art difficulties confronting the cybersecurity area in the face of data analytics. Traditional security solutions, employing traditional tools and methodologies, are no longer capable of embracing real-time large data network streams. Security analytics, or the use of structured data analytics to derive actionable knowledge and insights from streams in real time while adhering to governing rules, has been demonstrated by researchers to be a growing necessity for cybersecurity installations. Although the present usage of analytical solutions is far from revolutionary (as demonstrated by this Teradata research from 2013), awareness of adoption is gradually growing.

Recommendations

The discussion of this research was centred on two objectives: (1) analysing Malaysia's cyber security difficulties, and (2) proposing a holistic cybersecurity data analysis methodology for Malaysia to address cyber security challenges. Although Malaysia has cyberlaws in place to combat cybersecurity breaches, such as the Computer Crimes Act 1997, the Communications and Multimedia Act 1998, the Penal Code, the National Cyber Security Agency (NACSA) and the Malaysia CyberSecurity Strategy 2020-2024, the topic of cybercrime and cyber security is still very popular, and free data sets for analysis in this field are still scarce. Data analysis for cybersecurity will be more accurate to forecast and prevent cybercrime in Malaysia if more data in this industry becomes available and extracted with minimal human interaction.

Scientific Ethics Declaration

The authors declare that the scientific ethical and legal responsibility of this article published in EPSTEM journal belongs to the authors.

Acknowledgements or Notes

This article was presented as an oral presentation at the International Conference on Basic Sciences, Engineering and Technology (www.icbasnet.net) conference held in Istanbul/Turkey on August 25-28, 2022.

*This research is funded by the Malaysian Ministry of Education (MOE) through the Fundamental Research Grant Scheme (FRGS) FRGS/1/2019/SSI10/MMU/03/15. The authors alone are responsible for the views expressed in this article, which does not necessarily represent the views, decisions, or policies of MOE or the institutions with which the authors are affiliated. The funder had no role in study design, data collection and analysis, or preparation of the manuscript.

References

- Brewer, R. (2015). Cyber threats: reducing the time to detection and response. *Network Security*, 5, pp.5-8.
- Communications and Multimedia Act (1998). *National Cyber Security Agency (NACSA)*. <https://www.nacsa.gov.my/>
- Malaysia CyberSecurity Strategy 2020-2024 Compressed.pdf <https://asset.mkn.gov.my/web/wp-content/uploads/sites/3/2019/08/MalaysiaCyberSecurityStrategy2020-2024Compressed.pdf>
- Global Cybersecurity Index (2020). <https://www.itu.int/en/ITU-D/Cybersecurity/Pages/global-cybersecurity-index.aspx>
- Campos, J., Sharma, P., Jantunen, E., Baglee, D., & Fumagalli, L. (2016). The challenges of cybersecurity frameworks to protect data required for the development of advanced maintenance. *Procedia Cirp*, 47, 222-227.
- Lew, H. (2020, January 29). *Why malaysia should amend its cyber security laws*. Asia Law Portal
- Mok, O. (2021, February 19). *MyDIGITAL and Malaysia digital economy blueprint: how we can achieve 100pc internet access*. Malaysia | Malay Mail
- Roca, S. K.-L.-D.-V. (2019). Cybersecurity current challenges and Inria's research directions. *Le Chesnay Cedex, France: Inria*
- Teradata and Ponemon Institute (2013). Big data analytics in cyber defense, February. http://www.ponemon.org/local/upload/file/Big_Data_Analytics_in_Cyber_Defense_V12.pdf

Yaqoob, I., Ahmed, E., ur Rehman, M. H., Ahmed, A. I. A., Al-garadi, M. A., Imran, M., & Guizani, M. (2017). The rise of ransomware and emerging security challenges in the Internet of Things. *Computer Networks*, 129, 444-458.

Author Information

Shereen Khan

Multimedia University
Persiaran Multimedia , Cyberjaya 63100, Selangor, Malaysia
Contact e-mail: shereen.khan@mmu.edu.my

Tan Swee Leng Olivia

Multimedia University
Jalan Ayer Keroh Lama, 75450 Bukit Beruang, Melaka,
Malaysia

Nasreen Khan

Multimedia University, Malaysia
Persiaran Multimedia , Cyberjaya 63100, Selangor, Malaysia

Ng Kok Why

Multimedia University, Malaysia
Persiaran Multimedia , Cyberjaya 63100, Selangor, Malaysia

Swee Wei Tan

Multimedia University
Persiaran Multimedia , Cyberjaya 63100, Selangor, Malaysia

To cite this article:

Khan, S., Olivia, T.S.L., Khan, N., Why, N.K. & Tan, S. W. (2022). Data analytic for cyber security: a review of current framework solutions, challenges and trends. *The Eurasia Proceedings of Science, Technology, Engineering & Mathematics (EPSTEM)*, 18, 1-6.

The Eurasia Proceedings of Science, Technology, Engineering & Mathematics (EPSTEM), 2022

Volume 18, Pages 7-15

ICBASET 2022: International Conference on Basic Sciences, Engineering and Technology

On a Geometric Programming Approach to Profit Maximization: The Case of CES Technology

Vedran KOJIĆ
University of Zagreb

Abstract: The profit maximization problem takes a central place in the theory of the firm, especially when conditions for perfect competition hold. In this paper, we solve the profit maximization problem of a perfectly competitive firm when the constant elasticity of substitution (CES) production function with $n \geq 2$ inputs describes its technology. Commonly, this problem is solved by using multivariable differential calculus. However, to avoid tedious algebraic manipulations and bypass checking nontrivial necessary and sufficient conditions, we employ geometric programming (GP), and the power mean inequality (PMI) as an elegant complementary tool to multivariable calculus. Since the GP and the PMI are simple optimization techniques without derivatives, they can provide new insights into the given problem to managers, students, and other audiences who may be unfamiliar with multivariable differential calculus. Additionally, by using the properties of limits, we show that the solution to the profit maximization problem with Cobb-Douglas technology is a limiting case of our result.

Keywords: Profit maximization, Cobb-Douglas technology, CES technology, Geometric programming

Introduction

Since finding the optimum using differential calculus may be nontrivial and inelegant, the signomial geometric programming (SGP) technique with zero degrees of difficulty was proposed by (Liu, 2006) as a complementary approach to solving the profit maximization problem with Cobb-Douglas production function (CDPF). Further, (Kojić & Lukač, 2018) showed how the results from (Liu, 2006) can be obtained by solving an equivalent geometric programming (GP) problem with zero degrees of difficulty, providing proof that the (global) maximum profit in the case of CDPF has been achieved.

In this note, we solve a profit maximization problem where the firm's technology is given by the CES production function (CESPF). Furthermore, since the CESPF is a generalization of the CDPF, we show how the results by (Liu, 2006) and (Kojić & Lukač, 2018) can be derived from our results.

The paper is organized as follows. After the introduction, the notation and preliminaries are presented in the second section. The solution to the profit maximization problem with CESPF is the main result of the paper and it is given in the third section. The fourth section shows that the solution to the profit maximization problem with CDPF is a limiting case of our result. The fifth section concludes the paper.

Notations and preliminaries

Notations have been adopted from (Avvakumov et al., 2010), (Jehle & Reny, 2011), and (Liu, 2006):

- This is an Open Access article distributed under the terms of the Creative Commons Attribution-Noncommercial 4.0 Unported License, permitting all non-commercial use, distribution, and reproduction in any medium, provided the original work is properly cited.

- Selection and peer-review under responsibility of the Organizing Committee of the Conference

| | |
|-------------|---|
| p | market price per unit, $p > 0$ |
| A | scale of production, $A > 0$ |
| x_i | input quantities, $x_i > 0$ |
| v_i | input prices, $v_i > 0$ for all i |
| φ_i | elasticities of Cobb-Douglas production function (CDPF) $\varphi_i > 0$ for all i |
| x_i^{C-D} | the i^{th} component of the maximizer |
| π^{C-D} | maximum profit in the case of CDPF (i.e. Cobb-Douglas technology) |
| α_i | allocation coefficients of CES production function (CESPF, i.e. CES technology), $\alpha_i > 0$ for all i |
| σ | degree of homogeneity of CESPF |
| ρ | substitution coefficient of CESPF |
| x_i^{CES} | the i^{th} component of the maximizer |
| π^{CES} | maximum profit in the case of CESPF |

Considering CDPF with n inputs ($n \geq 2$), given by

$$f(x_1, x_2, \dots, x_n) = A \prod_{i=1}^n x_i^{\varphi_i}, \quad (1)$$

the profit maximization problem becomes

$$\pi^{C-D} = \max_{x_1, x_2, \dots, x_n > 0} p \left(A \prod_{i=1}^n x_i^{\varphi_i} \right) - \sum_{i=1}^n v_i x_i, \quad (2)$$

where

$$\sum_{i=1}^n \varphi_i < 1. \quad (3)$$

By using SGP, (Liu, 2006) obtained the result of problem (2) as follows:

$$\pi^{C-D} = \left(1 - \sum_{i=1}^n \varphi_i \right) (pA)^{1/(1-\sum_{i=1}^n \varphi_i)} \prod_{i=1}^n \left(\frac{v_i}{\varphi_i} \right)^{-\varphi_i/(1-\sum_{i=1}^n \varphi_i)}, \quad (4)$$

$$x_i^{C-D} = \frac{\pi^{C-D} \varphi_i}{v_i \left(1 - \sum_{j=1}^n \varphi_j \right)}, \quad (5)$$

for all $i=1, 2, \dots, n$. However, problem (2) can be converted into a GP problem with zero degrees of difficulty, and the same result (4)-(5) was obtained by (Kojić & Lukač, 2018).

Now, let us introduce CESPF as in (Avvakumov et al., 2010), defined by

$$\psi(x_1, x_2, \dots, x_n) = A \left(\sum_{i=1}^n \alpha_i x_i^{-\rho} \right)^{-\sigma/\rho}, \quad (6)$$

Where

$$\sum_{i=1}^n \alpha_i = 1, \quad (7)$$

$$\sigma > 0, \quad (8)$$

$$\rho > -1, \rho \neq 0. \quad (9)$$

Considering CESPF, the profit maximization problem of a perfectly competitive firm with CES technology becomes (Jehle & Reny, 2011):

$$\begin{aligned} \pi^{CES} &= \max_{y, x_1, x_2, \dots, x_n > 0} py - \sum_{i=1}^n v_i x_i \\ \text{s.t. } & A \left(\sum_{i=1}^n \alpha_i x_i^{-\rho} \right)^{-\sigma/\rho} \geq y. \end{aligned} \quad (10)$$

To solve (10), we will use a power mean inequality (see (Bullen, 2003)).

Lemma 1. (Power mean inequality) Let $n \geq 2$, $n \in \mathbb{N}$, $x_i > 0$, and $w_i > 0$, $i = 1, 2, \dots, n$, such that $w = \sum_{i=1}^n w_i$. Then, for all $r > 0$, the following inequality holds

$$\prod_{i=1}^n x_i^{w_i} \leq \left(\sum_{i=1}^n \frac{w_i}{w} x_i^r \right)^{w/r}. \quad (11)$$

Equality in (11) holds if and only if $x_1 = x_2 = \dots = x_n$.

The profit maximization problem with CES technology

Since the very discovery of geometric programming, it has been applied to various optimization problems in science and industry. In the economic theory of production, (Reklaitis et al., 1975) applied geometric programming to solve the firm's cost minimization problem with Cobb-Douglas and CES production functions. Mainly, they used power mean inequality in solving the cost minimization problem with CESPF using geometric programming. However, they didn't comment on the sign of the substitution coefficient ρ , which makes their analysis incomplete.

Another important problem in the theory of the firm is the profit maximization problem for the perfectly competitive firm. The profit maximization problems with Cobb-Douglas and CES production function and their solutions are very well known in the literature (Zevelev, 2014). These problems are usually solved using multivariable calculus (Avvakumov et al., 2010). Still, a geometric programming approach to the profit maximization problem with CESPF is the main result of this paper since, to the best of our knowledge, such an approach is unknown in the literature.

According to (Duffin et al., 1967), (Beightler & Philips, 1976) and (Boyd et al., 2007), problem (10) is equivalent to the following problem:

$$\max_{z, y, x_1, \dots, x_n > 0} z \quad (12)$$

$$\text{s.t. } py - \sum_{i=1}^n v_i x_i \geq z, \quad (13)$$

$$A \left(\sum_{i=1}^n \alpha_i x_i^{-\rho} \right)^{-\sigma/\rho} \geq y. \quad (14)$$

Since $\max f = 1/(\min (1/f))$ for a positive function f , instead of the problem (12)-(14) we will solve the problem (15)-(17):

$$\min_{z, y, x_1, \dots, x_n > 0} z^{-1} \quad (15)$$

$$\text{s.t. } p^{-1} y^{-1} z + \sum_{i=1}^n p^{-1} v_i x_i y^{-1} \leq 1, \quad (16)$$

$$A \left(\sum_{i=1}^n \alpha_i x_i^{-\rho} \right)^{-\sigma/\rho} \geq y. \quad (17)$$

Let us consider two cases regarding the value of the substitution coefficient of CESPF ρ from (9).

Case 1. $\rho > 0$

Since the degree of homogeneity σ is defined as a positive number (see (8)), and when $\rho > 0$, the function $x \mapsto x^{-\rho/\sigma}$ is decreasing (for all $x > 0$). In this case, the inequality (17) is equivalent to

$$A^{-\frac{\rho}{\sigma}} \left(\sum_{i=1}^n \alpha_i x_i^{-\rho} \right) \leq y^{-\frac{\rho}{\sigma}} \Leftrightarrow \sum_{i=1}^n A^{-\frac{\rho}{\sigma}} \alpha_i x_i^{-\rho} y^{\frac{\rho}{\sigma}} \leq 1, \quad (18)$$

which transforms the problem (15)-(17) into a GP problem (15)-(16) and (18) written in standard form. According to (Boyd et al., 2007) and (Duffin et al., 1967), the corresponding dual of (15)-(16) and (18) is the following problem:

$$M = \max_{\substack{\beta, \gamma, \delta_i, \varepsilon_i > 0 \\ i=1, 2, \dots, n}} \left(\frac{1}{\beta} \right)^\beta \cdot \left(\frac{p^{-1}}{\gamma} \right)^\gamma \cdot \prod_{i=1}^n \left(\left(\frac{p^{-1} v_i}{\delta_i} \right)^{\delta_i} \left(\frac{A^{-\rho/\sigma} \alpha_i}{\varepsilon_i} \right)^{\varepsilon_i} \right) \cdot \left(\gamma + \sum_{i=1}^n \delta_i \right)^{\gamma + \sum_{i=1}^n \delta_i} \cdot \left(\sum_{i=1}^n \varepsilon_i \right)^{\sum_{i=1}^n \varepsilon_i}, \quad (19)$$

s.t. $\beta = 1$

$$\begin{bmatrix} -1 & 1 & 0 & 0 & \dots & 0 & 0 & 0 & \dots & 0 \\ 0 & -1 & -1 & -1 & \dots & -1 & \rho/\sigma & \rho/\sigma & \dots & \rho/\sigma \\ 0 & 0 & 1 & 0 & \dots & 0 & -\rho & 0 & \dots & 0 \\ 0 & 0 & 0 & 1 & \dots & 0 & 0 & -\rho & \dots & 0 \\ \vdots & \vdots & \vdots & \vdots & \ddots & \vdots & \vdots & \vdots & \ddots & \vdots \\ 0 & 0 & 0 & 0 & \dots & 1 & 0 & 0 & 0 & -\rho \end{bmatrix}_{(n+2) \times (2n+2)} \cdot \begin{bmatrix} \beta \\ \gamma \\ \delta_1 \\ \vdots \\ \delta_n \\ \varepsilon_1 \\ \vdots \\ \varepsilon_n \end{bmatrix}_{(2n+2) \times 1} = \mathbf{0}, \quad (20)$$

where a null vector $\mathbf{0}$ in (20) has $n+2$ components, and $\beta > 0, \gamma > 0, \delta_i > 0, \varepsilon_i > 0, i = 1, 2, \dots, n$, are dual variables. From (20) we get

$$\beta = \gamma = 1, \quad (21)$$

$$\varepsilon_i = \frac{\delta_i}{\rho}, \quad i = 1, 2, \dots, n, \quad (22)$$

$$\sum_{i=1}^n \delta_i = \frac{\sigma}{1-\sigma}, \quad (23)$$

$$\sum_{i=1}^n \varepsilon_i = \frac{\sigma}{\rho(1-\sigma)}. \quad (24)$$

Note that from (8), (23) and the positivity of dual variables, it follows that the degree of homogeneity of CESPF must satisfy the following condition:

$$0 < \sigma < 1. \quad (25)$$

Furthermore, using (21)-(24), (19)-(20) becomes an unconstrained maximization problem

$$M = \max_{\substack{\delta_i > 0 \\ i=1, 2, \dots, n}} \left(\frac{p^{-1} A^{-1}}{1-\sigma} \right)^{\frac{1}{1-\sigma}} \left(\frac{\sigma}{1-\sigma} \right)^{\frac{\sigma}{\rho(1-\sigma)}} \prod_{i=1}^n \left(\frac{v_i \alpha_i^{1/\rho}}{\delta_i^{(\rho+1)/\rho}} \right)^{\delta_i}. \quad (26)$$

Let us solve (26) by using Lemma 1. Let

$$x_i = \frac{v_i \alpha_i^{1/\rho}}{\delta_i^{(\rho+1)/\rho}}, \quad w_i = \delta_i, \quad i = 1, 2, \dots, n, \quad (27)$$

$$w = w_1 + w_2 + \dots + w_n = \sum_{i=1}^n \delta_i \stackrel{(23)}{=} \frac{\sigma}{1-\sigma}. \quad (28)$$

According to (11), for all $r > 0$, the following inequality holds

$$\prod_{i=1}^n \left(\frac{v_i \alpha_i^{1/\rho}}{\delta_i^{(\rho+1)/\rho}} \right)^{\delta_i} \stackrel{(11)}{\leq} \left(\sum_{i=1}^n \frac{\delta_i}{\delta_1 + \dots + \delta_n} \left(\frac{v_i \alpha_i^{1/\rho}}{\delta_i^{(\rho+1)/\rho}} \right)^r \right)^{\frac{\delta_1 + \dots + \delta_n}{r}} = \left(\frac{1-\sigma}{\sigma} \right)^{\frac{\sigma}{r(1-\sigma)}} \left(\sum_{i=1}^n (v_i \alpha_i^{1/\rho})^r \delta_i^{1-r \cdot \frac{\rho+1}{\rho}} \right)^{\frac{\sigma}{r(1-\sigma)}}. \quad (29)$$

By choosing $r = \rho/(\rho+1)$, the right-hand side of (29) becomes the constant. Thus, from (26) and (29), we get

$$\left(\frac{p^{-1} A^{-1}}{1-\sigma} \right)^{\frac{1}{1-\sigma}} \left(\frac{\sigma}{1-\sigma} \right)^{\frac{\sigma}{\rho(1-\sigma)}} \prod_{i=1}^n \left(\frac{v_i \alpha_i^{1/\rho}}{\delta_i^{(\rho+1)/\rho}} \right)^{\delta_i} \leq \left(\frac{p^{-1} A^{-1}}{1-\sigma} \right)^{\frac{1}{1-\sigma}} \left(\frac{\sigma}{1-\sigma} \right)^{\frac{-\sigma}{1-\sigma}} \left(\sum_{i=1}^n v_i^{\frac{\rho}{\rho+1}} \alpha_i^{\frac{1}{\rho+1}} \right)^{\frac{(\rho+1)\sigma}{\rho(1-\sigma)}}. \quad (30)$$

Equality in (29)-(30) holds if and only if

$$\frac{v_i \alpha_i^{1/\rho}}{\delta_i^{(\rho+1)/\rho}} = \frac{v_1 \alpha_1^{1/\rho}}{\delta_1^{(\rho+1)/\rho}}, \quad i = 1, 2, \dots, n. \quad (31)$$

From (23) and (31) we get

$$\delta_i = \frac{\frac{\sigma}{1-\sigma} v_i^{\frac{\rho}{\rho+1}} \alpha_i^{\frac{1}{\rho+1}}}{\sum_{j=1}^n v_j^{\frac{\rho}{\rho+1}} \alpha_j^{\frac{1}{\rho+1}}}. \quad (32)$$

Thus, by definition of the strict global optimum, the strict global maximum M of (26), and at the same time of (19), is equal to the right-hand side of (30), and it is achieved if and only if $\delta_i, i=1,2,\dots,n$, satisfy (32). In addition, M represents the strict global minimum of (15)-(17). Furthermore, since $\max f = 1/(\min (1/f))$ for a positive function f , we can find π^{CES} from (10) via (12)-(17) as follows:

$$\pi^{CES} = M^{-1} = (pA(1-\sigma))^{1/(1-\sigma)} \left(\frac{\sigma}{1-\sigma} \right)^{\frac{\sigma}{1-\sigma}} \left(\sum_{i=1}^n v_i^{\frac{\rho}{\rho+1}} \alpha_i^{\frac{1}{\rho+1}} \right)^{\frac{-(1+\rho)\sigma}{\rho(1-\sigma)}}. \quad (33)$$

According to (Duffin et al., 1967), from (15)-(18) and (21)-(24), we have

$$z^{-1} = \beta M = M \Rightarrow z = M^{-1}, \quad (34)$$

$$p^{-1} y^{-1} z = \frac{\gamma}{\gamma + \sum_{j=1}^n \delta_j} = \frac{1}{1 + \sum_{j=1}^n \delta_j}, \quad (35)$$

$$p^{-1} v_i x_i y^{-1} = \frac{\delta_i}{\gamma + \sum_{j=1}^n \delta_j}, \quad i = 1, 2, \dots, n, \quad (36)$$

$$A^{-\rho/\sigma} \alpha_i x_i^{-\rho} y^{\rho/\sigma} = \frac{\varepsilon_i}{\sum_{j=1}^n \varepsilon_j}, \quad i = 1, 2, \dots, n, \quad (37)$$

from where we get

$$x_i^{CES} = \frac{\frac{\sigma}{1-\sigma} \left(\frac{\alpha_i}{v_i} \right)^{\frac{1}{\rho+1}}}{\sum_{k=1}^n v_k^{\frac{\rho}{\rho+1}} \alpha_k^{\frac{1}{\rho+1}}} \cdot \pi^{CES}, \quad i = 1, 2, \dots, n. \quad (38)$$

Thus, the strict global maximum of the profit maximization problem with CES technology π^{CES} is given by (33), and it is achieved for the input values given by (38).

Case 2. $-1 < \rho < 0$

If $-1 < \rho < 0$, then the function $x \mapsto x^{-\rho/\sigma}$ is increasing (for all $x > 0$). In this case, inequality (17) is equivalent to

$$A^{\frac{\rho}{\sigma}} \left(\sum_{i=1}^n \alpha_i x_i^{-\rho} \right) \geq y^{\frac{\rho}{\sigma}} \Leftrightarrow - \sum_{i=1}^n A^{\frac{\rho}{\sigma}} \alpha_i x_i^{-\rho} y^{\frac{\rho}{\sigma}} \leq -1, \quad (39)$$

so (15)-(17) becomes a signomial geometric programming problem (15)-(16) and (39). SGP problem (15)-(16) and (39) can be solved similarly to (15)-(16) and (18). The only difference is changing parameter $\rho < 0$ by $-\rho > 0$ into equations (19)-(24). From that, by doing some algebraic calculations, it follows that the solution in this case is

$$\pi^{CES} = (pA(1-\sigma))^{1/(1-\sigma)} \left(\frac{\sigma}{1-\sigma} \right)^{\frac{\sigma}{1-\sigma}} \left(\sum_{i=1}^n v_i^{\frac{-\rho}{1-\rho}} \alpha_i^{\frac{1}{1-\rho}} \right)^{\frac{-(1-\rho)\sigma}{-\rho(1-\sigma)}}, \quad (40)$$

$$x_i^{CES} = \frac{\frac{\sigma}{1-\sigma} \left(\frac{\alpha_i}{v_i} \right)^{\frac{1}{-\rho+1}}}{\sum_{k=1}^n v_k^{\frac{-\rho}{-\rho+1}} \alpha_k^{\frac{1}{-\rho+1}}} \cdot \pi^{CES}, \quad i = 1, 2, \dots, n. \quad (41)$$

Note that (40) and (41) have the same form as (33) and (38), respectively, where the only difference is the change of parameter ρ with $-\rho$.

The profit maximization problem with Cobb-Douglas technology

In this section, we show that the solution to the profit maximization problem with Cobb-Douglas technology given by (4)-(5) is the limiting case of (33) and (38) when $\rho > 0$, i.e. the limiting case of (40)-(41) when $-1 < \rho < 0$. Let us first show how the Cobb-Douglas production function can be obtained from the CES production function. Let CDPF be given by (1) where (3) holds. Let us define

$$\sigma = \sum_{i=1}^n \varphi_i, \quad (42)$$

$$\alpha_i = \frac{\varphi_i}{\sigma}, \quad i = 1, 2, \dots, n. \quad (43)$$

Note that (3) and (42) imply (25). Furthermore, note that

$$\sum_{i=1}^n \alpha_i \stackrel{(43)}{=} \sum_{i=1}^n \frac{\varphi_i}{\sigma} = \frac{1}{\sigma} \sum_{i=1}^n \varphi_i \stackrel{(42)}{=} 1. \quad (44)$$

Let

$$U = \lim_{\rho \rightarrow 0} A \left(\sum_{j=1}^n \alpha_j x_j^{-\rho} \right)^{-\frac{\sigma}{\rho}}. \quad (45)$$

Since (44) holds, by taking a natural logarithm and after applying L'Hospital's rule, from (45) we have

$$\begin{aligned} \ln U &= \ln A + \lim_{\rho \rightarrow 0} \frac{-\sigma \ln \left(\sum_{i=1}^n \alpha_i x_i^{-\rho} \right)}{\rho} \stackrel{L'H}{=} \ln A + \lim_{\rho \rightarrow 0} \frac{\sigma \sum_{i=1}^n (x_i^{-\rho} \ln x_i^{\alpha_i})}{\sum_{i=1}^n \alpha_i x_i^{-\rho}} = \\ &= \ln A + \frac{\sigma \sum_{i=1}^n \ln x_i^{\alpha_i}}{\sum_{i=1}^n \alpha_i} = \ln A + \frac{\sum_{i=1}^n \ln x_i^{\sigma \alpha_i}}{1} = \ln \left(A \prod_{i=1}^n x_i^{\sigma \alpha_i} \right) \stackrel{(43)}{=} \ln \left(A \prod_{i=1}^n x_i^{\alpha_i} \right). \end{aligned} \quad (46)$$

Then, from (46) we have

$$U = \lim_{\rho \rightarrow 0} A \left(\sum_{i=1}^n \alpha_i x_i^{-\rho} \right)^{-\frac{\sigma}{\rho}} = A \prod_{i=1}^n x_i^{\alpha_i}. \quad (47)$$

Thus, the Cobb-Douglas production function given by (1) is the limit when $\rho \rightarrow 0$ of the CES production function given by (6).

Further, let us show how π^{C-D} from (4) can be obtained from π^{CES} . From (33) we have

$$\begin{aligned} \lim_{\rho \rightarrow 0^+} \pi^{CES} &= \lim_{\rho \rightarrow 0} (pA(1-\sigma))^{1-\sigma} \left(\frac{\sigma}{1-\sigma} \right)^{\frac{\sigma}{1-\sigma}} \left(\sum_{i=1}^n v_i^{\frac{\rho}{\rho+1}} \alpha_i^{\frac{1}{\rho+1}} \right)^{\frac{-(\rho+1)\sigma}{\rho(1-\sigma)}} \\ &= (pA(1-\sigma))^{1-\sigma} \left(\frac{\sigma}{1-\sigma} \right)^{\frac{\sigma}{1-\sigma}} \cdot \Lambda, \end{aligned} \quad (48)$$

where

$$\Lambda = \lim_{\rho \rightarrow 0^+} \left(\sum_{i=1}^n v_i^{\frac{\rho}{\rho+1}} \alpha_i^{\frac{1}{\rho+1}} \right)^{\frac{-(1+\rho)\sigma}{\rho(1-\sigma)}}. \quad (49)$$

Since (44) holds, by taking a natural logarithm and after applying L'Hospital's rule, from (49) we have

$$\begin{aligned} \ln \Lambda &= \lim_{\rho \rightarrow 0^+} \frac{-(\rho+1)\sigma \ln \left(\sum_{i=1}^n v_i^{\frac{\rho}{\rho+1}} \alpha_i^{\frac{1}{\rho+1}} \right)}{\rho(1-\sigma)} = \\ &\stackrel{L'H}{=} \lim_{\rho \rightarrow 0^+} \frac{-\sigma \ln \left(\sum_{i=1}^n v_i^{\frac{\rho}{\rho+1}} \alpha_i^{\frac{1}{\rho+1}} \right) - (\rho+1)\sigma \left(\frac{1}{(\rho+1)^2} \sum_{i=1}^n v_i^{\frac{\rho}{\rho+1}} \alpha_i^{\frac{1}{\rho+1}} \ln \frac{v_i}{\alpha_i} \right)}{1-\sigma} \\ &= -\frac{\sigma}{1-\sigma} \sum_{i=1}^n \alpha_i \ln \frac{v_i}{\alpha_i} = \ln \prod_{i=1}^n \left(\frac{v_i}{\alpha_i} \right)^{\frac{\sigma \alpha_i}{1-\sigma}}. \end{aligned} \quad (50)$$

Thus, from (42)-(43) and (48)-(50) we have

$$\begin{aligned}
 \lim_{\rho \rightarrow 0^+} \pi^{CES} &= (pA(1-\sigma))^{1-\sigma} \left(\frac{\sigma}{1-\sigma} \right)^{\frac{\sigma}{1-\sigma}} \prod_{i=1}^n \left(\frac{v_i}{\alpha_i} \right)^{\frac{-\sigma \alpha_i}{1-\sigma}} \\
 &= (pA)^{1/(1-\sum_{i=1}^n \varphi_i)} (1-\sigma) \sigma^{\frac{\sigma}{1-\sigma}} \prod_{i=1}^n \left(\frac{v_i}{\varphi_i/\sigma} \right)^{\frac{-\varphi_i}{1-\sum_{i=1}^n \varphi_i}} \\
 &= (pA)^{1/(1-\sum_{i=1}^n \varphi_i)} (1-\sigma) \sigma^{\frac{\sigma}{1-\sigma}} \sigma^{\frac{-\sigma}{1-\sigma}} \prod_{i=1}^n \left(\frac{v_i}{\varphi_i} \right)^{\frac{-\varphi_i}{1-\sum_{i=1}^n \varphi_i}} \\
 &= (pA)^{1/(1-\sum_{i=1}^n \varphi_i)} \left(1 - \sum_{i=1}^n \varphi_i \right) \prod_{i=1}^n \left(\frac{v_i}{\varphi_i} \right)^{\frac{-\varphi_i}{1-\sum_{i=1}^n \varphi_i}} \\
 &= \pi^{C-D}.
 \end{aligned} \tag{51}$$

Thus, the profit π^{C-D} from (4) is the limit when $\rho \rightarrow 0^+$ of the profit π^{CES} from (33). When $-1 < \rho < 0$, by using a similar procedure, we can show that the profit π^{C-D} from (4) is the limit when $\rho \rightarrow 0^-$ of the profit π^{CES} from (40).

Finally, let us show how x_i^{C-D} from (5) can be obtained from x_i^{CES} , $i = 1, 2, \dots, n$. Let

$$V_i = \lim_{\rho \rightarrow 0^+} x_i^{CES}, \quad i = 1, 2, \dots, n. \tag{52}$$

Since (43)-(44) hold, from (38), (51) and (52) we have

$$\begin{aligned}
 V_i &= \lim_{\rho \rightarrow 0^+} \frac{\frac{\sigma}{1-\sigma} \left(\frac{\alpha_i}{v_i} \right)^{\frac{1}{\rho+1}}}{\sum_{k=1}^n v_k^{\frac{\rho}{\rho+1}} \alpha_k^{\frac{1}{\rho+1}}} \cdot \pi^{CES} = \lim_{\rho \rightarrow 0^+} \frac{\frac{\sigma}{1-\sigma} \left(\frac{\alpha_i}{v_i} \right)^{\frac{1}{\rho+1}}}{\sum_{k=1}^n v_k^{\frac{\rho}{\rho+1}} \alpha_k^{\frac{1}{\rho+1}}} \cdot \lim_{\rho \rightarrow 0^+} \pi^{CES} = \\
 &= \frac{\frac{\sigma}{1-\sigma} \cdot \frac{\alpha_i}{v_i}}{\sum_{k=1}^n 1 \cdot \alpha_k^1} \cdot \pi^{C-D} = \frac{\sigma}{1-\sigma} \cdot \frac{\varphi_i/\sigma}{v_i} \cdot \pi^{C-D} = \frac{\pi^{C-D} \varphi_i}{v_i \left(1 - \sum_{k=1}^n \varphi_k \right)} \\
 &= x_i^{C-D}.
 \end{aligned} \tag{53}$$

Thus, x_i^{C-D} from (5) is the limit when $\rho \rightarrow 0^+$ of x_i^{CES} , $i = 1, 2, \dots, n$, from (38). When $-1 < \rho < 0$, by using a similar procedure, we can show that x_i^{C-D} from (5) is the limit when $\rho \rightarrow 0^-$ of x_i^{CES} , $i = 1, 2, \dots, n$ from (41).

Conclusion

One of the most important problems in economics is the firm's profit maximization problem. In this paper, we solved the profit maximization problem with CES technology with $n \geq 2$ inputs using a geometric programming approach and power mean inequality. Unlike multivariable calculus, this procedure does not require checking nontrivial necessary and sufficient conditions. Instead, a unique solution followed by power mean inequality and the definition of a strict global maximum directly. Finally, by using L'Hospital rule only, we showed how the solution to the profit maximization problem with Cobb-Douglas technology could be derived from the CES technology case.

Recommendations

Given that the geometric programming approach to the profit maximization problem bypasses checking nontrivial necessary and sufficient conditions when multivariable calculus is used, educators could incorporate this technique into classrooms to present this important topic in a complementary way. Since geometric

programming and the power mean inequality are simple optimization techniques without derivatives, they can provide new insights into the given problem to managers, students, and other audiences who may be unfamiliar with multivariable calculus.

Scientific Ethics Declaration

The author declares that the scientific ethical and legal responsibility of this article published in EPSTEM journal belongs to the author.

Acknowledgements or Notes

This article was presented as an oral presentation at the International Conference on Basic Sciences, Engineering and Technology (www.icbasaset.net) conference held in Istanbul/Turkey on August 25-28, 2022.

No funding was received for conducting this study.

References

- Avvakumov, S. N., Kiselev, Yu. N., Orlov, M. V., & Taras'ev, A. M. (2010). Profit maximization problem for cobb-douglas and CES production function. *Computational Mathematics and Modeling*, 21, 336-378.
- Angeli, E., Wagner, J., Lawrick, E., Moore, K., Anderson, M., Soderland, L., & Brizee, A. (2010, May 5). General format. <http://owl.english.purdue.edu/owl/resource/560/01/> <https://doi.org/10.1007/s10598-010-9075-5>
- Boyd, S., Kim, S.-J., Vanderberghe, L., & Hassibi, A. (2007). A tutorial on geometric programming. *Optimization and Engineering*, 8, 67-127. <https://doi.org/10.1007/s11081-007-9001-7>
- Beightler, C. S., & Philips, D. T. (1976). Applied geometric programming. New York: John Wiley & Sons.
- Bullen, P. S. (2003). *Handbook of means and their inequalities*. Springer Dordrecht. <https://doi.org/10.1007/978-94-017-0399-4>
- Duffin, R. J., Peterson, E. L., & Zener, C. (1967). *Geometric programming – theory and applications*. New York: John Wiley & Sons.
- Jehle, G. A., & Reny, P. J. (2011). *Advanced microeconomic theory*. New Jersey: FT Prentice.
- Kojić, V. & Lukač, Z. (2018). Solving profit maximization problem in case of the Cobb-Douglas production function via weighted AG inequality and geometric programming. Proceedings from: *2018 IEEE International Conference on Industrial Engineering and Engineering Management (IEEM)*, Bangkok, Thailand, 1900-1903. <https://doi.org/10.1109/IEEM.2018.8607446>
- Liu, S. T. (2006). A geometric programming approach to profit maximization. *Applied Mathematics and Computation*, 182, 1093-1097. <https://doi.org/10.1016/j.amc.2006.04.061>
- Reklaitis G., Salas, V., & Whinston, A. (1975). *Duality and geometric programming*. <https://pure.iiasa.ac.at/id/eprint/283/1/WP-75-145.pdf>
- Zevelev, A. A. (2014, November). *Closed form solutions in economics*. <https://ssrn.com/abstract=2354226>

Author Information

Vedran Kojić

Faculty of Economics and Business, University of Zagreb
Trg J. F. Kennedyja 6, 10000 Zagreb, Croatia
Contact e-mail: vkojic@efzg.hr

To cite this article:

Kojić, V. (2022). On a geometric programming approach to profit maximization: the case of CES technology. *The Eurasia Proceedings of Science, Technology, Engineering & Mathematics (EPSTEM)*, 18, 7-15.

The Eurasia Proceedings of Science, Technology, Engineering & Mathematics (EPSTEM), 2022

Volume 18, Pages 16-21

ICBASSET 2022: International Conference on Basic Sciences, Engineering and Technology

De Novo Gold Nanoparticles Activate P53 by Inhibiting NF-Kb Signalling in Breast Cancer Cells

Muhammad SAFDAR

Gaziantep University

Mehmet OZASLAN

Gaziantep University

Abstract: The aim of this study was to make de novo gold nanoparticles (Au(0)NPs) that turn on p53 and turn off NF-kB signaling in SKBR3 breast cancer cells. The chemical method was used to make the erythromycin-based Au(0)NPs. Authentic techniques were used to figure out what these Au(0)NPs were like. In the end, relative gene expression studies were used to treat SKBR3 breast cancer cells with these Au(0)NPs as a nanomedicine. When Au(0)NPs were present, the levels of caspases 3, 8, and 9 changed, p53 was turned on, and NF-kB was turned off at the same time. Compared to normal breast cells, the number of breast cancer cells (SKBR3) that could live was cut down (CRL-4010). Gene expressions of caspases also showed that the data were correct. When AuNPs were used to treat breast cancer cells, it was found that p53 and NF-kB had the opposite relationship. The study laid out a first step for using newly made AuNPs as a chemotherapeutic agent to treat SKBR3 cells.

Keywords: Gold nanoparticles, Erythromycin, Gene expression, Cell Viability, Breast Cancer

Introduction

Patients with breast cancer are also more likely to become resistant to chemotherapy, and relapses of the disease are widely accepted (Sung et al., 2021). Following the development of multidrug resistance that is complicated due to many factors that cause, is a major problem for breast cancer treatment (Nedeljkovic & Damjanovic, 2019).

Researchers are interested in chemotherapies that use nanoparticles. When gold nanoparticles (AuNPs) are used to treat cancer, the results have been very positive (Mousavi et al., 2007; Shreyash et al., 2021). Not only do these particles stop the growth of cancers (Safdar et al., 2022; Safdar et al., 2019) other than normal cells, but they induce apoptosis that is the main goal of cancer drugs (López-Barrera et al., 2021), and you can easily see how they work by looking at caspases. Also, the action of gold nanoparticles on the tumour suppressor p53 (López-Barrera et al., 2021) that is involved in the apoptosis pathways (Kanamori et al., 2021). It is also known that NF-kB work inversely to p53, and breast cancer cells have too much of it (Ge et al., 2021). So, stopping NF-kB could be used as a chemotherapeutic target. Also, in some studies it is found that the p53 and NF-kB followed different pathways due to change of drugs in the tumor cells (Gottstein et al., 2013). Furthermore, it had been seen that if gene expression changes had been done in the p53 gene then it led to change NF-kB and finally induce different cancers (Fadaka et al., 2021). Even though there are some drugs that selectively turn on p53 or turn off NF-kB with multiple side effects. Therefore, it is a need of time for specific nano-drugs that can control different pathways to inhibit breast cancers. So, a major goal for making new cancer drugs is to turn on p53 and shut down the NF-kB pathway (Arshad et al., 2019; Safdar & Ozaslan, 2022; Safdar et al., 2021).

The purpose of this study was to synthesize de novo gold nanoparticles activate p53 by inhibiting NF-kB signalling in breast cancer cell lines by using MTT and qRT-PCR assays.

- This is an Open Access article distributed under the terms of the Creative Commons Attribution-Noncommercial 4.0 Unported License, permitting all non-commercial use, distribution, and reproduction in any medium, provided the original work is properly cited.

- Selection and peer-review under responsibility of the Organizing Committee of the Conference

Method

Preparation of gold nanoparticles

For the first time, it was shown that the er-AuNPs were made with the help of erythromycin (er) as a reducing agent and a capping agent. For the making of er-AuNPs, 0.5 mL of a 0.01 M solution of HAuCl₄ salts was put in a glass beaker and put on a hotplate at 100 °C for 20 minutes. Then, 0.1 mL of a 0.01 M solution of NaOH was added, and the mixture was left for 1 hour to develop its properties. The solution proceeded from yellow to purple, which shows that the AuNPs were there. Also, UV Vis, XRD, and FT-IR were used to find out more about these newly made AuNPs. Lastly, SKBR3 cell lines were used to test the cytotoxicity of these nanoparticles. The average size of AuNPs was between 10 and 50 nm. These particles were made in culture media with 0–200 g/mL of serum or no supplements.

Cell Culture

Human breast epithelium CRL-4010 and breast cancer cell line SKBR3 were grown in Dulbecco's modified Eagle's medium with 10% foetal calf serum and antibiotic-antimycotic solution (100 U/mL penicillin, 0.1 mg/ml streptomycin, and 0.25 g/mL amphotericin B). Cells were grown in a sterile, humidified, 37°C environment with 5% CO₂ until they reached full growth.

Cell Viability

Researchers used the MTT assay to measure how alive the cells were. In a 96-well plate with 3000 cells per well, er-AuNP was put in front of cells for 24 hours. Used media was thrown away and replaced with 10 mg/mL of MTT reagent and 100 L of new media (1:9). Another hour of incubation at 37 °C was given to the chromogen reaction to take place. The cells were washed with PBS, and 100 L/well of dimethyl sulfoxide was added to dissolve the formazan crystals. A microplate spectrophotometer was used to measure the absorbance at a wavelength of 505 nm (Molecular Devices). At least three separate experiments with at least duplicate samples were done.

qRT-PCR

Cells were grown in a 25 cm² flask, and the NucleoZOL method was used to get the total RNA from the cells (Macherey-Nagel, Germany). In a PCR thermal cycler, a "Precision Reverse Transcription Kit" (made by Qiagen in Germany) was used to do the reverse transcription (Applied BioSystems, USA). By comparing the transcript levels of NF-κB, p53, and caspases to the level of the housekeeping gene GAPDH, real-time PCR was used to find out how these levels changed. The reactions went through 40 cycles with 94 °C for 30 sec, 55-60°C for 45 sec, and 72 °C for 45 sec along with a final extension step of 72 °C for 4 min. Changes in gene expression between groups were found using the method called $2^{-\Delta\Delta CT}$.

Results

After 24 hours, the amount of AuNP were used to treat CRL-4010 and SKBR3 cells induced and evaluate the cell viability. But the response to treatment was stronger in SKBR2 cancer cells than in normal cells. Starting at a concentration of 50 g/ml, when AuNP was added to SKBR3 cells, the IC₅₀ of the cells went down. Cancer cells treated with AuNP showed clear signs of cell death, while normal breast cells lost much less cell viability (Fig. 1). So, we knew that AuNPs were selective for cancer cells because at a higher dose of 150 µg/ml, only 50% of the normal CRL-4010 cells were still alive.

In this study, we investigated how er-AuNP affected the various genes including p53, NF-κB and caspases in CRL-4010 and SKBR3 cell lines. These results showed that Casp3, Casp8, and Casp9 were higher in er-AuNP treated CRL-4010 cells compared to untreated control cells, but p53 and NF-κB gene expression was almost the same in both groups of cells. On the other hand, the mRNA transcripts for p53, Casp3, Casp8, and Casp9 went up a lot in the SKBR3 cells. But when AuNP was added to SKBR3 cells, NF-κB expression went down (Fig. 2). All of the genes selected were affected by the change in mRNA levels in SKBR3 cells.

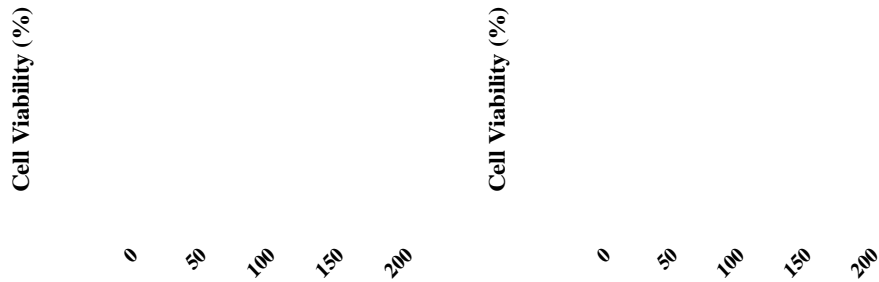


Figure. 1. Compared to CRL-4010 cell line, SKBR3 cell line was decreased when AuNPs were added. MTT showed that SKBR3 were more decreased than CRL-4010 and after being exposed to 0-200g/mL AuNP concentrations. All the data is represented in the form of *P 0.01; **P 0.001; ***P 0.0001.

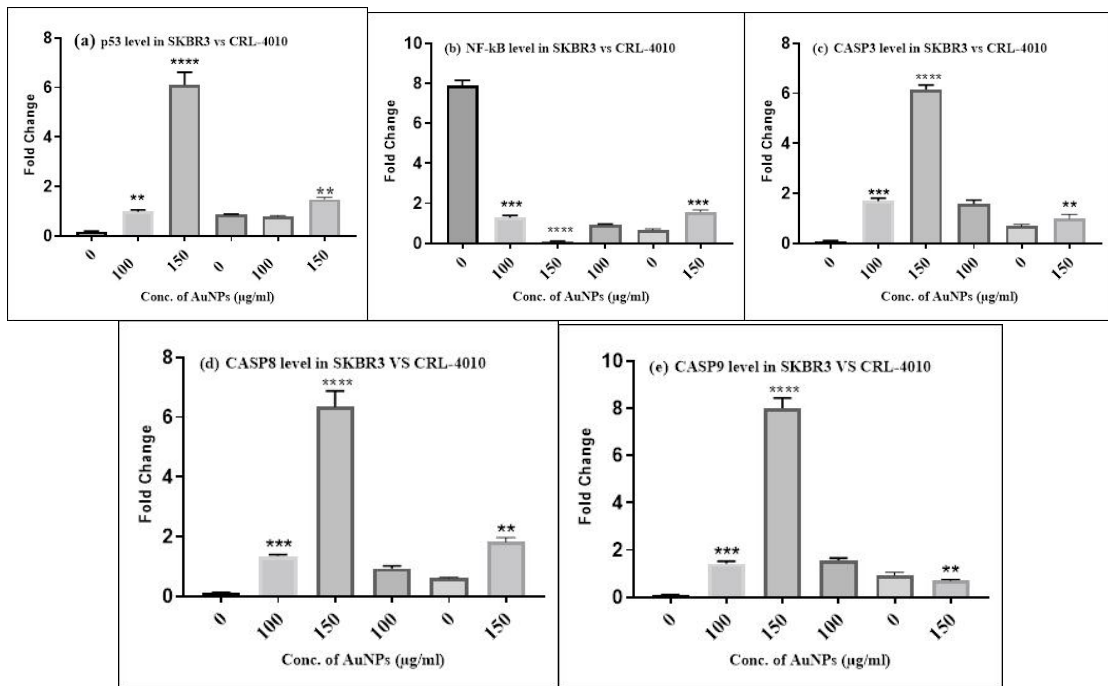


Figure. 2. When AuNP was added to SKBR3 for 24 hours, the p53 gene gene expression increased and the NF-kB gene expression dropped down. The amounts of targeted genes (p53, caspases 3, 8, and 9, and NF-kB) mRNA transcript continued to persist in CRL-4010 (control) cells. The levels of p53, caspases 3, 8, and 9, as well as the levels of NF-kB mRNA gene transcripts, were significantly changed in SKBR3 breast cancer cells. *P<0.05, **P<0.01 (Figure. 2a-e).

Discussion

Due to their unique ability to sense tumours, AuNPs have become very promising materials for treating malignant tumours. Because of this, AuNPs have been thought of for a long time as a possible tool for diagnosing and treating different types of cancer. In this study, we talked about the likely way that newly made er-AuNPs induce apoptosis in SKBR3 cells and how exposure to er-AuNPs changes in the targeted genes particularly p53 and NF-kB (Fig. 1&2). Previously, different nanoparticles were used by some researchers to show that these mechanisms were at work in human hepatocellular carcinoma cells (Ahmadian et al., 2018). It is also known that AuNPs have less toxicity as compared to other nanoparticles so they can be used as chemotherapeutics (Khan et al., 2021). Also, this study made it clear that 50-99 µg/ml concentrations of these nanoparticles were best on SKBR3 cells at the same concentration (cancer cells). Other concentrations, like 150 and 200 µg/ml, were very harmful to both healthy and cancerous cells. That was the real reason we did not use them in gene expression studies on both normal and cancer cells. Researchers may need to look into this more.

Nanomaterials also have a special property called cell-dependent cytotoxicity, which has been seen in HT29 and HeLa (Shejawal et al., 2021), MCF-7 (Uzma et al., 2020), and A459 (Niloy et al., 2021) cancer cells.

It is a known fact that the apoptosis is followed by both pathways (intrinsic and extrinsic) (Rajendran et al., 2021) that led to the planned death of the cells. The cytochrome C is a key protein that attach to Apaf-1 (Bock & Tait, 2020) that is released when a cell dies through the intrinsic pathway. Apaf1 turns on caspase 9, which turns on caspase 3, which is a very important part of cell death (Bock & Tait, 2020). Death receptors, on the other hand, turn on caspase 8, which then turns on caspase 3 (Muscari et al., 2020). The intrinsic pathway is now turned on by caspase 3 (Muscari et al., 2020; Safdar et al., 2020; Vo-Dinh et al., 2005). In this study, mRNA expression (caspase 9, 8, and 3) of the targeted genes were very low in normal CRL-4010 cells but it was more than four folds in cancerous SKBR3 cells. This shows that AuNPs work more specifically on cancer cells (Fig. 2). This meant that AuNPs sped up both the internal and external apoptotic cascades in breast cancer cells, which led to the death of the cells. Even when cancer cells were only exposed to 50 M of AuNPs, the expression of caspase 3 went up by a large amount (Safdar et al., 2021). So far as we know, this is the first report that shows how er-AuNPs affect both apoptotic cascades in breast cancer cells. Still, more research is needed to figure out how AuNPs cause cell death at the molecular level. One problem with this study was that it only used in-vitro experiments. More research will be needed to see how AuNPs work in in-vivo models before they can be used as a treatment for breast cancer.

Conclusion

So, these results showed that the newly synthesised and characterised er-AuNPs are a new and promising nanomaterial for a robust evidence-based analysis of chemotherapeutics. Using er-AuNPs could be a smart way to figure out where breast cancer could be spreading. Using relative gene expression studies, changes in caspases 3, 8, and 9 as well as dependence on p53 and NF-kB were found to be higher in SKBR3 than in normal breast cells (CRL-4010).

Recommendations

The study laid out the first step toward using er-AuNPs as a chemotherapeutic and suggested that more research to be done. Also, we recommend the nano-ELISA for further protein analysis.

Scientific Ethics Declaration

The authors declare that the scientific ethical and legal responsibility of this article published in EPSTEM journal belongs to the authors.

Acknowledgements or Notes

* This article was presented as an oral presentation at the International Conference on Basic Sciences, Engineering and Technology (www.icbaset.net) conference held in Istanbul/Turkey on August 25-28, 2022.

References

- Ahmadian, E., Dizaj, S. M., Rahimpour, E., Hasanzadeh, A., Eftekhari, A., Halajzadeh, J., & Ahmadian, H. (2018). Effect of silver nanoparticles in the induction of apoptosis on human hepatocellular carcinoma (HepG2) cell line. *Materials Science and Engineering: C*, *93*, 465-471.
- Arshad, M., Ozaslan, M., Ali, H., Safdar, M., Junejo, Y., & Babar, M. (2019). Molecular investigation of gold nanoparticles toxicity in mice model and p53 activation. *J Biol Sci*, *19*, 391-395.
- Bock, F. J., & Tait, S. W. (2020). Mitochondria as multifaceted regulators of cell death. *Nature Reviews Molecular Cell Biology*, *21*(2), 85-100.
- Fadaka, A., Aluko, O., Awawu, S. & Theledi, K. (2021). Green synthesis of gold nanoparticles using Pimenta dioica leaves aqueous extract and their application as photocatalyst, antioxidant, and antibacterial agents. *Journal of Multidisciplinary Applied Natural Science*, *1*(2).

- Ge, W., Wang, Y., Zheng, S., Zhao, D., Wang, X., Zhang, X., & Hu, Y. (2021). Nuclear iASPP determines cell fate by selectively inhibiting either p53 or NF- κ B. *Cell Death Discovery*, 7(1), 1-10.
- Gottstein, C., Wu, G., Wong, B. J., & Zasadzinski, J. A. (2013). Precise quantification of nanoparticle internalization. *ACS Nano*, 7(6), 4933-4945.
- Kanamori, Y., Finotti, A., Magno, L. D., Canettieri, G., Tahara, T., Timeus, F., . . . Fino, P. (2021). Enzymatic spermine metabolites induce apoptosis associated with increase of p53, caspase-3 and miR-34a in both neuroblastoma cells, SJNKP and the N-Myc-amplified form IMR5. *Cells*, 10(8), 1950.
- Khan, M. A., Singh, D., Ahmad, A., & Siddique, H. R. (2021). Revisiting inorganic nanoparticles as promising therapeutic agents: a paradigm shift in oncological theranostics. *European Journal of Pharmaceutical Sciences*, 164, 105892.
- López-Barrera, L. D., Díaz-Torres, R., Martínez-Rosas, J. R., Salazar, A. M., Rosales, C., & Ramírez-Noguera, P. (2021). Modification of proliferation and apoptosis in breast cancer cells by exposure of antioxidant nanoparticles due to modulation of the cellular redox state induced by doxorubicin exposure. *Pharmaceutics*, 13(8), 1251.
- Mousavi, S. M., Montazeri, A., Mohagheghi, M. A., Jarrahi, A. M., Harirchi, I., Najafi, M., & Ebrahimi, M. J. T. b. j. (2007). Breast cancer in Iran: an epidemiological review. *The Breast Journal*, 13(4), 383-391.
- Muscari, I., Adorisio, S., Liberati, A. M., Thuy, T. T., Van Sung, T., Cannarile, L., . . . Delfino, D. V. (2020). Bcl-xL overexpression decreases GILZ levels and inhibits glucocorticoid-induced activation of caspase-8 and caspase-3 in mouse thymocytes. *Journal of Translational Autoimmunity*, 3, 100035.
- Nedeljkovic, M., & Damjanovic, A. (2019). Mechanisms of chemotherapy resistance in triple-negative breast cancer-how we can rise to the challenge. *Cells*, 8(9). <https://doi.org/10.3390/cells8090957>
- Niloy, M. S., Shakil, M., Hossen, M., Alam, M., & Rosengren, R. J. (2021). Promise of gold nanomaterials as a lung cancer theranostic agent: a systematic review. *International Nano Letters*, 11(2), 93-111.
- Rajendran, I., Ponrasu, T., Rajaram, R., & Suguna, L. (2021). The apoptotic effect of ferulic acid-synthesized gold nanoparticles against human epidermoid carcinoma (A431) cells via activation of caspase-3 pathway. *Journal of Drug Delivery Science and Technology*, 63, 102478.
- Safdar, M., & Ozaslan, M. (2022). Enhanced catalytic, antibacterial and anti-cancer activities of erythromycin capped gold nanoparticles. *Journal of Inorganic and Organometallic Polymers and Materials*, 1-9.
- Safdar, M., Ozaslan, M., Junejo, Y., & Channa, I. S. (2022). Cytotoxic and anticancer activity of a novel synthesized tet-AuNPs simultaneously activates p53 and inhibits NF- κ B signaling in SKBR3 cell line. *Toxicology and Environmental Health Sciences*, 14(1), 69-76.
- Safdar, M., Ozaslan, M., Junejo, Y., & Channa, I. S. (2022). Cytotoxic and anticancer activity of a novel synthesized tet-AuNPs simultaneously activates p53 and inhibits NF- κ B signaling in SKBR3 cell line. *Toxicology and Environmental Health Sciences*, 14(1), 69-76.
- Safdar, M., Ozaslan, M., Khailany, R. A., Latif, S., Junejo, Y., Saeed, M., . . . Kanabe, B. O. (2019). Synthesis, characterization and applications of a novel platinum-based nanoparticles: catalytic, antibacterial and cytotoxic studies. *Journal of Inorganic and Organometallic Polymers and Materials*. <https://doi.org/10.1007/s10904-019-01387-7>
- Safdar, M., Ozaslan, M., Khailany, R. A., Latif, S., Junejo, Y., Saeed, M., . . . Materials. (2020). Synthesis, characterization and applications of a novel platinum-based nanoparticles: catalytic, antibacterial and cytotoxic studies. *30(7)*, 2430-2439.
- Shejawal, K. P., Randive, D. S., Bhinge, S. D., Bhutkar, M. A., Todkar, S. S., Mulla, A. S., & Jadhav, N. R. (2021). Green synthesis of silver, iron and gold nanoparticles of lycopene extracted from tomato: their characterization and cytotoxicity against COLO320DM, HT29 and Hella cell. *Journal of Materials Science: Materials in Medicine*, 32(2), 1-12.
- Shreyash, N., Sonker, M., Bajpai, S., & Tiwary, S. K. (2021). Review of the mechanism of nanocarriers and technological developments in the field of nanoparticles for applications in cancer theragnostics. *ACS Appl Bio Mater*, 4(3), 2307-2334. <https://doi.org/10.1021/acsabm.1c00020>
- Sung, H., Ferlay, J., Siegel, R. L., Laversanne, M., Soerjomataram, I., Jemal, A., & Bray, F. (2021). Global cancer statistics 2020: globocan estimates of incidence and mortality worldwide for 36 cancers in 185 countries. *CA Cancer J Clin*, 71(3), 209-249. <https://doi.org/10.3322/caac.21660>
- Uzma, M., Sunayana, N., Raghavendra, V. B., Madhu, C. S., Shanmuganathan, R., & Brindhadevi, K. (2020). Biogenic synthesis of gold nanoparticles using commiphora wightii and their cytotoxic effects on breast cancer cell line (MCF-7). *Process Biochemistry*, 92, 269-276.
- Vo-Dinh, T., Yan, F., & Wabuyele, M. B. (2005). Surface-enhanced Raman scattering for medical diagnostics and biological imaging. *Journal of Raman Spectroscopy: An International Journal for Original Work in all Aspects of Raman Spectroscopy, Including Higher Order Processes, and also Brillouin and Rayleigh Scattering*, 36(6-7), 640-647..

Author Information

Muhammad Safdar

Department of Biology, Gaziantep University
Gaziantep 27310, Turkey

Mehmet Ozaslan

Department of Biology, Gaziantep University
Gaziantep 27310, Turkey
Contact e-mail: ozaslanmd@yahoo.com

To cite this article:

Safdar, M. & Ozaslan, M. (2022). De novo gold nanoparticles activate P53 by inhibiting NF-Kb signalling in breast cancer cells. *The Eurasia Proceedings of Science, Technology, Engineering & Mathematics (EPSTEM)*, 18, 16-21.

The Eurasia Proceedings of Science, Technology, Engineering & Mathematics (EPSTEM), 2022

Volume 18, Pages 22-27

ICBASSET 2022: International Conference on Basic Sciences, Engineering and Technology

Mineralogical and Elemental Characterization of Conventional Asphalt of Peruvian Roadways by X-Ray Diffraction and Energy Dispersive X-ray Fluorescence

Jenny Aleida MONTOYA-BURGA

Universidad César Vallejo

Jorge Aurelio BRAVO-CABREJOS

Universidad Nacional Mayor de San Marcos (UNMSM)

Marlon Gastón FARFÁN-CÓRDOVA

Universidad César Vallejo

María Luisa CERÓN-LOAYZA

Universidad Nacional Mayor de San Marcos (UNMSM)

Felipe Américo REYES-NAVARRO

Universidad Nacional Mayor de San Marcos (UNMSM)

Abstract: This research deals with the characterization of a sample of conventional asphalt, which is used for the manufacture of roadways in the city of Trujillo, Peru. The sample has been designed by using the Marshall method, through which the optimal content of the asphalt mixture was determined for an adequate combination of the aggregates. This method includes the determination of the optimum content of asphalt cement, stability, unit weight, air voids, flow, voids in the mineral aggregate, and flow stability. The Marshall test was carried out after dosing for the traditional mixture. We have used two techniques: energy dispersive X-ray fluorescence and X-ray diffractometry. The identification and quantification of the chemical elements present was carried out by using energy dispersive X-ray fluorescence, and the mineralogical analysis, by using X-ray diffractometry. This work is useful as a source of reference information. Subsequently, it will allow the implementation of procedures for modifying asphalt mixtures to optimize their performance.

Keywords: Asphalt, Marshall method, X-ray diffraction, Energy dispersive, X-ray fluorescence

Introduction

All over the world, there is no human activity that does not require the use of communication routes, whether road, rail, sea, lake, river, or air. The importance and improvement of these routes keep close parallelism with the cultural, commercial, and industrial development of each country; they are the means by which religion, culture and commerce are introduced into the regions of primitive civilization of a country (Vignolo, 1943). There are two concepts closely related to roadways: bitumen and asphalt. Bitumen or bitumen asphalt is a black to dark brown, semi-solid organic material that gradually liquefies when heated. It is usually obtained as a residue from petroleum distillation by using atmospheric or vacuum distillation units. Asphalt is a natural or commercial mixture of bitumen and inert mineral matter. Natural asphalt occurs as surface deposits, or as a colloidal crude oil system near the surface. In America, the term *asphalt* is often synonymous with the material known in England as asphaltic bitumen or bitumen (Whitehead, 2005).

- This is an Open Access article distributed under the terms of the Creative Commons Attribution-Noncommercial 4.0 Unported License, permitting all non-commercial use, distribution, and reproduction in any medium, provided the original work is properly cited.

- Selection and peer-review under responsibility of the Organizing Committee of the Conference

© 2022 Published by ISRES Publishing: www.isres.org

Trujillo is the third most important city in Peru; however, due to various factors, it has a road infrastructure in poor conditions. This could improve with a detailed knowledge of the constituents of roads, which would allow defining asphalt modification mechanisms, and consequently, provide better performance to the roads.

The durability of asphalt pavements is directly influenced by the climate of the place where they are located. In addition, other parameters must be considered, such as the magnitude and frequency of the traffic loads, the properties of the materials that compose it, the characteristics of the subgrade, humidity, and the construction process, among others. Together, these parameters greatly affect pavement performance as well as increase its potential to develop permanent deformation failure (Warrior and Chang, 2015).

Due to the importance of pavements in population dynamics, all its components must comply with technical specifications that guarantee their good performance: from their preparation to the different tests to which they are subjected, depending on the function for which they are intended. In Peru, these tests are regulated by the Ministry of Transport and Communications. Thereupon, it is necessary to delve into the different aspects that are associated with the lifespan of pavements. In this work, we carried out elemental and mineralogical analyses of a conventional asphalt sample obtained by the Marshall method. We expect that the information obtained can serve as a reference for the elaboration of modified asphalts.

Materials and Methods

Before the analysis of the sample, we proceeded as indicated below.

Preparation of the Asphalt Mixture

The aggregates to be used in the asphalt mixture manufacturing are dried at a constant weight, that is, the sample is heated at 105 ± 0.5 °C for a certain time, after which it is weighed and then the procedure is repeated until no variation in mass is seen. After drying, the aggregates will be separated by dry sieving into suitable fractions. A detailed procedure for obtaining the asphalt mixture can be found in the Peruvian technical standard MTC E 504.

Method and Physical Techniques Applied

We have used the Marshall method to design the asphalt mixture. Also, the modified asphalt sample has been characterized by using the two techniques indicated below.

Marshall Method

We applied the Marshall test to the conventional mixture because it is the standard method of asphalt mixture design. The asphalt design content in the final paving mixture is determined by the following parameters: stability, unit weight, air void, flow, VMA, and stability/flow; VMA means Voids in Mineral Aggregate. The method is as follows: First, the asphalt content is determined for which the void content is 4%, and then the other parameters calculated and measured for this asphalt content are evaluated and compared with the design criteria. If all the criteria are met, the asphalt design content is optimal. Otherwise, we should make some readjustments or redesign the mix.

Energy Dispersive X-ray Fluorescence (EDXRF)

This technique allows detecting the presence of chemical elements with atomic number Z equal to and greater than 13 by detecting the characteristic X-rays emitted by atoms. The energy of these rays increases with Z , and they can be detected as long as they have enough energy to penetrate the window in the detector. Due to this limitation, the Na ($Z=11$) and Mg ($Z=12$) peaks cannot be recorded in the EDXRF spectrum. The source used emits X-rays in two components: one spectrum with a continuous distribution from 0 to 30 keV, and the other containing the L and M characteristic X-rays from silver atoms, which are produced by the bombardment of the silver anode by energetic electrons. Consequently, the EDXRF spectrum have three main components: a continuous component provoked by the scattering of the x-rays from the continuous component of the source, a

discrete spectrum produced by the scattering of the silver characteristic X-rays from the source, and a discrete spectrum of the characteristic X-rays emitted by the sample according to the elements it contains.

In the Archaeometry Laboratory of the Faculty of Physical Sciences (UNMSM), we determined the chemical composition of the sample by using a portable EDXRF equipment, Amptek brand, with a silver anode that operated at 30 kV and 15 μ A. Irradiation was carried out with the following setting: (a) incidence and exit angles of around 45°, (b) distance from sample to X-ray source: 4 cm, and (c) distance from sample to detector: 2 cm approx. The operating voltage and the applied current were regulated so that the counting rate did not exceed 5000 cts/s.

X-ray Diffraction (XRD)

This technique allows for the identification of the mineralogical phases in the sample. It is also known as X-ray crystallography and is based on the diffraction of X-rays by matter, especially when it is crystalline. This diffraction is an elastic scattering, which originates interferences. This technique uses a beam of X-rays which, upon encountering a crystal, are reflected in specific directions determined by the wavelength of the X-rays, lattice parameters, and orientation of the crystal.

Thus, we conveyed the sample to the Bizalab private laboratory, where the measurements on the sample carried out by using an Endeavor D4 diffractometer, Bruker model, with a copper tube that operated at 40kV and 40 mA. Likewise, a 2θ angular scan from 5° to 70° and a step of 0.02°/s was used. After obtaining the data, we identified the mineral phases by using the JCPDS-ICDD database. JCPDS means Joint Committee of Powder Diffraction Standards, and ICDD, International Center for Diffraction Data.

Discussion and Results

Table 1 shows the corresponding results of applying the Marshall method. Therein it is specified the parameters of Optimum Asphalt Content, stability, Unit Weight, Air Voids, Flow, VMA, Stability/Flow. The data are suitable so that the asphalt design content is optimal.

Table 1: Data from the Marshall test for the conventional asphalt mixture

| Characteristics of the Asphalt Mixture | |
|--|---------|
| Optimum Asphalt Content (%) | 5.30 |
| Stability (kg.) | 1215 |
| Unit Weight (kg/m ³) | 2.342 |
| Air Voids (%) | 4.00 |
| Flow (mm) | 3.35 |
| VMA (%) | 14.78 |
| Stability/Flow (kg/cm) | 3626.87 |

In the EDXRF spectra, we observe that the peaks are positioned at certain energy values which indicate the presence of the chemical element in the sample. Symbols for the corresponding chemical elements are identified on top of the peaks. The height of the peaks is an indicator of the concentration of the chemical element in the sample. The EDXRF spectrum of the sample is presented in Figure 1. Table 2 details the corresponding quantitative elemental analysis. Figure 2 shows graphically the results of elemental concentration for the sample studied.

Figure 3 shows the X-ray diffractogram of the sample, which, concerning its mineralogical composition, registers the presence of quartz (SiO₂), clinocllore (Mg,Fe²⁺)₅Al₂Si₃O₁₀(OH)₈, albite Na_{0,986}(Al_{1,005}Si_{2,995}O₈), and muscovite KAl₃Si₃O₁₀(OH)₂. The presence of Muscovite is not desirable, since, from the point of view of road construction, the presence of clay minerals results in greater use of bitumen. In addition, the lifespan of the pavement is reduced due to the low mechanical resistance of clay minerals (Geber and Gömze, 2015). An additional and important consequence of the small particle size is the high surface area to volume ratio (Parker & Rae, 1998). An indicator of the relative importance of surface effects is the specific surface area of a grain, which increases as the particle size decreases (Kaliakin et al., 2014). Thus, the presence of albite is not convenient either, since feldspars increase the specific surface area and decrease the mechanical resistance of the pavement (Geber & Gömze, 2015).

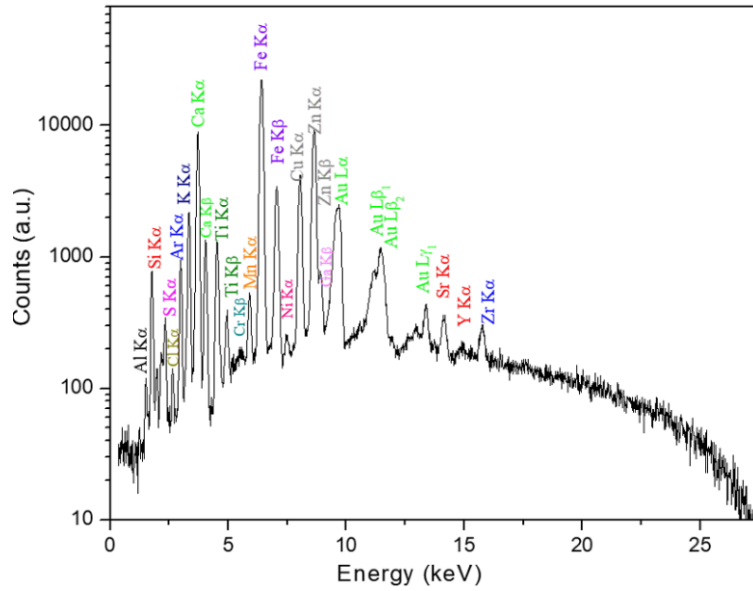


Figure 1. Energy dispersive X-ray fluorescence spectrum of the sample studied.

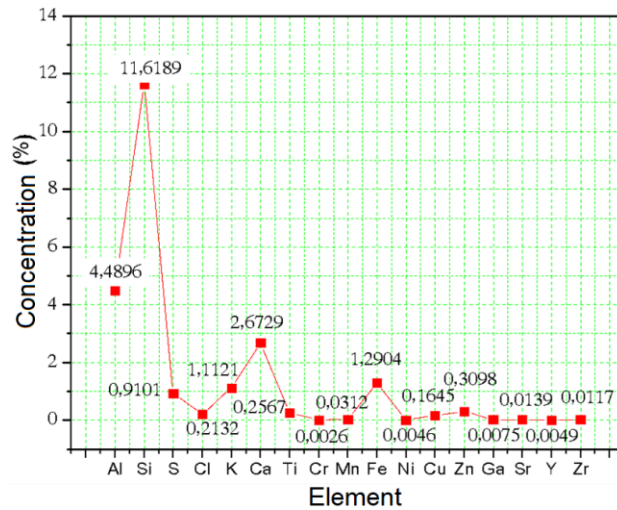


Figure 2. Graphic representation of quantitative analysis of the sample studied.

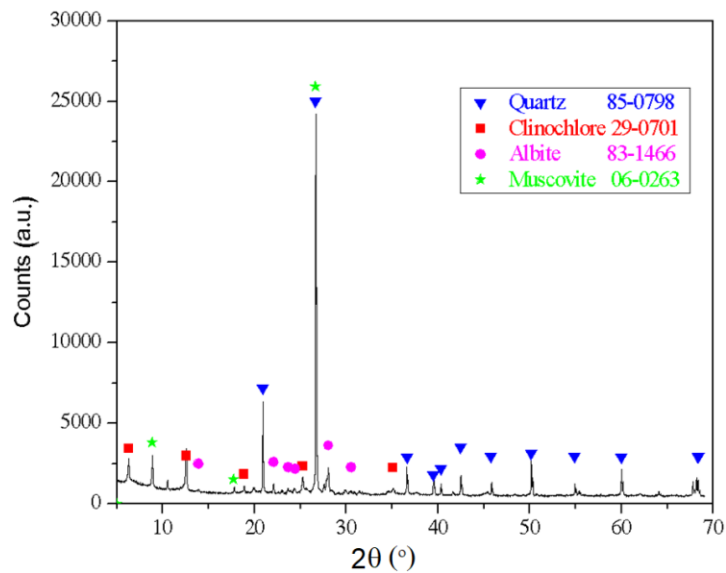


Figure 3. X-ray diffractogram of the sample. We noted the mineral composition and the codes from the JCPDS.

Conclusions

The sample studied presents aluminium, silicon, and calcium as major elements; to a lesser extent, sulphur, potassium, and iron are observed. Chlorine, titanium, chromium, manganese, nickel, copper, zinc, gallium, strontium, yttrium, and zirconium are minor elements. The mineralogical composition of the sample is formed by quartz, clinocllore, albite, and muscovite. We expect that the information obtained is useful so that modification procedures for asphalt mixtures are subsequently implemented to optimize their performance.

Recommendations

This work can be extended with the manufacturing of additional samples by the Marshal method, which have other percentages of optimum asphalt content and VMA.

Scientific Ethics Declaration

The authors declare that the scientific ethical and legal responsibility of this article published in EPSTEM journal belongs to the authors.

Acknowledgements

This article was presented as a poster presentation at the International Conference on Basic Sciences, Engineering and Technology (www.icbaset.net) conference held in Istanbul/Turkey on August 25-28, 2022.

References

- Cáceres, C. (2007). *Análisis de la metodología Superpave para el diseño de mezclas asfálticas en México* (Analysis of the Superpave methodology for the design of asphalt mixtures in Mexico), (Licentiate thesis). Universidad de las Américas Puebla. http://catarina.udlap.mx/u_dl_a/tales/documentos/lic/caceres_m_ca/
- Geber, R., & Gömze, L. (2010). Characterization of mineral materials as asphalt fillers. *Materials Science Forum*, 659, 471-476. <https://doi.org/10.4028/www.scientific.net/MSF.659.471>
- Huamán, N., & Chang, C. (2016). *La deformación permanente en las mezclas y el consecuente deterioro de los pavimentos asfálticos en el Perú* (Permanent deformation in mixtures and the consequent deterioration of asphalt pavements in Peru). *Perfiles de ingeniería*, 11 (11), 23-31. https://doi.org/10.31381/perfiles_ingenieria.v2i11.402
- Kaliakin, V., Mashayekhi, M., & Nieto-Leal, A. (2014). The time- and temperature-related behavior of clays: Microscopic considerations and macroscopic modelling. In L. R. Wesley (Ed.), *Clays and clay minerals: Geological origin, mechanical properties and industrial applications* (pp 1-44), Nova Publishers.
- Minaya, S., & Ordoñez, A. (2001). *Manual de laboratorio — Ensayos para pavimentos: Ensayos y agregados para pavimentos* (Laboratory manual — tests for pavements: Tests and aggregates for pavements). Universidad Nacional de ingeniería (UNI), Lima, Perú. https://www.academia.edu/6949875/MANUAL_DE_ENSAYOS_PARA_PAVIMENTOS
- Rae, J., & Parker, A. (1998). Environmental Interactions of Clays: Clays in Environmental Studies. IN J. Rae and A. Parker (Eds.), *Environmental Interactions of Clays: Clays and the Environment*. (pp 1-5). Springer.
- Vignolo, C. (1943). *Vías de comunicación en el Perú* (Communication routes in Peru). *Revista de la Universidad Católica del Perú*, 2, 81-91. <https://repositorio.pucp.edu.pe/index/bitstream/handle/123456789/53462/vias%20de%20comunicacion%20en%20el%20peru.pdf?sequence=1&isAllowed=y>
- Whitehead, E. V. (2005). Asphaltenes and asphalts. In T. F. Yen and G. V. Chilingarian (Eds.), *Fuel oil chemistry and asphaltenes* (pp 95-108), Elsevier.

Author Information

Jenny Aleida Montoya Burga

¹Universidad César Vallejo.

Av. Víctor Larco 1770, Trujillo, La libertad, Perú.

²Laboratorio de Análisis de Suelos, Facultad de Ciencias Físicas, UNMSM.

Av. Germán Amézaga 375, Cercado de Lima, Perú.

Contact e-mail: jmontoyab@ucvvirtual.edu.pe

Jorge Aurelio Bravo Cabrejos

Laboratorio de Análisis de Suelos, Facultad de Ciencias Físicas, UNMSM.

Av. Germán Amézaga 375, Cercado de Lima, Perú.

Marlon Gastón Farfán-Córdova

Universidad César Vallejo.

Instituto de Investigación en Ciencia y Tecnología.

Av. Víctor Larco 1770, Trujillo, La libertad, Perú.

María Luisa Cerón Loayza

Laboratorio de Análisis de Suelos, Facultad de Ciencias Físicas, UNMSM.

Av. Germán Amézaga 375, Cercado de Lima, Perú

Felipe Américo Reyes Navarro

Laboratorio de Análisis de Suelos, Facultad de Ciencias

Físicas, UNMSM.

Av. Germán Amézaga 375, Cercado de Lima, Perú.

To cite this article:

Montoya Burga, J.A., Bravo Cabrejos, J.A., Farfán-Córdova, M.G., Cerón Loayza, M.L., & Reyes Navarro, F.A. (2022). Mineralogical and elemental characterization of conventional asphalt of Peruvian roadways by x-ray diffractometry and energy dispersive x-ray fluorescence. *The Eurasia Proceedings of Science, Technology, Engineering & Mathematics (EPSTEM)*, 18, 22-27.

The Eurasia Proceedings of Science, Technology, Engineering & Mathematics (EPSTEM), 2022

Volume 18, Pages 28-36

ICBASSET 2022: International Conference on Basic Sciences, Engineering and Technology

Development of Two-Dimensional Thermal Analysis Code for the Analysis of 3D Printed PLA Parts

Buryan APACOGU-TURAN
İstanbul Technical University

Kadir KIRKKOPRU
İstanbul Technical University

Abstract: Fused Deposition Modelling is one of the main 3D printing methods to manufacture plastic parts. The strength of the printed part by FDM is dependent on polymer diffusion between printed layers. The polymer diffusion between two neighboring layers occur not only during the extrusion of the hot top layer, but also during the production of consecutive layers due to thermal conduction. The heat diffusion from upper layers enhances the curing of polymers, which consequently affects the strength of the part. Therefore, the history of the temperature variations - curing time and curing temperature - should be analyzed to predict the strength of the part. The goal of this study is to develop a two-dimensional transient thermal analysis solver for the investigation of time-dependent thermal changes during the printing process. This solver is developed with the use of finite difference method employed under implicit scheme. The transient temperature pattern is qualitatively compatible to the experimental results in literature. The solver can be utilized for further thermal analyses to correlate temperature, polymer diffusion and strength with the inclusion of deposition path in the third dimension.

Keywords: Heat transfer, Simulation, Computational methods, Additive manufacturing, Polymers

Introduction

Additive manufacturing technologies have been developing in recent years. In three-dimensional printers, which can be of different types for different types of materials, Fused-Deposition Modeling (FDM) is widely used to produce plastic parts. In this method, plastic filaments are melted through a moving nozzle and laid in layers on a surface. The polymer structures inside the plastic layers provide this adhesion by diffusing from one layer to the next (Wool & O'Connor, 1981).

Thanks to this approach, rapid prototyping can be performed with low costs. When compared to traditional manufacturing technologies such as CNC, it is seen that FDM method is a production method that consumes much less energy and generates much less waste (Faludi, Bayley, Boghal, & Iribarne, 2015). On the other hand; quality problems are observed in parts produced with FDM (Bikas, Stavropoulos, & Chryssolouris, 2016). The high durability of the part that comes out at the end of the production process depends on the completion of the diffusion of polymers (Bartolai, Simpson, & Xie, 2018). The ratio of the strength (σ_{weld}) of the part produced by FDM to the strength (σ_{∞}) of the bulk part with fully developed bonds gives the Bonding Degree (D_h) (Yang & Pitchumani, 2002):

$$D_h(t) = \frac{\sigma}{\sigma_{\infty}} \quad (1)$$

- This is an Open Access article distributed under the terms of the Creative Commons Attribution-Noncommercial 4.0 Unported License, permitting all non-commercial use, distribution, and reproduction in any medium, provided the original work is properly cited.

- Selection and peer-review under responsibility of the Organizing Committee of the Conference

According to Edward; a polymer is contained in a virtual tube where it does not interact with other polymers around it (Edward, 1988). The time required for the polymer to come out of this tube is called the reptation time (τ_{rep}). Materials that exceed the reptation time are able to form bonds that provide strength. According to Edward's Tube Theory; the shorter the reptation time, the faster the binding occurs. The reptation time is affected by the temperature of the polymer-polymer interlayer and the time-dependent variation of its temperature. The correlation showing this situation is as follows (Bartolai, Simpson, & Xie, 2018) :

$$\left| D_h(t) = \frac{\sigma_{weld}}{\sigma_{UTS}} \right. \quad (2)$$

In polymer-polymer interlayers that do not reach the reptation time, the durability (σ_{weld}) becomes lower. The welding time of the parts that cannot reach the reptation time is shown with t_{weld} . σ_{weld} is proportional to $(t_{weld})^{1/4}$ (Jud, Kausch, & Williams, 1981). With the help of this relation, the expression for the degree of bonding can be written in terms of times as follows:

$$\left| \frac{\sigma_{weld}}{\sigma_{UTS}} = \left(\frac{t_{weld}}{\tau_{rep}} \right)^{1/4} \right. \quad (3)$$

The main reason for quality problems is the variation of interlayer bond strength (polymer diffusion) depending on temperature and time-dependent changes in temperature (Yang & Pitchumani, 2002). In addition, the temperature in the interlayers and the history of temperature change affect the t_{weld} . For example; while the manufacturing process is at layer 30, how the temperature in layer 5 changes or rises above the glass transition temperature (T_g) will affect bonding. Hence, it is important to monitor the temperature of each layer during the production process. Time intervals above T_g at different layers should be examined for the estimation of bonding degree. It is expected that the layer with the shortest binding time will have the weakest point.

In an experimental study (Coogan & Kazmer, Bond and part strength in fused deposition modeling, 2017) it was observed that the strength of the upper layers was higher in the production scenario tested. It is stated that a comprehensive heat transfer analysis model and software is needed to predict which layer is the weakest in different scenarios. The authors in another study (Coogan & Kazmer, Healing simulation for bond strength prediction of FDM, 2017) modeled the top 2 layers by making 1-dimensional heat transfer calculation and stated that a two-dimensional analysis including fiber thickness should be performed. In scope of this study, a two-dimensional transient heat transfer analysis code is developed. The effect of parameters related to heat transfer during FDM, such as extrusion temperature, layer thickness, heating-cooling profile, production speed, substrate (base platform) surface temperature, should be examined.

Computational Methodology

Governing Equation and Discretization

Time-dependent heat diffusion equation is used to calculate transient temperature values inside a solid domain (Equation 4) (Bergman & Adrienne, 2017). Note that below equation assumes that conductivity of the material is constant and uniform.

$$\left| \frac{\partial^2 T}{\partial x^2} + \frac{\partial^2 T}{\partial y^2} + \frac{\partial^2 T}{\partial z^2} + \frac{q}{k} = \frac{\rho c_p}{k} \frac{\partial T}{\partial t} \right. \quad (4)$$

Here x , y , z , T , ρ , c_p , q , k , t denotes x-coordinate, y-coordinate, z-coordinate, temperature, density of the polymer, specific heat of the polymer, volumetric heat generation rate, conductivity of the polymer and time, respectively.

Simplified version of this equation with no-heat generation assumption and two-dimensional approximation, the equation reduces to Equation 5:

$$\left| \frac{\partial^2 T}{\partial x^2} + \frac{\partial^2 T}{\partial y^2} = \frac{\rho c_p}{k} \frac{\partial T}{\partial t} \right. \quad (5)$$

With second-order central difference discretization in space, first-order backward difference in time, and implicit solution scheme, discretized form of the equation is obtained as follows:

$$\frac{T_{i-1,j}^n - 2T_{i,j}^n + T_{i+1,j}^n}{(\Delta x)^2} + \frac{T_{i,j-1}^n - 2T_{i,j}^n + T_{i,j+1}^n}{(\Delta y)^2} = \frac{\rho c_p}{k} \frac{T_{i,j}^n - T_{i,j}^{n-1}}{\Delta t} \quad (6)$$

Equation 6 contains i and j indices for the nodes representing discretization on x and y coordinates as shown in Figure 1. The superscripted index n denotes discretion in time. Δx , Δy and Δt are mesh sizes on x -direction, y -direction, and time.

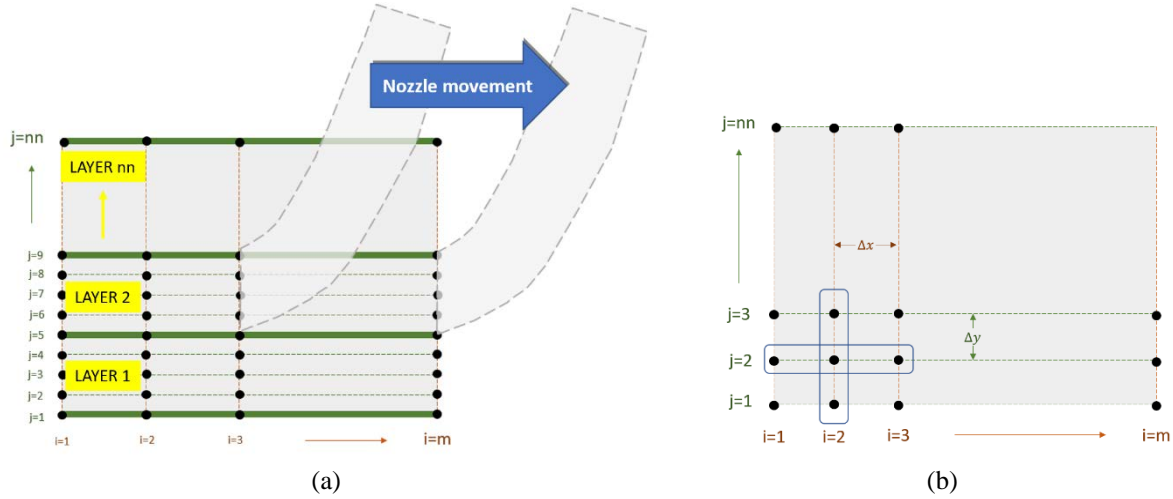


Figure 1. Domain and nozzle movement (a), Stencil of discretization (b)

With the help of the scheme in Equation 6 for discretization at all nodal locations, multiple equations are obtained. Total number of unknowns (nodal temperatures) are equal to the total number of equations and these equations constructs a matrix system. Note that coefficients of nodal temperatures at n^{th} time, so called a , b , c in Equation 4, and nodal temperature at $(n-1)^{\text{th}}$ time step are known values.

$$a T_{i,j}^n + b T_{i-1,j}^n + b T_{i+1,j}^n + c T_{i,j-1}^n + c T_{i,j+1}^n = T_{i,j}^{n-1} \quad (7)$$

$$\begin{bmatrix} a & b & & & c & & c & & \\ & b & a & b & & & c & & c \\ & & b & a & b & & & & c \\ c & & & b & a & b & & & \\ & c & & & b & a & b & & \\ c & & c & & & & & & \\ & & & & & & & & \\ & & & & & & & & \\ & & & c & & c & & & b & a \end{bmatrix} \begin{bmatrix} T_{1,1}^n \\ T_{2,1}^n \\ T_{3,1}^n \\ \vdots \\ \vdots \\ T_{m,nn}^n \end{bmatrix} = \begin{bmatrix} T_{1,1}^{n-1} \\ T_{2,1}^{n-1} \\ T_{3,1}^{n-1} \\ \vdots \\ \vdots \\ T_{m,nn}^{n-1} \end{bmatrix} \quad (8)$$

Where $a = (1 + 2Fo_x + 2Fo_y)$, $b = -Fo_x$, $c = -Fo_y$.

Dimensionless numbers in these coefficients are defined as $Fo_x = \frac{\alpha \Delta t}{(\Delta x)^2}$, $Fo_y = \frac{\alpha \Delta t}{(\Delta y)^2}$ where $\frac{k}{\rho c_p} = \alpha$.

The matrix system in Equation 8 has a form $A X = B$, where A is the coefficient matrix, X is unknown vector and B is known vector. Solving this matrix equation, nodal temperatures at n^{th} time are obtained by using the temperature values in the previous time step $(n-1)$. The calculation procedure starts with the utilization of initial temperature at $t=0$ sec as an initial condition and progresses until the end time of the simulation. In other words, by replacing the newly obtained X -vector with the B -vector, the solution advances in time (using $n=0$ as starting point for $n=1$, using $n=1$ for $n=2$, and so on).

The coefficient matrix (A) can be created with the help of a code and the matrix equation can be solved in a computer environment with the do-loops as marching in time. In scope of this study, a special code is developed by using Fortran 90 programming language to analyze heat transfer in a growing solid domain continuously changing boundaries and boundary conditions. In addition, the GMRES matrix solver (Turan & Eceder, 2011), which employs Newton-Krylov Method (Brown & Saad, 1989), is utilized to speed up the calculation process.

Initial and Boundary Conditions

The general representation of the applied boundary conditions is depicted in Figure 2.

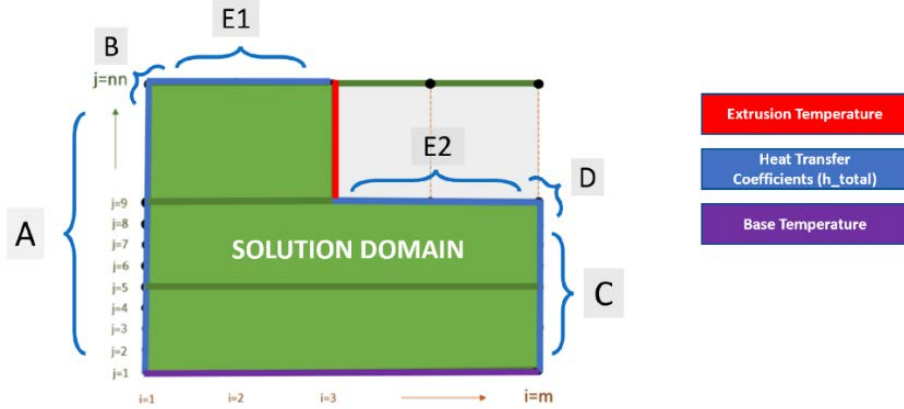


Figure 2. Boundary conditions

Blue lines in Figure 2, which consists of A, B, C, D, E1, E2 edges and corners, are subjected to an effective heat transfer coefficient that embodies convection and radiation heat transfer coefficients. After some algebraic manipulation, the concluding boundary equations are given in Table 1.

$$Q = h_{effective} A (T_{i,j}^n - T_{\infty}) \tag{9}$$

$$h_{effective} = h_{radiation} + h_{convection} \tag{10}$$

$$h_{radiation} = (T_{i,j}^{n-1} + T_{\infty}) [(T_{i,j}^{n-1}) + T_{\infty}^2] \tag{11}$$

$$Bi_x = \frac{h_{effective} \Delta x}{k} \tag{12}$$

$$Bi_y = \frac{h_{effective} \Delta y}{k} \tag{13}$$

Table 1. Equations at boundaries with heat transfer coefficients

| | |
|----------------------------|--|
| 1. A 2. Left Edge | 3. |
| | 4. $(2Fo_x + 2Fo_y + 2Bi_x Fo_x + 1)T_{i,j}^n - 2Fo_x T_{i+1,j}^n - Fo_y T_{i,j-1}^n - Fo_y T_{i,j+1}^n = 2Bi_x Fo_x T_{\infty} + T_{i,j}^{n-1}$ |
| 6. B 7. Top-Left Corner | 5. 8. |

| | | |
|-------------------------------|--|--|
| | | $9. \left\{ \frac{(2Fo_x + 2Fo_y + 2Bi_x Fo_x + 2Bi_y Fo_y + 1)T_{ij}^n - 2Fo_x T_{i+1,j}^n - 2Fo_y T_{i,j-1}^n}{10.} = 2Bi_x Fo_x T_\infty + 2Bi_y Fo_y T_\infty + T_{ij}^n \right.$ |
| 11. C 12. Right Edge | | $14. \left\{ \frac{(2Fo_x + 2Fo_y + 2Bi_x Fo_x + 1)T_{ij}^n - 2Fo_x T_{i-1,j}^n - Fo_y T_{i,j-1}^n - Fo_y T_{i,j+1}^n}{15.} = 2Bi_x Fo_x T_\infty + T_{ij}^{n-1} \right.$ |
| 16. D 17. Top-Right Corner | | $19. \left\{ \frac{(2Fo_x + 2Fo_y + 2Bi_x Fo_x + 2Bi_y Fo_y + 1)T_{ij}^n - 2Fo_x T_{i-1,j}^n - 2Fo_y T_{i,j-1}^n}{20.} = 2Bi_x Fo_x T_\infty + 2Bi_y Fo_y T_\infty + T_{ij}^n \right.$ |
| 21. E1 & E2 22. Top Edge | | $24. \left\{ \frac{(2Fo_x + 2Fo_y + 2Bi_y Fo_y + 1)T_{ij}^n - Fo_x T_{i+1,j}^n - Fo_x T_{i-1,j}^n - 2Fo_y T_{i,j-1}^n}{25.} = 2Bi_y Fo_y T_\infty + T_{ij}^{n-1} \right.$ |

Note that radiative heat transfer coefficient is calculated by using the nodal temperature in previous time step.

In Figure 2, the extrusion temperature is shown as red line to define primary heat source. The boundary condition on this edge is applied as $T_{i,j}^n = T_{extrusion}$. Same approach is employed for the base temperature, which is a constant value, $T_{i,j}^n = T_{base}$.

Parameters for Preliminary Analysis

Assumptions:

- The temperature of the melted plastic coming from the nozzle is constant.
- Material properties are homogenous inside the solution domain.

Boundary Conditions:

- The extrusion temperature is equal to 210 °C.
- Base temperature is 60 °C.
- Air temperature is assumed to be 20 °C.
- The speed of nozzle (production speed) is 60 mm/s.

Material Properties:

Temperature-dependent material properties are used for the accurate calculation of matrix coefficients. Fitted equations to the property data provided in literature (Sin, Rahmat, & Rahman, 2012) are as follows:

- Conductivity (T in Kelvin), $k=0.130 \text{ W/m-K}$
- Specific Heat of PLA;
 For $T > 330 \text{ K}$; $c_p \text{ (J/kg-K)} = 1.031698 * T + 1677.2415$
 For $T < 330 \text{ K}$; $c_p \text{ (J/kg-K)} = 3.969 * T + 159.72$
- Density of PLA (T in Celsius);
 $\rho \text{ (kg/m}^3\text{)} = 1240 \text{ kg/m}^3$

The Geometry and Computational Parameters:

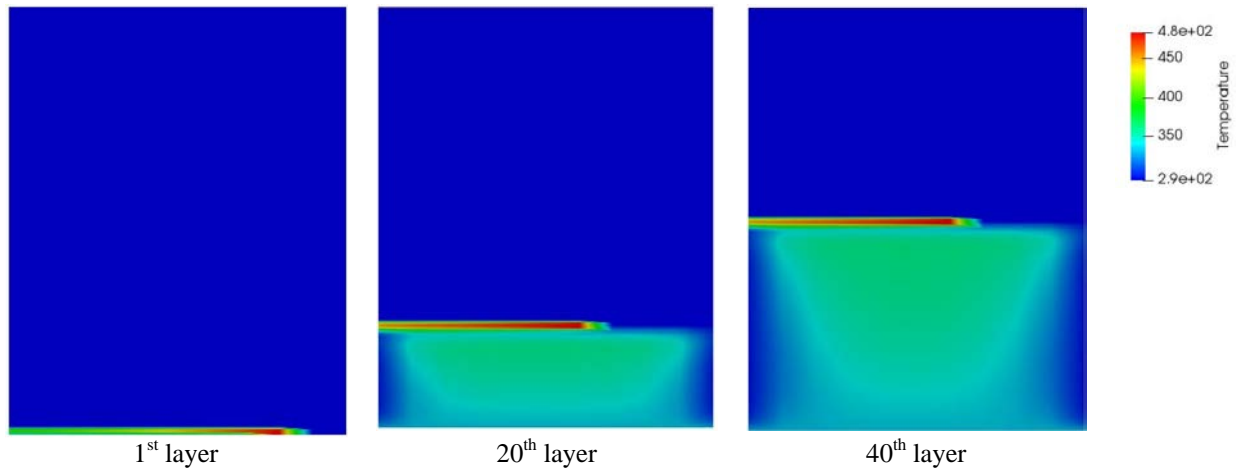
- X-direction: Width of the part is 19 mm, and it is divided into 10 segments ($\Delta x=1.9 \text{ mm}$).
- Y-direction: Layer thickness is 0.3 mm, and the total height is 25 mm which approximately corresponds to printing of 80 layers. Each layer (0.3 mm) is discretized by 3 nodes to resolve layer thickness ($\Delta y=0.10 \text{ mm}$).
- Time: The algorithm is designed to advance 1 node at every time step. The time step size, $\Delta t = \Delta x / \text{speed}$, is calculated as 0.03167 seconds.

Between consecutive layers, a time delay is defined to allow cooling process taking place during the production in third dimension. Intra-layer printing time is calculated with considering total area to be printed at each layer. With using the geometrical parameters, intra-layer delay is estimated as 3.8 seconds that corresponds to 120 time steps/layer. Following the completion of the printing process, an ultimate cooling time of 1,600 steps (~50 seconds between 10,280th and 11,880th time steps) is defined after the completion of the printing to observe cool down.

Results and Discussion

Preliminary Simulation Results

Preliminary results are obtained with the assumption that convective heat transfer coefficient is equal to $500 \text{ W/m}^2\text{-K}$ and $T_{\text{base}}=60 \text{ }^\circ\text{C}$. Contour plots in Figure 3 visualize temperature changes inside the printed part at different timesteps. Heat diffusion inside the domain, cooling effects from top, left and right boundaries are clearly observed. Thermal energy deposited during the printing process keeps layers above T_g at hotter locations. Note that T_g is between $50 \text{ }^\circ\text{C}$ and $80 \text{ }^\circ\text{C}$ for PLA (Matyjaszewski & Möller, 2012).



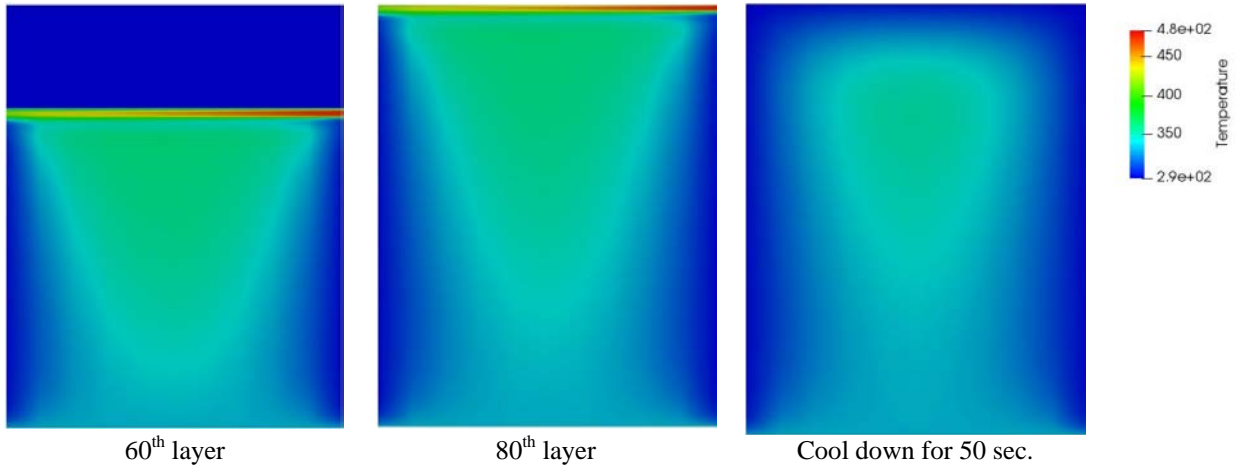


Figure 3. Computed temperature contour plots at different time steps (T in Kelvins)

Time history of nodal temperatures at the center of 2nd, 20th, 40th and 60th layers are given in Figure 4.

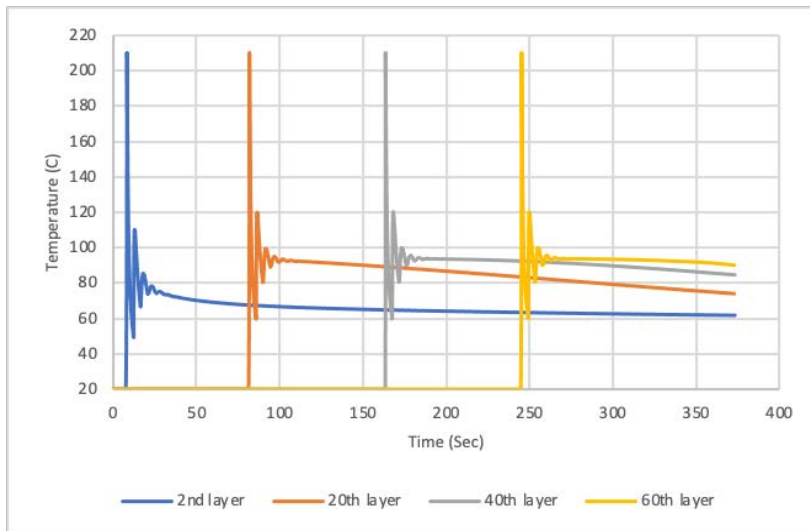


Figure 4. Nodal temperatures at the center node of layers

An experimental study in literature experimentally analyzed the effect of processing conditions on the bonding quality of FDM polymer filaments (Sun, Rizvi, Bellehumeur, & Gu, 2008). The time history of temperature data shows peaks with frequencies dependent on the printing speed and the printing path.

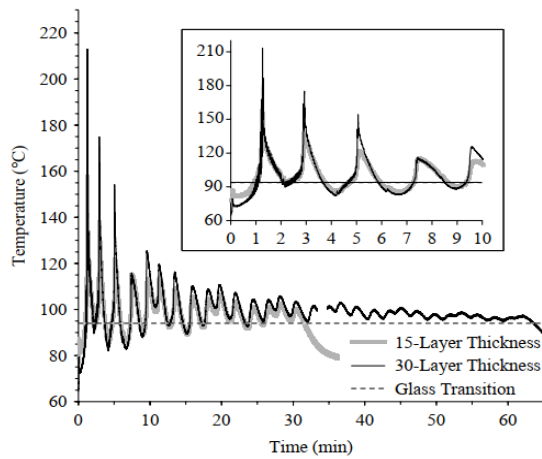


Figure 5. The time history of the measured temperature by k-type thermocouple during FDM (Sun, Rizvi, Bellehumeur, & Gu, 2008)

Conclusion

In scope of this study, a Fortran code is developed for the modeling of transient two-dimensional heat diffusion equation to understand history of temperature during 3D printing process via FDM. A matrix equation is obtained at each time step due to implicit time scheme which assures convergence of the solution regardless of the mesh size. The matrix is solved with the help of Newton-Krylov algorithm at each time step. A delay time is defined between layers and matrix is solved under convection and radiation boundary conditions at this time interval to consider the cool down period due to continuing extrusion process in the third dimension at the same layer.

During the simulation of the printing process, convection and radiation boundary conditions are applied to capture accurate cooling rate. $500 \text{ W/m}^2\text{-K}$ as the convective heat transfer coefficient (HTC) is applied to see the cooling pattern clearly. This number is the upper limit of the generic range of convection coefficients of air; $2.5\text{-}25 \text{ W/m}^2\text{-K}$ for natural convection, and $100\text{-}500 \text{ W/m}^2\text{-K}$ for forced convection (Kosky, Balmer, Keat, & Wise, 2013). It is important to remark that this elevated HTC intrinsically compensates lacking cooling effects in the third dimension which is expected to have the highest contribution to the overall heat transfer since front and back surfaces have relatively large areas compared to the other sides.

The two-dimensional code can be calibrated with the use of measured temperatures via infrared camera. Then, the calibrated code can be used for the estimation of t_{weld} , total welding time above glass temperature, at different production parameters. A $t_{\text{weld}}\text{-}\sigma$ correlation can be developed with tensile tests of the parts that are manufactured under corresponding production parameters. The authors continue to work tensile tests for the determination of a $t_{\text{weld}}\text{-}\sigma$ correlation for PLA.

Recommendations

As a future work, modeling of the third dimension with actual printing path is recommended. Convection from back and front surfaces contributes to cooling which has an impact on time history of temperatures. Further improvement of the code to include discretization of the third dimension may result in more accurate estimation of t_{weld} .

Scientific Ethics Declaration

The authors declare that the scientific ethical and legal responsibility of this article published in EPSTEM journal belongs to the authors.

Acknowledgements and Notes

* This article was presented as an oral presentation at the International Conference on Basic Sciences, Engineering and Technology (www.icbaset.net) conference held in Istanbul/Turkey on August 25-28, 2022.

* This research was supported by Simularge A.Ş. and its cloud infrastructure to run developed algorithms. We thank Dr. Erhan TURAN, CTO of Simularge A.Ş., for his insights that greatly assisted the research.

References

- Bartolai, J., Simpson, J., & Xie, R. (2018). Predicting strength of additively manufactured thermoplastic polymer parts produced using material extrusion. *Rapid Prototyping Journal*, 24(2), 321-332.
- Bergman, T. L., & Adrienne, L. S. (2017). *Fundamentals of Heat and Mass Transfer*. Wiley.
- Bikas, H., Stavropoulos, P., & Chryssolouris, G. (2016). Additive manufacturing methods and modelling approaches: a critical review. *Int. J. Adv. Manuf. Technology*, 83, 389-405.
- Coogan, T., & Kazmer, D. (2017). Bond and part strength in fused deposition modeling. *Rapid Prototyping Journal*, 23(2), 414-422.

- Coogan, T., & Kazmer, D. (2017). Healing simulation for bond strength prediction of FDM. *Rapid Prototyping Journal*, 23(3), 551-561.
- Faludi, J., Bayley, C., Boghal, S., & Iribarne, M. (2015). Comparing environmental impacts of additive manufacturing vs. traditional machining via life-cycle assessment. *Rapid Prototyping Journal*, 21(1), 14-33.
- Jud, K., Kausch, H., & Williams, J. (1981). Fracture mechanics studies of crack healing and welding polymers. *Journal of Materials Science*, 16(1), 204-210.
- Kosky, P., Balmer, R., Keat, W., & Wise, G. (2013). Mechanical engineering. In *Exploring Engineering - an Introduction to Engineering and Design* (p. 264). Academic Press.
- Matyjaszewski, K., & Möller, M. (2012). *Polymer science: a comprehensive reference*. Elsevier Science.
- Sin, L. T., Rahmat, A. R., & Rahman, W. W. (2012). *PLA handbook series: polylactic acid - pla biopolymer technology and applications*. Plastics Design Library.
- Sun, Q., Rizvi, G., Bellehumeur, C., & Gu, P. (2008). Effect of processing conditions on the bonding quality of FDM polymer filaments. *Rapid Prototyping Journal*, 14(2), 72-80.
- Turan, E., & Eceder, A. (2011). Analysis of a bimetallic slab in non-isothermal flow. *Proceedings of the Institution of Mechanical Engineers, Part C: Journal of Mechanical Engineering Science*, 225(3), 658-672.
- Wool, R., & O'Connor, K. (1981). A theory of crack healing in polymers. *Journal of Applied Physics*, 52, 5953-5963.
- Yang, F., & Pitchumani, R. (2002). Healing of thermoplastic polymers at an interface under nonisothermal conditions. *Macromolecules*, 35, 3213-3224.

Author Information

Buryan Apacoglu-Turan

Istanbul Technical University
Faculty of Mechanical Engineering, Türkiye
Contact e-mail: apacoglu@itu.edu.tr

Kadir Kirkkopru

Istanbul Technical University
Faculty of Mechanical Engineering, Türkiye

To cite this article:

Apacoglu-Turan, B. & Kirkkopru, K. (2022). Development of two-dimensional thermal analysis code for the analysis of 3D printed PLA parts. *The Eurasia Proceedings of Science, Technology, Engineering & Mathematics (EPSTEM)*, 18, 28-36.

The Eurasia Proceedings of Science, Technology, Engineering & Mathematics (EPSTEM), 2022

Volume 18, Pages 37-45

ICBASSET 2022: International Conference on Basic Sciences, Engineering and Technology

Finite Element Method for Analysis of Off-Center Connected Continuous Beams

Albena DOICHEVA

University of Architecture, Civil Engineering and Geodesy (UACEG)

Abstract: The study of the structural elements goes through the premise of their centric support and centric connection. In reality, it is common to see elements with different cross-sections connected by offset axes, for example to align some of their edges, or those that are supported with off-center supports. Such inter-element eccentricities and off-center supports leads to a change in the stress-strain state from the traditional ones known from the available literature and university textbooks. In previous publications with participation of the author, exact nonlinear and approximate analytic solutions of similar problems for beams under various loading, support and connection conditions have already been published. The finite element method provides an approximate approach for computer analysis. In this paper, results obtained through a computer program created in the MATLAB, based on a finite element accounting for eccentricity in connection and off-centering of support, are demonstrated. The results shows values in the diagrams of internal forces differing by up to 15-30% compared to the classical theory of centric connection and centric supporting.

Keywords: Continuous beam, Different cross-sections, Inter-element eccentricities, Off-center supports, Finite element method

Introduction

In construction practice, it is often assumed that beams and systems of bodies are connected under the premise of their axial support and axial connection. In real structure, however, there is often a divergence from this assumption. The presence of different operating conditions of the structural elements causes the emergence of a more special stressed and strained state. This is proven in a number of studies with the participation of the author (Mladenov & Doicheva, 2011; Doicheva & Mladenov, 2009). Inferences were made in both, linear and non-linear analysis. The latter case is based on the exact differential equation of the deformed beam axis

$$\frac{d^2\varphi_i}{ds_i^2} + \frac{F_i}{EI} \left(1 - \frac{F_i}{EA} \cos\varphi_i \right) \sin\varphi_i = 0 \text{ and the elastic analogy theorem (Mladenov, 1985-86).}$$

The practical application of the obtained results requires an approach applicable to modern computing technology. Over the past few decades, the finite element method (Bankov & Pavlova 1989; Gallagher, 1984; Bhatti, 2005) has proven to be a reliable means of solving complex stress and strain states. In this paper FEM will be used to study continuous beams without and with joints. However, a corresponding finite element is required for this purpose. A stiffness matrix of such a beam-type finite element was obtained by the force method in (Mladenov et al., 2011-2012). Another so-called direct approach will be applied here (Gallagher, 1984; Gavin, 2011).

Method

- This is an Open Access article distributed under the terms of the Creative Commons Attribution-Noncommercial 4.0 Unported License, permitting all non-commercial use, distribution, and reproduction in any medium, provided the original work is properly cited.

- Selection and peer-review under responsibility of the Organizing Committee of the Conference

© 2022 Published by ISRES Publishing: www.isres.org

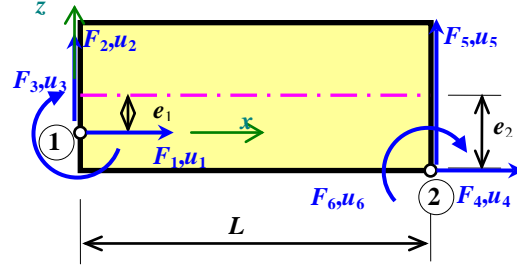


Figure 1. Finite element for unsymmetrical support with nodal forces and displacements

Figure 1 presents the type of finite element with length L , eccentricities e_1 and e_2 , respectively, at nodes 1 and 2, nodal forces, nodal moments as well as unknown displacements and unknown rotations. From now on, for brevity, we will only talk about nodal forces and displacements in a generalized sense. The element is subjected to special bending and normal force. The physico-mechanical characteristics of the cross-section are: E - modulus of elasticity, I - principal moment of inertia, A - area of the cross-section and $i = \sqrt{I/A}$ - radii of gyration.

Derivation of Stiffness Matrix by Direct Approach

The fields of displacements (Gallagher, 1984) $u(x) = a_1x + a_2$; $w(x) = a_3x^3 + a_4x^2 + a_5x + a_6$ with $w'(x) = 3a_3x^2 + 2a_4x + a_5$ have values for the endpoints respectively:

$$u(0) = a_2; u(L) = a_1L + a_2; w'(0) = a_5; u_3 \approx -w'(0); w'(L) = 3a_3L^2 + 2a_4L + a_5; u_6 \approx -w'(L) \quad (1)$$

On the other hand (Figure 1),

$$u(0) = u_1 + e_1u_3 = u_1 - e_1w'(0) = u_1 - e_1a_5, \quad \text{and} \quad u(L) = u_4 + e_2u_6 = u_4 - e_2w'(L) = u_4 - e_2(3a_3L^2 + 2a_4L + a_5).$$

From here follows the relation $\{\mathbf{u}\} = [\mathbf{B}]\{\mathbf{a}\}$; $\det(\mathbf{B}) = -L^5$, from where for the coefficients of the displacement functions we can write $\{\mathbf{a}\} = [\mathbf{B}^{-1}]\{\mathbf{u}\}$, therefore:

$$\begin{Bmatrix} a_1 \\ a_2 \\ a_3 \\ a_4 \\ a_5 \\ a_6 \end{Bmatrix} = \begin{bmatrix} -1/L & 1/L & 0 & -e_1/L & 0 & e_2/L \\ 1 & 0 & 0 & e_1 & 0 & 0 \\ 0 & 0 & 2/L^3 & -1/L^2 & -2/L^3 & -1/L^2 \\ 0 & 0 & -3/L^2 & 2/L & 3/L^2 & 1/L \\ 0 & 0 & 0 & -1 & 0 & 0 \\ 0 & 0 & 1 & 0 & 0 & 0 \end{bmatrix} \begin{Bmatrix} u_1 \\ u_4 \\ u_2 = (w_1) \\ u_3 = (a_1) \\ u_5 = (w_2) \\ u_6 = (a_2) \end{Bmatrix} \quad (2)$$

Thus, the longitudinal displacement as a function of the nodal displacements is $u(x) = (u_4 - u_1 + e_2u_6 - e_1u_3)x/L + u_1 + e_1u_3$, and for the axial linear strain is written $\varepsilon_x = u'(x) = (u_4 - u_1 + e_2u_6 - e_1u_3)/L$. Using Hooke's law, the normal stress and hence the normal force in the beam is determined:

$$\mathbf{N} = \sigma_x A = EA\varepsilon_x = \frac{EA}{L} [-1 \quad 1 \quad 0 \quad -e_1 \quad 0 \quad e_2] \{\mathbf{u}\} \quad (3)$$

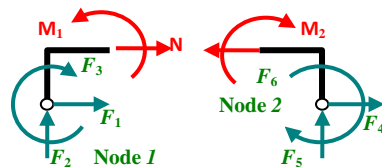


Figure 2. Internal forces at the finite element boundary

On the other hand, the relationship between the normal force and the nodal forces is (see figure 2) $F_{1/4} = \mp N$, so:

$$\begin{Bmatrix} F_1 \\ F_4 \end{Bmatrix} = \frac{EA}{L} \begin{bmatrix} 1 & -1 & 0 & e_1 & 0 & -e_2 \\ -1 & 1 & 0 & -e_1 & 0 & e_2 \end{bmatrix} \{\mathbf{u}\} \quad (4)$$

The following coefficients a_3, a_4, a_5, a_6 are expressed by (2)

$$a_3 = \frac{2u_2}{L^3} - \frac{u_3}{L^2} - \frac{2u_5}{L^3} - \frac{u_6}{L^2}; \quad a_4 = -\frac{3u_2}{L^2} + \frac{2u_3}{L^2} + \frac{3u_5}{L^2} + \frac{u_6}{L^2}; \quad a_5 = -u_3; \quad a_6 = u_2. \quad (5)$$

Substituting (5) into the transverse displacement function yields:

$$w(x) = \left(2 \frac{x^3}{L^3} - 3 \frac{x^2}{L^2} + 1\right) u_2 + x \left(2 \frac{x}{L} - \frac{x^2}{L^2} - 1\right) u_3 + \left(3 \frac{x^2}{L^2} - 2 \frac{x^3}{L^3}\right) u_5 + x \left(\frac{x}{L} - \frac{x^2}{L^2}\right) u_6. \quad (6)$$

This result is recorded in matrix form $w(x) = [\mathbf{N}]\{\Delta\} = [N_1 \ N_2 \ N_3 \ N_4]\{\Delta\}$, where $\{\Delta\} = [u_2 \ u_3 \ u_5 \ u_6]^T$. N_i are called interpolation functions or shape functions (Gallagher, 1984).

The dependence between the bending moments defined in the end sections is used as follows: $M_1 = -F_1 e_1 + F_3$; $M_2 = F_4 e_2 - F_6$ and the derivatives $w'(0)$ and $w'(L)$, bearing in mind that $M(x) = EIw''(x)$, a system of two linear equations with four unknowns is obtained. Since F_1 and F_4 are already defined, from the above expressions we extract F_3 and F_6 , i.e.

$$\begin{Bmatrix} F_3 \\ F_6 \end{Bmatrix} = \frac{EI}{L^3 i^2} \begin{bmatrix} L^2 e_1 & -L^2 e_1 & -6Li^2 & L^2(4i^2 + e_1^2) & 6Li^2 & L^2(2i^2 - e_1 e_2) \\ -L^2 e_2 & L^2 e_2 & -6Li^2 & L^2(2i^2 - e_1 e_2) & 6Li^2 & L^2(4i^2 + e_2^2) \end{bmatrix} \{\mathbf{u}\}. \quad (7)$$

Finally, through the expressions for F_1, F_3, F_4, F_6 and the conditions for equilibrium of the forces is found:

$$\begin{Bmatrix} F_2 \\ F_5 \end{Bmatrix} = \frac{EI}{L^3 i^2} \begin{bmatrix} 0 & 0 & 12i^2 & -6Li^2 & -12i^2 & -6Li^2 \\ 0 & 0 & -12i^2 & 6Li^2 & 12i^2 & 6Li^2 \end{bmatrix} \{\mathbf{u}\}. \quad (8)$$

Written together (4, 7, 8) give the stiffness matrix of the finite element considering the influence of only the bending moment and the normal force:

$$\begin{Bmatrix} F_1 \\ F_2 \\ F_3 \\ F_4 \\ F_5 \\ F_6 \end{Bmatrix} = \frac{1}{L^3 i^2} \begin{bmatrix} L^2 & 0 & L^2 e_1 & -L^2 & 0 & -L^2 e_2 \\ 0 & 12i^2 & -6Li^2 & 0 & -12i^2 & -6Li^2 \\ L^2 e_1 & -6Li^2 & L^2(4i^2 + e_1^2) & -L^2 e_1 & 6Li^2 & L^2(2i^2 - e_1 e_2) \\ -L^2 & 0 & -L^2 e_1 & L^2 & 0 & L^2 e_2 \\ 0 & -12i^2 & 6Li^2 & 0 & 12i^2 & 6Li^2 \\ -L^2 e_2 & -6Li^2 & L^2(2i^2 - e_1 e_2) & L^2 e_2 & 6Li^2 & L^2(4i^2 + e_2^2) \end{bmatrix} \begin{Bmatrix} ELu_1 \\ ELu_2 \\ ELu_3 \\ ELu_4 \\ ELu_5 \\ ELu_6 \end{Bmatrix}. \quad (9)$$

Geometric Stiffness Matrix

The element with pre-deformation length dx due to bending only is elongated to dl (Figure 3). Furthermore

$$dl = \sqrt{(dx)^2 + (dw)^2} \approx (1 + w'^2/2)dx. \quad (10)$$

Therefore, the absolute extension of the element with length dx is $dl - dx = (w'^2/2)dx$.

The differentially small work of the normal force from this extension will be $d\pi = N(x) (w'^2 dx)/2$, and for the entire beam will be $\Pi_G = \int_0^L (N(x) w'^2) dx / 2$, which is exactly the potential energy of deformation.

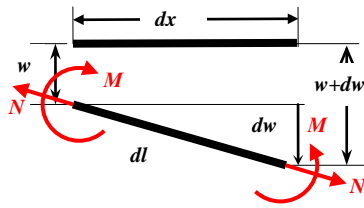


Figure 3. Infinitesimal length deformation

At a constant normal force $N = N$ we will have $\left(N \int_0^L w'^2 dx \right) / 2$.

$$\left(\bar{\Pi}_G = \frac{\Pi_G}{N} \right) = \frac{1}{2} \int_0^L w'^2 dx = \frac{(6u_2^2 - 12u_2u_5 + 6u_5^2)}{10L} - \frac{(u_2 - u_5)(u_3 + u_6)}{10} + L \frac{2u_3^2 - u_3u_6 + 2u_6^2}{30}. \quad (11)$$

From Castigliano's inverse theorem, we obtain the forces F_{iG} , and the geometric stiffness matrix, which is due only to the influence of a constant normal force and the bending deformation, takes the known form (Gallagher, 1984; Gavin, 2011):

$$\begin{Bmatrix} F_{1G} \\ F_{2G} \\ F_{3G} \\ F_{4G} \\ F_{5G} \\ F_{6G} \end{Bmatrix} = N \begin{bmatrix} 0 & 0 & 0 & 0 & 0 & 0 \\ 0 & 6/5L & -1/10 & 0 & -6/5L & -1/10 \\ 0 & -1/10 & 2L/15 & 0 & 1/10 & -L/30 \\ 0 & 0 & 0 & 0 & 0 & 0 \\ 0 & -6/5L & 1/10 & 0 & 6/5L & 1/10 \\ 0 & -1/10 & -L/30 & 0 & 1/10 & 2L/15 \end{bmatrix} \begin{Bmatrix} u_1 \\ u_2 \\ u_3 \\ u_4 \\ u_5 \\ u_6 \end{Bmatrix} = \frac{N}{EI} \begin{bmatrix} 0 & 0 & 0 & 0 & 0 & 0 \\ 0 & 6/5L & -1/10 & 0 & -6/5L & -1/10 \\ 0 & -1/10 & 2L/15 & 0 & 1/10 & -L/30 \\ 0 & 0 & 0 & 0 & 0 & 0 \\ 0 & -6/5L & 1/10 & 0 & 6/5L & 1/10 \\ 0 & -1/10 & -L/30 & 0 & 1/10 & 2L/15 \end{bmatrix} \begin{Bmatrix} Elu_1 \\ Elu_2 \\ Elu_3 \\ Elu_4 \\ Elu_5 \\ Elu_6 \end{Bmatrix}. \quad (12)$$

The use of the geometric stiffness matrix in addition to the basic one turns out to be very useful in the iterative determination of a critical load in frame systems in the Euler sense (Gallagher, 1984; Saouma, 2002)

Results and Discussion

The calculations were performed with a program running in the MATLAB (MATLAB R2017b) environment.

First Example

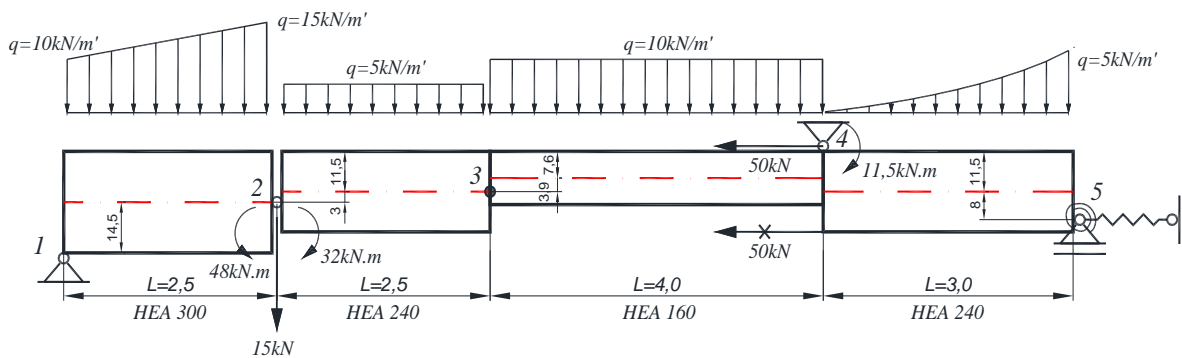


Figure 4. The joint is in the first element axis

Figure 4 shows a beam composed of 4 elements, two of which are with equal cross-section. All sections are aligned along the upper edge of the section, which leads to the divergence of their axes. The connection between

the first and second section is with joint. Initially, the joint is in the first element axis. The concentrated forces and moments are introduced at the elements nodes. The stiffnesses of the linear and rotational springs are related to the stiffnesses of the beam. The linear springs is brought to the stiffness of tension (compression) of the beam by coefficient ζ , as $k_i = \zeta_i \frac{EA_i}{L_i}$. The stiffness of the rotational springs is reduced to the bending stiffness of the beam by the coefficient γ and is $c_i = \gamma_i \frac{EI_i}{L_i}$. In the example considered are accepted $\zeta = 0,25$ and $\gamma = 0,5$.

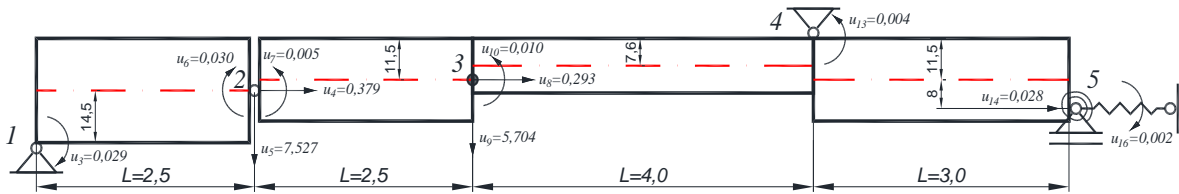


Figure 5. Displacements and rotations in the nodes

The results are shown graphically in Figure 5 and Figure 6.

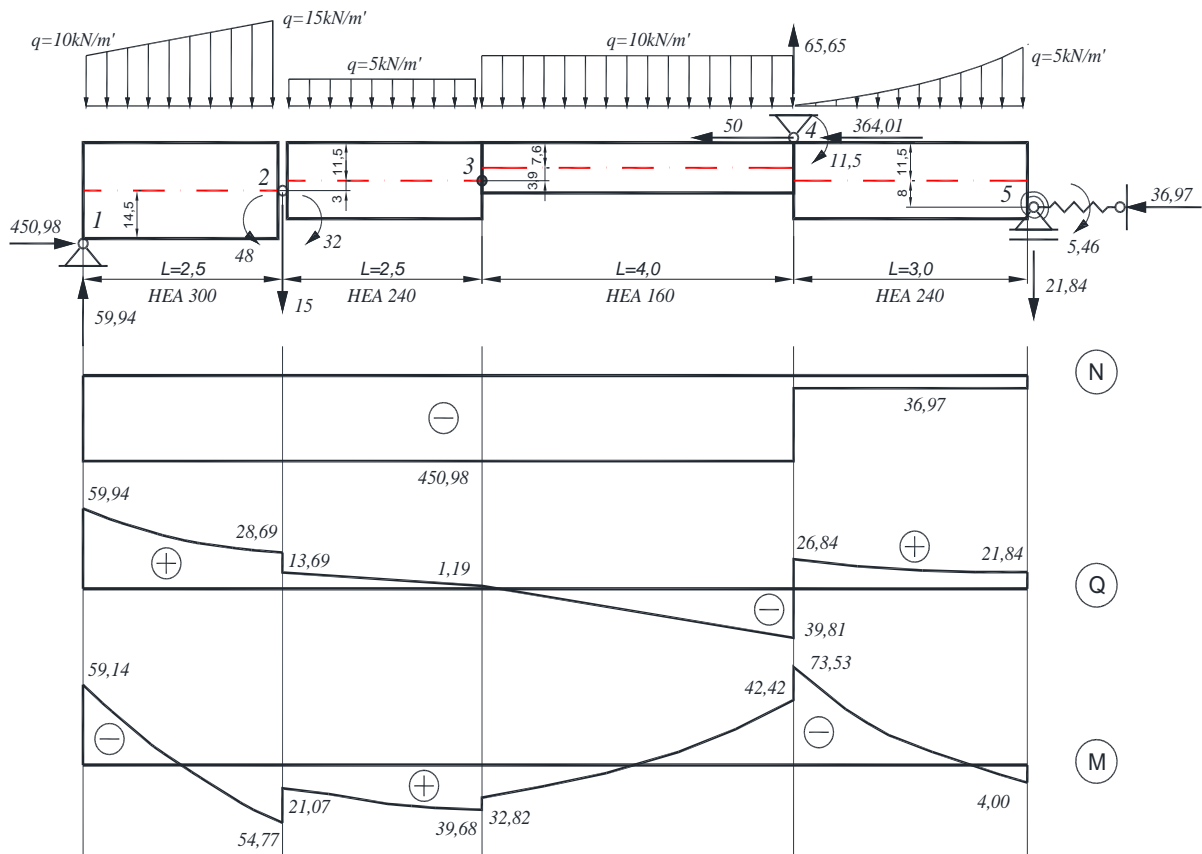


Figure 6. Initial force when the joint is in the first element axis

The second case is when the joint is located along the lower edge of the second element and all other conditions from the first case are preserved, Figure 7.

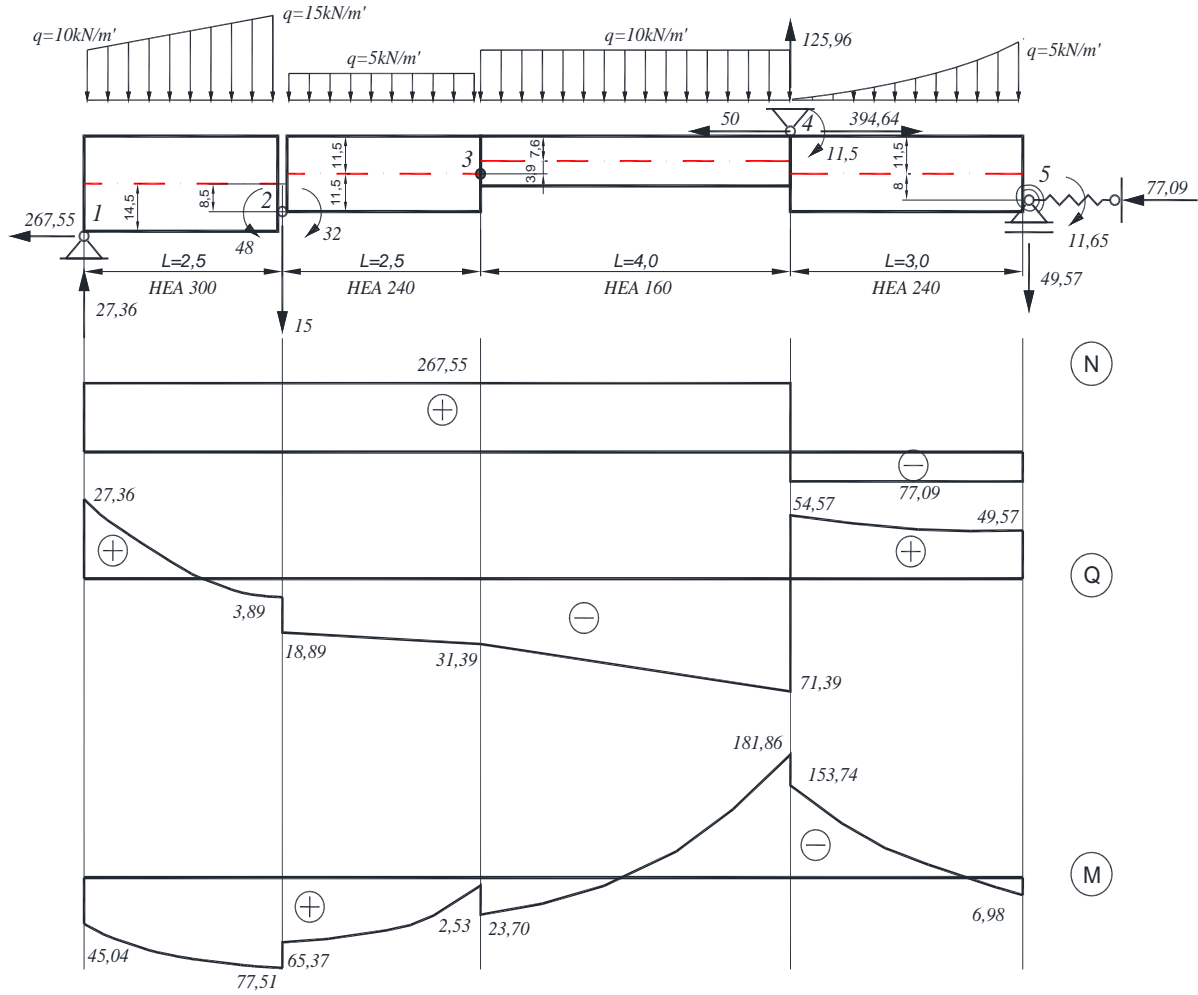


Figure 7. Beam with joint on the lower edge of the second element

In the two cases of joint position, the initial forces have different values. The large axial force is striking and the fact that if in the first case normal force is compressive, then in the second it is tensile.

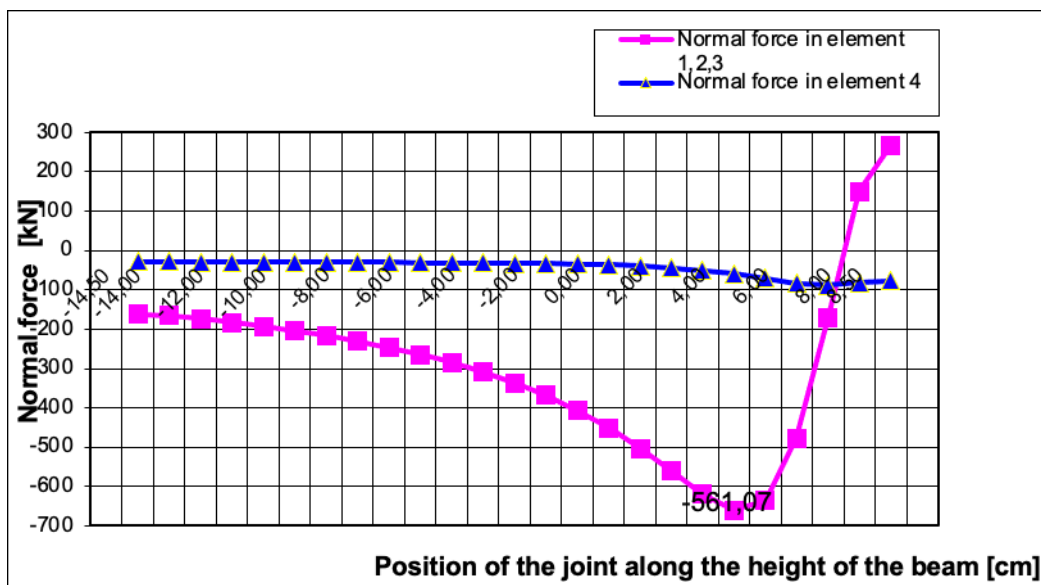


Figure 8. Change in normal force when moving the joint along the height of the beam

The limit of variation of the normal force during the displacement of the joint along the height of the beam is shown in Figure 8. When placing the joint around the upper edge on the beam, the horizontal force is compressive. This force numerically exceeds the vertical transverse loads by about two times and continues to increase as the joint moves towards the axis. The extreme value is slightly below the axis of the first element. Moving the joint to the bottom edge of a second element results in a rapid reset and reversal to the tension direction with a value commensurate with the maximum compressive force. The example is indicative for the importance of research on the different position of intermediate joints in non-axial connection and off-center support of continuous beams.

Second Example

A classic example about the occurrence of a complex stressed and strained state caused by the off-center support along the lower or upper edge is the crane beam (Figure 9).

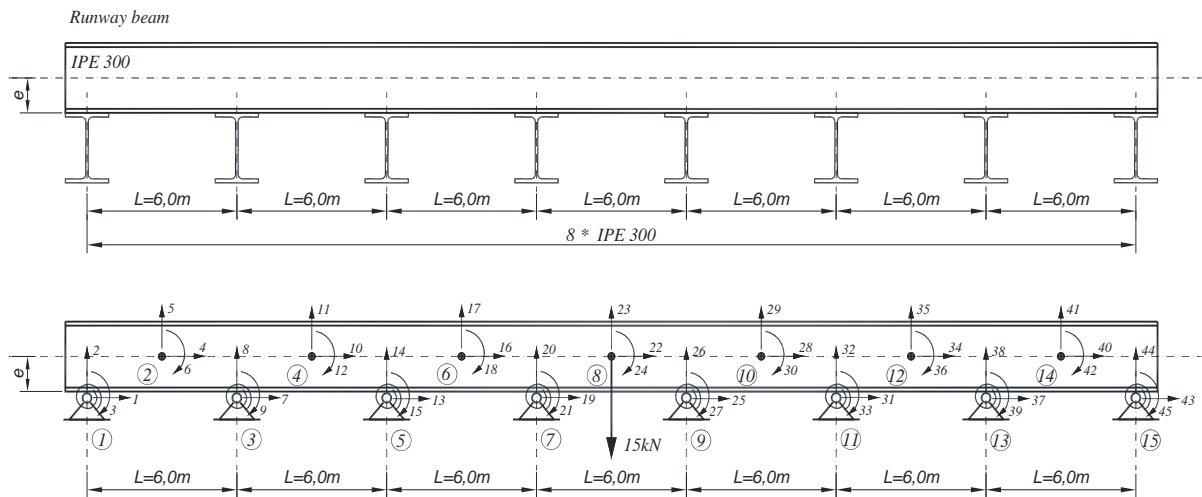


Figure 9. Crane beam

The crane beam is made of an IPE 300 profile. The crane beam is supported on an analogous profiles with a cross section of IPE 300. The bolted connections between the profiles are modeled as fixed supports. There will be a tendency to torsion on the support beams, which will lead to the occurrence of an additional moment accounted by the rotation springs in the supports. Their coefficient $c = \frac{GI_t}{L}$ has the value

$$c = \frac{8000 \cdot 10^4 \cdot 19,77 \cdot 10^{-8}}{0,20} = 79,08 \frac{\text{kN.m}}{\text{rad}}$$

On the other hand, the coefficient of the rotation spring reduced to the bending stiffness of the beam is $c = \gamma \frac{EI}{L_i}$, where L_i is the length of the i -th finite element to which the

$$\text{stiffness of the spring is reduced. It follows that } \gamma = \frac{cL_i}{EI} = \frac{79,08 \cdot 3}{2,1 \cdot 10^8 \cdot 8356 \cdot 10^{-8}} = 0,0135$$

The results of the program are shown in Figure 10.

The large horizontal force in the loaded span of the beam, which exceeds the value of the transverse load as well as the jumps into the moment diagram in the area of the supports are striking. They are explained precisely by the displacement of the supports from the axis. If the supports were at the axis, as is commonly assumed, then the moment diagram values would be as shown by the dashed line. They differ from the real ones by 14.5% in the span of the beam and 27% in the area above the support. There is a case where, if the support is in the axis, like the classical cases, the beam will be dimensioned as a special bending. The presence of a horizontal force, however, requires that it be considered as a bending combined with tension or compression.

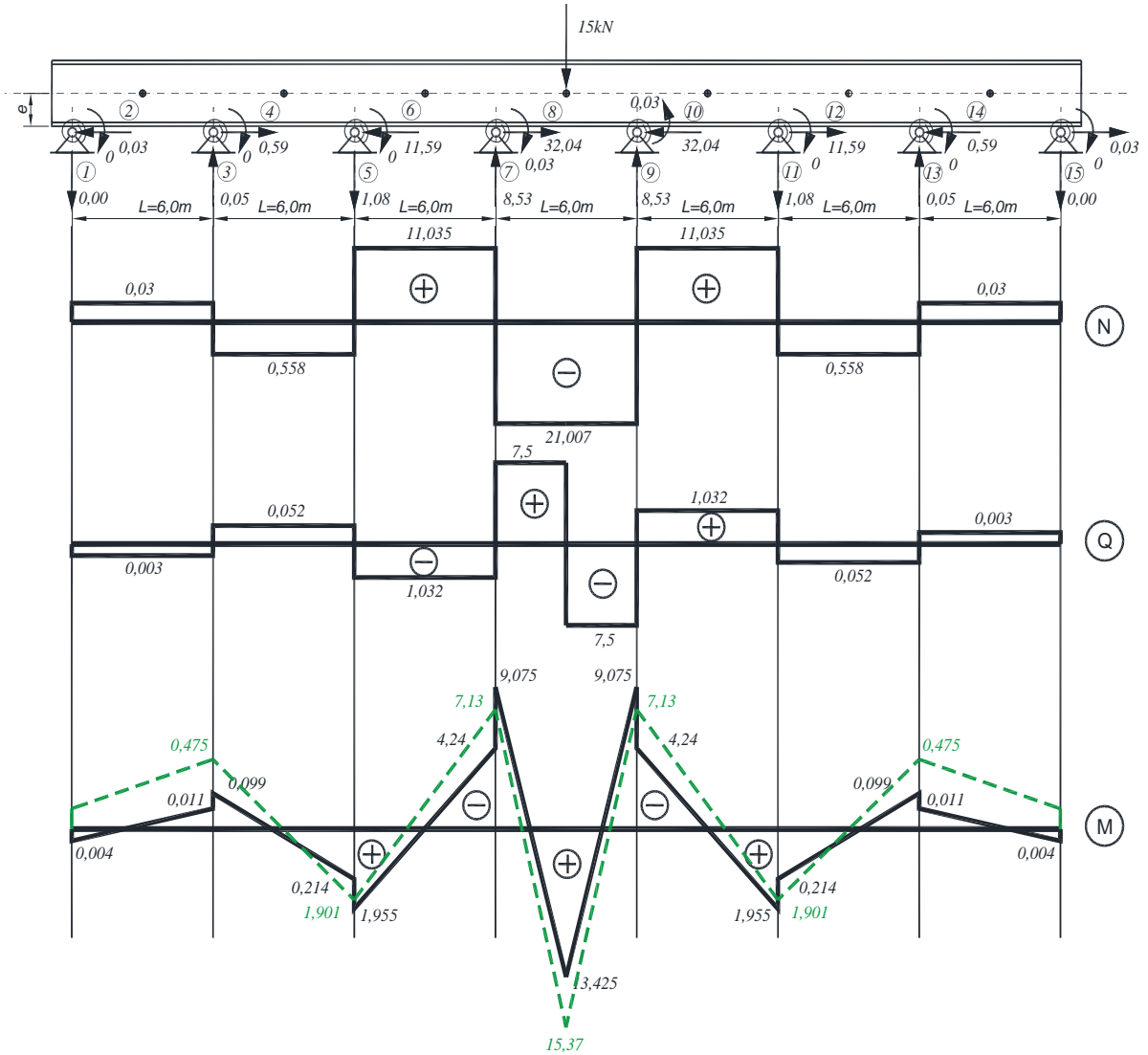


Figure 10. Numerical results for crane beam

Conclusion

The stiffness matrix for off-center connection of the finite elements is derived.

Examples of beams with off-center support and eccentric connection are considered.

The influence on the internal forces at the different positions of the connecting joint between two elements of a continuous beam is shown.

The values of the normal forces, which many times exceed the vertical loads are demonstrated.

An example of a crane beam shows the effect of off-center supports on the stress and strain state. Large horizontal forces are observed. Bending moments over some supports and in the some span of the beam exceed those obtained when the beam is axially supported between 14,5-27%

Scientific Ethics Declaration

The author declares that the scientific ethical and legal responsibility of this article published in EPSTEM journal belongs to the author.

Notes

This article was presented as an oral presentation at the International Conference on Basic Sciences, Engineering and Technology (www.icbasaset.net) conference held in Istanbul/Turkey on August 25-28, 2022.

References

- Bankov, B., & Pavlova, J., (1989). Calculation of building structures using the finite element method. *Technika*, Sofia (In Bulgarian).
- Bhatti, M. A., (2005). *Fundamental FE analysis and applications*, John Willey & Sons, New Jersey
- Doicheva A., & Mladenov K., (2009). A problem of an off-centre supported beam with an elastic link. Third Symposium on bridges "Design and construction of bridges" UACEG - Sofia, *Civil Engineering - Bulgaria*, 4, 11-16. (In Bulgarian).
- Gallagher, R. (1984). Finite element method. *Fundamentals*, Mir, Moscow (In Russian).
- Gavin, H., (2011). *CE 131L. Matrix structural analysis*. Duke University, Department of Civil and Environmental Engineering.
- MATLAB R2017b. The MathWorks Inc., Natick, USA.
- Mladenov, K., (1985-86). Theorem of elastic analogy, annual of higher institute of architecture and civil engineering – Sofia, XXXII, 5, 76-84 (In Bulgarian).
- Mladenov, K., & Doicheva, A. (2011). A study of off-center supported beams with large deflections. "*Civil Engineering" Bulgaria*, No 1, 10-22. (In Bulgarian).
- Mladenov, K., Doicheva, A. & Kochev, P., (2011). Development of finite beam element for off-center transfer of forces. *Annual of the University of architecture, civil engineering and geodesy*, XLV, VIII, *Scientific Research*, 213-227. (In Bulgarian).
- Saouma, V. E., (2002). *Lecture notes in finite element framed structures*. Department of Civil Environmental and Architectural Engineering, University of Colorado, Boulder.

Author Information

Albena Doicheva

University of Architecture, Civil Engineering and Geodesy (UACEG)
Bulgaria, Sofia 1164, 1 Hristo Smirnenski Blvd., Bulgaria
Contact e-mail: doicheva_fhe@uacg.bg

To cite this article:

Doicheva, A. (2022). Finite element method for analysis of off-center connected continuous beams. *The Eurasia Proceedings of Science, Technology, Engineering & Mathematics (EPSTEM)*, 18, 37-45.

The Eurasia Proceedings of Science, Technology, Engineering & Mathematics (EPSTEM), 2022

Volume 18, Pages 46-54

ICBASSET 2022: International Conference on Basic Sciences, Engineering and Technology

Dynamic Control of Non-Linearly Tapering FGM Beams

Khalid EL HARTI

Moulay Ismail University

Rachid SAADANI

Moulay Ismail University

Miloud RAHMOUNE

Moulay Ismail University

Abstract: This work presents the dynamics and active vibration control of a non-uniform functionally graded beam. Thanks to the strong use of beams and specifically with non-uniform section, in the different industrial applications, such as helicopter rotor blades, wind turbines, space and marine structures, we present in this article, a comparison of linearly and non-linearly tapering beams. The FGM beam is equipped with four layers of piezoelectric materials as sensors and actuators, bonded on the upper and lower surfaces of the main structure, on different finite elements to see the influence of its location on the dynamics and active control. In this study, the Timoshenko beam's theory combined with FEM is applied to a beam divided into a finite number of elements. Hamilton's principle is applied to generate the equation of motion. The structure is modeled analytically and numerically and the simulation results are presented at the end. The optimal LQG control with Kalman filtering is applied.

Keywords: Vibration, LQG-kalman control, FGM, Piezoelectric materials, Timoshenko's beam theory

Introduction

The mathematical finite element model of Euler Bernoulli has shown its limitations because it does not take into account shear effects, rotational inertia, axial displacements etc... In order to remedy this, we model our smart structure by the Timoshenko shear deformation theory. Timoshenko's beam model corrects the classical beam model by considering the effects of first order transverse shear deformation and axial displacements. Thus, the Timoshenko's beam theory overcomes the disadvantages of the EB's beam theory and the resulting mathematical model is closer to an exact model. For isotropic beams, Timoshenko's theory takes into account six fundamental global deformations (bending and transverse shearing in two directions, extension and torsion). In this model, a plane cross-section perpendicular to the beam axis before deformation no longer remains normal to the beam axis after deformation due to shear. The derivation of normality is produced by a transverse shear which is assumed to be constant over the cross section. Thus, the Timoshenko beam model performs better than the EB's model for the accurate prediction of the response of a beam and is of additional importance in the dynamics of the structure and the control of its vibrations.

In the mid-1980s, a new class of composites, called functionally graded materials (FGMs), emerged thanks to a group of Japanese scientists (Koizumi, 1997). That year, Japanese researchers faced a problem that required a specific type of composite material that could withstand a very large temperature difference in a space project. These materials exhibit a gradual change in their composition as a function of volume (Bharti et al., 2013). These composites are widely used in various engineering applications due to their high temperature resistance.

- This is an Open Access article distributed under the terms of the Creative Commons Attribution-Noncommercial 4.0 Unported License, permitting all non-commercial use, distribution, and reproduction in any medium, provided the original work is properly cited.

- Selection and peer-review under responsibility of the Organizing Committee of the Conference

Mechanical structures are often subject to vibrations from various sources. These vibrations are generally sources of problems affecting the proper functioning of many systems and processes in different industrial sectors and many engineering fields such as automotive, aeronautics, naval... Thanks to the strong use of beams and specifically with non-uniform section, in the different industrial applications, such as helicopter rotor blades, wind turbines, space and marine structures. These systems increasingly integrate more composite materials in the manufacture of structures. The amplitude of vibrations can cause a significant number of problems such as damage or fatigue of structures. One solution to such a problem is active vibration control (AVC) (Beards 1996).

Examples of systems where AVC can be applied are numerous, such as fans, vehicle interiors, precision equipment, engines, electric and hydraulic drives, noise barriers and enclosures... (Bendine et al., 2016, El Harti et al., 2017, Panda et al., 2016). There have been extensive theoretical and experimental studies on FGM structures that have been published, especially beams and are still of interest to researchers because of their applications. (El Harti et al., 2017) studied the AVC of an FGM beam with a piezo-materials with a new geometry. They also addressed the active control of the porous Euler-Bernoulli FGM beam in a thermal environment with symmetrically bonded piezo materials (El Harti et al., 2020), as well as the dynamic analysis and AVC of the distributed piezo-thermo-elastic porous FGM beam modeled by the FEM (El Harti et al., 2021). (Sahabni & Cunedioğlu, 2020) studied the free vibration analysis of cracked FG non-uniform beams. (Ebrahimi & Hashemi, 2017) investigated the vibration analysis of non-uniform FG porous beams under thermal loading. (Kumar et al., 2015) analyzed the geometrically nonlinear free vibration of axially FG taper beams. (Chen, 2021) studied the vibration analysis of axially FG Timoshenko beams with non-uniform section-cross. (Huang et al., 2013) examined the free vibration of axially functionally graded Timoshenko beam with non-uniform cross section. (Ozdemir et al., 2010) presented a study of the vibration analysis of a rotating tapered beam using DTM. (Eberle & Oberguggenberger, 2022) established a new method for estimating the bending stiffness curve of non-uniform Euler-Bernoulli beams using static deflection data.

Mathematical Formulation

A non-uniform FG beam with dimension $\overline{(L \times b(x) \times h)}$, the width $\overline{b(x)}$ is considered variable in this study. The general equations for the cross-sectional area, width and moment of inertia of the beam are given by (Ebrahimi & Hashemi, 2017):

$$\begin{cases} \overline{b(x)} = b_0 \left(1 - C_b \frac{x}{L}\right)^m \\ \overline{A(x)} = A_0 \left(1 - C_b \frac{x}{L}\right)^m \\ \overline{I_y(x)} = I_{y0} \left(1 - C_b \frac{x}{L}\right)^m \end{cases} \quad (1)$$

The width taper ratio $\overline{(C_b)}$ must satisfy $\overline{0 \leq C_b < 1}$ for $\overline{A(x)}$ and $\overline{I_y(x)}$ to be positive. Knowing the width quantities at the embedding and free end of the structure, the width taper ratio can be calculated as follows:

$$\overline{C_b} = 1 - \frac{\overline{b}}{\overline{b_c}} \quad (2)$$

In this study, the beam shrink linearly (m=1). The quantities of cross sectional area, moment of inertia at the beam embedment can be written as follows:

$$\begin{cases} \overline{A_0} = \overline{b_0 h} \\ \overline{I_{y0}} = \frac{\overline{b_0 h^3}}{12} \end{cases} \quad (3)$$

The properties of the materials vary from pure metal on the bottom side to pure ceramic on the top side using power law, presented as follows: (El Harti et al., 2020).

$$\overline{V_c} = \left(\frac{z}{h}\right)^k = 1 - V_m \quad (4)$$

According to the theory of Timoshenko, the longitudinal and transverse displacements are written, respectively (Friedman & Kosmatka, 1993):

$$\overline{u(x, y, z, t)} = z\theta(x, t) \quad \overline{w(x, y, z, t)} = w(x, t) \quad (5)$$

The nonzero components of strain can be written by (Eisenberger & Abramovich, 1997):

$$\left\{ \begin{array}{l} \epsilon_{xx} = z \frac{\partial \theta}{\partial x} \\ \gamma_{xz} = \frac{\partial w}{\partial x} + \theta \end{array} \right. \quad (6)$$

The equations of motion are derived via the Hamilton's principle:

$$\delta \int_{t_1}^{t_2} (\delta U - \delta T - \delta W_e) dt = 0 \quad (7)$$

with $\overline{\delta U}$, $\overline{\delta T}$, $\overline{\delta W_e}$ represent the variations of strain energy, kinetic energy and the work of external forces, respectively.

The strain energy U of the element can be written as:

$$U = \frac{1}{2} \int_0^l \begin{bmatrix} \frac{\partial \theta}{\partial x} \\ \frac{\partial w}{\partial x} + \theta \end{bmatrix}^T \begin{bmatrix} EI & 0 \\ 0 & KGA \end{bmatrix} \begin{bmatrix} \frac{\partial \theta}{\partial x} \\ \frac{\partial w}{\partial x} + \theta \end{bmatrix} dx \quad (8)$$

where E, G, I and ρ are respectively, Young modulus, shear modulus, the area moment of inertia of the cross-section and the mass density, and $K = 10(1 + \nu)/(12 + 11\nu)$ being the shear coefficient (Cowper, 1996).

The kinetic energy of the element is given as:

$$T = \frac{1}{2} \int_0^l \begin{bmatrix} \frac{\partial w}{\partial t} \\ \frac{\partial \theta}{\partial t} \end{bmatrix}^T \begin{bmatrix} \rho A & 0 \\ 0 & \rho I \end{bmatrix} \begin{bmatrix} \frac{\partial w}{\partial t} \\ \frac{\partial \theta}{\partial t} \end{bmatrix} dx \quad (9)$$

The total work $\overline{W_e}$ due to the external forces in the beam is given by:

$$\overline{W_e} = \int_0^l \begin{bmatrix} w \\ \theta \end{bmatrix}^T \begin{bmatrix} q_d \\ m \end{bmatrix} dx \quad (10)$$

Finite Element Formulation

The equations governing the beam based on the Timoshenko theory could be satisfied if their polynomial order in \overline{w} is far greater by one order of $\overline{\theta}$ (Friedman & Kosmatka, 1993). Using the boundary conditions for the embedded-free beam, the transversal displacement $\overline{w}(x, t)$ and its first, second spatial derivatives are given in matrix form as:

$$\overline{w}(x, t) [N_w] [q] \quad \overline{\dot{w}}(x, t) [N_{\dot{w}}] [q] \quad \overline{\ddot{w}}(x, t) [N_{\ddot{w}}] [q] \quad (11)$$

With

$$q = [w_1 \quad \theta_1 \quad w_2 \quad \theta_2]^T \quad (12)$$

The equation of motion's element is developed by substituting the shape functions in the Hamilton principle, then integrating over the entire length of the element:

$$\overline{M\ddot{q} + Kq} = 0 \quad (13)$$

where the elementary mass matrices of the piezoelectric and FGM elements are expressed respectively as:

$$\overline{[M^P]} = \frac{1}{2} \int_0^{l_p} \begin{bmatrix} N_w \\ N_\theta \end{bmatrix}^T \begin{bmatrix} \rho_p A_p & 0 \\ 0 & \rho_p I_p \end{bmatrix} \begin{bmatrix} N_w \\ N_\theta \end{bmatrix} dx \quad (14)$$

$$\overline{[M^{FGM}]} = \frac{1}{2} \int_0^{l_b} \begin{bmatrix} N_w \\ N_\theta \end{bmatrix}^T \begin{bmatrix} C_1 & 0 \\ 0 & C_2 \end{bmatrix} \begin{bmatrix} N_w \\ N_\theta \end{bmatrix} dx \quad (15)$$

and the elementary stiffness matrices of the piezoelectric and FGM elements are also expressed respectively as:

$$\overline{[K^P]} = \frac{1}{2} \int_0^{l_p} \begin{bmatrix} \frac{\partial N_\theta}{\partial x} \\ \frac{\partial N_w}{\partial x} + N_\theta \end{bmatrix}^T \begin{bmatrix} E_p I_p & 0 \\ 0 & K G_p A_p \end{bmatrix} \begin{bmatrix} \frac{\partial N_\theta}{\partial x} \\ \frac{\partial N_w}{\partial x} + N_\theta \end{bmatrix} dx \quad (16)$$

$$\overline{[K^{FGM}]} = \frac{1}{2} \int_0^{l_b} \begin{bmatrix} \frac{\partial N_\theta}{\partial x} \\ \frac{\partial N_w}{\partial x} + N_\theta \end{bmatrix}^T \begin{bmatrix} C_3 & 0 \\ 0 & C_4 \end{bmatrix} \begin{bmatrix} \frac{\partial N_\theta}{\partial x} \\ \frac{\partial N_w}{\partial x} + N_\theta \end{bmatrix} dx \quad (17)$$

with $\overline{C_1}$, $\overline{C_2}$, $\overline{C_3}$, and $\overline{C_4}$ are constants which depend on the characteristics of the FGM material, given by (El Harti et al., 2019).

Piezoelectric Equations

The linear piezoelectric coupling between the elastic field and the electric field can be expressed by the direct and inverse piezoelectric constitutive equation (Aldraihem et al., 1997, Anjanappa & BI, 1994) as:

$$\overline{D_z} = d_{31} \sigma + e^s E \quad \overline{D_z} = d_{31} E_f + S^c \epsilon \quad (18)$$

The voltage will be applied as an input to the actuator with an accurate gain depending on the degree of damping desired.

$$V^c(t) = G_c e_{31} z b \int_0^{l_p} n_1^T \dot{q} dx \quad (19)$$

where $z = \left(\frac{h}{2} + t_s\right)$, and $\overline{e_{31}}$ being the piezoelectric stress/load constant.

$$\overline{V_1^c(t)} = S_c \begin{bmatrix} 0 & -1 & 0 & 1 \end{bmatrix} \quad (20)$$

$$\overline{V_2^c(t)} = -S_c \begin{bmatrix} 0 & -1 & 0 & 1 \end{bmatrix} \quad (21)$$

where $\overline{S_s} = G_c e_{31} z_1 b$ is called the sensor constant.

Dynamic Equation

The dynamic equation of the structure and the control equation are finally given by:

$$\overline{M^* \ddot{g} + C^* \dot{g} + K^* g = f_{ext}^* + f_{ctr1}^* + f_{ctr2}^*} \quad (22)$$

The state space model in MIMO mode is given by:

$$\overline{\dot{x} = Ax(t) + Bu(t) + Er(t)} \quad (23)$$

$$\overline{y(t) = C^T x(t) + Du(t)} \quad (24)$$

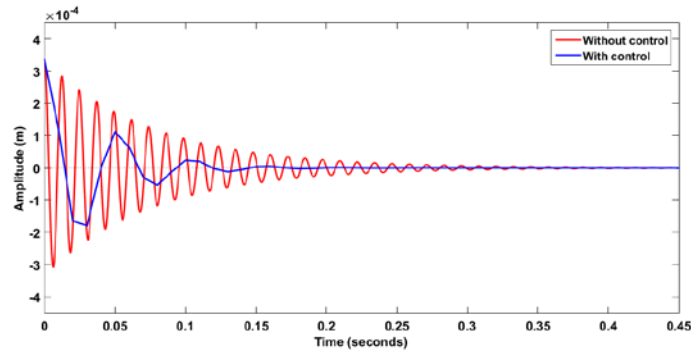
Results and Discussion

In the aim to validate the control's procedure, we consider an embedded-free FGM beam with a non-uniform section, partially covered by four layers of piezoelectric materials. A pulse of amplitude (1N) is applied as external force. The figures below show the response of the beam to the pulse. In all results, we presents the comparison of the responses, with and without control, varying the location of piezoelectric actuators as well as the taper ratio, and the power index. The geometrical and physical characteristics of the materials are shown in (Table 1).

Table 1. Geometric and physical characteristics of the structure

| Physical properties | FG material | Material (PZT) Sensor/Actuator |
|------------------------------|--|--|
| Length (m) | $\overline{L = 5 \times l_b = 0.}$ | $\overline{t_p = 0.05}$ |
| Width (m) | $\overline{b = 0.03}$ $\overline{b_0 = 0.02}$ | $\overline{b = 0.03}$ $\overline{b_0 = 0.02}$ |
| Thickness (m) | $\overline{h = 0.002}$ | $\overline{t_s = t_a = 0.00001}$ |
| Density (Kg/m ³) | $\overline{\rho_m = 2780}$ $\overline{\rho_c = 3800}$ | $\overline{\rho_p = 7700}$ |
| Young's Modulus (G Pa) | $\overline{E_m = 70}$ $\overline{E_c = 380}$ | $\overline{E_p = 68.1}$ |
| Poisson's ratio | $\overline{\nu_m = 0.3}$ $\overline{\nu_c = 0.3}$ | $\overline{\nu_p = 0.3}$ |
| PZT Strain constants (m/V) | | $\overline{d_{31} = 125 \times 10^{-12}}$ |
| PZT Stress constant (Vm/N) | | $\overline{g_{31} = 10.5 \times 10^{-3}}$ |

Figure 1 shows the variation of the width from b=3 to b=2, keeping the power index k=1. Figure 2 presents the variation of the power index for k=(0.5; 1; 5) and b=2. in the first two figures, the actuator pair is in the FE2. Figure 3 shows the variation of the actuator pair between FE2 and FE3 for k=1 and b=2.



(a) b=3

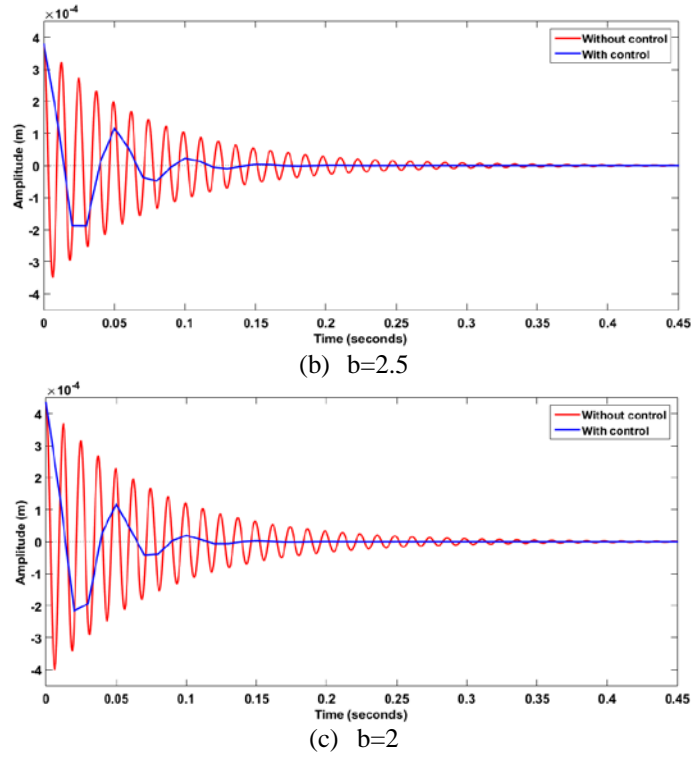
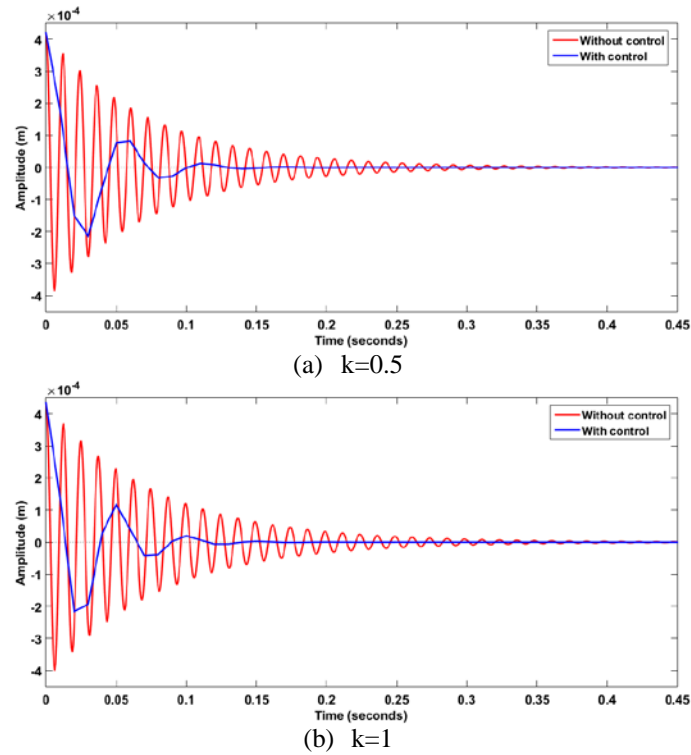


Figure 1. Impulse response of the smart beam for $k=1$ (Actuators in FE2)

From (figure 1), we find that the increase in the width taper ratio (decrease in the width) between $b=3$ and $b=2$, implies increases in the amplitudes of the vibrations. The decrease in width implies a decrease in the mass matrix, it means that the structure becomes less resistive.



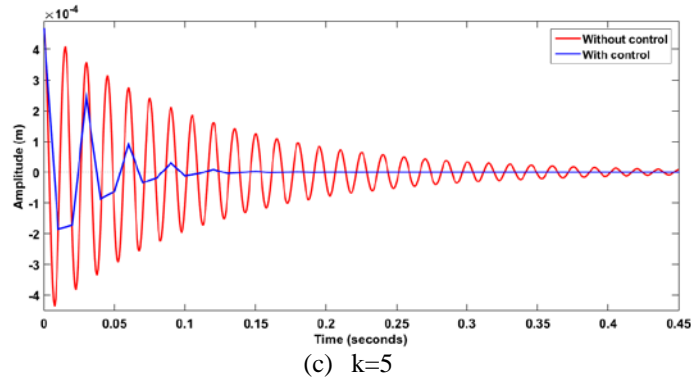


Figure 2. Impulse response of the smart beam for $b=2$ (Actuators in FE2)

Figure 2 shows the variation of the power index. From the figure, we find that the increase in the power index between $k=0.5$ and $k=5$, implies an increase in the vibration amplitudes. This increase is due to the fact that the increase in the power index, the beam contains more metal than ceramic, the thing which explains the weakness of the matrix of matrix and rigidity.

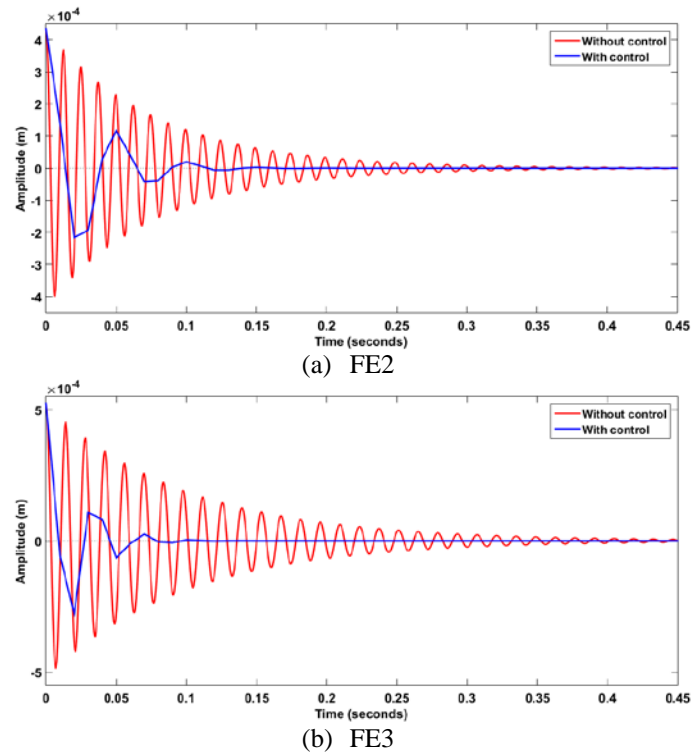


Figure 3. Impulse response of the smart beam for $k=1$ and $b=2$

From Figure 3, the displacement of the actuator pair from the embedded end to the free end implies an increase in the vibration amplitudes. This increase is explained, that the displacement of a quantity of material towards the free end is equivalent to an increase in the excitation force.

Conclusion

In order to study the dynamics and active control of a non-uniform section FGM beam, based on Timoshenko theory and FEM, we consider a free-embedded FGM beam containing four layers of piezoelectric materials. The analysis of results shows that the increase in the power index, the increase in the width taper ratio as well as the displacement of the pair of actuators towards the free end, imply increases in the amplitudes of the vibrations. also the comparison of the responses in open and closed loop shows the success of the LQG-Kalman active control procedure.

Scientific Ethics Declaration

The authors declare that the scientific ethical and legal responsibility of this article published in EPSTEM journal belongs to the authors.

Acknowledgements or Notes

This article was presented as an oral presentation at the International Conference on Basic Sciences, Engineering and Technology (www.icbaset.net) conference held in Istanbul/Turkey on August 25-28, 2022.

References

- Aldraihem, O. J., Wetherhold, R. C., & Singh, T. (1997). Distributed control of laminated beams: Timoshenko theory vs. Euler-Bernoulli theory. *Journal of Intelligent Material Systems and Structures*, 8(2), 149-157.
- Anjanappa, M., & Bi, J. (1994). Magnetostrictive mini actuators for smart structure applications. *Smart Materials and Structures*, 3(4), 383.
- Beards, C. E. (1996). *Structural vibration: analysis and damping*, 1st ed. Arnold: London, UK.
- Bendine, K., Boukhoulda, F. B., Nouari, M., & Satla, Z. (2016). Active vibration control of functionally graded beams with piezoelectric layers based on higher order shear deformation theory. *Earthquake Engineering and Engineering Vibration*, 15(4), 611-620.
- Bharti, I., Gupta, N., & Gupta, K. M. (2013). Novel applications of functionally graded nano, optoelectronic and thermoelectric materials. *International Journal of Materials, Mechanics and Manufacturing*, 1(3), 221-224.
- Chen, W. R. (2021). Vibration analysis of axially functionally graded Timoshenko beams with non-uniform cross-section. *Latin American Journal of Solids and Structures*, 18.
- Cowper, G. R. (1996). The shear coefficient in Timoshenko's beam theory. *ASME J. App. Mech.*, 33, 335-340.
- Eberle, R. & Oberguggenberger, M. (2022). A new method for estimating the bending stiffness curve of non-uniform Euler-Bernoulli beams using static deflection data. *Applied Mathematical Modelling*, 105, 514-533.
- Ebrahimi, F. & Hashemi, M. (2017). Vibration analysis of non-uniform imperfect functionally graded beams with porosities in thermal environment. *Journal of Mechanics*, 33(6):739-757.
- Eisenberger, M. & Abramovich, H. (1997). Shape control of non-symmetric piezolaminated composite beams. *Computers and Structures*, 38, 565-571.
- El Harti, K., Sanbi, M., Rahmoune, M., Saadani, R., Agounoun, R., Bentaleb, M., & Rahmoune, M. (2017). Active vibration control of sandwich FGM beam with piezoelectric sensor/actuator. *Int. J. Appl. Eng. Res*, 12(20), 9338-9345.
- El Harti, K., Rahmoune, M., Sanbi, M., Saadani, R., Bentaleb, M., & Rahmoune, M. (2019, February). Finite element model of vibration control for an exponential functionally graded Timoshenko beam with distributed piezoelectric sensor/actuator. *Actuators Vol. 8*, No. 1, p. 19.
- El Harti, K., Rahmoune, M., Sanbi, M., Saadani, R., Bentaleb, M., & Rahmoune, M. (2020). Dynamic control of Euler Bernoulli FG porous beam under thermal loading with bonded piezoelectric materials. *Ferroelectrics*, 558(1), 104-116.
- El Harti, K., Sanbi, M., Saadani, R., Bentaleb, M., & Rahmoune, M. (2021). Dynamic analysis and active control of distributed piezothermoelastic FGM composite beam with porosities modeled by the finite element method. *Composites: Mechanics, Computations, Applications: An International Journal*, 12.1.
- Friedman, Z. & Kosmatka, J. B. (1993). An improved two-node Timoshenko beam finite element. *Computers and Structures*, 47 (3), 473-481.
- Huang, Y., Yang, L. E., & Luo, Q. Z. (2013). Free vibration of axially functionally graded Timoshenko beams with non-uniform cross-section. *Composites Part B: Engineering*, 45(1), 1493-1498.
- Koizumi, M. (1997). FGM activities in Japan. *Compos. Part B Eng.*, 28, 1-4.
- Kumar, S., Mitra, A. & Roy, H. (2015). Geometrically nonlinear free vibration analysis of axially functionally graded taper beams. *Engineering Science and Technology. An International Journal*, 18(4), 579-593.
- Ozdemir Ozgumus, O. & Kaya, M. O. (2010). Vibration analysis of a rotating tapered Timoshenko beam using DTM. *Meccanica*, 45(1), 33-42.
- Panda, R. K., Nayak, B., & Sarangi, S. K. (2016). Active vibration control of smart functionally graded beams. *Procedia Engineering*, 144, 551-559.

Shabani, S. & Cunedioğlu, Y. (2020). Free vibration analysis of cracked functionally graded non-uniform beams. *Materials Research Express*, 7(1):015707.

Author Information

Khalid El Harti

Laboratory of Advanced Materials Studies and Applications,
Fs-Est, Moulay Ismail University,
Meknes, Morocco.
Contact e-mail: elhartikhalid@gmail.com

Rachid Saadani

Laboratory of Advanced Materials Studies and Applications,
Fs-Est, Moulay Ismail University,
Meknes, Morocco

Miloud Rahmoune

Laboratory of Advanced Materials Studies and Applications,
Fs-Est, Moulay Ismail University,
Meknes, Morocco

To cite this article:

El Harti, K., Saadani, R. & Rahmoune, M. (2022). Dynamic control of non-linearly tapering fgm beams. *The Eurasia Proceedings of Science, Technology, Engineering & Mathematics (EPSTEM)*, 18, 46-54.

The Eurasia Proceedings of Science, Technology, Engineering & Mathematics (EPSTEM), 2022

Volume 18, Pages 55-63

ICBASSET 2022: International Conference on Basic Sciences, Engineering and Technology

Moisture Absorption Behavior of CP5 Composite Materials Used in Industry

Băilă DIANA-IRINEL

University Politehnica of Bucharest

Păcurar RĂZVAN

Technical University of Cluj-Napoca

Păcurar ANCUȚA

Technical University of Cluj-Napoca

Abstract: In engineering practice, perhaps the most interesting aspect of woodworking deals with the relationship between wood and moisture. The plywood composite presents hygroscopicity characteristic, as the wood and reaction almost like a sponge, will gain or lose moisture from the air based upon the conditions of the surrounding environment. When the tree is in the green state, is first felled, it contains a very large amount of moisture existing in two different forms: as free water that is contained as liquid in the pores or vessels of the wood itself and as bound water, trapped within the cell walls. After that the wood is exposed to the air and immediately loose free water and the wood does not contract or otherwise change in dimension, it is in the state of drying and it is called the fiber saturation point. The moisture content in each piece of CP5 composite material is expressed as a percentage of the weight of the water and oven-dry weight of CP5 composite material. The moisture absorption depends on the wood type, density of wood and it is influenced by the environmental temperature, this is an aspect very important in the furniture industry. The moisture absorption test is generally used for quality control purposes and to measure the degradation of the quality for the wood and composite materials.

Keywords: Isotherm absorption, Composite materials, Rate of moisture, SEM analysis, Thermostat enclosure

Introduction

Variation of the moisture content can cause wood to shrink and swell and alter its dimensions, affecting all wood properties. In the same time, the manufacturing, gluing, and finishing of wood and its mechanical, thermal, and acoustic properties are influenced by moisture content, this can increase weight 100 percent or more, with great effects on transportation costs. For realizing traction tests for the CP5 composite samples on the temperature and hygroscopic control, it was used an enclosure thermostat controlled in temperature and humidity.

The humidity can influence too, the processing operations, especially drying, preservative treatment, and pulping. The moisture content of CP5 composite material can be calculated based on its current and oven-dry weight. In the case of wood, the hygroscopic value varies between 30 to 100 percent, in function of species, position of the wood in the tree or year seasons. In this article we used a climate room with control system and an electric moisture meter portable that can measure the change of electrical properties of CP5 composite material, in function of changing moisture content. In the case of carbon-fiber-reinforced polymer matrix composites, the high specific strength, stiffness, and good chemical resistance, make them attractive for applications in aerospace components, sporting goods, civil structures, and marine vehicles, but humidity

- This is an Open Access article distributed under the terms of the Creative Commons Attribution-Noncommercial 4.0 Unported License, permitting all non-commercial use, distribution, and reproduction in any medium, provided the original work is properly cited.

- Selection and peer-review under responsibility of the Organizing Committee of the Conference

absorption can reduce their mechanical properties (Costa, 2006). For the basalt fibre reinforced polymer matrix composites, the moisture absorption influences considerable the mechanical properties (Pandian, 2014). By example for carica papaya fiber reinforced polymeric composites, the moisture absorption affects the thickness swelling behaviors on mechanical performances (Saravanakumaar, 2022).

Fiber-reinforced polymer composites may offer numerous attractive features such as low cost, high specific performance, and ease of production. But their durability and sustained performance depend of severe and changing environmental conditions. Property drop was observed to be much more significant for the samples that were exposed to lower freezing temperatures before moisture absorption (Hamidi, 2017). For the natural fiber composites was investigated the value of Fickian diffusivity constant, moisture equilibrium content and correction factor. Tests were carried out on composite plates, which was a combination of sugar palm fiber and epoxy resins and two different fiber compositions have been chosen which were 10% and 20% by weight and it is shown that, for composite plates that contain higher fiber composition, the moisture absorption rate is even higher (Leman, 2008).

Method

For establish the moisture value for the CP5 composite samples in function of the temperature and hygroscopic control, it was used an enclosure thermostat controlled in temperature and humidity. The thermostat enclosure is composed of the following elements:

- the inner tube of welded stainless steel sealed and exhaust bung;
- mineral wool insulation;

Two joints in silicon;

Door opener with wedge-thermal bridges: The principle of heating enclosure it is realized using the caloric resistances in stainless steel, arranged behind a table screen. The cooling is accomplished by a fluid evaporation condenser in a shifter in the form of copper tube. Concerning the adjusting the temperature, the cooling it is regulated using a tuning electro valve, been equipped with a cold circuit. The heating it is made using under voltage heating resistances with a static relay. For controlled humidity it is used a solenoid feed, a cold drying racket, electro valves that inject compressed and dried air.

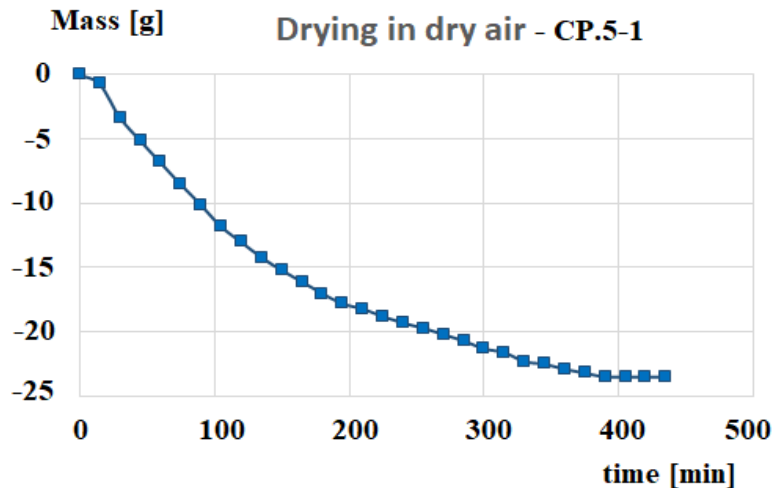


Figure1.Drying in dry air for C.P.5-1 composite material

Results and Discussion

In this research, it was studied the moisture behavior for traction tests for the CP5 composite material. For CP5 composite material is shown the experimental values of absorption coefficients for moisture 1%H, at the temperature of 100°C in the Table 1.

Table 1. Moisture coefficients for CP5 composite material at 1%H and the temperature of 100°C

| Temperature [oC] | Time [min] | Humidity [H] | Mass [g] |
|------------------|------------|--------------|----------|
| 25.4 | 0 | 1 | 0 |
| 79.8 | 15 | 1 | -0.7 |
| 102.3 | 30 | 1 | -3.3 |
| 102.3 | 45 | 1 | -5.1 |
| 102.4 | 60 | 1 | -6.8 |
| 102.4 | 75 | 1 | -8.5 |
| 102.4 | 90 | 1 | -10.1 |
| 102.5 | 105 | 1 | -11.8 |
| 102.6 | 120 | 1 | -13 |
| 102.4 | 135 | 1 | -14.2 |
| 102.6 | 150 | 1 | -15.2 |
| 102.7 | 165 | 1 | -16.1 |
| 102.6 | 180 | 1 | -17 |
| 102.4 | 195 | 1 | -17.8 |
| 102.6 | 210 | 1 | -18.2 |
| 102.6 | 225 | 1 | -18.8 |
| 102.6 | 240 | 1 | -19.3 |
| 102.4 | 255 | 1 | -19.7 |
| 102.4 | 270 | 1 | -20.2 |
| 102.5 | 285 | 1 | -20.7 |
| 102.6 | 300 | 1 | -21.3 |
| 102.6 | 315 | 1 | -21.6 |
| 102.6 | 330 | 1 | -22.3 |
| 102.6 | 345 | 1 | -22.5 |
| 102.4 | 360 | 1 | -22.9 |
| 102.4 | 375 | 1 | -23.2 |
| 102.6 | 390 | 1 | -23.5 |
| 102.6 | 405 | 1 | -23.5 |
| 102.4 | 420 | 1 | -23.5 |
| 102.6 | 435 | 1 | -23.5 |

In the Table 2 is presented the variation of the experimental mass values in function of time for the CP5 composite material for temperature of 20°C and different moisture values and in the table 3 are presented the mass value in function of time at the temperature of 40°C and different moisture values (20%H, 40%H, 60%H, 80%H). In the figure 2 is shown the curve of variation between the mass values and time for the temperature of 20°C and different wettability coefficients (20%H, 40%H, 60%H, 80% H) and in the figure 3 it is represented the variation curve in the same conditions, but for the temperature of 40°C.

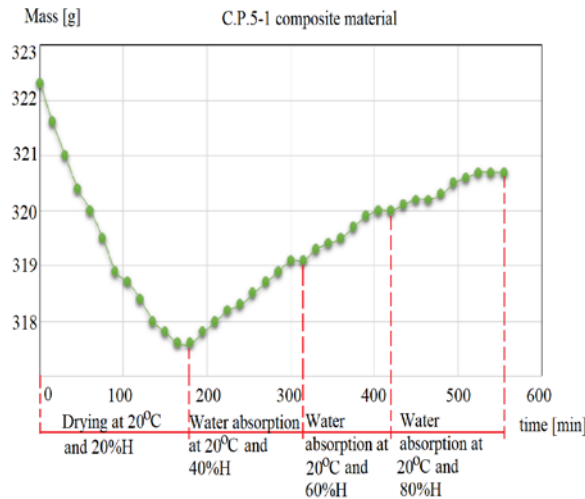


Figure 2. Curve of variation between the mass values and time for the temperature of 20°C and different moisture levels (20%H, 40%H, 60%H, 80% H).

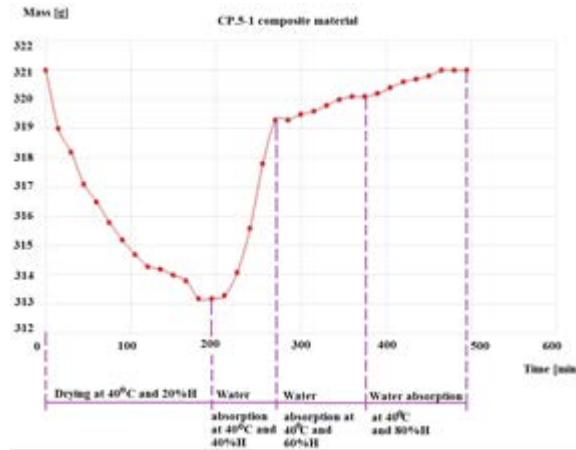


Figure 3. Curve of variation between the mass values and time for the temperature of 40°C and different moisture levels (20%H, 40%H, 60%H, 80%H)

Table 2. Mass variation in time for CP5 composite material at different moisture coefficients (20%H,40%H, 60%H, 80%H) and the temperature of 20°C

| Temperature [oC] | Time [min] | Humidity [H] | Mass [g] |
|------------------|------------|--------------|----------|
| 19.8 | 0 | 20 | 323.3 |
| 19.8 | 15 | 20 | 322.6 |
| 19.9 | 30 | 20 | 322 |
| 19.9 | 45 | 20 | 321.4 |
| 19.9 | 60 | 20 | 321 |
| 19.8 | 75 | 20 | 320.5 |
| 20 | 90 | 20 | 319.9 |
| 19.9 | 105 | 20 | 319.7 |
| 19.9 | 120 | 20 | 319.4 |
| 20.1 | 135 | 20 | 319 |
| 20.1 | 150 | 20 | 318.8 |
| 20 | 165 | 20 | 318.6 |
| 20 | 180 | 20 | 318.6 |
| 20 | 195 | 40 | 318.8 |
| 19.9 | 210 | 40 | 319 |
| 19.9 | 225 | 40 | 319.2 |
| 19.8 | 240 | 40 | 319.3 |
| 19.8 | 255 | 40 | 319.5 |
| 20 | 270 | 40 | 319.7 |
| 20 | 285 | 40 | 319.9 |
| 20 | 300 | 40 | 320.1 |
| 20 | 315 | 40 | 320.1 |
| 19.9 | 330 | 40 | 320.3 |
| 20.1 | 345 | 60 | 320.4 |
| 20.1 | 360 | 60 | 320.5 |
| 20 | 375 | 60 | 320.7 |
| 20 | 390 | 60 | 320.9 |
| 20 | 405 | 60 | 321 |
| 20.1 | 420 | 60 | 321 |
| 20.1 | 435 | 80 | 321.1 |
| 20.1 | 450 | 80 | 321.2 |
| 19.9 | 465 | 80 | 321.2 |
| 19.9 | 480 | 80 | 321.3 |
| 19.9 | 495 | 80 | 321.5 |
| 20 | 510 | 80 | 321.5 |
| 20 | 525 | 80 | 321.7 |
| 20 | 540 | 80 | 321.7 |
| 20 | 555 | 80 | 321.7 |

Table 3. Mass variation in time for CP5 composite material at different moisture coefficients (20%H, 40%H, 60%H, 80%H) and the temperature of 40°C

| Temperature [°C] | Time [min] | Humidity [H] | Mass [g] |
|------------------|------------|--------------|----------|
| 39.8 | 0 | 20 | 301.8 |
| 39.7 | 15 | 20 | 302.6 |
| 39.9 | 30 | 20 | 304.2 |
| 39.8 | 45 | 20 | 306.2 |
| 39.9 | 60 | 20 | 309.8 |
| 40 | 75 | 20 | 311.8 |
| 39.8 | 90 | 20 | 312.3 |
| 39.7 | 105 | 20 | 314 |
| 40 | 120 | 20 | 315.7 |
| 39.9 | 135 | 20 | 316.8 |
| 39.8 | 150 | 20 | 317.2 |
| 40 | 165 | 20 | 317.6 |
| 39.9 | 180 | 20 | 318.2 |
| 40 | 195 | 20 | 318.2 |
| 40 | 210 | 40 | 318.3 |
| 40.1 | 225 | 40 | 318.8 |
| 39.8 | 240 | 40 | 319.2 |
| 39.9 | 255 | 40 | 319.4 |
| 39.9 | 270 | 40 | 319.3 |
| 40 | 285 | 60 | 319.3 |
| 40.1 | 300 | 60 | 319.5 |
| 40.1 | 315 | 60 | 319.6 |
| 39.9 | 330 | 60 | 319.8 |
| 39.9 | 345 | 60 | 320 |
| 40 | 360 | 60 | 320.1 |
| 40.1 | 375 | 60 | 320.1 |
| 40 | 390 | 80 | 320.2 |
| 40 | 405 | 80 | 320.4 |
| 40 | 420 | 80 | 320.6 |
| 40.1 | 435 | 80 | 320.7 |
| 40.1 | 450 | 80 | 320.8 |
| 40 | 465 | 80 | 321 |
| 40 | 480 | 80 | 321 |
| 40.1 | 495 | 80 | 321 |

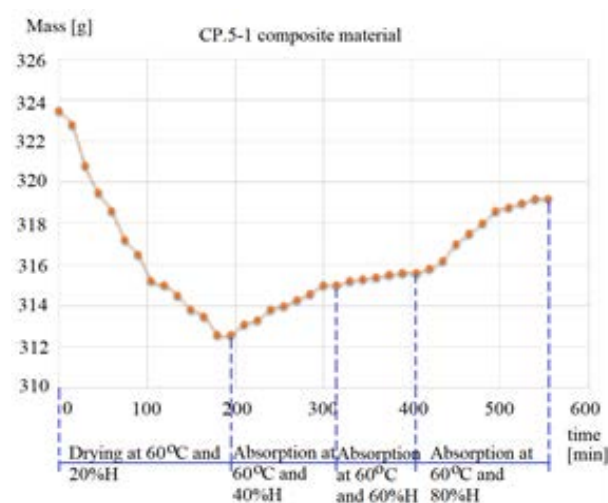


Figure.4. Curve of variation between the mass values and time for the temperature of 60°C and different moisture levels (20%H, 40%H, 60%H, 80% H).

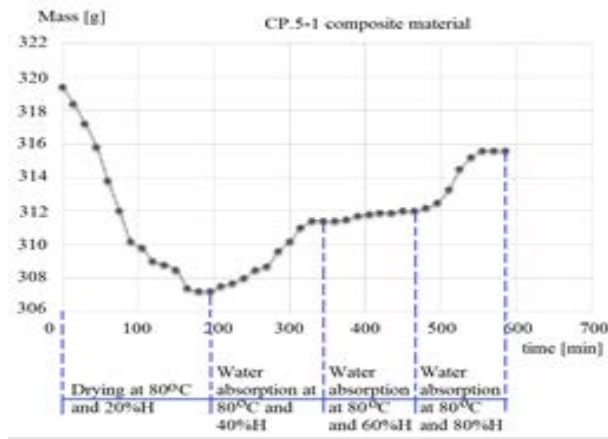


Figure 5. Curve of variation between the mass values and time for the temperature of 80°C and different moisture levels (20%H, 40%H, 60%H, 80%H)

Table 4. Mass variation in time for CP5 composite material at different moisture coefficients (20%H,40%H, 60%H, 80%H) and the temperature of 60oC

| Temperature [°C] | Time [min] | Humidity [H] | Mass [g] |
|------------------|------------|--------------|----------|
| 59.8 | 0 | 20 | 323.5 |
| 60 | 15 | 20 | 322.8 |
| 59.9 | 30 | 20 | 320.8 |
| 59.9 | 45 | 20 | 319.5 |
| 59.8 | 60 | 20 | 318.6 |
| 59.8 | 75 | 20 | 317.2 |
| 59.9 | 90 | 20 | 316.5 |
| 59.9 | 105 | 20 | 315.2 |
| 59.9 | 120 | 20 | 315 |
| 60.1 | 135 | 20 | 314.5 |
| 60 | 150 | 20 | 313.8 |
| 60.1 | 165 | 20 | 313.5 |
| 59.9 | 180 | 20 | 312.6 |
| 59.8 | 195 | 20 | 312.6 |
| 59.9 | 210 | 40 | 313.1 |
| 60 | 225 | 40 | 313.3 |
| 60 | 240 | 40 | 313.8 |
| 59.8 | 255 | 40 | 314 |
| 60 | 270 | 40 | 314.3 |
| 59.9 | 285 | 40 | 314.6 |
| 60 | 300 | 40 | 315 |
| 60.1 | 315 | 40 | 315 |
| 59.9 | 330 | 60 | 315.2 |
| 60 | 345 | 60 | 315.3 |
| 60 | 360 | 60 | 315.4 |
| 59.8 | 375 | 60 | 315.5 |
| 59.8 | 390 | 60 | 315.6 |
| 59.9 | 405 | 60 | 315.6 |
| 60.1 | 420 | 60 | 315.8 |
| 60.1 | 435 | 80 | 316.2 |
| 60.1 | 450 | 80 | 317 |
| 59.9 | 465 | 80 | 317.5 |
| 59.9 | 480 | 80 | 318 |
| 60 | 495 | 80 | 318.6 |
| 59.8 | 510 | 80 | 318.8 |
| 60 | 525 | 80 | 319 |
| 60 | 540 | 80 | 319.2 |
| 60 | 555 | 80 | 319.2 |

Table 5. Mass variation in time for CP5 composite material at different moisture coefficients (20%H, 40%H, 60%H, 80%H) and the temperature of 80°C

| Temperature [°C] | Time [min] | Humidity [H] | Mass [g] |
|------------------|------------|--------------|----------|
| 79.7 | 0 | 20 | 319.4 |
| 79.7 | 15 | 20 | 318.4 |
| 79.6 | 30 | 20 | 317.2 |
| 79.6 | 45 | 20 | 315.8 |
| 79.6 | 60 | 20 | 313.8 |
| 79.7 | 75 | 20 | 312 |
| 79.7 | 90 | 20 | 310.2 |
| 79.6 | 105 | 20 | 309.8 |
| 79.8 | 120 | 20 | 309 |
| 79.8 | 135 | 20 | 308.8 |
| 79.7 | 150 | 20 | 308.5 |
| 79.7 | 165 | 20 | 307.4 |
| 79.8 | 180 | 20 | 307.2 |
| 79.8 | 195 | 20 | 307.2 |
| 79.7 | 210 | 40 | 307.5 |
| 79.8 | 225 | 40 | 307.7 |
| 79.8 | 240 | 40 | 308 |
| 79.8 | 255 | 40 | 308.5 |
| 79.6 | 270 | 40 | 308.7 |
| 79.7 | 285 | 40 | 309.6 |
| 79.7 | 300 | 40 | 310.2 |
| 79.8 | 315 | 40 | 311 |
| 79.8 | 330 | 40 | 311.4 |
| 79.8 | 345 | 40 | 311.4 |
| 79.9 | 360 | 60 | 311.4 |
| 79.9 | 375 | 60 | 311.5 |
| 79.9 | 390 | 60 | 311.7 |
| 79.8 | 405 | 60 | 311.8 |
| 79.8 | 420 | 60 | 311.9 |
| 79.7 | 435 | 80 | 311.9 |
| 79.7 | 450 | 80 | 312 |
| 79.9 | 465 | 80 | 312 |
| 79.8 | 480 | 80 | 312.2 |
| 79.9 | 495 | 80 | 312.5 |
| 79.7 | 510 | 80 | 313.3 |
| 79.8 | 525 | 80 | 314.5 |
| 79.8 | 540 | 80 | 315.2 |
| 79.8 | 555 | 80 | 315.6 |
| 79.8 | 570 | 80 | 315.6 |
| 79.7 | 585 | 80 | 315.6 |

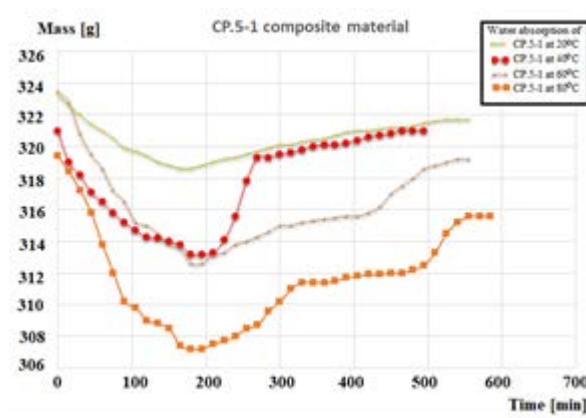


Figure 6. Curves of the variation of the mass during the time in function of different temperatures



Figure 7. SEM analyses plywood CP5 composite

In the Table 4 is establish the variation of the mass values during on time for the CP5 composite material for temperature of 60°C and different moisture values and in the table 5 is shown the mass value variation in function of time at the temperature of 80°C using different moisture values (20%H, 40%H, 60%H, 80%H). In the figure 4 is presented the curve of variation between the mass values and time for the temperature of 60°C and different wettability coefficients (20%H, 40%H, 60%H, 80% H) and in the figure 5 it is shown the variation curve in the same conditions, for the temperature of 80°C. In the figure 6 can remarck the different curves that show the variation of the mass during the time for the CP5 composite material. In figure 7 is presented the microscopic structure of CP5 composite material.

Conclusion

Due to the urge of developing environmentally friendly materials, researches in new dimensions evolved .This new dimension focuses on developing eco friendly material with good mechanical strength. The CP5 composite materials presents a higher moisture resistance in comparisons with different other composites. At the humidity value of 20%H, can remarck a drying process for the composite materials, if it increases the humidity values, can remarck an increase of mass values proportional with the humidity percents, because of the water absorption in the composite materials, although the temperature rises. Its superior properties will certainly help Composite engineers, researchers, manufacturers in developing environment friendly materials for a better tomorrow in future and could substitute the synthetic plastic and non degradable plastic.

Scientific Ethics Declaration

The authors declare that the scientific ethical and legal responsibility of this article published in EPSTEM journal belongs to the authors.

Acknowledgement

This article was presented as an oral presentation at the International Conference on Basic Sciences, Engineering and Technology (www.icbaset.net) conference held in Istanbul/Turkey on August 25-28, 2022.

This work has been funded by the EEA & Norway Grant, with project title “European network for 3D printing of biomimetic mechatronic systems”, Acronym EMERALD - Nr. Contract 21-COP-0019/ F-SEE-026/06.2021.

References

Amuthakkannan, P., Vairavan, M., Thangaiah, W. & Uthayakumar, M. (2014). Effect of moisture absorption behavior on mechanical properties of basalt fibre reinforced polymer matrix composites, *Journal of Composites*, Article ID 587980.

- Costa, M., Rezende, M.C. & Almeida, S. (2006). Effect of void content on the moisture absorption in polymeric composites, *Polymer-Plastics Technology and Engineering* 45(6),691-698.
- Hamidi, Y., Aktas, L. & Altan, M. (2017). Thermal history effects on moisture absorption of fiber-reinforced polymer composites, *AIP Conference Proceedings* 1914, 030012.
- Leman, Z., Sapuan, S.M., Saifol, A.M., Maleque, M.A. & Ahmad, M. (2008), Moisture absorption behavior of sugar palm fiber reinforced epoxy composites, *Materials&Design* 29(8), 1666-1670.
- Saravanakumar, A., Senthilkumar, A., Rajan, B., Rajini, N., Ismail, S., Mohammad, F. & Al-Lohedan, H. (2022). Effects of moisture absorption and thickness swelling behaviors on mechanical performances of carica papaya fiber reinforced polymeric composites, *Journal of Natural Fibers*, <https://doi.org/10.1080/15440478.2022.2051668>.

Author Information

Băilă Diana-Irinel

University Politehnica of Bucharest, Romania
Blv.Splaiul Independenței, no.313, sector 6, cod 060042,
Bucharest, Romania
Contact e-mail: baila_d@yahoo.com

Păcurar Răzvan

Technical University of Cluj-Napoca, Romania
Faculty of Machine Building, Department of Manufacturing
Engineering, Blv. Muncii, no. 103-105, 400641, Cluj-
Napoca, Romania

Păcurar Ancuța

Technical University of Cluj-Napoca, Romania
Faculty of Machine Building, Department of Manufacturing
Engineering, Blv. Muncii, no. 103-105, 400641, Cluj-
Napoca, Romania

To cite this article:

Diana-Irinel, B., Răzvan, P. & Ancuța, P. (2022). Moisture absorption of CP5 composite materials used in industry. *The Eurasia Proceedings of Science, Technology, Engineering & Mathematics (EPSTEM)*, 18, 55-63.

The Eurasia Proceedings of Science, Technology, Engineering & Mathematics (EPSTEM), 2022

Volume 18, Pages 64-71

ICBASSET 2022: International Conference on Basic Sciences, Engineering and Technology

Smart Cities: Using GIS Technology in Urban Infrastructure Development at Migration Areas

Bushra ZALLOOM
Zarqa University

Abstract: Technology played a vital role in urban planning and urban infrastructure development. The Geographic Information System (GIS) can help in creating smart cities by analyzing the required issues and present them for local communities. It can improve utilization of existing infrastructure capacity thus improving quality of life, it can also provide a guidance about mobility and the best use for available services. Smart cities promise that with increasing connectedness, services and quality of life can be improved. The intent of smart cities is to make urbanization more inclusive, bringing together public and private sectors, connecting urban centers with periphery, delivering services for all users alike, and integrating the migrants and poor into their community. This research aim at highlighting the advantages of using GIS technology in urban infrastructure development at Migration Areas in Amman the capital of Jordan that welcomes waves of immigration during the last decades which affect its infrastructure, basic services, and socio-economic situation. It focuses on one of the neighborhood and discover the challenges and opportunities based on the infrastructure development analyses using the GIS. The findings of this research confirm the essential need for smart cities with more inclusive plan to help in decreasing the vulnerability of both refugees and host communities thus enhance the social sustainability.

Keywords: Smart Cities, Urban Infrastructure, GIS, Migration Areas, Amman

Introduction

Smart city is the city of tomorrow. It tries to identify a smarter option to maximize the individuals satisfaction and accelerate urban socio-cultural and economic development (Cathelat, 2019). The smart city information system is built on four principles: Planning and engineering, data-driven performance, operational efficiency, and civic inclusion. However, According to Cathelat (2019:41) “the current reality of smart cities is that there aren’t any. At the end of the day, most so-called smart cities are just cities with a few or several standout smart projects”. Still, there are many initiatives in Jordan for a Smart city that are initiated to achieve one or more of the following objectives:

1. Efficiency of Services: Make the best effective use of public resources, and provide a high level of citizen service.
2. Sustainability: Develop the city with considering the environmental, economic and social impacts.
3. Mobility: Make it easy for all users to move in the city, whether by foot, bike, car, public transport.
4. Safety and Security: Improve public safety and security in every-day life, as well as being best possibly prepared for emergencies and disasters.
5. Economic Growth: Attract businesses, investors, citizens and visitors.
6. City Reputation: Constantly improve the city’s image and reputation.

These objectives can be achieved by using various types of technology such as GIS, online forums, online survey, and digital media throughout the decision-making process, these tools connect cities at the national and international levels and foster knowledge exchange among various parties, it also increases the public awareness among stakeholders for the importance of good data management and urban observatory platforms for future.

Since its development in the 1970s, the GIS is used in planning and developing the urban infrastructure, it becomes easier to analyze the collected data and bring many proposals to the ground (Banerjee, 2020). Today, a growing number of cities rely on GIS to model the real world at every stage of planning and development of a Smart City as it can incorporate a huge number of variables. There are various applications of GIS that help in developing the urban infrastructure in a smart way by analyzing the required issues and present them for individuals (Consortium, 2019). It can improve utilization of existing infrastructure thus improving quality of life, it can also provide the best practices for various types of mobility. In urban infrastructure projects the GIS is used based on a number of steps (Consortium, 2019):

1. Creation of the Urban Digital Model that illustrates the components of the urban built and natural environments.
2. Creation of the Sensing Layer that comprises sensors used for monitoring urban networks and infrastructures.
3. Analysis of Data by converting real-time and historical data into operational data that improves the security, efficiency and quality of urban systems.
4. Interactive Visualization of urban components and sensors maps. Users can utilize these maps to access static and dynamic data concerning urban systems.
5. The Control Layer that allows real-time visualization of these devices as well as their status. It could also visualize errors in device command.

Accordingly, this paper provide context on the national refugee situation in Jordan. Then, it highlights how Jordan can transform the migration challenges into spatial and urban infrastructure investment and create smart communities by using the GIS technology throughout planning stages. the GIS technology is used in studying the current condition of urban infrastructure at one of the migrants' areas in Amman, called the Al Hashmi Al Janoubi neighborhood, to help in developing this area in a smart way. Finally, this paper summarizes the urban challenges and opportunities that can be addressed through future development strategies.

Method

The research methodology consists of data collection, literature revision, and field observation. Stakeholders were asked to identify existing challenges in current infrastructure. These were categorized under the four main topics: Natural Environment, Urban Environment, Infrastructure Projects, and Refugee Integration. Moreover, Geographic Information System (GIS) is used to undertake the spatial analysis throughout the proposed plans, and assess the accessibility to public facilities.

National Context: Refugees in Jordan

Since its independence in 1946, Jordan has been a safe paradise to approximately 4 million refugees including Circassian, Palestinians, Iraqis, Syrians, and Yemeni, and others. Today, Jordan is hosting 89 refugees per 1,000 inhabitants (UNHCR, 2018). These refugees have become an important part of the country's population and social fabric. The extraordinary numbers of refugees from surrounding countries have significantly affected Jordan throughout its history, and played a vital role in shaping the country's politics, economy, community, and urban characteristics (Zalloom, 2020).

Figure (1) illustrates the refugee population density based on the nationality, indicating the highest refugee presence for Palestinians, Syrians, and Iraqis at the Amman city (UN-Habitat, 2022). This analysis supported the selection of the neighborhood that has been affected by the refugee influx.

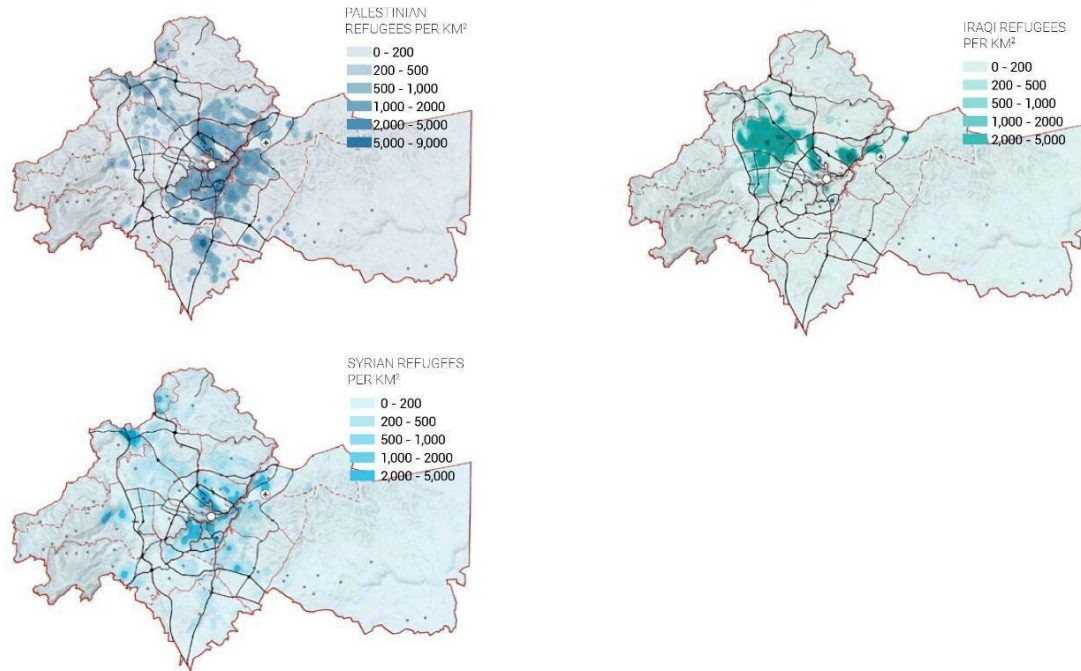


Figure 1. Refugee population density in Amman city (Source: UN-Habitat 2022)

After ten years of the Syrian Crisis and their immigration to Jordan, it becomes clear that the infrastructure, basic services, and economies of Jordanian cities are affected. The need for a more inclusive plan that help in decreasing the vulnerability of both refugees and host communities and provide longer-term sustainable solutions is appeared (Government of Jordan, 2020). Accordingly, national and international efforts are made to cope with this urban transformation, and to improve access to services and socioeconomic opportunities for displaced and host communities.

Applying GIS Technology in a Migrants' Area in Amman

Since 2011, municipal services in Amman, the capital of Jordan, have been significantly affected by the Syrian refugee crises. The waves of refugees from camps to urban areas has a major impact on the capacity of infrastructure and public facilities, such as education, health, public space, transportation, and natural resources (United Nations Jordan, 2021). The rapid displacement of populations to urban settings had major spatial, economic, environmental, and social impacts, which maximize the challenges that facing Amman Municipality such as, the lack of access to acceptable basic service infrastructure, the lack of affordable housing. These challenges affecting the refugees as well as the host communities. The urban sprawl and inefficient urban planning have led to the insufficient distribution and access to services and infrastructure which may cause critical issues. This negatively impacts their economic and social sustainability, thus, has resulted in the inefficient use of valuable resource and has left communities facing increased long-term problems, a lack of self-reliance, and insufficient access to urban services. Therefore, studying and analyzing the areas where migrants come and live is very essential.

The collection of accurate data helps in planning and decision-making process, thus, allows for achieving sustainable urban development. Developing and implementing efficient and reliable plans requires accurate, comprehensive, and up-to-date data to understand the urban needs of the population. However, inaccurate data lead to spatial inequalities in service supplying, housing, education, and public space development. Unfortunately, the available data at municipalities only considers local citizens, rather than all inhabitants, including the refugees, this may result in inadequate resource provisioning and inequitable services' distribution.

Using the modern technology such as GIS helps in filling these gaps when collecting and analyzing data, and help in creating guidance for the current and future planning of the city, which should be aligned to the Sustainable Development Strategy. It is an analytic tool that spatially integrates and analyzes urban indicators

and attributes at the city levels by creating multi layers (Banerjee 2020, Zalloom 2020). Furthermore, applying the Sustainable Development Goals (SDGs) is essential as it helps in supporting the selected neighborhood to become more inclusive, safe, resilient, and sustainable. Urban planning strategies that built on infrastructure investments aim to benefit migrant communities, enhance the quality of their life, and create better opportunities for economic investment (UN-Habitat, 2022). In this manner, public can participate in decision making process and they involve in all planning stages from the beginning.

Accordingly, a spatial plan is developed for Al Hashmi Al Janoubi neighborhood in Amman. The area of study is one of the most affected areas with influx of refugees, it has an area of 0.43 km², a total population of 14,100 inhabitants, therefore, a population density is 32,118.4 person/ km² (UN-Habitat, 2022). Figure (2) shows the land use of the compacted neighborhood, the satellite image was combined with the available data by using the GIS technology. The created figure shows the residential land use within the neighborhood that mainly comprises of types C, type D, and the unplanned zones while the area has no assigned commercial land uses within its boundaries, instead, small commercial shops that are usually on the ground floor of mixed-use buildings are used to serve residents.

The residential types “C” and “D” according to the “Law of Planning of Cities, Villages, and Buildings, No.79” can have up to four floors, with minimum setbacks of 2.5 meters at “D” type and 3 meters at “C” type. This distance allow people to contact daily, thus, have a strong relationship that enhance the social sustainability of the area. Furthermore, the project is underpinned site visits to visually assess the current situation and to interact with the residents in the neighborhood, the field observation for the neighborhood found housing in good condition and structure, but still the existing public infrastructure, the walkways, and street furniture are not acceptable and need maintenance.

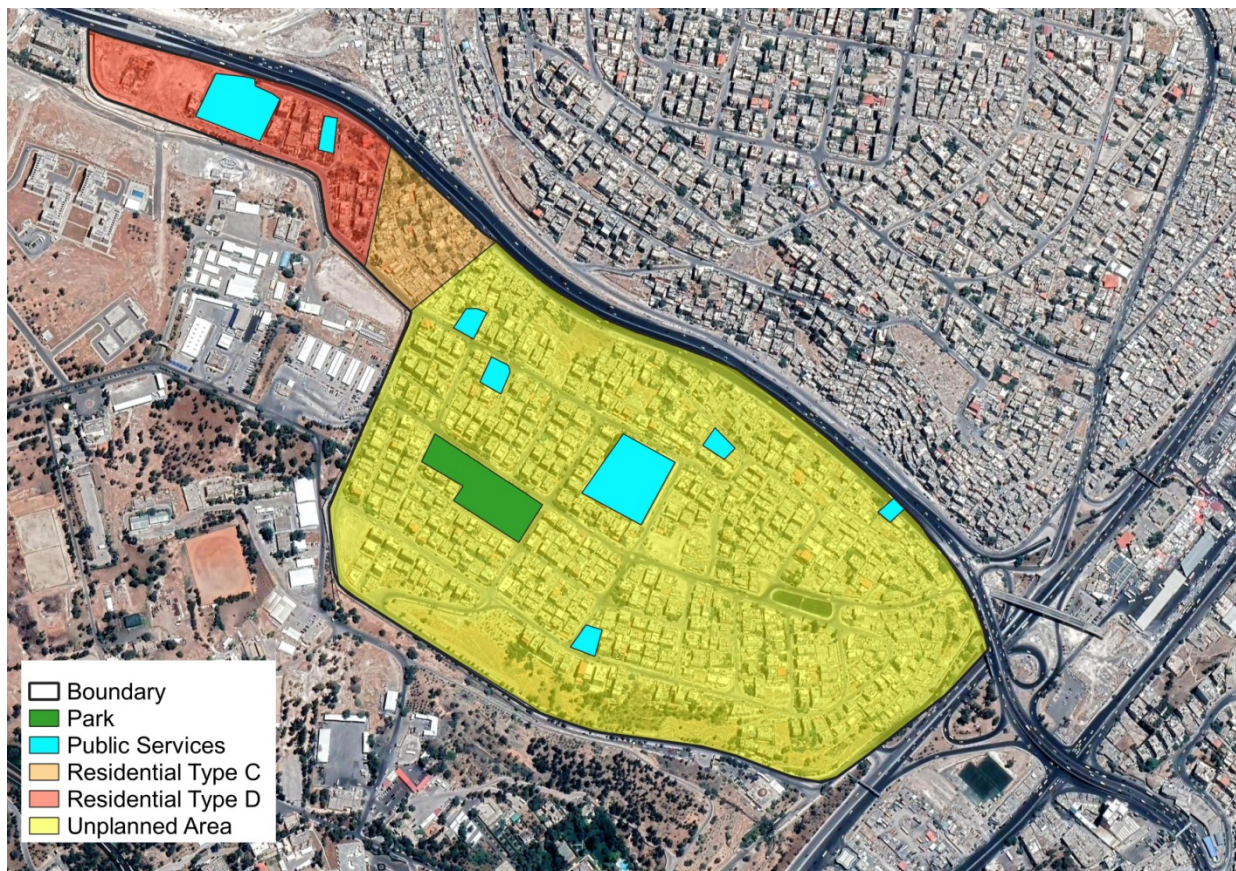


Figure 2. Satellite image shows the compacted neighborhood

Al Hashmi Al Janoubi neighborhood is further analyzed by the GIS program based on its context, refugee presence, access to transportation, access to basic services, and access to public facilities. It was used to undertake the spatial analysis throughout the proposed plans, and assess the accessibility to public facilities within a walkable distance of 15 to 30-minute. The site analysis shows that there are three schools for male and females, four mosques, one public park, and one public health center (Figure 3). The accessibility to these services is very high. Moreover, the street network analysis shows that all services located within a walkable

distance, 40.9% of the population have access to these services within a 5-minute walking distance and 100% within a 15-minute (Figure 4). The preparation of urban planning analyses for the selected area will help in proposing various planning scenarios and arranging priorities that improve living conditions thus enhancing the quality of life; these priorities can be identified, discussed, and converted to actions. It gives a comprehensive spatial understanding of the existing situation as a basis for decision-making. This provides a unique opportunity for stakeholders with different mandates to work together to connect short-term plans with long-term strategies and investments, enabling the development of more inclusive communities.

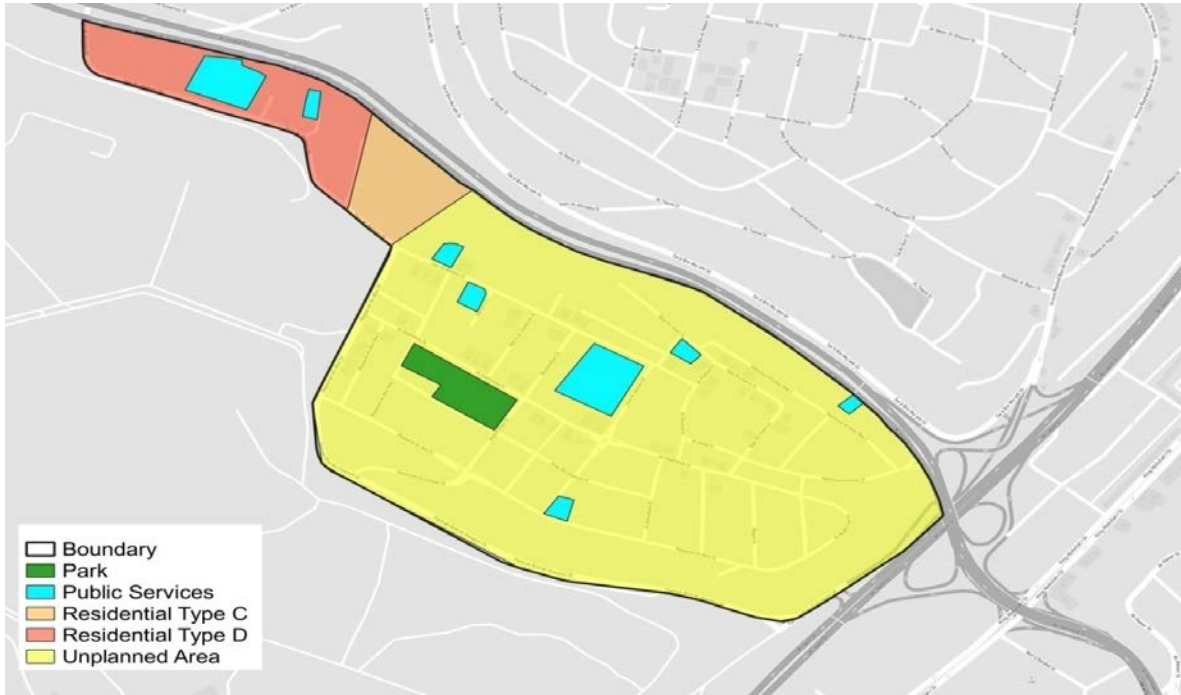


Figure 3. Land use map

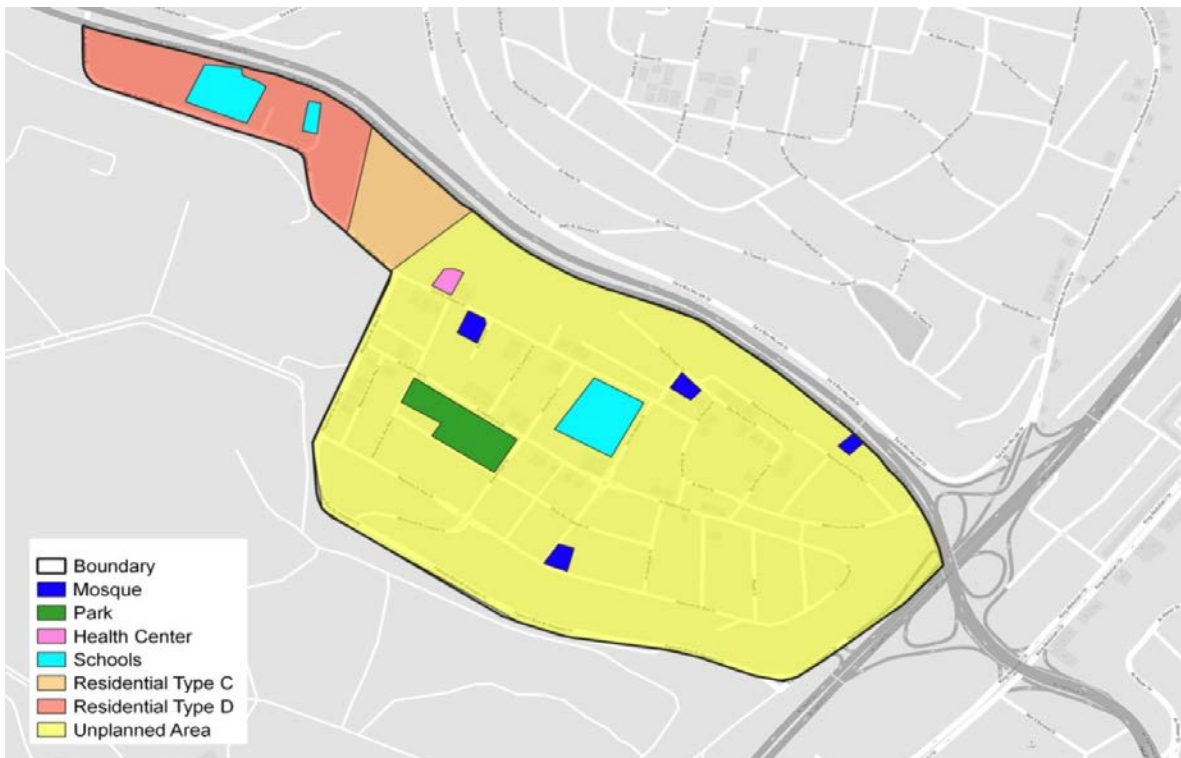


Figure 4. Access to public services

Findings: Challenges and Opportunities

The spatial planning of Amman has revealed various strategic challenges accompanied with the waves of migrations at various levels. At the national level, the major challenge identified is unequal urbanization, whereby weak urban planning practices and influxes of refugees have led to inadequate distribution and access to basic services and public facilities. Accordingly, this rapid urban growth has resulted in urban sprawl that increased the demand on services, thus maximize the pressure on Greater Amman Municipality, who have limited resources to fulfill this gap. This has impacted the quality-of-service, as well as the quality of life for locals and immigrants. Moreover, the lack of affordable adequate housing has become a critical issue due to the inflated prices of land, construction, and energy. Furthermore, inadequate transportation has resulted in major environmental, economic, and social challenges, as public transportation is slow, costly, and time consuming, thus, mainly used by the refugees and locals with low incomes. Refugees and host communities are currently facing outstanding challenges caused by the COVID-19 pandemic, which has resulted in increasing unemployment rates. The Municipality has limited capacity to support local economic development, while also facing constraints to finance service delivery.

At the neighborhood level, it was discovered that Al Hashmi Al Janoubi neighborhood in Amman lack access to health care facilities as it has only one public health center, although it is located within a walkable distance but still not enough to fulfill the residents' and migrants' needs. The neighborhood also has some challenges concerning road maintenance, whereby there is a need for speed bumps, pedestrian crossings, pedestrian bridges on the main roads, safe walkways, street-lighting and furniture.

The neighborhood has no assigned commercial land uses within its boundaries, instead, small commercial shops that are usually on the ground floor of mixed-use buildings are used to serve residents. It is clear that the outdated "Law of Planning of Cities, Villages, and Buildings, No.79", which was established in 1966 affected the land use, the facility distribution, as well as the urban fabric. Furthermore, the area lack of children facilities and it is not designed for people with disabilities, besides the lack of maintenance and rehabilitation of the existing public recreational facilities, and a lack of green elements and spaces. There are also some concerns about the safety of the park at nights as it becomes a men domain and cannot be used by women and children.

Although these challenges specifically affect the achievement of the SDGs goals, but still, there is a significant opportunity to address the challenges associated with migration. At the national level, the Syrian refugee crisis can be transformed into a development opportunity that attracts new investments and boosts the local economy. Amman has a high proportion of youth where more than half of the population are under 25 years old (The Department of Statistics, 2020). This means that there is a growing labor force, less demand on health facilities, and reduced dependency rates. Moreover, the COVID-19 pandemic and restrictions raised awareness on the importance of spatial planning, the availability of green open space, of investing the vacant lands for green open spaces, urban agriculture to reduce unemployment, mitigate climate change impact, enhance the residents' socio-economic conditions, and achieve food security. Likewise, developing adequate mobility options will give the opportunity of minimizing the environmental impact and increasing the residents' socioeconomic conditions and access to job opportunities. The strategic location of Amman, and the enhancement of affordable and accessible public transport is an important opportunity that can enhance the socioeconomic opportunities. As there are several planned infrastructure projects and investments that will help in promoting sustainability and improving the delivery of services.

At the neighborhood level, the study confirms that there is an opportunity to improve access to healthcare through constructing a comprehensive health centre and upgrading the existing primary health centre within the neighborhood. The mobility of residents could be enhanced through restoring the road infrastructure, adding various means of street furniture such as lighting poles, waste containers and benches, extending a public transport route into the neighborhoods, as well as adding pedestrian bridges. There are also opportunities to encourage diversity in commercial facilities by establishing community centre training centre, and by improving the public spaces, which can host various social activities, bazaars, cafes and restaurants, thus boost the livability of the public areas.

Conclusion

Technology played a fundamental role in urban infrastructure development. The Geographic Information System (GIS) is used to provide a better understanding of the urban context at different levels, it helps in

creating smart cities by analyzing the collected data and transform them into maps. The analyses outcomes are then presented for local communities and stakeholders. This research aim at highlighting the advantages of Using GIS Technology in urban infrastructure development at Migration Areas in Amman the capital of Jordan.

The waves of emigration have played a vital role in shaping the country's politics, economy, and urban characteristics. A specific neighborhood in Amman is selected as an example to understand the impacts of these migrations based on the infrastructure development analyses using the GIS. The findings of this research confirm the essential need for smart cities with more inclusive plan to help in decreasing the vulnerability of both refugees and host communities thus enhance the social sustainability.

Recommendations

It is recommended that the findings of this research considered as a foundation for decision- making when developing the urban infrastructure at the migration areas. The challenges and opportunities identified in this spatial planning for the selected neighborhood can be entry points for future national and international strategies.

Scientific Ethics Declaration

The author declares that the scientific ethical and legal responsibility of this article published in EPSTEM journal belongs to the author.

Acknowledgements

This article was presented as an oral presentation at the International Conference on Basic Sciences, Engineering and Technology (www.icbasnet.net) conference held in Istanbul/Turkey on August 25-28, 2022.

The author acknowledge the Dean of Scientific Research at Zarqa University in Jordan for funding this research. Special thanks to Eng. Mais Malik Atiyat for preparing the GIS maps.

References

- Banerjee, S., Chakraborty, C., & Das, D. (2020). An approach towards GIS application in smart city urban planning. In *Internet of Things and Secure Smart Environments* (pp. 71-110). Chapman and Hall/CRC.
- Cathelat, B. (2019). *Smartcities shaping the society of 2030*. Paris: UNESCO and NETEXPLO. Aralık, 21, 2021.
- Consortium (2019). *What is the use of application of GIS services in smart cities?* July 7, 2022. <https://giscindia.com/use-application-gis-services-smart-cities/>
- Government of Jordan. (2020). *Jordan response plan for the Syria crisis 2020-2022*. Retrieved April 21, 2022, from Ministry of Planning and International Cooperation
- The Department of Statistics. (2020). *Estimated population of 2020 and some of selected data*. Retrieved April 21, 2022, The Department of Statistics: http://dosweb.dos.gov.jo/DataBank/Population_Estimares/PopulationEstimates
- UNHCR. (2018, February). *UNHCR Jordan factsheet - February 2018*. Retrieved April 21, 2022, from ReliefWeb: <https://reliefweb.int/report/jordan/unhcr-jordan-factsheet-february-2018>
- UN-Habitat (2022, March). *AMMAN SPATIAL PROFILE*. Retrieved from United Nations Jordan: https://jordan.un.org/sites/default/files/2022-04/220411-final_amman_profile_0.pdf
- United Nations Jordan (2021, July 04). *Together we learn: supporting inclusive education for refugees in Jordan*. Retrieved from United Nations Jordan: <https://jordan.un.org/en/134455-together-we-learn-supporting-inclusive-education-refugees-jord>
- Zalloom, B. (2020). Enhancing tourism by reconnecting the fragmented landscape of wadi araba in Jordan. *Journal of Urban Planning and Development*. 146(3): 05020010. [https://doi.org/10.1061/\(ASCE\)UP.1943-5444.0000592](https://doi.org/10.1061/(ASCE)UP.1943-5444.0000592)

Author Information

Bushra Zalloom

Zarqa University

Zarqa, Jordan

Contact e-mail: bzalloom@zu.edu.jo

To cite this article:

Zalloom, B. (2022). Smart cities: Using GIS technology in urban infrastructure development at migration areas. *The Eurasia Proceedings of Science, Technology, Engineering & Mathematics (EPSTEM)*, 18, 64-71.

The Eurasia Proceedings of Science, Technology, Engineering & Mathematics (EPSTEM), 2022

Volume 18, Pages 72-80

ICBASET 2022: International Conference on Basic Sciences, Engineering and Technology

The Preparation of Montmorillonite/Carrageenan-Composite Hydrogel for Chromium (VI) Removal from Aqueous Solution

Gulen Oytun AKALIN

Aksaray University

Abstract: In this study, Montmorillonite/Carrageenan (MMT/CG)-composite hydrogel was synthesized for removal of Chromium (VI) from aqueous solution. The chemical structure, morphological property and thermal decomposition of (MMT/CG)-composite hydrogel has been evaluated by Fourier Transform Infrared Spectroscopy (FTIR), Scanning Electron Microscope Spectroscopy (SEM) and thermogravimetric analysis (TGA), respectively. The X-ray data of (MMT/CG)-composite hydrogel was researched crystallite properties. The results of (MMT/CG)-composite hydrogel CG, and MMT powders had compared each other to research the efficiency of MMT. The efficiency of adsorption parameters (contact time, initial feed concentration, and pH) on Chromium (VI) ion adsorbing capacity of (MMT/CG)-composite hydrogel was also investigated by UV-vis diffusive reflectance spectra. The adsorption capacity enhanced with the adding of MMT in hydrogel. The adsorption process was determined by the Langmuir isotherm model. According to the findings, the MMT/CG-composite hydrogel can be utilized as a suitable adsorbent to removal of Chromium (VI) from aqueous solution.

Keywords: Montmorillonite, Carrageenan, Hydrogel, Adsorption, chromium (VI)

Introduction

Water pollution is increasing day by day following the rapid industrial improvement. Industrial wastes, pesticides, detergents, agricultural fertilizers, dyestuffs, and heavy metals are major pollutions. Heavy metals must be effectively removed from water sources due to their toxic and carcinogenic properties.

Ion exchange, chemical precipitation, chemical oxidation/reduction, reverse osmosis, and ultrafiltration methods are frequently used to remove heavy metal ions. However, these methods have low efficiency and high cost, and they cause significant waste problem. Adsorption is another alternative method (Islam, Angove, & Morton, 2019). It is the accumulation of a substance on the surface of the second phase by passing from one phase to the other, or the retention of adsorbent molecules dissolved in the liquid phase on a solid adsorbent surface or the adhesion phenomenon that occurs at the phase interface because of the concentration change at the boundary surface. It occurs between solid-liquid or solid-gas phases. It has advantages such as low cost, simplicity of design, low energy requirement, high efficiency, ease of use, and reuse of adsorbents. The adsorption method becomes more prominent when environmentally friendly, non-toxic, cheap, and safe adsorbents are used. (Dakiky et al., 2002). In recent years, there has been a lot of research for alternative low-cost materials that are effective and biodegradable, such as hydrogels, agricultural wastes, and clays.

Hydrogels are inexpensive polymeric materials which include hydrophilic groups (such as -COOH, -SO₃H, -OH, -NH₂, -CONH, -CONH₂, etc.). They can easily swell in water due to their hydrophilic groups. They are extremely used in heavy metal removal systems because of their high-water holding capacity, biocompatibility, and biodegradability (Ahmed, 2015). Several natural polymers such as gelatin, carboxymethyl cellulose, pectin, chitosan, alginate, carrageenan etc. are utilized for formation of hydrogels.

- This is an Open Access article distributed under the terms of the Creative Commons Attribution-Noncommercial 4.0 Unported License, permitting all non-commercial use, distribution, and reproduction in any medium, provided the original work is properly cited.

- Selection and peer-review under responsibility of the Organizing Committee of the Conference

Carrageenan is obtained from *Rhodophyceae class* seaweed by some extraction methods from red algae species. It is a linear polysaccharide produced from the most common red algae *Chondrus Crispus* and *Gigartina Mamillosa*. It consists of large and highly elastic molecules in a coiled helical structure. Its flexible structures enable to generate gel forms at room temperature. (Sharma et al., 2022). Thanks to these properties, it is used as a thickener and stabilizer in the food industry and other industrial fields.

Clays are good adsorbent for heavy metal ions, polymer nanocomposites, catalyst, photochemical reactions, and biosensors. They have high chemical and mechanical stabilities and several surface and structure properties. Montmorillonite (MMT) is the commonly preferred clay for industrial utilization. MMT is an alteration forming of volcanic tuff and ash, product of bentonite beds, and of wall rock and pegmatite dikes bordering hydrothermal mineral deposits. It is non-toxic and low-cost, but its adsorption capability is limited by its poor water permeability. To overcome this limitation, MMT can be blended with other materials such as CMC, PVA, PMMA etc. to generate composite hydrogels (Ianchis et al., 2020; Kaşgöz, & Durmus, 2008). These composites have high water permeability, and they are used as adsorbents for heavy metal removal. However, the use of MMT/Carrageenan-composite hydrogels as adsorbent for heavy metal removal has not been studied. In this research, MMT/Carrageenan-composite hydrogels were prepared for $Cr(VI)$ ions removal. The adsorption capacity of $Cr(VI)$ ions by changing the MMT/CG mass ratio, pH of $Cr(VI)$ solution, initial $Cr(VI)$ concentration and contact time were investigated. To describe the adsorption character, adsorption isotherm model was examined.

Materials and Methods

Sodium-MMT with a zeta potential of -39.3 mV and a cationic exchange capacity of 71 mequiv/100 g was purchased from Southern Clay (USA) was supplied by Ciba Specialty Chemicals (Thailand). CG and Glutaraldehyde were supplied by Sigma Aldrich.

Preparation of MMT/Carrageenan-Composite Hydrogels

The MMT/CG suspensions were prepared by adding MMT (0.1, 0.2 and 0.3 w/v) to the 1% (w/v) CG solution under vigorous dispersion for 1 hr. 100 ml of MMT/CG suspension was added dropwise to 0.2% (w/v) glutaraldehyde solution using a peristaltic pump for the MMT/CG ratios of 0.1:1, 0.2:1 and 0.3:1 respectively. After the stirring for 1 h, the solidified MMT/CG-composite hydrogels were obtained, they washed with distilled water several times and then dried at 60°C for 24 h.

Characterization of MMT/CG Hydrogels

The MMT, Carrageenan and MMT/Carrageenan composite hydrogels were performed by Fourier transform infrared (FTIR) spectrophotometry (FT-IR Shimadzu IR-Prestige 2) using KBr. The measurement was scanned between 400 and 4000 cm^{-1} . The crystallinity of the samples was performed by wide-angle X-ray diffraction (XRD; Diffractometer Bruker D8 Advance). The X-ray diffractometer was done at 40 kV and 50 mA, with $Cu-K\alpha$ radiation source ($\lambda=1.54060 \text{ \AA}$). The morphology of the composite hydrogels was visualized by scanning electron microscopy (SEM; model Quanta 250, FEI). Thermal analysis of the composite hydrogels were determined by thermogravimetric analysis (TGA; TG/DTA 7300 Hitachi) under nitrogen gas flow from 30°C to 800°C at a heating rate of 10°C/min.

Adsorption Studies

The influence of contact time, pH, and initial concentration of $Cr(VI)$ solution on adsorption was investigated. The adsorption was performed on a shaker (120 rpm) at 25°C using 0.2 g MMT/CG composite hydrogels (MMT/CG mass ratio 0.1:1.0 and 0.3:1.0), and 50 mL of $Cr(VI)$ solution (80 mg/L) in a 125-mL conical flask. The $Cr(VI)$ solution was collected at certain time intervals and the residual $Cr(VI)$ concentration was measured using a UV-vis spectrophotometer (Shimadzu-18A UV-Visible spectrophotometer) at 540 nm (Alemayehu, Singh, & Tessema, 2012).

The amount of adsorbed $Cr(VI)$ concentration at time t was determined from Equation 1:

$$Q_t = \frac{(C_0 - C_t) V}{W} \quad (1)$$

Q_t is amount of adsorbed $Cr(VI)$ per amount of hydrogel at time t (mg/g), C_0 is initial $Cr(VI)$ concentration (mg/L), C_t is $Cr(VI)$ concentration at time t (mg/L), W is weight of dried composite hydrogels (g) and V is volume of $Cr(VI)$ solution (L).

The equilibrium adsorption capacity (Q_e) of the composite hydrogels was determined from Equation 2:

$$Q_e = \frac{(C_0 - C_e) V}{W} \quad (2)$$

where C_0 and C_e are initial concentration and equilibrium concentration of $Cr(VI)$ in solution (mg/L) respectively, V is volume of $Cr(VI)$ solution (L) and W is weight of dried composite hydrogels (g).

Results and Discussion

FTIR

The FTIR spectra of the MMT powder, CG powder and MMT/CG hydrogel (with MMT/CG mass ratio of 0.3:1 as representative sample) are given in Figure 1. The characteristic peaks of CG at 1291 cm^{-1} (the $O = S = O$ stretching vibration of C-4 position of galactose), 929 cm^{-1} (C-O-C vibration mode of the 3,6-anhydro-D-galactose residue) and 844 cm^{-1} (the $-O-SO_3$ stretching vibration of C-4 position of galactose) are occurred in the MMT/CG composite hydrogel (Pereira et.al, 2003). The hydrogel and CG powder both had a broad absorption peak at $3500-3000\text{ cm}^{-1}$, representing the $-OH$ stretching mode. The absorption at 2920 cm^{-1} was observed due to C-O groups and the interlayer C-H stretching. The absorption at 1500 cm^{-1} was represented for the $-CH_2$ stretching. The absorption at 1080 cm^{-1} for glycosidic linkage, the absorption at 933 cm^{-1} for C-O of 3,6-anhydro-D-galactose and the absorption at 850 cm^{-1} for C-O-SO₃ of D-galactose-4-sulfate were obtained. The functional groups of Al-O and Si-O of MMT in the MMT/CG-composite hydrogel were occurred between 400 and 600 cm^{-1} , which was absent in the CG powder. (Hayati-Ashtiani, 2011). This can be proved by the formation of MMT/CG hydrogel.

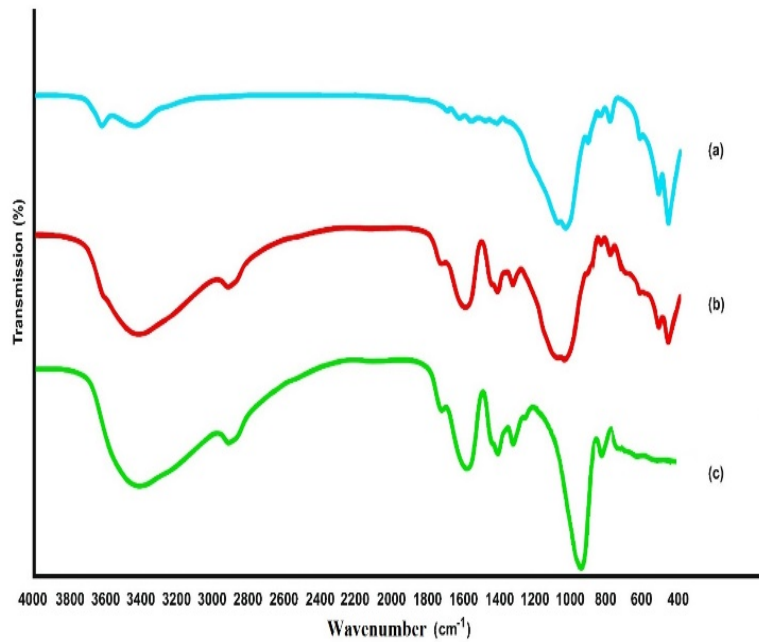


Figure 1. FTIR spectra of a) MMT powder, b) MMT/CG hydrogel, c) CG powder

XRD

The XRD diffractograms of the MMT powder, CG powder, MMT/CG-composite hydrogel (with MMT/CG mass ratio of 0.3:1 as representative sample) are shown in Figure 2. The sharp characteristic peak of MMT at nearly $6.00^{\circ}2\theta$ was observed, whereas this peak was not occurred in the diffractogram of CG powder and MMT/CG hydrogel. This can be explained by the connection of CG molecules into the MMT layer. Additionally, two peak were observed at $20\text{-}25^{\circ}2\theta$ for MMT powder, whereas CG powder, MMT/CG-composite hydrogel have a wider peak.

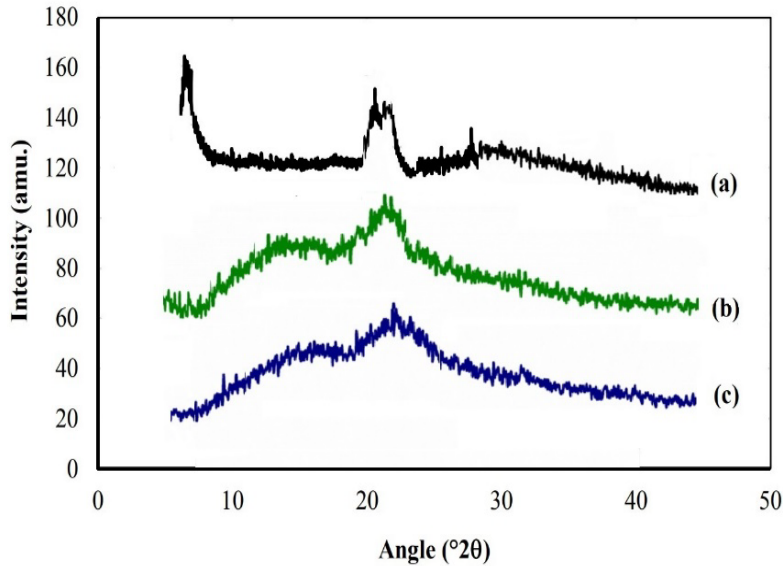
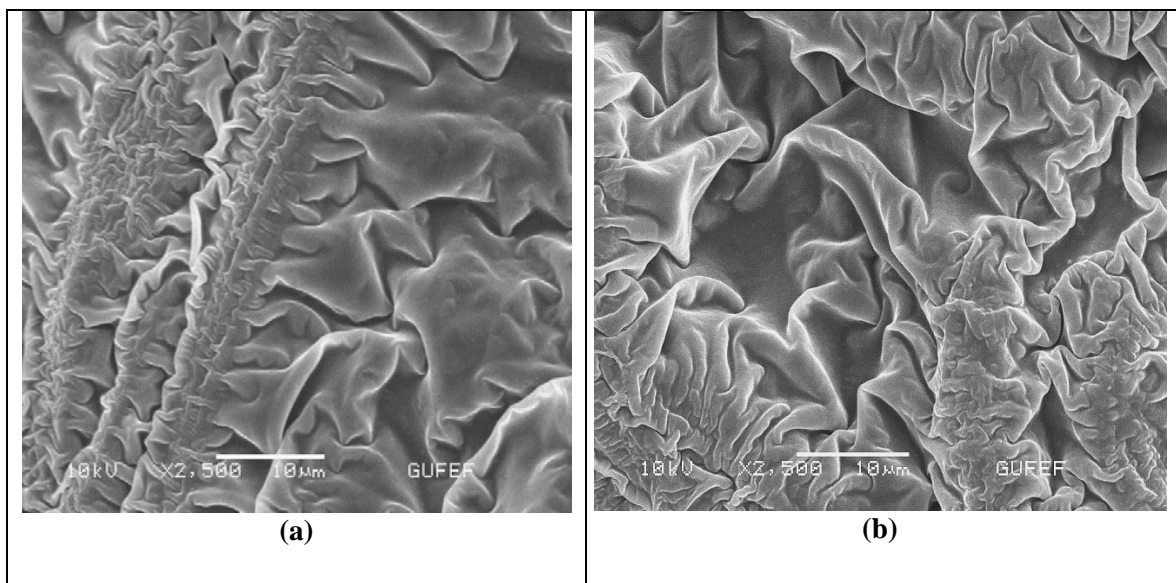


Figure. 2. XRD diffractograms of a) MMT powder, b) MMT/CG, c) CG powder

SEM

SEM images of MMT/CMC-composite hydrogels with different mass ratios are given in Figure 3. It was clearly seen that the surfaces of all hydrogels were rough. The most roughness was observed for MMT/CG (0.3:1) hydrogel. Surface roughness increased with increasing amount of MMT. This can be explained by the fact that the movement of the CG polymer chains may be interrupted by increasing the content of MMT, this causing the roughness to increase.



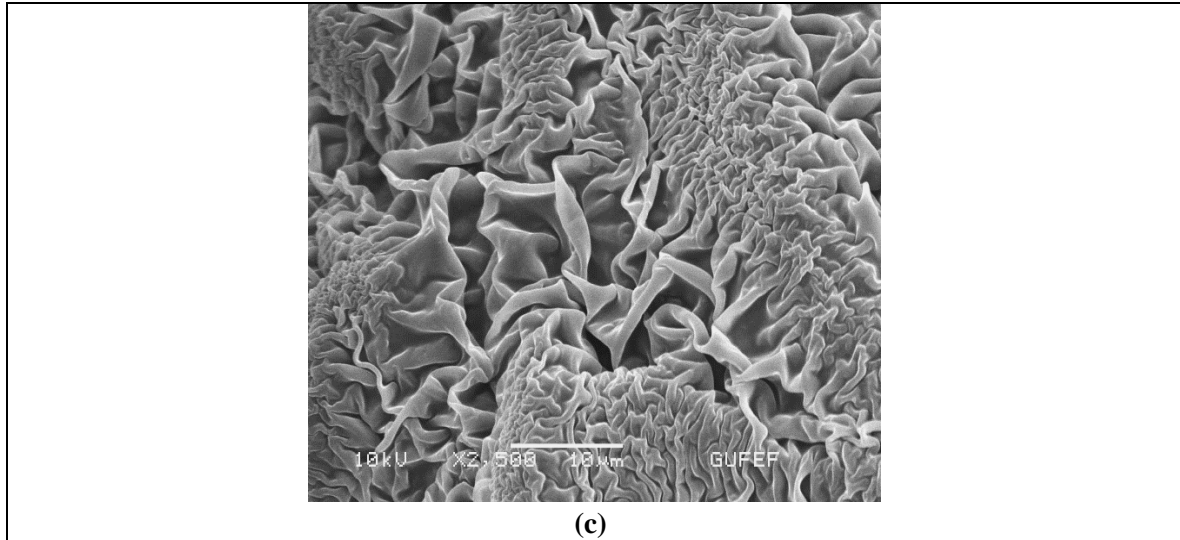


Figure 3. SEM images of the MMT/CG-composite hydrogel at MMT/CG mass ratios of (a) 0.1:1, (b) 0.2:1 and (c) 0.3:1

Thermal Analysis

The thermal properties of hydrogels were researched by TGA analysis. The TGA thermogram of the MMT/CG hydrogel, compared with those of the CG and MMT powders and, is given in Figure 4. At 25°C to 800°C, the weight loss (%) of the MMT/CG hydrogel was lower than that of CG powder, which demonstrated a good thermal stability of the MMT/CG-composite hydrogel than that of the CG powder. The results are compatible with the literature (Rojisitthisak et.al, 2019).

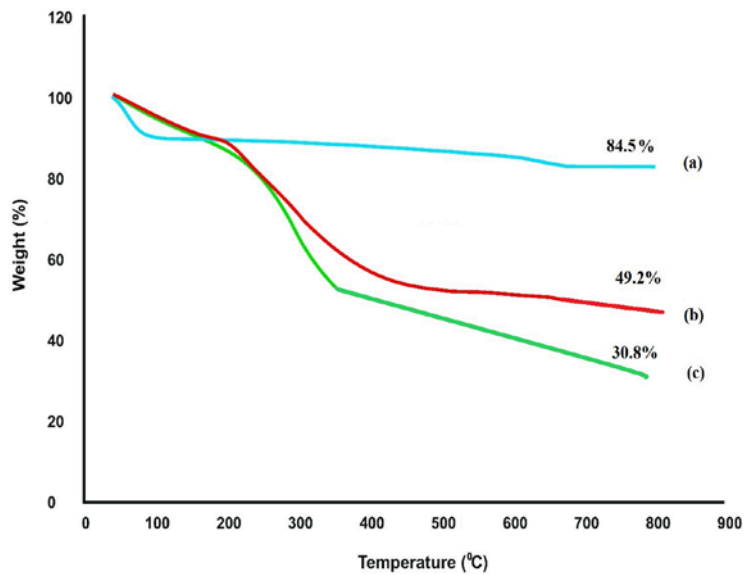


Figure 4. TGA thermogram of a) MMT powder, b) MMT/CG, c) CG powder

Adsorption Studies

The effects of contact time on the adsorption capacity (Q_t) of MMT/CG-composite hydrogels (mass ratio of MMT/CG 0.1:1 and 0.3:1) (initial concentration = 80 mg/L, without adjusted pH) were researched. While the contact time increased, the uptake rate of Cr (VI) ions accelerated and then, it reached a constant value. Firstly, the functional groups of the structure interact with metal ion easily. Thus, the adsorption became to increase. Over time, the adsorption rate slowed down and reached equilibrium. The adsorption capacity values increased gradually till 300 min and then the rate slowed down. The equilibrium adsorption value was found to be 71.4 ± 0.4 mg/g for MMT/CG hydrogel (0.1:1), while the equilibrium adsorption value was found to be 77.2 ± 0.3

mg/g for MMT/CG hydrogel (0.3:1). This difference can be explained by the increment of MMT made easier the penetration of water containing metal ion into the structure and so, the adsorption rate increased (Yang et. al, 2018).

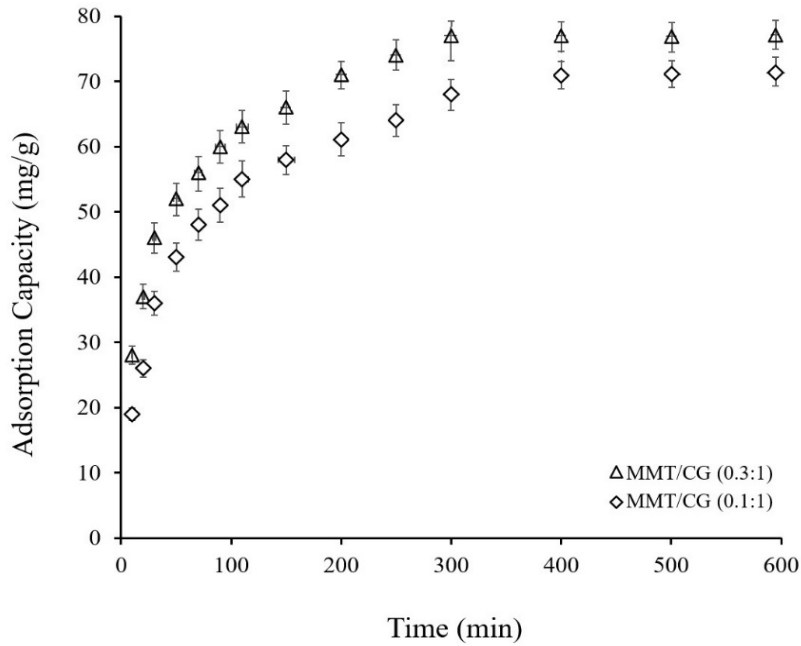


Figure 5. Effect of contact time on *Cr(VI)* metal ions adsorption capacity of MMT/CG hydrogel (initial metal ion concentration = 80 mg/L, without adjusted pH). Data are shown as mean ± SD of 3 independent trials.

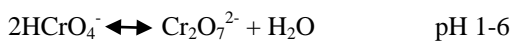
Table 1. Equilibrium swelling degree of MMT/CG hydrogel beads

| Samples | Swelling Degree (%) | Time |
|------------------|---------------------|---------|
| MMT/CG (0.1:1.0) | 65.4± 0.2 | 600 min |
| MMT/CG (0.1:1.0) | 72.4± 0.6 | 600 min |

Note: Data are shown as mean ± SD of 3 independent trials

The effect of pH on the adsorption efficiency of MMT/CG hydrogel (0.1:1.0 and 0.3:1.0) is given in Figure 6. Samples were put into 50 mL of *Cr(VI)* solutions (80 mg/l) of different pH values. Initially, the adsorption increased speedily until pH 6. The maximum adsorption was obtained at pH 6 and then, it steadily decreased. Similar findings were reported in literature.

According to literature, *Cr(VI)* have various oxoanionic forms in aqueous solution at different pH. At pH 1.0, it is in the form of H_2CrO_4 . Between pH 1–6, it is in the form of $HCrO_4^-$, which dimerizes to $Cr_2O_7^{2-}$ within the release of water molecules into the medium. Above pH 6, $Cr_2O_7^{2-}$ are reduced to form CrO_4^{2-} . formed, the electrostatic attraction increases thanks to this ionic form and the adsorption capacity also increases. Above pH 6, Cr (VI) is in the form of $Cr_2O_4^{2-}$. The positively charged adsorbent adsorbed Cr (VI) metal ions. After pH 6, two diavalent negative ions ($Cr_2O_4^{2-}$ and CrO_4^{2-}) exist in the medium. These ions alter the charge of the composite hydrogel from positive to negative, thus the electrostatic interaction between adsorbent to metal ions is decreased (Bhattacharyya & Sen Gupta, 2006; Khan et.al, 2017; Lei, Su, & Tian, 2018).



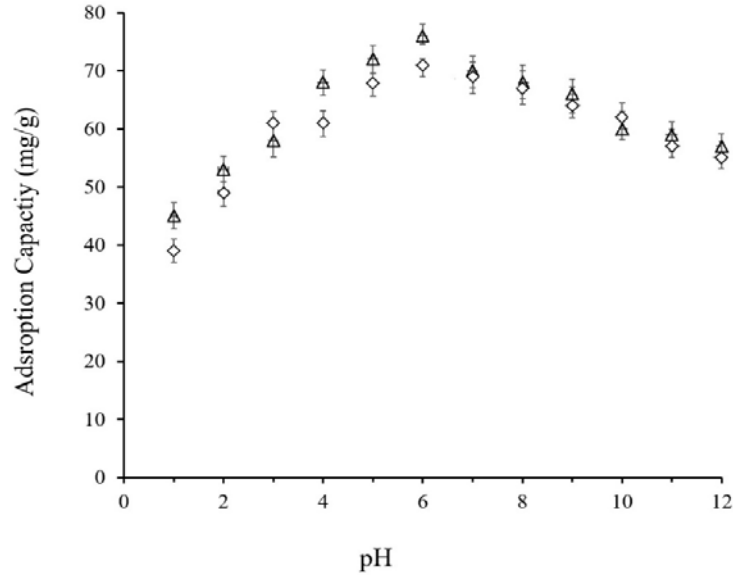


Figure 6. The effect of pH on the adsorption of $Cr(VI)$ ions (under the conditions initial $Cr(VI)$ concentration of 80 mg/L, temperature 25°C in period of 600 min). Results shown are mean \pm standard deviation, n = 3.

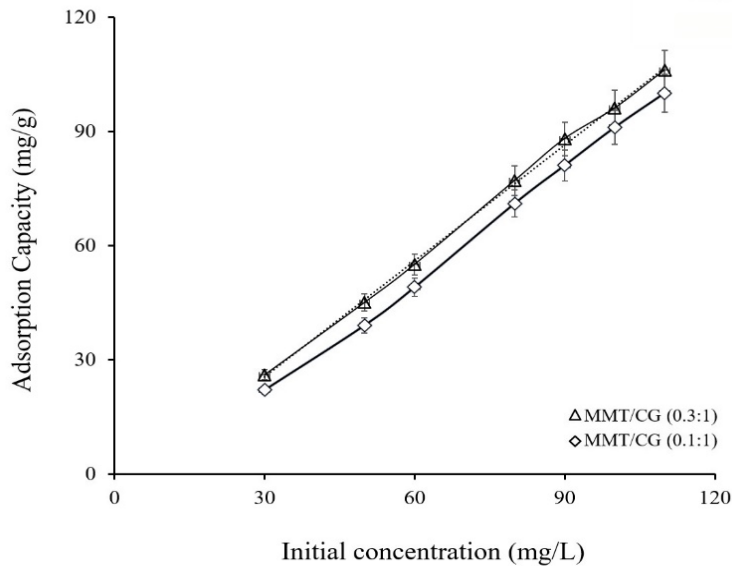


Figure 7. Effect of initial concentration on $Cr(VI)$ metal ions adsorption capacity of MMT/CG hydrogel (pH = 7, contact time=600 min). Data are shown as mean \pm SD of 3 independent trials.

The adsorption capacity (Q_t) of MMT/CG-composite hydrogels (mass ratio of MMT/CG 0.1:1 and 0.3:1) were investigated, the results are given in Figure 4. The adsorption capacity depends on initial concentration (C_i), in other words, Q_t changed directly with C_i (Maity, & Ray 2016). The amount of adsorbed metal ions enhanced with increasing C_i value, so Q_t was increased. Q_t value of MMT/CG (0.3:1) changed from 26 to 106 mg/g, while Q_t value of MMT/CG (0.1:1) ranged from 22 to 100 mg/g. The highest Q_t value was obtained for MMT/CG (0.3:1).

An adsorption isotherm uses for the determination between the content of a metal ions adsorbed on adsorbent and the amount of the dissolved metal ions in solution at equilibrium. Additionally, it can describe the interaction between adsorbent and metal ions. Langmuir isotherm is commonly utilized to model the adsorption of metal ions on polymeric absorbent (Yu et.al, 2017; Yan et. al, 2018; Vilela et.al, 2019). According to this isotherm, adsorption takes place in certain homogeneous regions on the adsorbent, and no further adsorption takes place in the place occupied by the adsorbate.

Langmuir isotherm model was utilized for detecting the adsorption isotherm. The isotherm equation is given in below:

$$1/Q_e = \frac{1}{Q_{max} \cdot b \cdot C_e} + \frac{1}{Q_{max}} \quad (1)$$

where Q_e is the adsorption capacity of the adsorbent at equilibrium, C_e is the metal ion concentration at equilibrium time, b is the Langmuir constant and Q_{max} is the maximum monolayer adsorption capacity. The correlation coefficient (R^2) was calculated for two samples from the graph. R^2 was found to be 0.9980 and 0.9984 for MMT/CG (0.1:1.0) and MMT/CG (0.3:1.0), respectively. The correlation coefficient close to 1 represents monolayer adsorption of metal ions on the adsorbent.

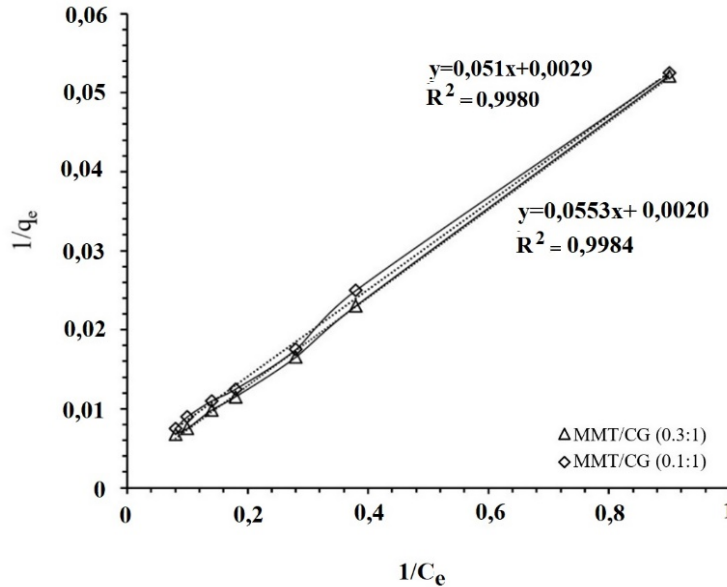


Figure 8. Langmuir isotherm for adsorption of Cr (VI) ions (under the conditions pH=6, temperature 25°C in period of 600 min).

Conclusions

Composite MMT/CG-hydrogels have the potential for being used as a polymeric adsorbent for the removal of Cr(VI) metal ions from aqueous solution. The maximum adsorption capacity of MMT/CG at a mass ratio of 0.3:1. The adsorption process can be described by the Langmuir isotherm model.

Scientific Ethics Declaration

The author declares that the scientific ethical and legal responsibility of this article published in EPSTEM journal belongs to the author.

Acknowledgements or Notes

* This article was presented as an oral presentation at the International Conference on Basic Sciences, Engineering and Technology (www.icbaset.net) conference held in Istanbul/Turkey on August 25-28, 2022.

References

Ahmed, E. M. (2015). Hydrogel: preparation, characterization, and applications: A review. *Journal of advanced research*, 6(2), 105-121.

- Alemayehu, D. D., Singh, S. K. & Tessema, D. A. (2012). Assessment of the adsorption capacities of fired clay soils from Jimma (Ethiopia) for the removal of Cr (VI) from aqueous solution. *Universal Journal of Environmental Research & Technology*, 2(5).
- Bhattacharyya, K. G. & Sen Gupta, S. (2006). Adsorption of chromium (VI) from water by clays. *Industrial & Engineering Chemistry Research*, 45(21), 7232-7240.
- Dakiky, M., Khamis, M., Manassra, A. & Mer'Eb, M. (2002). Selective adsorption of chromium (VI) in industrial wastewater using low-cost abundantly available adsorbents. *Advances in Environmental Research*, 6(4), 533-540.
- Hayati-Ashtiani, M. (2011). Characterization of nano-porous bentonite (montmorillonite) particles using FTIR and BET-BJH analyses. *Particle & Particle Systems Characterization*, 28(3-4), 71-76.
- Ianchis, R., Ninciuleanu, C. M., Gifu, I. C., Alexandrescu, E., Nistor, C. L., Nitu, S. & Petcu, C. (2020). Hydrogel-clay nanocomposites as carriers for controlled release. *Current Medicinal Chemistry*, 27(6), 919-954.
- Islam, M. A., Angove, M. J. & Morton, D. W. (2019). Recent innovative research on chromium (VI) adsorption mechanism. *Environmental Nanotechnology, Monitoring & Management*, 12, 100267.
- Kaşgöz, H. & Durmus, A. (2008). Dye removal by a novel hydrogel-clay nanocomposite with enhanced swelling properties. *Polymers for Advanced Technologies*, 19(7), 838-845.
- Khan, T. A., Nazir, M., Ali, I. & Kumar, A. (2017). Removal of chromium (VI) from aqueous solution using guar gum-nano zinc oxide biocomposite adsorbent. *Arabian Journal of Chemistry*, 10, S2388-S2398.
- Lei, Y., Su, H. & Tian, F. (2018). A novel nitrogen enriched hydrochar adsorbents derived from salix biomass for Cr (VI) adsorption. *Scientific reports*, 8(1), 1-9.
- Maity, J. & Ray, S. K. (2016). Enhanced adsorption of Cr (VI) from water by guar gum based composite hydrogels. *International Journal of Biological Macromolecules*, 89, 246-255.
- Pereira, L., Sousa, A., Coelho, H., Amado, A. M. & Ribeiro-Claro, P. J. (2003). Use of FTIR, FT-Raman and ¹³C-NMR spectroscopy for identification of some seaweed phycocolloids. *Biomolecular Engineering*, 20(4-6), 223-228.
- Rojstithsak, P., Hansapaiboon, S., Sorasitthyanukarn, F. N. & Limpanart, S. (2019). Montmorillonite/carboxymethylcellulose-composite hydrogel beads as biodegradable adsorbent for dye removal. *Maejo International Journal of Science and Technology*, 13(3), 170-184.
- Sharma, G., Khosla, A., Kumar, A., Kaushal, N., Sharma, S., Naushad, M., ... & Stadler, F. J. (2022). A comprehensive review on the removal of noxious pollutants using carrageenan based advanced adsorbents. *Chemosphere*, 289, 133100.
- Vilela, P. B., Dalalibera, A., Duminelli, E. C., Becegato, V. A. & Paulino, A. T. (2019). Adsorption and removal of chromium (VI) contained in aqueous solutions using a chitosan-based hydrogel. *Environmental Science and Pollution Research*, 26(28), 28481-28489.
- Yan, E., Cao, M., Ren, X., Jiang, J., An, Q., Zhang, Z., ... & Zhang, D. (2018). Synthesis of Fe₃O₄ nanoparticles functionalized polyvinyl alcohol/chitosan magnetic composite hydrogel as an efficient adsorbent for chromium (VI) removal. *Journal of Physics and Chemistry of Solids*, 121, 102-109.
- Yang, X., Li, F., Xia, M., Luo, F. & Jiang, Y. (2018). Investigation on the micro-structure and adsorption capacity of cellulosic biomass carbon based montmorillonite composite. *Microporous and Mesoporous Materials*, 256, 18-24.
- Yu, P., Wang, H. Q., Bao, R. Y., Liu, Z., Yang, W., Xie, B. H. & Yang, M. B. (2017). Self-assembled sponge-like chitosan/reduced graphene oxide/montmorillonite composite hydrogels without cross-linking of chitosan for effective Cr (VI) sorption. *ACS Sustainable Chemistry & Engineering*, 5(2), 1557-1566.

Author Information

Gülen Oytun Akalin

Aksaray University
Medical Laboratory Program, Department of Medical Services and Techniques,
Vocational School of Health Service,
Contact e-mail: gulenoynakalin@hotmail.com

To cite this article:

Akalin, G. O. (2022). The preparation of montmorillonite/carrageenan-composite hydrogel for chromium (VI) removal from aqueous solution. *The Eurasia Proceedings of Science, Technology, Engineering & Mathematics (EPSTEM)*, 18, 72-80.

Duty Cycle Detection Method for High Speed Input-Output Systems

Karen MELIKYAN

National Polytechnic University of Armenia (NPUA)

Abstract: A clock coupled duty cycle detection method for high speed input-output is presented in this paper. In High speed systems duty cycle (DC) of output signal needs to be calibrated at 50% for having acceptable performance in the system. The proposed method introduces a synchronous signal in the output of system with 50% duty cycle with maximum 1 % error over process, voltage, and temperature (PVT). Proposed method also compensate input referred offset of DC detector which helps to improve overall system performance. The duty cycle detection method was implemented in 16nm technology with a power supply of 1.2V. With this type of designed architecture, the circuit can provide up to 5Gbps frequency data signal. Experimental results show that proposed architecture is reliable, and it can work operative in high frequency intervals. The presented circuit can be implemented in special serial links of several standards such as Peripheral Component Interconnect (PCI), Universal Serial Bus (USB) and Double Data Rate (DDR).

Keywords: Duty Cycle, detector, high speed, calibration, process-voltage-temperature (PVT)

Introduction

The speed of many systems increases year by year. One of them are DDR systems (Wang, 2015) (Figure 1). Providing a good performance in them become more difficult. So, there arise problems with parameters, such as DC distortion, offset, jitter etc.

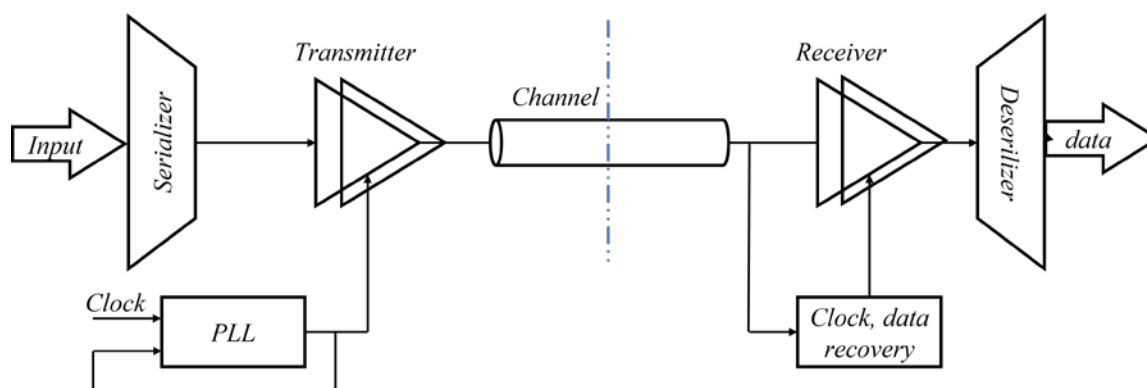


Figure 1. High speed system

Duty Cycle

DC is one of the most important parameters in high speed I/O circuit analyzes. If DC of circuit is not meet 50% specification, then we can have functional error, which can impact on data loss (Sindhu, 2015). DC signal basically measured (1) by pulse width (PW) and the period of signal components (Figure 2).

$$DC = (PW/Per) * 100\% \quad (1)$$

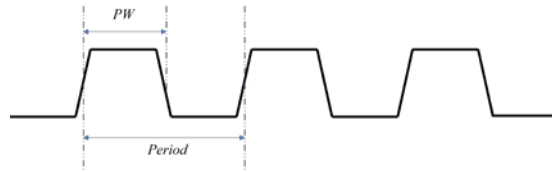


Figure 2. DC main components

Duty Cycle Detection Importance

The DC correction circuit (Melikyan, 2015) main blocks are adjuster and detector (Figure 3). The adjuster regulates a code for getting desired DC and send it to DC detector. The main function of detector is a correct measure of the DC error (%), make a right decision to send it to output and end operation, or continue corrective operation with sending signal to DC adjuster for requesting a new code.

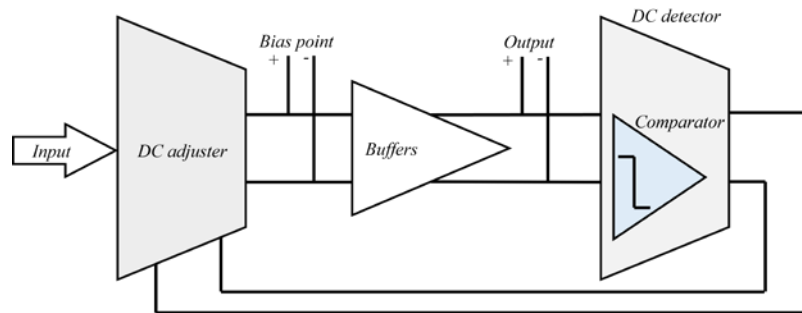


Figure 3. Block diagram of DC correction circuit

As nowadays circuits are working in the high frequency regions (Chien, 2019). The transistors and junctions in them get stressed while operating. So, for having acceptable performance in the system reliable architecture must be designed for DC detector, which can satisfy DC correcting circuit requirements.

Proposed Method of Duty Cycle Detection

Architecture of Duty Cycle Detector

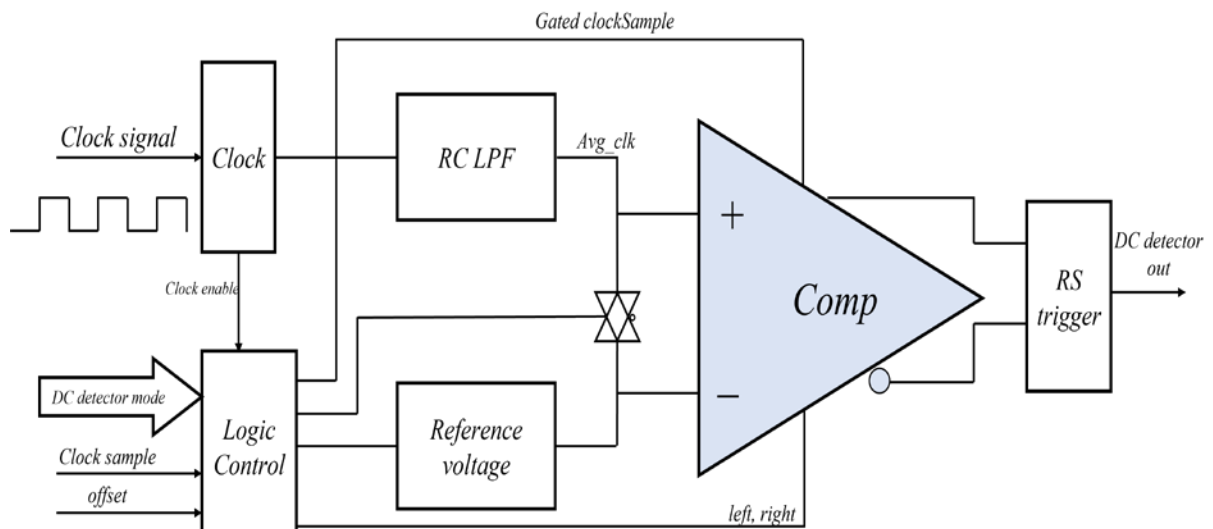


Figure 4. DC detector block diagram

The macro contains (Figure 4),

- digital control logic.
- analog DC detector core, including a mux for two input clocks, two RC tanks, and a comparator

The DC detector has two different functional modes: offset calibration mode and mission mode. The comparator offset is first calibrated in the offset calibration mode. Once it is done, the offset code is stored and used for the mission mode. In power down mode the analog DC detector is not measuring the incoming clock signals. The compactor is in the precharge mode with disabled offset legs. The two inverters are off and the two RC tank outputs are weakly driven to VSS.

Offset calibration mode: The offset code is incremented one by one to check when the comparator output toggles. The offset code is then stored and applied for the mission mode. It should be programmable between min and max code. The offset code either generated by the state-machine or can be overwritten by users. Also sweeping can't be wrapped around. It will be stopped at min or max value. Control and status register (CSR) default for the offset should be equivalent to no offset in the comparator.

The offset receive 5-bit binary code, MSB is the signed bit (1 is negative). Default and reset value is: 5'b00000 (this is the state of no offset). Min value is -15(5b'11111) and the max value +15(5b'01111). Mission mode: clk_sel chooses between the two input clocks. The average of the input clock signal is compared against the voltage divider output that is ideally at VDD/2. The comparator is either 1 or 0 depending on the relative relationship between the average clock and the reference voltage.

Operation Principle

The DC detecting algorithm is shown in block diagram (Figure 5). The Phase Locked Loop (PLL) provides the clock signal. Which pass trough RC filter, where clock signal become fixed in almost half of VDD level ($\sim VDD/2$). Logic control block also is in level choosing mode, which will be fixed in the appropriate RC filter and value of signal becomes $\sim VDD/2$. After both signals have been fixed in $\sim VDD/2$ level they pass into key, which corrects offset code when circuit works in offset mode.

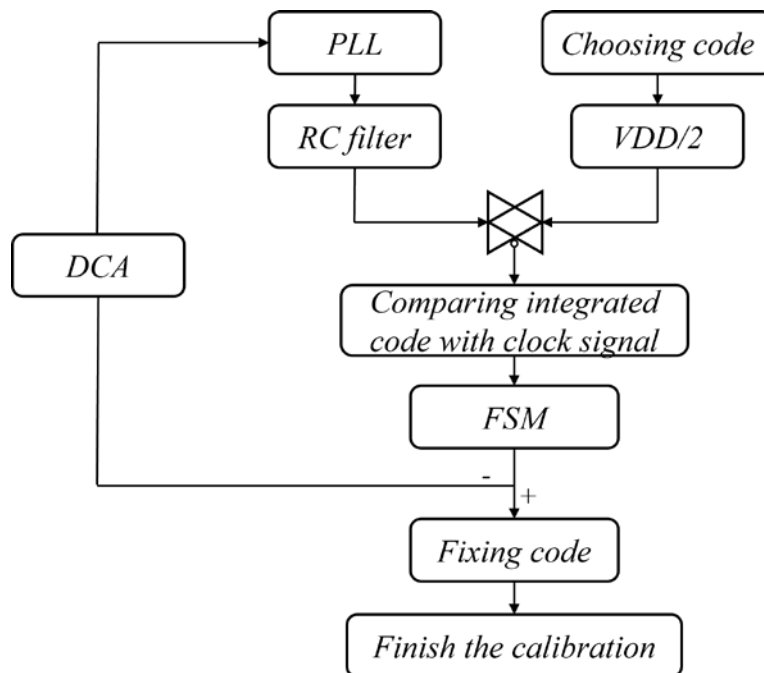


Figure 5. DC detector block diagram

In case of the mission mode the signal from PLL and choosed code get compared with each other to get information about signals level difference (error of DC detector), which must meet DC min/max error value specification. In the case when DC error is out of advisable specification of DC detector, finite state machine (FSM) enters the signal to DC adjuster block where the code will be changed and sent back to PLL block. FSM

passes the code and calibrates it until finding the best output signal. After getting acceptable performance FSM fixes code and finishes calibration.

Results and Discussion

Simulations have been performed using circuit level simulator Hspice for 20 PVT corners (Hspice, 2010), including SS (slow-slow), TT (typical-typical), FF (fast-fast), SF (slow-fast), FS (fast-slow) with supply voltage and temperature variations to evaluate DC detection and offset correction of system, for 5Gbps frequency.

After starting operation circuit enters phase of settling. In the moment when settling time was ended, clock signal and chosen code get the appropriate voltage levels, the DC detection phase starts. In the end of operation comparator detects the DC (%) with the error percentage. In Figure 6 are shown DC detection results for FF corner, which is the worst corner in this case (Cosmosscope, 2018).

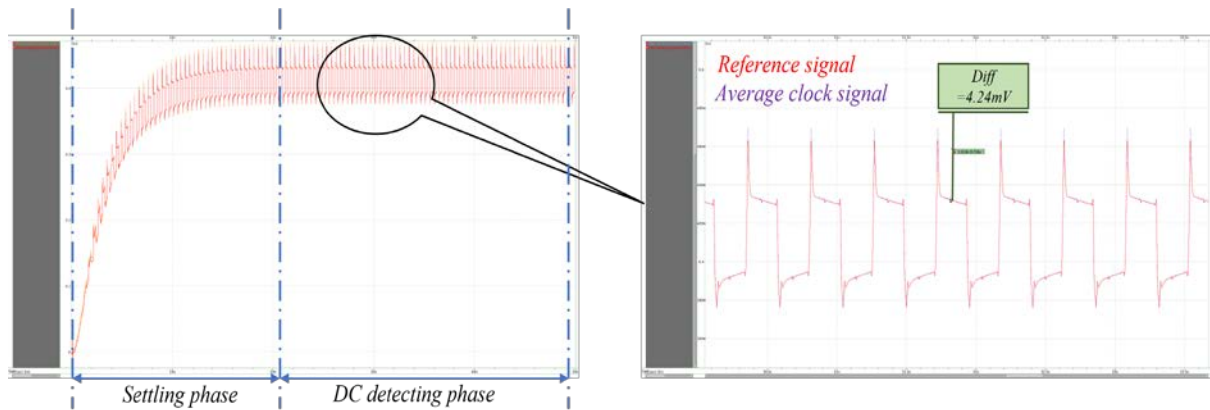


Figure 6. DC detected error in ff corner

In table 1 shown results of TT, FF and SS corners for DC and DC error min/max value.

| Variables | Max difference on gate (mV) | DC detection max error (%) | DC (%) |
|-----------|-----------------------------|----------------------------|--------|
| TT | 0.73 | 0.09 | 50.01 |
| FF | 4.24 | 0.54 | 50.61 |
| SS | 1 | 0.12 | 49.24 |

Conclusion

DC detection method designed for detecting error of DC in special high speed input-output systems. DC detection circuit used in method assist to maximum error and provide signals only with minimum DC error. The error maximum variation is $50\% \pm 1\%$. The architecture also corrects the offset of circuit with special offset mode implementing.

In high speed systems for 28nm and below processes it is hard to provide good performance without DC detection. So, this type of detection method is very important in special input-output circuits, due to huge PVT variations, which can have impact on the performance of the system. The approached method can be implemented for special input-output protocols of several standards such as DDR, USB, PCI.

Scientific Ethics Declaration

The author declares that the scientific ethical and legal responsibility of this article published in EPSTEM journal belongs to the author.

Acknowledgements or Notes

* This article was presented as an oral presentation at the International Conference on Basic Sciences, Engineering and Technology (www.icbaset.net) conference held in Istanbul/Turkey on August 25-28, 2022.

* This paper was supported by National Armenian Polytechnic University (NPUA). I thank my colleagues from Microelectronics and biomedical equipment department, who provided insight and expertise that greatly assisted the research.

References

- Chien, Y., L. & Heng, S., H. (2019). Design of a 0.8GHz-3GHz duty-cycle corrector with a 20%-80% input duty cycle. *IEEE International Conference on Consumer Electronics - Taiwan (ICCE-TW)*, 9, 59-62.
- Cosmoscope Reference Manual (2018), *Synopsys Inc*, 130.
- Hspice Application Manual (2010), *Synopsys Inc.*, 196.
- Melikyan, V., Sahakyan, A., Hekimyan, A., Trdatyan, D., Shishmanyanyan, A. & Kazakhyan, T. (2015). Low power duty cycle adjustment simple method in high speed serial links. *IEEE East-West Design & Test Symposium (EWDTS)*, 1-4.
- Sindhu, M. & Jamuna, V. (2015). Highly reconfigurable pulse width control circuit with programmable duty cycle. *2nd International Conference on Electronics and Communication Systems (ICECS)*, 2, 303-309.
- Wang, X., & Hu, Q., (2015). Analysis and optimization of combined equalizer for high speed serial links. *IEEE 9th International Conference on Anti-counterfeiting, Security, and Identification (ASID)*, 9, 43-46.

Author Information

Karen Melikyan

National Polytechnic University of Armenia
105 Teryan St, Yerevan, Armenia
Contact e-mail: melikyan@synopsys.com

To cite this article:

Melikyan, K. (2022). Duty cycle detection method for high speed input-output systems. *The Eurasia Proceedings of Science, Technology, Engineering & Mathematics (EPSTEM)*, 18, 81-85.

The Eurasia Proceedings of Science, Technology, Engineering & Mathematics (EPSTEM), 2022

Volume 18, Pages 86-101

ICBASSET 2022: International Conference on Basic Sciences, Engineering and Technology

Exploring the Risky Areas Due to Landslide Using Decision Tree Analysis: Case Study Tasmania, Australia

Mahyat SHAFAPOURTEHRANY
Bogazici University

Abstract: Landslide is one of the natural hazards that considers a serious threat to both humans' lives and properties. Tasmania, Australia is one of those regions where landslides caused considerable damage to people and the State. Landslide damages can be reduced, even stopped, if proper land condition and planning assessment has been done. The main influencing parameters in landslide occurrences are topography, precipitation, and geological formation. Those parameters along with other influencing parameters have been used in landslide susceptibility mapping. In order to have a reliable analysis, a robust method of Decision Tree (DT) has been used to perform susceptibility mapping. According to the hierarchy structure of DT, geology and slope have been selected as the most influential parameters in landslide susceptibility. In order to evaluate the reliability of the outcomes, Area Under the Curve (AUC) has been utilized. Success and prediction rates were 87.64% and 84% respectively. Subsequently, risky features such as buildings, schools, hotels, etc. have been used in overlay analysis in a GIS environment with "very high" and "high" susceptibility classes. The outcome of this research can assist planning parties to secure vulnerable regions and consider those areas in their future decision-making strategies.

Keywords: Landslide, Decision Tree (DT), Vulnerability, GIS, Tasmania

Introduction

Natural hazards are a great threat to both lives and properties worldwide (Jia et al., 2021). These include flooding, wildfire, earthquake, landslides, etc. Among natural disasters, landslides can cause serious losses directly or indirectly to the society and economy (Del Soldato et al., 2017). They are related to the characteristics of the slope of the terrain (Sim et al., 2022). One way to minimize the damage of landslides is to recognize the susceptible regions that are most likely to occur (Park et al., 2018). In the natural hazard scope, a susceptibility map recognizes regions that are more or less disposed to a potential landslide occurrence using low to high possibility values/classes (Ballabio & Sterlacchini, 2012). Susceptibility assessment has been implemented by several researchers to prevent or reduce actual damage from natural hazards. Until now, various methodological approaches including qualitative and quantitative methods have been applied for landslide susceptibility mapping (Reichenbach et al., 2018).

There is a variety of methods available in the literature to identify landslide susceptible areas such as frequency ratio (FR) (Lee & Sambath, 2006), logistic regression (LR) (Lee, 2005), index of entropy (IoE) (Pourghasemi, Mohammady, et al., 2012), the weight of evidence (WoE) (Lee & Choi, 2004), evidential belief function (EBF) (Althwaynee et al., 2012), statistical index (Regmi et al., 2014), analytical hierarchy process (AHP) (Kumar & Anbalagan, 2016), fuzzy logic (Pourghasemi, Pradhan, et al., 2012), fuzzy rule-based classifiers (Pham, Tien Bui, et al., 2016), neuro-fuzzy models multivariate adaptive regression splines (MARS) (Chu et al., 2019), random forest (RF) (Hong et al., 2019), (DT) (Park et al., 2018), Artificial neural network (ANN) (Lee et al., 2004), and support vector machines (SVM) (H. R. Pourghasemi et al., 2013), and etc. Each of the aforementioned methods has advantages and disadvantages (Reichenbach et al., 2018). Though, machine learning is a category of methods that are repeatedly used in natural hazard studies (Korup & Stolle, 2014).

- This is an Open Access article distributed under the terms of the Creative Commons Attribution-Noncommercial 4.0 Unported License, permitting all non-commercial use, distribution, and reproduction in any medium, provided the original work is properly cited.

- Selection and peer-review under responsibility of the Organizing Committee of the Conference

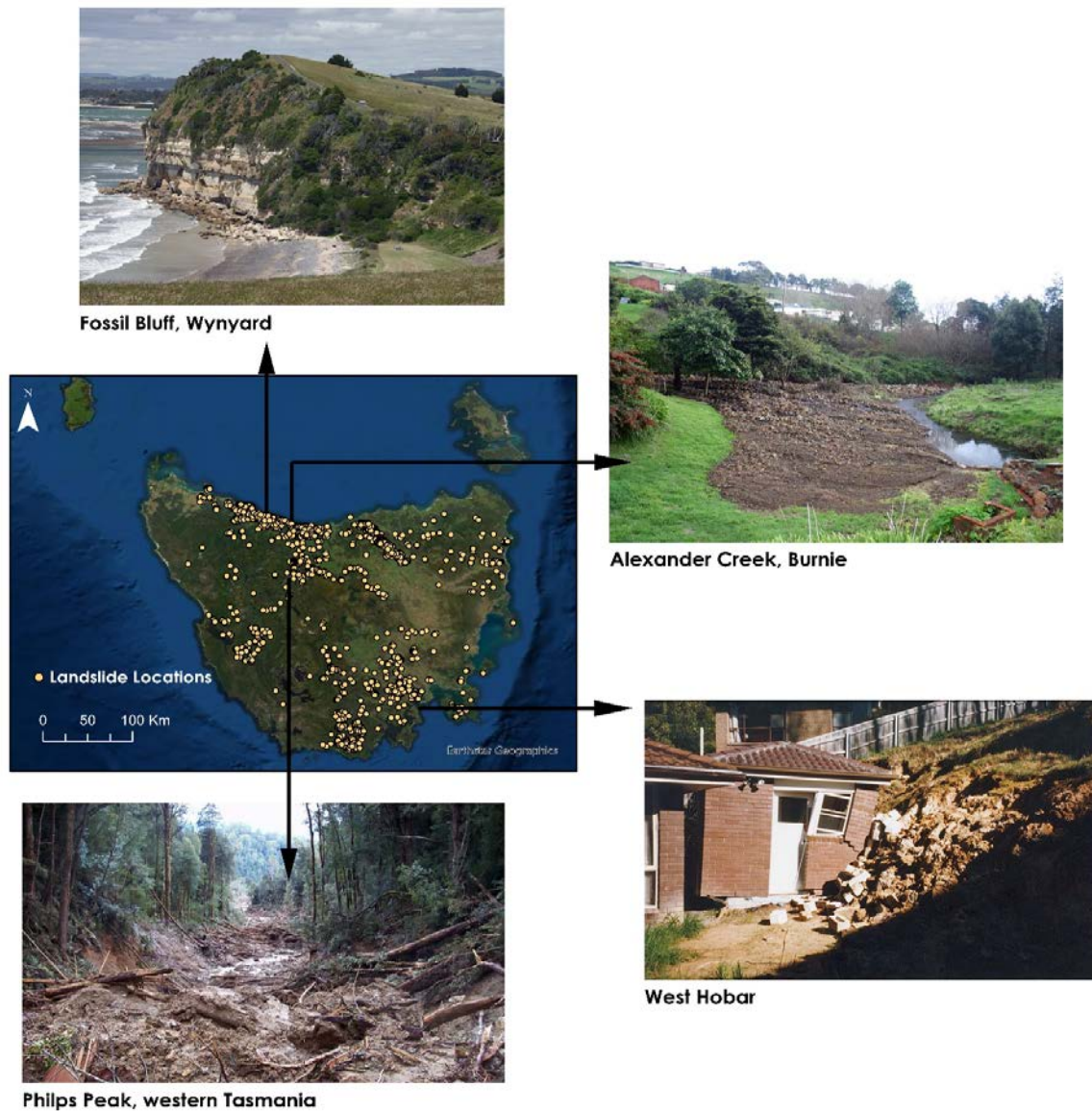


Figure 1. Distribution of landslides in Tasmania along with a few examples of the affected areas (BAY)

Machine learning is related to a set of methods that distinguish patterns in the dataset and use them to predict future scenarios (Jain et al., 2020). One of the differences between machine learning methods and other approaches is that without any pre-defined rules from experts, they can learn their own mappings between parametric rules directly from the data. This characteristic is advantageous in the case that the number of factors is considerably large and their physical properties are quite complex, as in the case of landslide (Merghadi et al., 2020). Hence, the machine learning approach to landslide response may assist to avoid many of the limitations of physics-based algorithms. In this study, we applied the machine learning method of DT using landslide data collected in the 1950s.

Australia has been affected by several landslides in the past (Roodposhti et al., 2019). Some lands in Tasmania are susceptible to slope instability (Slee & McIntosh, 2022). In some cases, the financial damage to people and the State reaches millions of dollars. However, there is no information source that people can use to get informed about landslide risk (Mazengarb, 2005). In addition, neither the insurance company nor the Tasmanian government provides coverage for those damages (Roodposhti et al., 2019). Without any doubt, such disasters and their destructive impacts can be avoided if the ground conditions are evaluated and assessed prior to the planning and construction (Dai et al., 2002).

In order to create safer and sustainable communities land use planning strategies are required (Chakraborty & Anbalagan, 2013; Sultana & Tan, 2021). Some of the planning actions are: to avoid development in areas that will increase the likelihood of landslide risk; to remove or modify structures in risky zones; to recognize high-

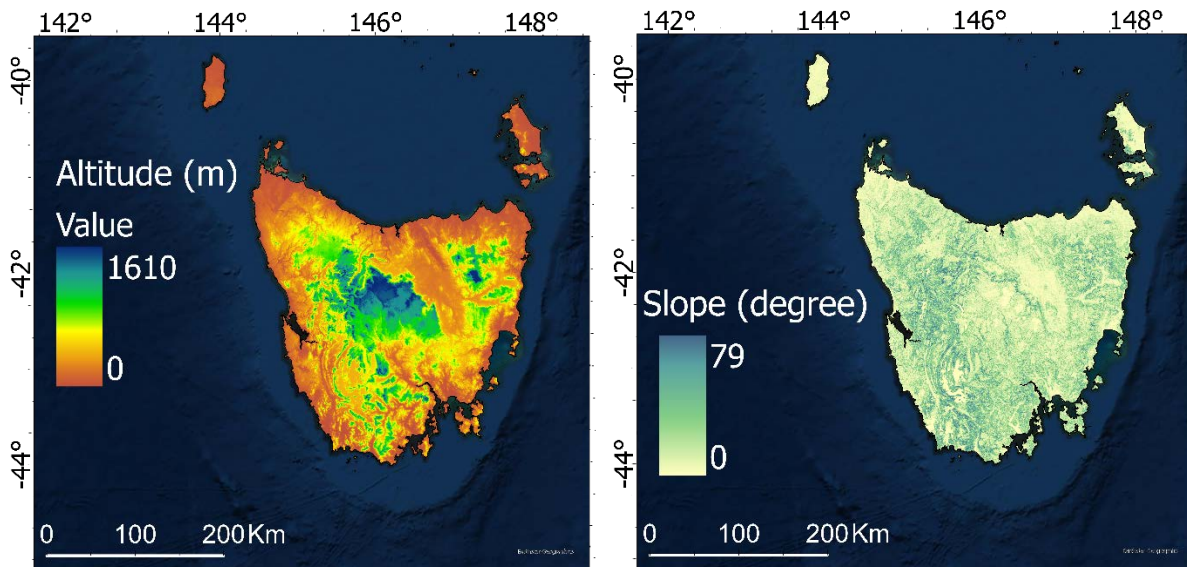
risk areas through zoning and overlay controls, and to avoid developments that are more likely to contribute to increased landslide risk.

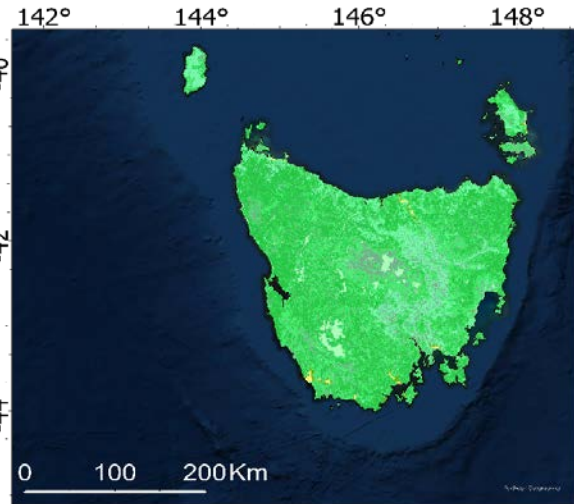
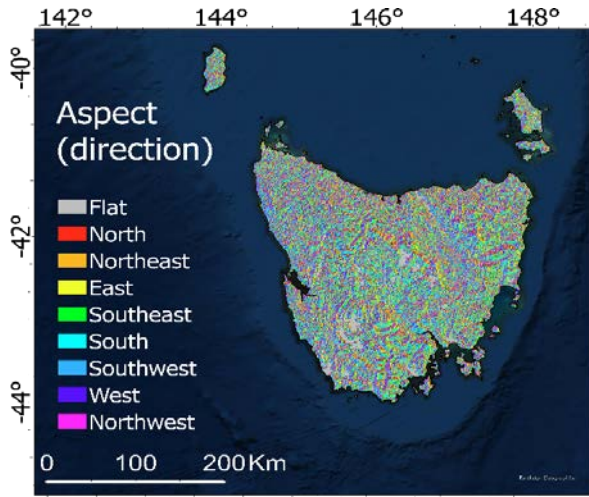
According to the above information, since landslide conditions in Tasmania received less attention in the literature, this study contributes to a better understanding of the landslide risky areas in Tasmania, Australia by overlaying the landslide susceptible areas with risky locations. Using this analysis to identify the risky areas can be a great tool for several end-users (private and public sectors), intended for landslide mitigation purposes at both local and international levels.

Study Area and Data Used

Landslides are common in Tasmania due to the natural geological processes over long-time scales (Figure 1). Due to its varied topographical, geological, and geomorphic processes, including the effects of past and present climates, landslides occur in a variety of sizes and types (Mazengarb & Stevenson, 2010). Mineral Resources Tasmania (MRT) stated that due to the nature and magnitude of the known past landslides, similar events occurring today would have the potential for significant damage in the future (<https://www.mrt.tas.gov.au/home>). The five major landslide types (slide, flow, fall, topple and spread) all can happen in Tasmania, with slides (both shallow and deepseated) and flows being the most common types. A number of landslides are a combination of movement types. The material that moves is classed as rock, earth, or debris.

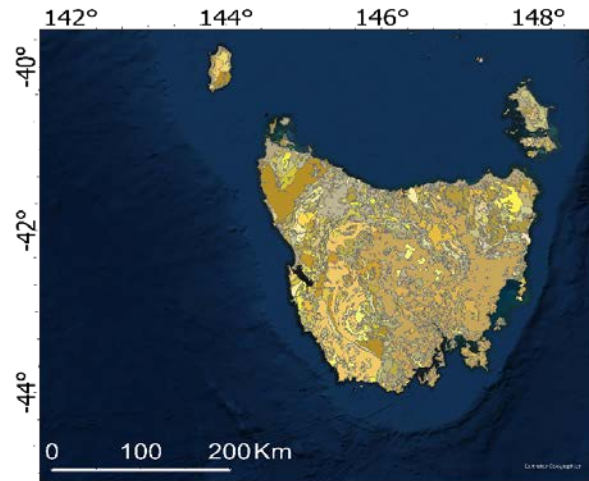
In order to have efficient mitigation strategies, defining the landslide conditioning factors must be also highlighted throughout the spatial domain (Roodposhti et al., 2019). A relevant and reliable landslide conditioning factors dataset with accurate landslide inventories is essential for landslide susceptibility analysis. Both datasets' precision has a direct impact on the final outcomes (Meena et al., 2022). For the current research, the conditioning factors are altitude, slope, aspect, forest, geology, landuse/cover (LULC), Normalized Difference Vegetation Index (NDVI), rain, distance to the river, distance to road, and soil (Figure 2). Each factor was resized to a 30×30 m grid. Each one of these factors has an impact on landslide occurrence in a region.





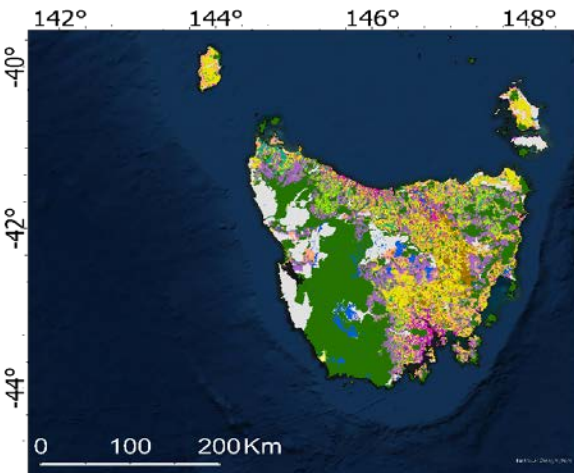
Forest types

- Extraction Sites
- Hummock Grasses - Sparse
- Inland Waterbodies
- Irrigated Cropping
- Irrigated Pasture
- Rainfed Cropping
- Rainfed Pasture
- Salt Lakes
- Sedges - Open
- Shrub - Closed
- Shrub - Open
- Shrub - Scattered
- Shrub - Sparse
- Tree - Closed
- Tree - Open
- Tree - Scattered
- Tree - Sparse
- Tussock Grasses - Open
- Tussock Grasses - Sparse



Geology

- Cgge
- Cggy
- Cglt
- Czrb
- Czc
- Czcc
- Czi
- Czu
- Dfmy
- Dgab
- Dgak
- Dgap
- Dgb1
- Dgb10
- Dgb11
- Dgb12
- Dgb13
- Dgb14
- Dgb15
- Dgb16
- Dgb2
- Dgb3
- Dgb4
- Dgb5
- Dgb6
- Dgb7
- Dgb8
- Dgb9
- Dgci
- Dgcp
- Dgcs
- Dgcm
- Dgdb
- Dgdb1
- Dgdb2
- Dgdb3
- Dgdb4
- Dgdb5
- Dgdb6
- Dgdb7
- Dgdb8
- Dgdb9
- Dgdb10
- Dgdb11
- Dgdb12
- Dgdb13
- Dgdb14
- Dgdb15
- Dgdb16
- Dgdb17
- Dgdb18
- Dgdb19
- Dgdb20
- Dgdb21
- Dgdb22
- Dgdb23
- Dgdb24
- Dgdb25
- Dgdb26
- Dgdb27
- Dgdb28
- Dgdb29
- Dgdb30
- Dgdb31
- Dgdb32
- Dgdb33
- Dgdb34
- Dgdb35
- Dgdb36
- Dgdb37
- Dgdb38
- Dgdb39
- Dgdb40
- Dgdb41
- Dgdb42
- Dgdb43
- Dgdb44
- Dgdb45
- Dgdb46
- Dgdb47
- Dgdb48
- Dgdb49
- Dgdb50
- Dgdb51
- Dgdb52
- Dgdb53
- Dgdb54
- Dgdb55
- Dgdb56
- Dgdb57
- Dgdb58
- Dgdb59
- Dgdb60
- Dgdb61
- Dgdb62
- Dgdb63
- Dgdb64
- Dgdb65
- Dgdb66
- Dgdb67
- Dgdb68
- Dgdb69
- Dgdb70
- Dgdb71
- Dgdb72
- Dgdb73
- Dgdb74
- Dgdb75
- Dgdb76
- Dgdb77
- Dgdb78
- Dgdb79
- Dgdb80
- Dgdb81
- Dgdb82
- Dgdb83
- Dgdb84
- Dgdb85
- Dgdb86
- Dgdb87
- Dgdb88
- Dgdb89
- Dgdb90
- Dgdb91
- Dgdb92
- Dgdb93
- Dgdb94
- Dgdb95
- Dgdb96
- Dgdb97
- Dgdb98
- Dgdb99
- Dgdb100
- Dgdb101
- Dgdb102
- Dgdb103
- Dgdb104
- Dgdb105
- Dgdb106
- Dgdb107
- Dgdb108
- Dgdb109
- Dgdb110
- Dgdb111
- Dgdb112
- Dgdb113
- Dgdb114
- Dgdb115
- Dgdb116
- Dgdb117
- Dgdb118
- Dgdb119
- Dgdb120
- Dgdb121
- Dgdb122
- Dgdb123
- Dgdb124
- Dgdb125
- Dgdb126
- Dgdb127
- Dgdb128
- Dgdb129
- Dgdb130
- Dgdb131
- Dgdb132
- Dgdb133
- Dgdb134
- Dgdb135
- Dgdb136
- Dgdb137
- Dgdb138
- Dgdb139
- Dgdb140
- Dgdb141
- Dgdb142
- Dgdb143
- Dgdb144
- Dgdb145
- Dgdb146
- Dgdb147
- Dgdb148
- Dgdb149
- Dgdb150
- Dgdb151
- Dgdb152
- Dgdb153
- Dgdb154
- Dgdb155
- Dgdb156
- Dgdb157
- Dgdb158
- Dgdb159
- Dgdb160
- Dgdb161
- Dgdb162
- Dgdb163
- Dgdb164
- Dgdb165
- Dgdb166
- Dgdb167
- Dgdb168
- Dgdb169
- Dgdb170
- Dgdb171
- Dgdb172
- Dgdb173
- Dgdb174
- Dgdb175
- Dgdb176
- Dgdb177
- Dgdb178
- Dgdb179
- Dgdb180
- Dgdb181
- Dgdb182
- Dgdb183
- Dgdb184
- Dgdb185
- Dgdb186
- Dgdb187
- Dgdb188
- Dgdb189
- Dgdb190
- Dgdb191
- Dgdb192
- Dgdb193
- Dgdb194
- Dgdb195
- Dgdb196
- Dgdb197
- Dgdb198
- Dgdb199
- Dgdb200



LULC

- Dryland cropping
- Dryland horticulture
- Grazing modified pastures
- Grazing native vegetation
- Intensive horticulture and animal production
- Irrigated cropping
- Irrigated horticulture
- Irrigated pastures
- Land in transition
- Minimal use
- Mining and waste
- Nature conservation
- Other protected areas
- Plantation forests (commercial and other)
- Production native forests
- Rural residential and farm infrastructure
- Urban intensive uses
- Water

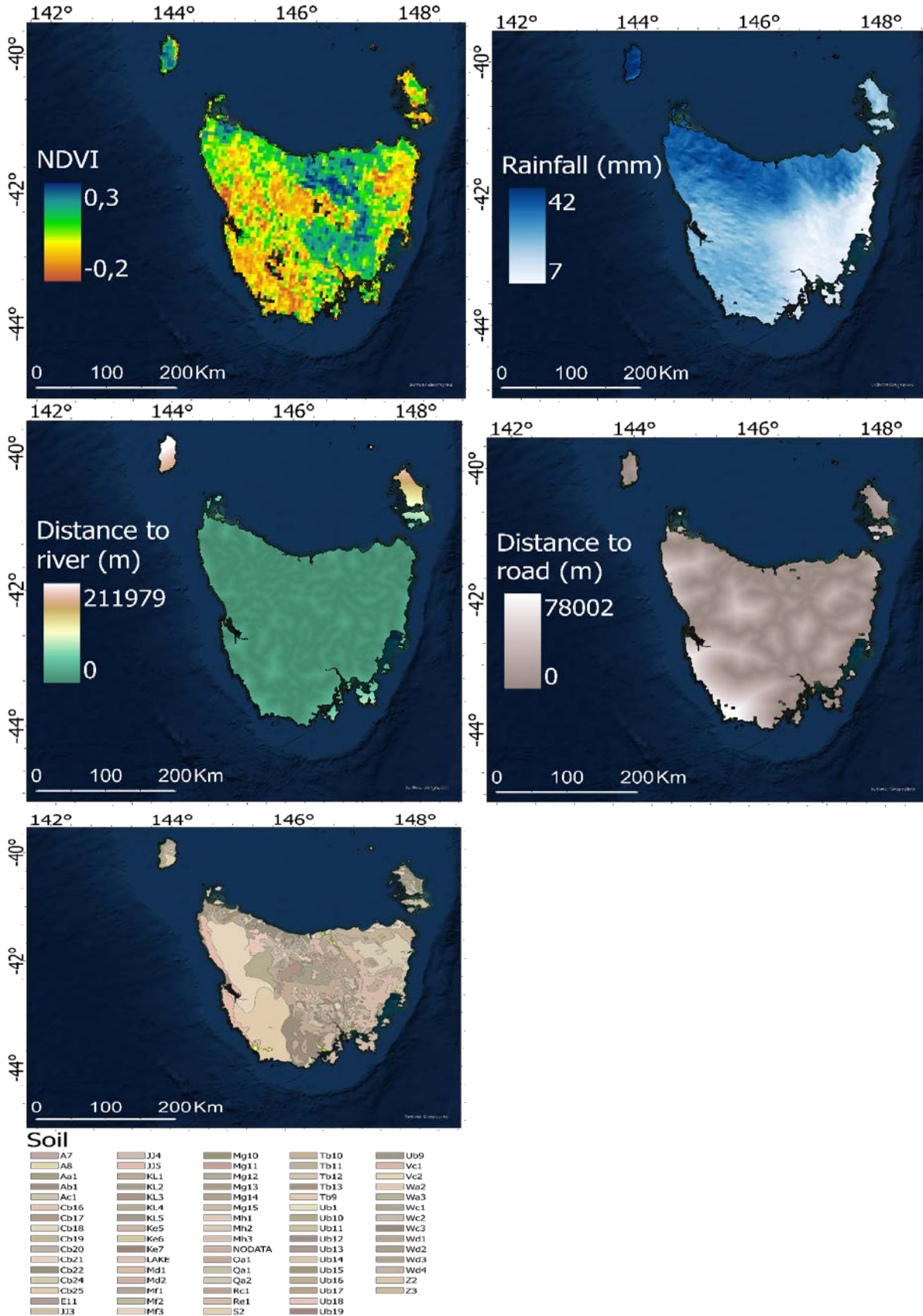


Figure 2. Landslide conditioning factors

Regarding the risky features, the Tasmania government website provided a set of factors such as ambulance, buildings, children and elderly population density, cultural places, educational places, entertainment places, governmental places, heritage Tasmania features, hotels, kindergarten, medical services, police stations, primary

infant schools, private reserves, and tourist features. The aforementioned dataset has been used in risk analysis which will be described in the following sections.

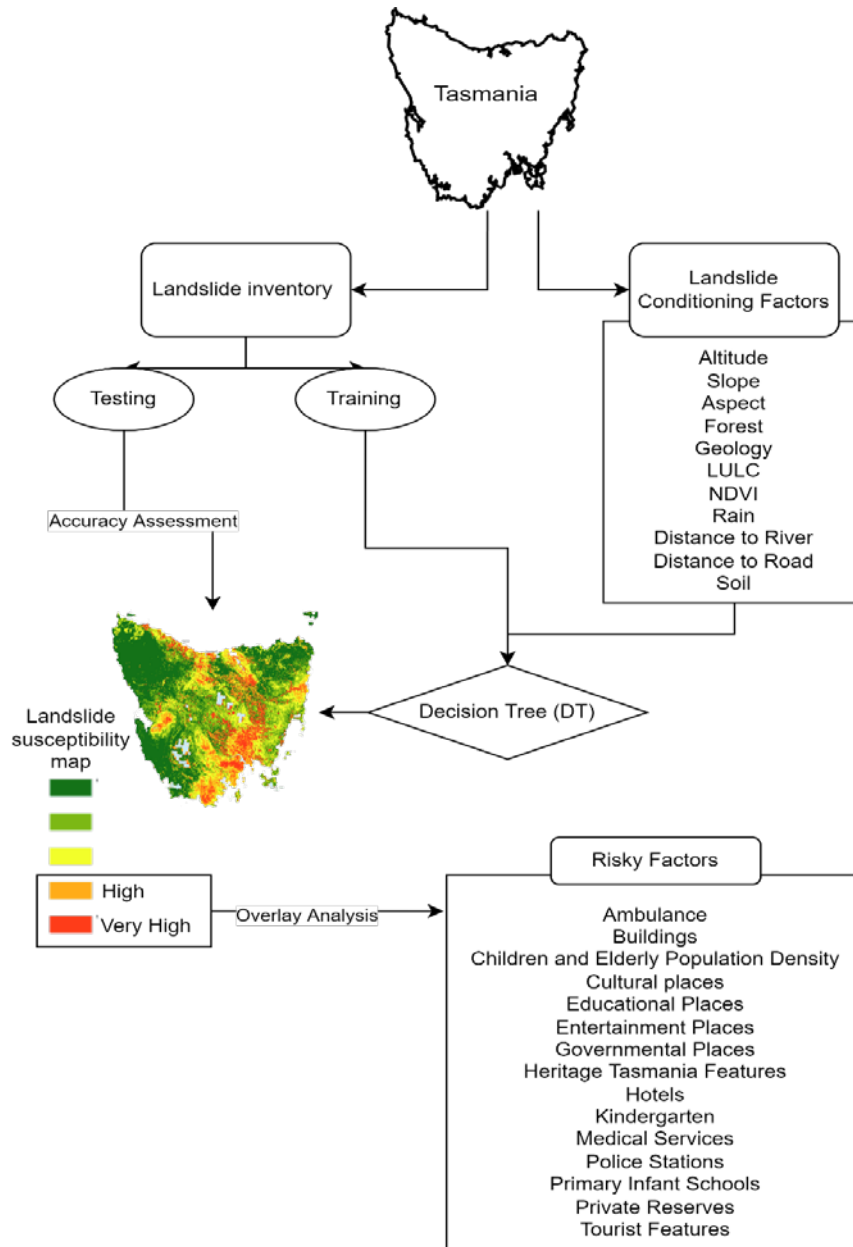


Figure 3. Flowchart

Methodology

Analyzing the correlation between “landslide conditioning factors” and “landslide inventory” is the first stage in landslide susceptibility analysis. Therefore, according to the flowchart (Figure 3), both datasets of conditioning and inventory have been produced. As has been mentioned landslide database has been received from MRT which includes the landslide locations since the 1950s. A total of 600 landslides were randomly selected; 70% of them were used as training data and 30% as validation data. The same number of non-landslide points were randomly selected from the free-landslide regions. Subsequently, values of 1 and 0 were assigned to landslide pixels and non-landslide pixels respectively. In order to perform DT, all dataset needs to be converted into ASCII (American Standard Code for Information Interchange) format. ArcGIS was used to convert all of the input data into ASCII data. Then, landslide training data and landslide conditioning factors were analyzed while using the DT method in the SPSS environment to calculate the landslide susceptibility index and build a

andslide susceptibility map in the study area. Classes with the highest susceptibility were overlaid on risky features derived from different sources.

Decision Tree (DT)

DT is one of the machine learning methods that consider a predictive modeling technique. It can precisely identify the structural patterns in data and represent them graphically as tree structures. Another advantage of DT is that pre-defined correlation between the variables is not required (Saito et al., 2009). DT can explain data and use it predictively, it can also ingest data calculated at varying scales, purely on the non-linear relationship without the need for assumptions based on frequency distributions (Kheir et al., 2010). Consequently, each factor can be considered input into the model. DT has been used as a rule-based technique in numerous natural hazard studies (Chen et al., 2017; Jaafari et al., 2018; Tehrany et al., 2013). DT groups the landslide conditioning factors hierarchically according to levels of susceptibility. The aim is to create a set of decision rules that can form the basis for predicting the outcome from the input dataset. Thus, the rules are generated by the analysis of a set of conditioning factors, with the purpose of predicting an outcome from a similar set of variable factors. Due to the proficiency of DT, this method was used to analyze the correlation between the landslide conditioning factors and the training dataset. Using DT-CHAID the conditioning factor that is selected at each step is the one representing the strongest relationship with the landslide occurrence susceptibility.

Accuracy Assessment

AUC is a popular, comprehensive quantitative method of accuracy assessment, by which the prediction and success rates may be evaluated (Pham, Pradhan, et al., 2016). The proficiency of AUC in evaluating the susceptibility mapping outcomes has been demonstrated successfully in a number of studies (H. Pourghasemi et al., 2013; Pourtaghi et al., 2016; Xu et al., 2012). AUC evaluates the existence of the known landslide inventory data and the acquired probability map. It starts by dividing the landslide probability map into categories of equal area, and hierarchically ranking respective values from minimum to maximum in ArcGIS. AUC starts by sorting the calculated values of all cells into descending order, thus ranking each prediction hierarchically. Thereafter, the values of cells were divided into 100 classes with 1% accumulation intervals. The presence of landslide in each interval is measured using the “Tabulate area” tool in ArcGIS as the next step. The success and prediction curves determine the percentage of landslides in each probability category.

Results and Discussion

DT has been applied and a landslide susceptibility map has been created by classifying the derived map into five classes of “low”, “very low”, “moderate”, “high”, and “very high” (Figure 4) using a well-known quantile classification technique (Baeza et al., 2016). Based on the DT tree structure, the most influential landslide conditioning factors affecting the landslide distribution were geology and slope, as they were selected at the top of the branch. The most susceptible combination of conditioning factors contributing to the high landslide susceptibility was as follow: starting with slope (between 32-58°), as well as the decision root continued by the rainfall greater than 10mm, and NDVI <-0.1. Areas exhibiting these characteristics were classified as 100% susceptible to landslides (Table 1).

Table 1. The most susceptible combination of conditioning factors

| Factors | Range | DT Rules |
|----------|------------|----------|
| Slope | 0-72° | 32-58° |
| Rainfall | 6.6-42.4mm | >10mm |
| NDVI | 0-67° | <-0.1 |

The landslide susceptibility map is presented in Figure 4. It depicted where the slope failure may occur spatially in the future.

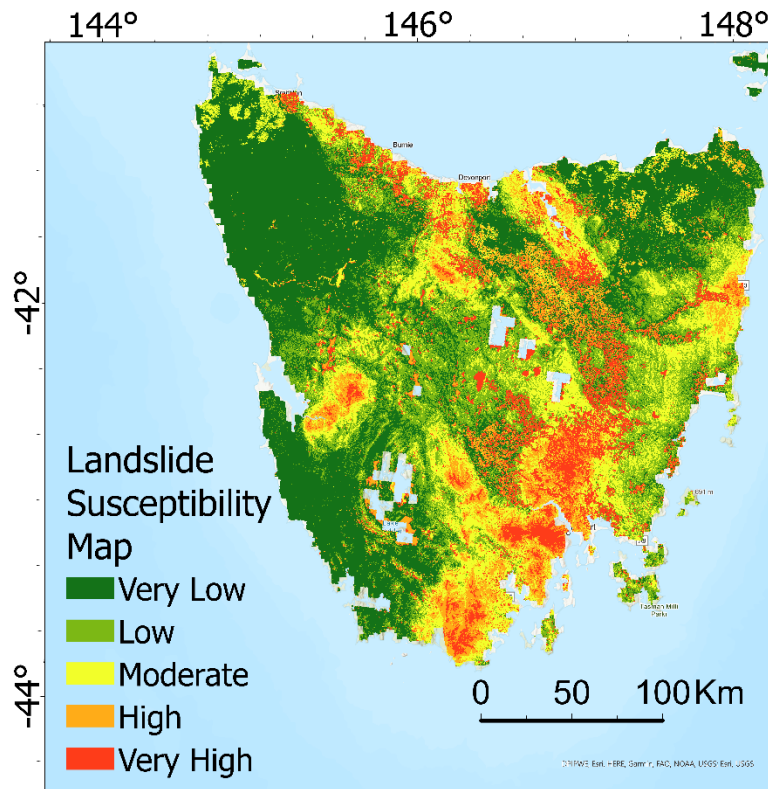
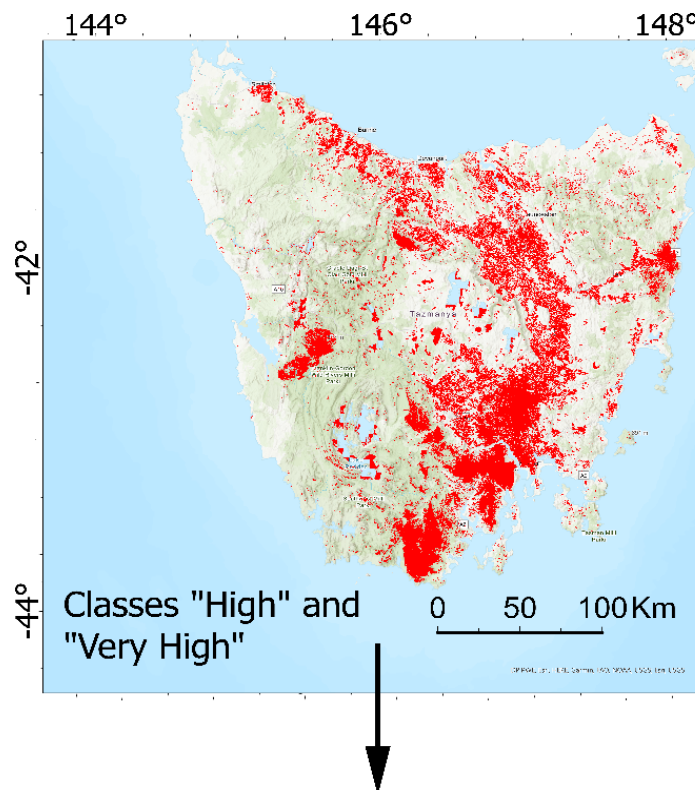
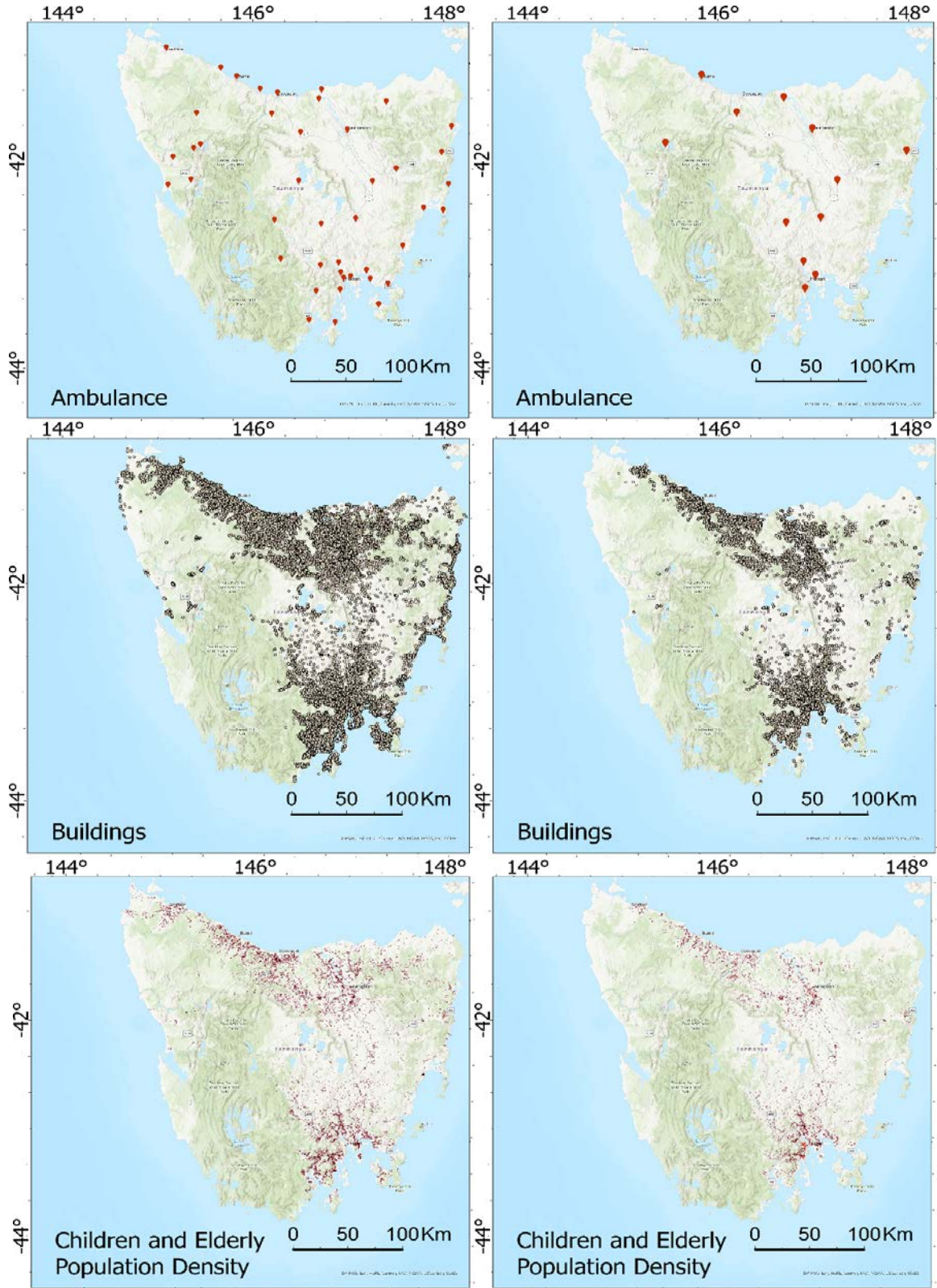
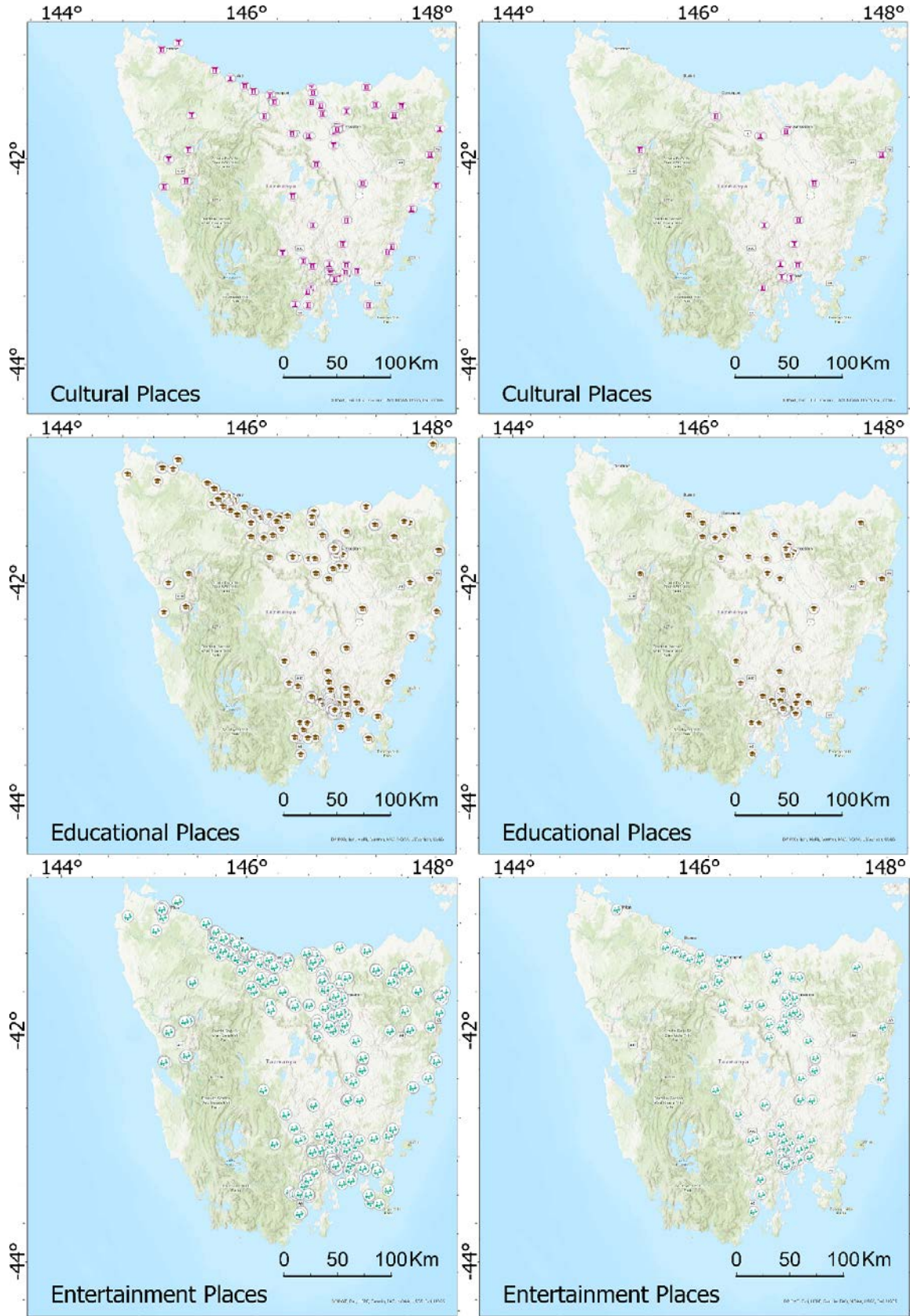
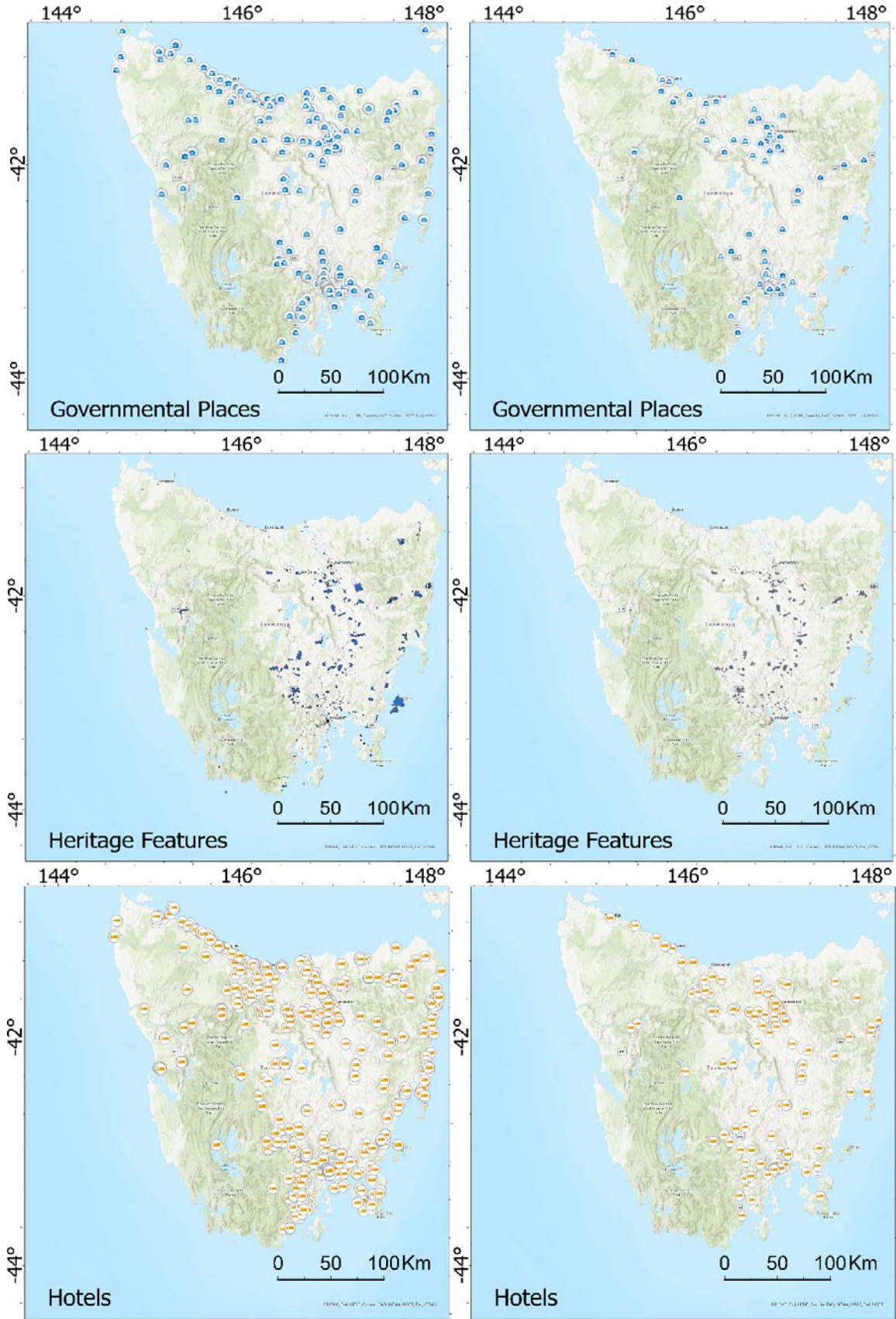


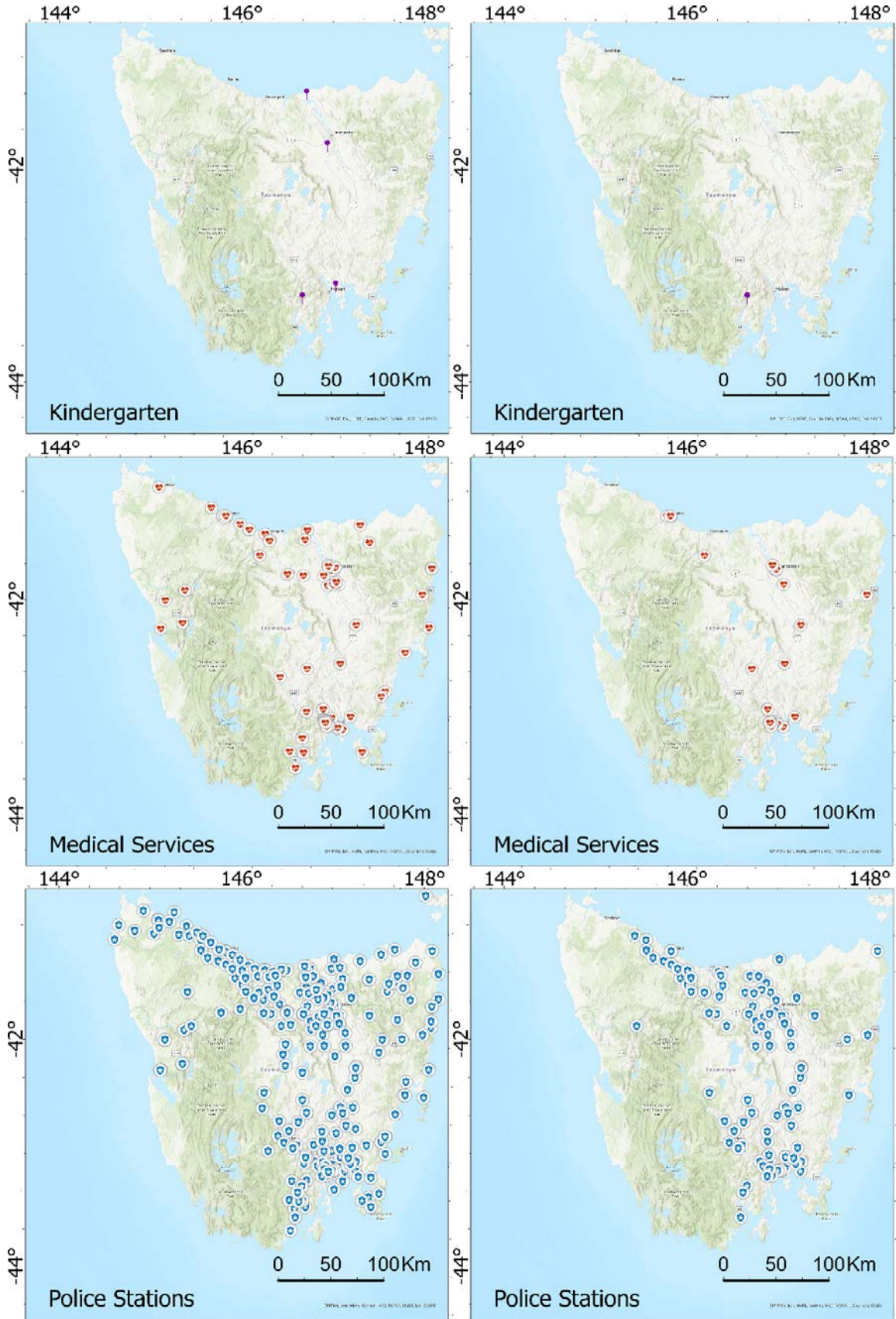
Figure 4. Landslide susceptibility map











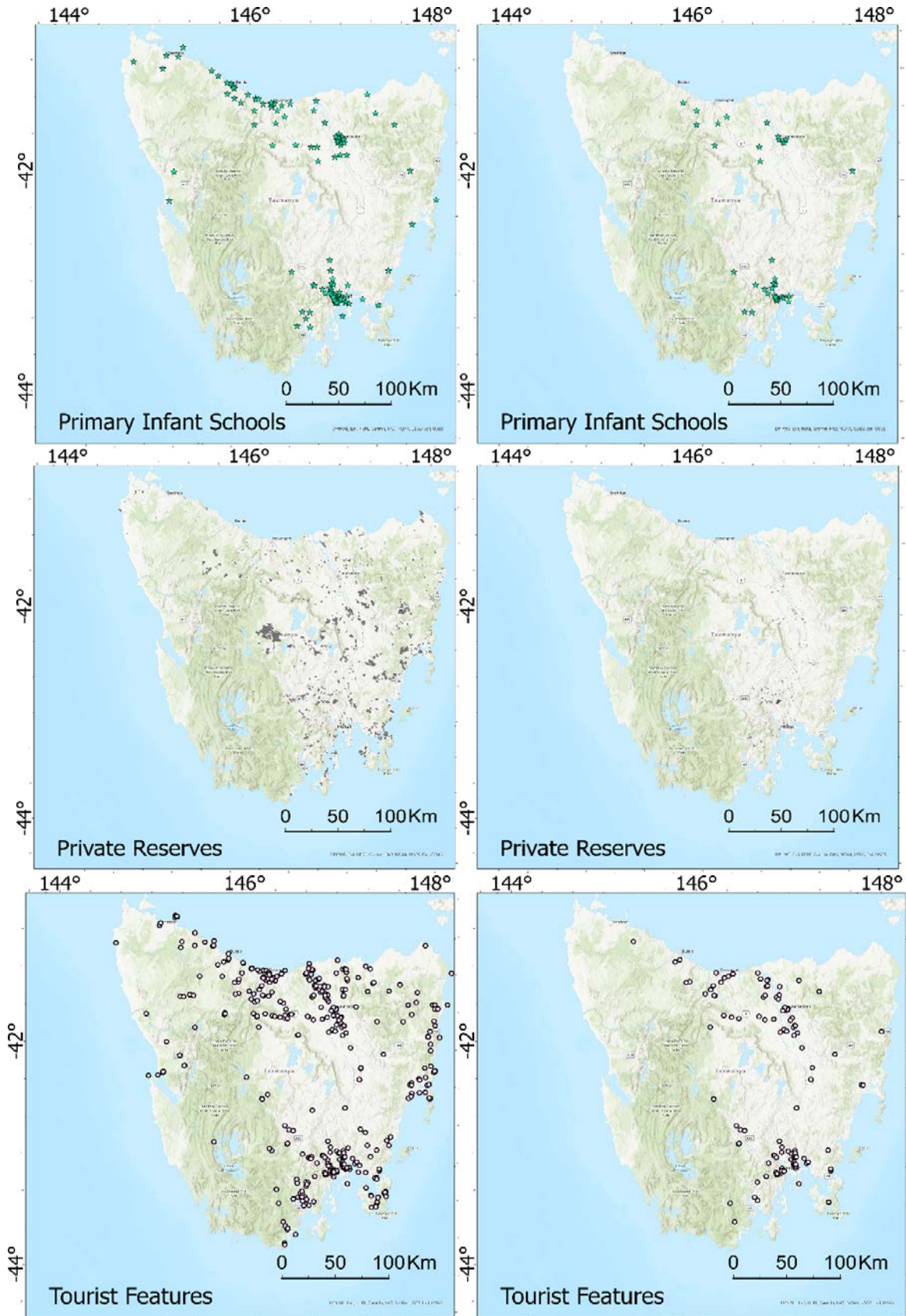


Figure 5. Risky features

As it can be seen in Figure 4, the majority of the susceptible areas are located southeast, center, and north regions. AUC has been applied and success and prediction rates were 87.64% and 84% respectively. In order to evaluate which features are at risk from these susceptible areas, overlay analysis has been implemented. The

classes of “very high” and “high” have been used to be overlaid with ambulances, buildings, children and elderly population density, cultural places, educational places, entertainment places, governmental places, heritage Tasmania feature, hotels, kindergarten, medical services, police stations, primary infant schools, private reserves, and tourist features. Figure 5 represented the features that fall into the highest susceptible zones.

According to Figure 5, 142 touristic places; 39 primary and infant schools; 122 police stations; 45 medical services; Huonville Primary School Kindergarten; 210 hotels; 217 governmental places; 94 education places; 30 cultural places; 30% buildings; 12 ambulances; 186 entertainment places; 744 private reserves; and 2195 heritage features are located in highest susceptible zones. The derived output can considerably assist different sectors such as governments, insurance, tourism, and etc.

Conclusion

All societies are affected by natural hazards in one form or another. Whilst landslides do not present the most significant danger in Tasmania, the cost to the community over time from economic and social perspectives is considerable. This study aimed to evaluate the existence of risky features in high landslide susceptibility zones in Tasmania. DT as one of the robust machine learning methods has been used to evaluate the correlations among landslide conditioning factors and landslide inventory. Susceptible zones were detected and risky features such as hotels, children and elderly population, etc. have been overlaid with the produced map. Through this analysis, some risky features have been detected in classes of “very high” and “high” susceptibility. For instance, among all kindergartens in Tasmania, Huonville Primary School Kindergarten has been located in risky zones. From 291,698 buildings in Tasmania, 82,736 buildings have been located in risky zones. Such information can significantly be helpful in future management plans. It can be used as a basis for more detailed and deep risk assessments in Tasmania.

Scientific Ethics Declaration

The author declares that the scientific ethical and legal responsibility of this article published in EPSTEM journal belongs to the author.

References

- Althuwaynee, O. F., Pradhan, B., & Lee, S. (2012). Application of an evidential belief function model in landslide susceptibility mapping. *Computers & Geosciences*, *44*, 120-135.
- Baeza, C., Lantada, N., & Amorim, S. (2016). Statistical and spatial analysis of landslide susceptibility maps with different classification systems. *Environmental Earth Sciences*, *75*(19), 1-17.
- Ballabio, C., & Sterlacchini, S. (2012). Support vector machines for landslide susceptibility mapping: the Staffora River Basin case study, Italy. *Mathematical geosciences*, *44*(1), 47-70. BAY, E. Landslide Map Series.
- Chakraborty, D., & Anbalagan, R. (2013). Landslide hazard analysis and management: A case study from Nainital, India. In *Earth System Processes and Disaster Management* (pp. 141-154). Springer.
- Chen, W., Xie, X., Peng, J., Wang, J., Duan, Z., & Hong, H. (2017). GIS-based landslide susceptibility modelling: a comparative assessment of kernel logistic regression, Naïve-Bayes tree, and alternating decision tree models. *Geomatics, Natural Hazards and Risk*, *8*(2), 950-973.
- Chu, L., Wang, L.-J., Jiang, J., Liu, X., Sawada, K., & Zhang, J. (2019). Comparison of landslide susceptibility maps using random forest and multivariate adaptive regression spline models in combination with catchment map units. *Geosciences Journal*, *23*(2), 341-355.
- Dai, F., Lee, C. F., & Ngai, Y. Y. (2002). Landslide risk assessment and management: an overview. *Engineering Geology*, *64*(1), 65-87.
- Del Soldato, M., Bianchini, S., Calcaterra, D., De Vita, P., Martire, D. D., Tomás, R., & Casagli, N. (2017). A new approach for landslide-induced damage assessment. *Geomatics, Natural Hazards and Risk*, *8*(2), 1524-1537.
- Hong, H., Miao, Y., Liu, J., & Zhu, A.-X. (2019). Exploring the effects of the design and quantity of absence data on the performance of random forest-based landslide susceptibility mapping. *Catena*, *176*, 45-64.
- Jaafari, A., Zenner, E. K., & Pham, B. T. (2018). Wildfire spatial pattern analysis in the Zagros Mountains, Iran: A comparative study of decision tree based classifiers. *Ecological informatics*, *43*, 200-211.

- Jain, P., Coogan, S. C., Subramanian, S. G., Crowley, M., Taylor, S., & Flannigan, M. D. (2020). A review of machine learning applications in wildfire science and management. *Environmental Reviews*, 28(4), 478-505.
- Jia, G., Alvioli, M., Gariano, S. L., Marchesini, I., Guzzetti, F., & Tang, Q. (2021). A global landslide non-susceptibility map. *Geomorphology*, 389, 107804.
- Kheir, R. B., Greve, M. H., Abdallah, C., & Dalgaard, T. (2010). Spatial soil zinc content distribution from terrain parameters: A GIS-based decision-tree model in Lebanon. *Environmental Pollution*, 158(2), 520-528.
- Korup, O. & Stolle, A. (2014). Landslide prediction from machine learning. *Geology Today*, 30(1), 26-33.
- Kumar, R. & Anbalagan, R. (2016). Landslide susceptibility mapping using analytical hierarchy process (AHP) in Tehri reservoir rim region, Uttarakhand. *Journal of the Geological Society of India*, 87(3), 271-286.
- Lee, S. (2005). Application of logistic regression model and its validation for landslide susceptibility mapping using GIS and remote sensing data. *International Journal of Remote Sensing*, 26(7), 1477-1491.
- Lee, S. & Choi, J. (2004). Landslide susceptibility mapping using GIS and the weight-of-evidence model. *International Journal of Geographical Information Science*, 18(8), 789-814.
- Lee, S., Ryu, J.-H., Won, J.-S. & Park, H.-J. (2004). Determination and application of the weights for landslide susceptibility mapping using an artificial neural network. *Engineering Geology*, 71(3-4), 289-302.
- Lee, S. & Sambath, T. (2006). Landslide susceptibility mapping in the Damrei Romel area, Cambodia using frequency ratio and logistic regression models. *Environmental Geology*, 50(6), 847-855.
- Mazengarb, C. (2005). *The Tasmanian landslide hazard map series: methodology*. Department of Infrastructure, Energy and Resources Hobart, Australia.
- Mazengarb, C. & Stevenson, M. (2010). *Tasmanian landslide map series: user guide and technical methodology*. Tasmanian Geological Survey.
- Meena, S. R., Puliero, S., Bhuyan, K., Floris, M. & Catani, F. (2022). Assessing the importance of conditioning factor selection in landslide susceptibility for the province of Belluno (region of Veneto, northeastern Italy). *Natural hazards and earth system sciences*, 22(4), 1395-1417.
- Merghadi, A., Yunus, A. P., Dou, J., Whiteley, J., ThaiPham, B., Bui, D. T., Avtar, R. & Abderrahmane, B. (2020). Machine learning methods for landslide susceptibility studies: A comparative overview of algorithm performance. *Earth-Science Reviews*, 207, 103225.
- Park, S.-J., Lee, C.-W., Lee, S. & Lee, M.-J. (2018). Landslide susceptibility mapping and comparison using decision tree models: A Case Study of Jumunjin Area, Korea. *Remote Sensing*, 10(10), 1545.
- Pham, B. T., Pradhan, B., Bui, D. T., Prakash, I. & Dholakia, M. (2016). A comparative study of different machine learning methods for landslide susceptibility assessment: A case study of Uttarakhand area (India). *Environmental Modelling & Software*, 84, 240-250.
- Pham, B. T., Tien Bui, D., Prakash, I. & Dholakia, M. (2016). Rotation forest fuzzy rule-based classifier ensemble for spatial prediction of landslides using GIS. *Natural Hazards*, 83(1), 97-127.
- Pourghasemi, H., Moradi, H. & Fatemi Aghda, S. (2013). Landslide susceptibility mapping by binary logistic regression, analytical hierarchy process, and statistical index models and assessment of their performances. *Natural Hazards*, 69(1), 749-779.
- Pourghasemi, H. R., Jirandeh, A. G., Pradhan, B., Xu, C. & Gokceoglu, C. (2013). Landslide susceptibility mapping using support vector machine and GIS at the Golestan Province, Iran. *Journal of Earth System Science*, 122(2), 349-369.
- Pourghasemi, H. R., Mohammady, M. & Pradhan, B. (2012). Landslide susceptibility mapping using index of entropy and conditional probability models in GIS: Safarood Basin, Iran. *Catena*, 97, 71-84.
- Pourghasemi, H. R., Pradhan, B. & Gokceoglu, C. (2012). Application of fuzzy logic and analytical hierarchy process (AHP) to landslide susceptibility mapping at Haraz watershed, Iran. *Natural hazards*, 63(2), 965-996.
- Pourtaghi, Z. S., Pourghasemi, H. R., Aretano, R. & Semeraro, T. (2016). Investigation of general indicators influencing on forest fire and its susceptibility modeling using different data mining techniques. *Ecological Indicators*, 64, 72-84.
- Regmi, A. D., Devkota, K. C., Yoshida, K., Pradhan, B., Pourghasemi, H. R., Kumamoto, T. & Akgun, A. (2014). Application of frequency ratio, statistical index, and weights-of-evidence models and their comparison in landslide susceptibility mapping in Central Nepal Himalaya. *Arabian Journal of Geosciences*, 7(2), 725-742.
- Reichenbach, P., Rossi, M., Malamud, B. D., Mihir, M. & Guzzetti, F. (2018). A review of statistically-based landslide susceptibility models. *Earth-Science Reviews*, 180, 60-91.
- Roodposhti, M. S., Aryal, J. & Pradhan, B. (2019). A novel rule-based approach in mapping landslide susceptibility. *Sensors*, 19(10), 2274.
- Saito, H., Nakayama, D. & Matsuyama, H. (2009). Comparison of landslide susceptibility based on a decision-tree model and actual landslide occurrence: the Akaishi Mountains, Japan. *Geomorphology*, 109(3-4), 108-121.

- Sim, K. B., Lee, M. L. & Wong, S. Y. (2022). A review of landslide acceptable risk and tolerable risk. *Geoenvironmental Disasters*, 9(1), 1-17.
- Slee, A. & McIntosh, P. D. (2022). History of slope instability in the Oldina plantation, Tasmania. *New Zealand Journal of Forestry Science*, 52.
- Sultana, N. & Tan, S. (2021). Landslide mitigation strategies in southeast Bangladesh: lessons learned from the institutional responses. *International Journal of Disaster Risk Reduction*, 62, 102402.
- Tehrany, M. S., Pradhan, B. & Jebur, M. N. (2013). Spatial prediction of flood susceptible areas using rule based decision tree (DT) and a novel ensemble bivariate and multivariate statistical models in GIS. *Journal of hydrology*, 504, 69-79.
- Xu, C., Xu, X., Dai, F. & Saraf, A. K. (2012). Comparison of different models for susceptibility mapping of earthquake triggered landslides related with the 2008 Wenchuan earthquake in China. *Computers & Geosciences*, 46, 317-329.

Author Information

Mahyat Shafapourtehrany

Kandilli Observatory and Earthquake Research Institute,
Department of Geodesy, Bogazici University, 34680
Cengelkoy, Istanbul, Turkey
Contact e-mail: mahyat.shafapour@boun.edu.tr

To cite this article:

Shafapourtehrany, M. (2022). Exploring the risky areas due to landslide using decision tree analysis: case study. Tasmania, Australia The Eurasia Proceedings of Science, Technology, Engineering & Mathematics (EPSTEM), 18, 86-101.

Determination of Moisture Content and Morphological Characteristics of MDF Composite Materials Used For Industrial Products

Băilă Diana-IRINEL

University Politehnica of Bucharest, Romania

Păcurar RĂZVAN

Technical University of Cluj-Napoca, Romania

Păcurar ANCUȚA

Technical University of Cluj-Napoca, Romania

Abstract: The growing concern for the environment, in relation to the need for more versatile polymer-based materials, has led to a high interest in research into polymer composites filled with natural-organic fillers, which come from renewable sources. MDF is a high grade, composite material and it is made from recycled wood fibers and resin and it is less expensive. This composite material is dried and pressed to produce dense, stable sheets and because of this process, MDF does not warp or crack like wood. And since MDF is made from small particles, it doesn't have noticeable grain patterns, showed by electronic microscopy. This will result in a smoother finish on the industrial product.

In generally, the wood contracts or expands when it is exposed to changing heat and humidity and can appear some cracks on the industrial products.

In this paper were realized water absorption tests on the MDF samples, in function of different temperature and humidity levels. The water absorption content for each piece of MDF composite material is represented as a percentage of the weight of the water and oven-dry weight.

The humidity absorption depends on the composite material type, their structure, and it depends on the environment in which the product is used.

The quality and moisture resistance of a composite material is extremely important for the durability and degradation degree of an industrial product.

Keywords: MDF composite material, moisture, thermostat enclosure, microscopic structure.

Introduction

In generally, the moisture absorption is known to alter many of the mechanical properties of polymer-based composites. For ultrasonic characterization of moisture content can be based on the transmission of acoustic waves through composite plates.

The composite materials are used in many fields, such as automotive, aeronautic, transport, construction, armament, furniture, etc., because of their attractive mechanical properties, high rigidity, low relative weight, and much higher moisture resistance than wood (Saravanakumaar, 2022).

The effect of water absorption/desorption on their mechanical properties was remarked and can induce severe changes in the material behavior.

In literature, it was observed that a lowering of the glass transition temperature with water content and the appearance of microcracks due to induced residual stresses. At the same time, the moisture content generates swelling and density variations. The most commonly methods for characterization are: weight measurements or nuclear magnetic resonance spectroscopy, unfortunately but they are generally destructive. Moisture content can be estimated using acoustic waves, determining the change of the material mechanical properties. The method is nondestructive and allows in situ measurements (Fortineau, 2007).

Wood is a hygroscopic material. The moisture content of a wood sample is expressed by the percentage of the mass of water present in the sample to the relative anhydrous mass. The wood must be dried before being used in the various industries; therefore, it is necessary to carry out a control of its humidity. Wood drying can be done either in the atmosphere or in furnaces or both at the same time.

- This is an Open Access article distributed under the terms of the Creative Commons Attribution-Noncommercial 4.0 Unported License, permitting all non-commercial use, distribution, and reproduction in any medium, provided the original work is properly cited.

- Selection and peer-review under responsibility of the Organizing Committee of the Conference

Most drying processes use a system with a temperature and humidity-controlled thermostat enclosure. Most of the mechanical and physical properties of wood or composite material depend on the final humidity (Hamidi, 2017). Generally, the composite material can be degraded by a drying process due to the severe conditions to which it is subjected. In this study are presented the effects of drying and the types of defects that result. The humidity contained in fresh or dry wood can be evaluated at 35% for fir and can increase up to 300% for red wood (Leman, 2008).

To measure the moisture of the composite materials there are several methods, but the most common used are:

- by oven-drying;
- distillation;
- the electrical method.

The oven-drying method is not very precise, because the wood is dried at high temperatures above $103\pm 2^{\circ}\text{C}$. The method considers that the lost weight corresponds to the evaporated water, but it does not consider that volatile extractions are also lost by evaporation.

The distillation method presents a modification compared to the oven-drying method because the wet wood is dried in immiscible water where there is a solvent for the volatile extractions.

The electrical method is often used to measure moisture content in composite materials because it gives immediate and accurate results.

MDF is a highly stable material compared with solid wood. The effect of water content change on tensile strength of MDF board is basically similar as the static flexural strength, but the change rate is not as large as in the static flexural strength. The tensile strength decreases by 2%-3% in rapport with the increase by 1% of the water content.

The static flexural strength and tensile strength for the MDF board are the highest, if the moisture content is between 3%-5%. The water in the MDF board plays, in this case, a similar role to the binding force between the fibers. The moisture content exceeding this value will weaken the binding force between fibers (Magalhaes, 2021).

Method

The whole of the thermostatically controlled enclosure regulated in temperature and humidity includes: a test enclosure with its conditioning, the installation support, in which the machinery and the control panel are placed.

The measuring device used is of the H.M.P.230 type and is a microprocessor transmitter for measuring the relative humidity and air temperature. Based on these data, the absolute humidity can be calculated, dew point temperature, temperature humidity relationship and wet bulb temperature. The samples of MDF.12 are introduced in a enclosure thermostat controlled in temperature and humidity. The thermostat enclosure is constituted of the next elements: the inner tube of welded stainless steel sealed and exhaust bung; mineral wool insulation; 2 joints in silicon; door opener with wedge-thermal bridges.

Cold production is carried out by evaporation of a refrigerant fluid in a finned copper tube exchanger, located behind the screen plate. The cooling capacity can be increased by injecting liquid nitrogen into the enceinte volume.

Hot production is carried out by heat release from armored resistors with stainless steel fins, arranged behind the screen plate. Air circulation is carried out by a fan motor with an external motor. Conditioned air is sucked in and discharged into the workspace. This technique allows a very good homogeneity, the streams of cold and hot air being very strongly brushed.

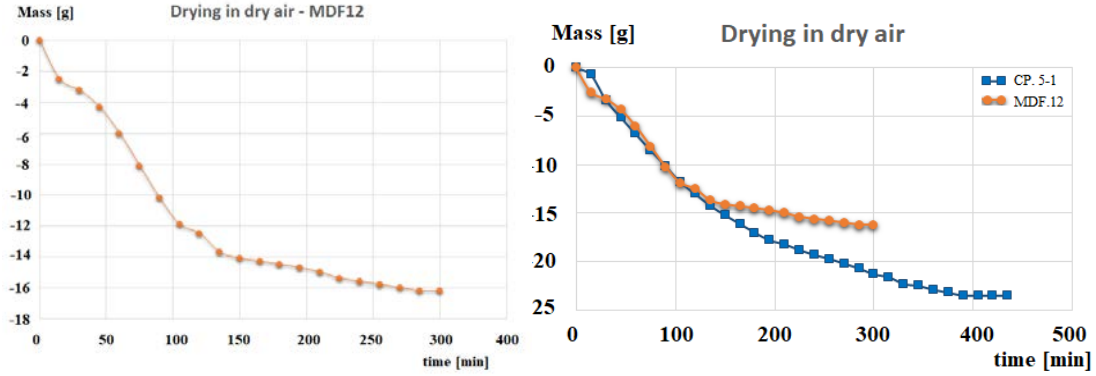


Fig.1.Drying in dry air for MDF.12 composite material Fig.2. Comparison of drying behavior of the two composite materials

The control of the humidity it is realized by a solenoid feed, a cold drying racket and the electro valves for inject compressed and dried air. In the figure 1, it is represented the graph concerning the drying in dry air for MDF.12 composite material, and in figure 2 can remark MDF.12 lose less mass after drying than CP.5-1 composite material.

Results and Discussion

The water absorption behavior for traction tests for the MDF.12 composite material was established and the moisture coefficients of MDF.12 composite material, for the temperature of 100°C and humidity level of 1%H are presented in the table 1.

Table 1. Moisture coefficients for MDF.12 composite material at 1%H and the temperature of 100°C

| Temperature [°C] | Time [min] | Humidity [H] | Mass [g] |
|------------------|------------|--------------|----------|
| 103 | 0 | 1 | 0 |
| 102.9 | 15 | 1 | -2.5 |
| 102.7 | 30 | 1 | -3.2 |
| 102.6 | 45 | 1 | -4.3 |
| 102.5 | 60 | 1 | -6 |
| 102.6 | 75 | 1 | -8.1 |
| 102.5 | 90 | 1 | -10.2 |
| 102.5 | 105 | 1 | -11.9 |
| 102.5 | 120 | 1 | -12.5 |
| 102.6 | 135 | 1 | -13.7 |
| 102.6 | 150 | 1 | -14.1 |
| 102.5 | 165 | 1 | -14.3 |
| 102.5 | 180 | 1 | -14.5 |
| 102.4 | 195 | 1 | -14.7 |
| 102.6 | 210 | 1 | -15 |
| 102.4 | 225 | 1 | -15.4 |
| 102.5 | 240 | 1 | -15.6 |
| 102.6 | 255 | 1 | -15.8 |
| 102.5 | 270 | 1 | -16 |
| 102.5 | 285 | 1 | -16.2 |
| 102.6 | 300 | 1 | -16.2 |

The variation of the experimental mass values in rapport of time for the MDF.12 composite material for temperature of 20°C and different moisture values is shown in the table 2 and in the table 3 are presented the modification of the mass value during the time at the temperature of 40°C and different moisture values (20%H, 40%H, 60%H, 80%H). In the figure 3 is determinate the graph of MDF.12 composite material concerning the variation between the mass values and time for the temperature of 20°C and different wettability coefficients (20%H, 40%H, 60%H, 80% H), respectively, in the figure 4 is represented the variation graph for the similar conditions at the temperature of 40°C.

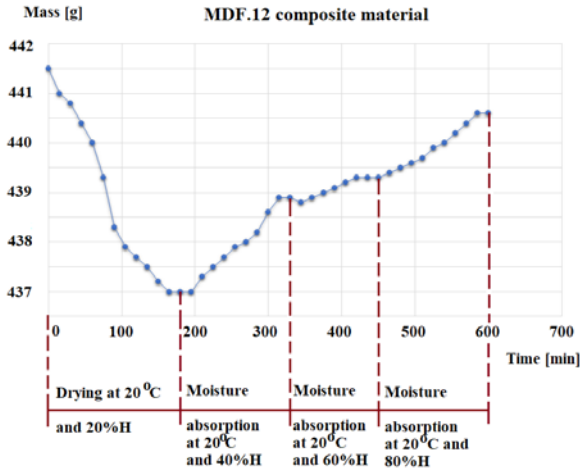


Fig.3. Graph of variation between the mass values and time for the temperature of 20°C and different moisture coefficients (20%H, 40%H, 60%H, 80% H)

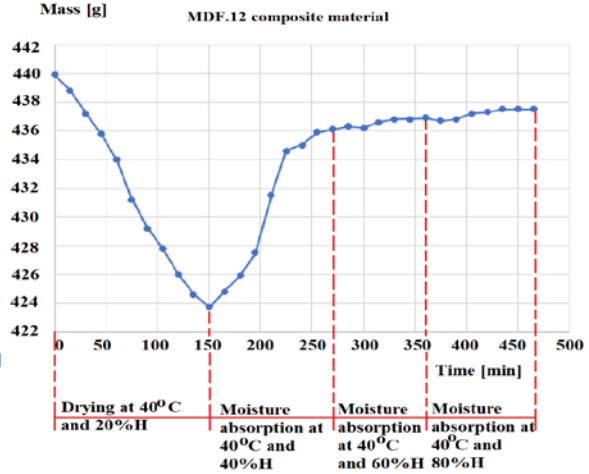


Fig.4. Graph of variation between the mass values and time for the temperature of 40°C and different moisture coefficients (20%H, 40%H, 60%H, 80% H)

Table 2. Mass variation in time for MDF.12 composite material at different moisture coefficients (20%H,40%H, 60%H, 80%H) and the temperature of 20°C

| Temperature [°C] | Time [min] | Humidity [H] | Mass [g] |
|------------------|------------|--------------|----------|
| 19.9 | 0 | 20 | 441.5 |
| 19.9 | 15 | 20 | 441 |
| 19.9 | 30 | 20 | 440.8 |
| 19.8 | 45 | 20 | 440.4 |
| 19.8 | 60 | 20 | 440 |
| 19.9 | 75 | 20 | 439.3 |
| 20.1 | 90 | 20 | 438.3 |
| 19.8 | 105 | 20 | 437.9 |
| 19.9 | 120 | 20 | 437.7 |
| 20 | 135 | 20 | 437.5 |
| 20 | 150 | 20 | 437.2 |
| 20 | 165 | 20 | 437 |
| 20 | 180 | 20 | 437 |
| 20 | 195 | 40 | 437 |
| 20 | 210 | 40 | 437.3 |
| 20 | 225 | 40 | 437.5 |
| 20 | 240 | 40 | 437.7 |
| 19.9 | 255 | 40 | 437.9 |
| 19.9 | 270 | 40 | 438 |
| 19.9 | 285 | 40 | 438.2 |
| 20 | 300 | 40 | 438.6 |
| 20 | 315 | 40 | 438.9 |
| 20 | 330 | 40 | 438.9 |
| 20 | 345 | 60 | 438.8 |
| 20.1 | 360 | 60 | 438.9 |
| 20.1 | 375 | 60 | 439 |
| 20.1 | 390 | 60 | 439.1 |
| 20 | 405 | 60 | 439.2 |
| 20 | 420 | 60 | 439.3 |
| 20 | 435 | 60 | 439.3 |
| 20.1 | 450 | 60 | 439.3 |
| 20 | 465 | 80 | 439.4 |
| 20 | 480 | 80 | 439.5 |
| 20 | 495 | 80 | 439.6 |
| 20.1 | 510 | 80 | 439.7 |
| 19.9 | 525 | 80 | 439.9 |
| 19.9 | 540 | 80 | 440 |
| 19.9 | 555 | 80 | 440.2 |
| 19.9 | 570 | 80 | 440.4 |
| 19.8 | 585 | 80 | 440.6 |
| 19.8 | 600 | 80 | 440.6 |

Table 3. Mass variation in time for MDF.12 composite material at different moisture coefficients (20%H, 40%H, 60%H, 80%H) and the temperature of 40°C

| Temperature [°C] | Time [min] | Humidity [H] | Mass [g] |
|------------------|------------|--------------|----------|
| 39.7 | 0 | 20 | 441.9 |
| 39.7 | 15 | 20 | 440.8 |
| 39.8 | 30 | 20 | 439.2 |
| 39.8 | 45 | 20 | 437.8 |
| 39.9 | 60 | 20 | 436 |
| 40.1 | 75 | 20 | 433.2 |
| 39.8 | 90 | 20 | 431.2 |
| 39.9 | 105 | 20 | 429.8 |
| 40 | 120 | 20 | 428 |
| 40 | 135 | 20 | 426.6 |
| 40 | 150 | 20 | 425.7 |
| 40 | 165 | 40 | 426.8 |
| 40 | 180 | 40 | 427.9 |
| 40 | 195 | 40 | 429.5 |
| 40 | 210 | 40 | 433.5 |
| 40 | 225 | 40 | 436.6 |
| 39.9 | 240 | 40 | 437 |
| 39.9 | 255 | 40 | 437.9 |
| 39.9 | 270 | 40 | 438.1 |
| 40 | 285 | 60 | 438.3 |
| 40 | 300 | 60 | 438.2 |
| 40 | 315 | 60 | 438.6 |
| 40 | 330 | 60 | 438.8 |
| 40.1 | 345 | 60 | 438.8 |
| 40.1 | 360 | 60 | 438.9 |
| 40.1 | 375 | 80 | 438.7 |
| 40 | 390 | 80 | 438.8 |
| 40 | 405 | 80 | 439.2 |
| 40 | 420 | 80 | 439.3 |
| 40.1 | 435 | 80 | 439.5 |
| 40 | 450 | 80 | 439.5 |
| 40 | 465 | 80 | 439.5 |

The variation of the mass values in function of the time for the MDF.12 composite material for temperature of 60°C and different moisture values is determined in the table 4 and in the table 5 is presented the mass value variation during the time at the temperature of 80°C for different moisture values (20%H, 40%H, 60%H, 80%H). The graph of variation of MDF.12 composite material between the mass values and time for the temperature of 60°C and different wettability coefficients (20%H, 40%H, 60%H, 80% H) is represented in figure 5 and in the figure 6 it is presented the variation graph for the similar conditions, for the temperature of 80°C.

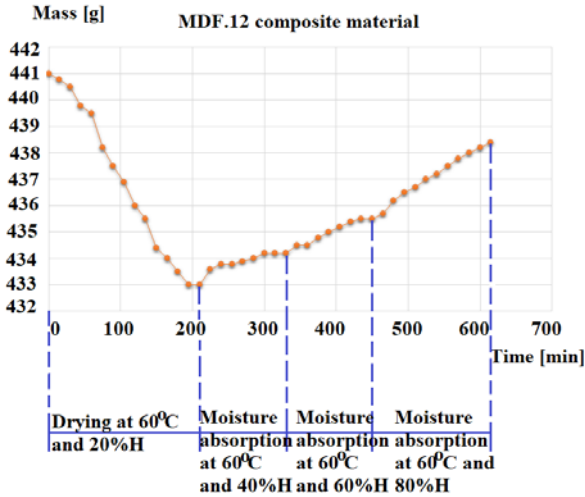


Fig.5. Graph of variation between the mass values and time for the temperature of 60°C and different wettability coefficients (20%H, 40%H, 60%H, 80% H)

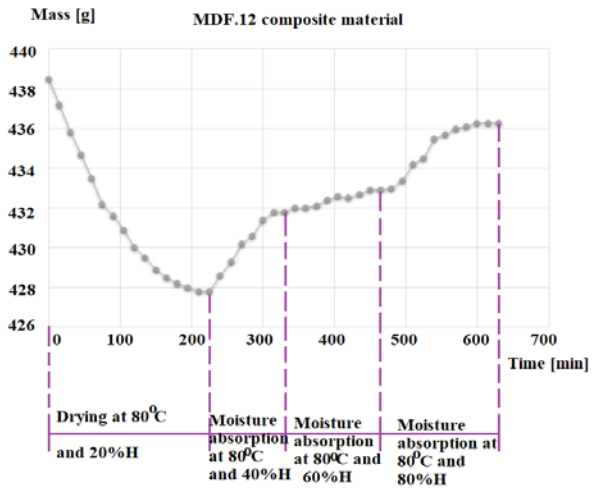


Fig.6. Graph of variation between the mass values and time for the temperature of 80°C and different wettability coefficients (20%H, 40%H, 60%H, 80%H)

Table 4. Mass variation in time for MDF.12 composite material at different moisture coefficients (20%H,40%H, 60% H, 80% H) and the temperature of 60°C

| Temperature [°C] | Time [min] | Humidity [H] | Mass [g] |
|------------------|------------|--------------|----------|
| 59.8 | 0 | 20 | 441 |
| 60 | 15 | 20 | 440.8 |
| 59.9 | 30 | 20 | 440.5 |
| 59.9 | 45 | 20 | 439.8 |
| 59.9 | 60 | 20 | 439.5 |
| 59.9 | 75 | 20 | 438.2 |
| 59.8 | 90 | 20 | 437.5 |
| 60 | 105 | 20 | 436.9 |
| 60.1 | 120 | 20 | 436 |
| 60 | 135 | 20 | 435.5 |
| 60 | 150 | 20 | 434.4 |
| 60 | 165 | 20 | 434 |
| 60.2 | 180 | 20 | 433.5 |
| 59.9 | 195 | 20 | 433 |
| 59.9 | 210 | 20 | 433 |
| 59.9 | 225 | 40 | 433.6 |
| 59.8 | 240 | 40 | 433.8 |
| 59.7 | 255 | 40 | 433.8 |
| 60.1 | 270 | 40 | 433.9 |
| 59.8 | 285 | 40 | 434 |
| 59.9 | 300 | 40 | 434.2 |
| 59.9 | 315 | 40 | 434.2 |
| 60 | 330 | 40 | 434.2 |
| 60 | 345 | 60 | 434.5 |
| 60.1 | 360 | 60 | 434.5 |
| 59.9 | 375 | 60 | 434.8 |
| 59.9 | 390 | 60 | 435 |
| 60 | 405 | 60 | 435.2 |
| 60 | 420 | 60 | 435.4 |
| 60 | 435 | 60 | 435.5 |
| 60.1 | 450 | 60 | 435.5 |
| 60 | 465 | 80 | 435.7 |
| 60 | 480 | 80 | 436.2 |
| 60.1 | 495 | 80 | 436.5 |
| 59.9 | 510 | 80 | 436.7 |
| 59.9 | 525 | 80 | 437 |
| 59.9 | 540 | 80 | 437.2 |
| 60 | 555 | 80 | 437.5 |
| 60.1 | 570 | 80 | 437.8 |
| 60 | 585 | 80 | 438 |
| 60 | 600 | 80 | 438.2 |
| 60 | 615 | 80 | 438.4 |

Table 5. Mass variation in time for MDF.12 composite material at different moisture coefficients (20%H, 40%H, 60% H, 80% H) and the temperature of 80°C

| Temperature [°C] | Time [min] | Humidity [H] | Mass [g] |
|------------------|------------|--------------|----------|
| 79.8 | 0 | 20 | 438.5 |
| 79.6 | 15 | 20 | 437.2 |
| 79.7 | 30 | 20 | 435.8 |
| 79.6 | 45 | 20 | 434.7 |
| 79.6 | 60 | 20 | 433.5 |
| 79.8 | 75 | 20 | 432.2 |
| 79.8 | 90 | 20 | 431.6 |
| 79.8 | 105 | 20 | 430.9 |
| 79.6 | 120 | 20 | 430 |
| 79.7 | 135 | 20 | 429.5 |
| 79.8 | 150 | 20 | 428.9 |
| 79.6 | 165 | 20 | 428.5 |
| 79.7 | 180 | 20 | 428.2 |
| 79.6 | 195 | 20 | 428 |
| 79.6 | 210 | 20 | 427.8 |
| 79.7 | 225 | 20 | 427.8 |
| 79.8 | 240 | 40 | 428.6 |
| 79.8 | 255 | 40 | 429.3 |
| 79.7 | 270 | 40 | 430.2 |
| 79.6 | 285 | 40 | 430.6 |
| 79.6 | 300 | 40 | 431.4 |
| 79.8 | 315 | 40 | 431.8 |
| 79.8 | 330 | 40 | 431.8 |
| 79.9 | 345 | 60 | 432 |
| 79.9 | 360 | 60 | 432 |
| 79.8 | 375 | 60 | 432.1 |
| 79.9 | 390 | 60 | 432.4 |
| 79.8 | 405 | 60 | 432.6 |
| 79.8 | 420 | 60 | 432.5 |
| 79.8 | 435 | 60 | 432.7 |
| 79.8 | 450 | 60 | 432.9 |
| 79.7 | 465 | 60 | 432.9 |
| 79.8 | 480 | 80 | 433 |
| 79.8 | 495 | 80 | 433.4 |
| 79.7 | 510 | 80 | 434.2 |
| 79.8 | 525 | 80 | 434.5 |
| 79.7 | 540 | 80 | 435.5 |
| 79.7 | 555 | 80 | 435.7 |
| 79.8 | 570 | 80 | 436 |
| 79.8 | 585 | 80 | 436.1 |
| 79.8 | 600 | 80 | 436.3 |
| 79.8 | 615 | 80 | 436.3 |
| 79.8 | 630 | 80 | 436.3 |

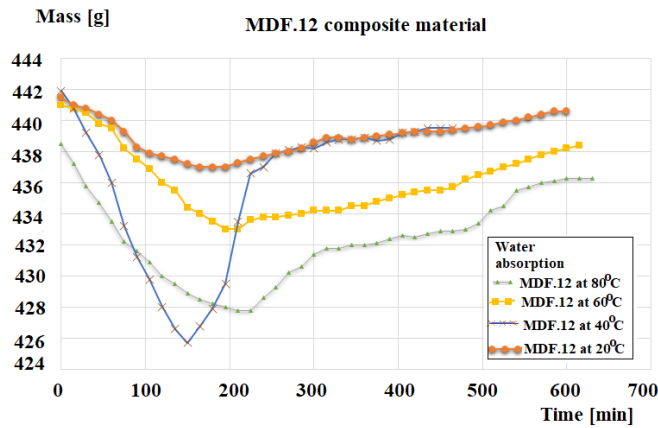


Fig.7. Curves of the variation of the mass during the time in function of different temperatures for MDF.12

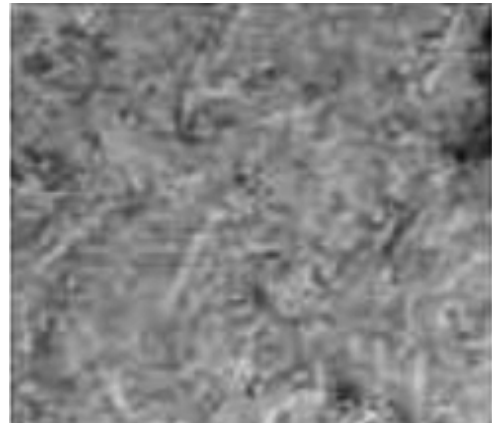


Fig.8. SEM analyses MDF.12 composite material

In the figure 7 are shown the curves that present the variation of the mass during the time for the MDF.12 composite material and can remark when the temperature and humidity increase, the mass of the material increases, to a critical point of humidity, when a water saturation of the fiber occurs. In figure 8 is presented the microscopic structure of MDF.12 composite material.

Conclusion

MDF.12 composite material present high strength and high efficiency, elastic modulus is better than steel, with excellent creep resistance, corrosion resistance, light weight, good flexibility and for this it is used in a variety of industries. The MDF.12 composite materials has a higher moisture resistance in comparisons with different other composites and absorbs less water than CP.05 composite material.

At the temperature of 20°C, all composites have a drying process for the composite materials, if it increases the temperatures and it varies the humidity values, can remark an increase of mass values proportional with the humidity percents, because of the water absorption in the composite materials, although the temperature rises.

Due to the superior mechanical properties, these composite materials of MDF.12 type will be able to successfully replace non-degradable plastics, being degradable materials.

Scientific Ethics Declaration

The authors declare that the scientific ethical and legal responsibility of this article published in EPSTEM journal belongs to the authors.

Acknowledgement

This work has been funded by the EEA & Norway Grant, with project title “European network for 3D printing of biomimetic mechatronic systems”, Acronym EMERALD - Nr. Contract 21-COP-0019/ F-SEE-026/06.2021.

References

- Fortineau, J., Le Clezio E., Vander Meulen, F. & Feuillard, G. (2007). *Moisture content characterization in composite materials based on ultrasonic transmission measurements*, Journal of Applied Physics 101, 114911
- Hamidi, Y., Aktas, L. & Altan, M. (2017). *Thermal history effects on moisture absorption of fiber-reinforced polymer composites*, AIP Conference Proceedings 1914, 030012.
- Leman, Z., Sapuan, S.M., Saifol, A.M., Maleque, M.A. & Ahmad, M. (2008), *Moisture absorption behavior of sugar palm fiber reinforced epoxy composites*, Materials&Design 29(8), 1666-1670.

Magalhaes, R., Nogueira, B., Samaritana, C., Paiva, N., Ferra, J., Magalhaes, F., Martins, J. & Carvalho, L. (2021). *Effect of panel moisture content on internal bond strength and thickness swelling of medium density Fiberboard*, Polymers, 13, 114, DOI: 10.3390/polym13010114

Saravanakumar, A., Senthilkumar, A., Rajan, B., Rajini, N., Ismail, S., Mohammad, F. & Al-Lohedan, H. (2022). *Effects of moisture absorption and thickness swelling behaviors on mechanical performances of carica papaya fiber reinforced polymeric composites*, Journal of Natural Fibers, doi:10.1080/15440478.2022.2051668.

Author Information

Băilă Diana-Irinel 1

University Politehnica of Bucharest, Romania
Blv.Splaiul Independenței, no.313, sector 6, cod 060042,
Bucharest, Romania
Contact e-mail: *baila_d@yahoo.com*

Păcurar Răzvan 2

Technical University of Cluj-Napoca, Romania
Faculty of Machine Building, Department of Manufacturing
Engineering, Blv. Muncii, no. 103-105, 400641, Cluj-
Napoca, Romania

Păcurar Ancuța 3

Technical University of Cluj-Napoca, Romania
Faculty of Machine Building, Department of Manufacturing
Engineering, Blv. Muncii, no. 103-105, 400641, Cluj-
Napoca, Romania

A Study on Wetlands of a Peruvian Bay Through the Hydrometer Method and X-Ray Diffraction

María Luisa CERÓN LOAYZA
Universidad Nacional Mayor de San Marcos, Perú

Marlon Gastón FARFÁN-CÓRDOVA
Universidad César Vallejo, Perú

Jenny Aleida MONTOYA BURGA
Universidad César Vallejo, Perú

Fanny MORI ESCOBAR
Universidad Nacional Mayor de San Marcos, Perú

Felipe Américo REYES NAVARRO
Universidad Nacional Mayor de San Marcos, Perú

Abstract: We have carried out research on the contamination levels of sediments provoked by mining tailings at the Peruvian Ite Bay (Ite District, Tacna Region). These tailings are from the Toquepala and Cuajone mines. Specifically, we have sampled the wetlands of the Ite bay, in the zone of the mouth of the mining tailings, an area where there are no anthropogenic discharges of domestic origin. This research is important because all the fauna and flora of the sector would be in danger of disappearing. Therefore, we have extracted samples at three points at depths 0, 25 and 50 cm, respectively. Next, we have determined the texture of sediments by the hydrometer method as well as characterized the samples by X-ray diffraction. The results of the texture test indicate that the samples are sandy soil, which is natural because the area is close to the seashore. X-ray diffraction results show the presence of zinc sulfide and goethite contaminants. In a small percentage, we found the vermiculite contaminant. To establish the degree of contamination existing in the sampling area, we have carried out similar studies for sandy soil samples in an area we consider free of contaminants.

Keywords: Sediments, X-Ray Diffraction, The Hydrometer Method, Peruvian Bay.

Introduction

Currently, the wetlands of the Peruvian Ite Bay represent an ecosystem of the highest natural value, internationally recognized as an Important Bird Area since it has the highest population of waterfowl in the Republic of Peru. This makes it a natural resource that needs to be managed to ensure its sustainability for the benefit of the local community, that is, actions need to be taken for its conservation (Ibárcena Fernández, 2011; Crompton, 2019). Ite Bay is located in the Tacna Region, Jorge Basadre Grohmann Province, Ite District, namely, in a place called *Playa Inglesa* (English beach), formed by an artificial beach of mining tailings. In addition, there are no anthropogenic discharges of domestic origin in the area. The water that feeds the wetlands comes from the filtrations of the *Quebrada Honda* (deep gorge) dam, where the mining tailings generated by the Cuajone and Toquepala mines are currently stored. These mining tailings have contaminated the wetlands with heavy metals a long time ago, endangering all the fauna and flora on the surroundings (Santos Jallath, 2007).

Thus, our research work aims to carry out an experimental study through both the determination of the soil texture class by the hydrometer method and mineral characterization by X-ray diffraction. This research will help to carry out an environmental impact assessment in the previously mentioned area.

Methodology

Sample Collection

We travelled to the area where the mining tailings flow into the Ite Bay (Figure 1), approximately 111 km from the Toquepala and Cuajone mines. Therein, we have extracted samples from three points. At each point, we have taken them at 3 different depths: 0 cm, 25 cm and 50 cm with the aim of carrying out a study of the levels of heavy metals in the area. Table 1. The latitude and longitude of each points studied is as follows: -17.907368°

- This is an Open Access article distributed under the terms of the Creative Commons Attribution-Noncommercial 4.0 Unported License, permitting all non-commercial use, distribution, and reproduction in any medium, provided the original work is properly cited.

- Selection and peer-review under responsibility of the Organizing Committee of the Conference

and -70.957904° (Point 01), -17.908491 and -70.958014 (Point 02), and -17.907249 and -70.959548 (Point 03).



Figure 1. Location of the Peruvian Ite bay. *Carretera Costanera Sur* means South Coastal Road.

Preparation of samples

In our Soil Analysis Laboratory of the National University of San Marcos, we poured a small portion of the collected soils into a beaker. Next, to obtain a dry soil, we taken it to an oven at an approximately 80°C for approximately 5 minutes. Afterwards, we proceed to sieving, which consists of passing the samples dried through a sieve with 2 mm openings in order to separate the soil into two portions: the one that is retained in the sieve (material greater than 2 mm) and the portion of soil that passes through it (material less than 2 mm).

The hydrometer method

By this one we can determine the percentages of sand, silt, and clay contained in a soil sample. Soil texture refers to the relative proportion of sand, silt, and clay in the soil. Texture classification is based on the number of particles less than 2 mm in diameter. The fractions according to the respective size are called soil separates. The texture terms are defined in a graphical way in a triangular diagram that represents the values of the three fractions mentioned above. Soil class names basically consist of the following terms: sand, silt, clay, and loam. In these texture terms, the content of gravel is dispensed; these terms refer to the fraction of the soil that is studied in any soil analysis laboratory and it is known as fine soil. Thereupon, a soil having 25% sand, 25% silt, and 50% clay is said to have a clay texture.

Determination of the texture class by the hydrometer method

First, we dry and sieve the samples lesser than 2 mm. Then, we use a 50-g soil sample if it had a fine texture else we use 100 g. Next, we place the sample into a 1000-ml container and add 600 ml of distilled water and 5-10 ml of a dispersing agent, and shake it. It is recommended to leave the sample to stand overnight for better dispersion. Afterwards, the sample is shaken for approximately 20 minutes and, thereupon, the Bouyoucos densimeter must be immersed and the respective readings are made at 40 s, 2 h and 4 h. Likewise, we measure the temperature of the solution before and when taking the readings. Finally we determine the soil texture by using the soil texture triangle.

Sample characterization by X-ray diffraction

For the structural identification of the minerals and crystallographic phases present in the samples studied, we use the X-ray diffractometry (XRD) technique (James, 1962). Thus, we have used a BRUKER diffractometer, model D8-Focus, with $\text{Cu-K}\alpha$ radiation (20 kV, 40 mA) with $\lambda = 1.54178 \text{ \AA}$ and a vertical goniometer. The scan angle was $4^{\circ} < 2\theta < 70^{\circ}$ and the scan rate was $0.02^{\circ}/\text{step}$ with a time of 3 s per step.

Results and Discussion

On the one hand, according to the analysis carried out by the soil texture testing by the hydrometer method (Table 2), we obtained as follows: all of three soil samples extracted at point 01 have a high percentage of sand; specifically, 84.68%, 86.68% and 82.68% sand at a depth of 0, 25 and 50 cm, respectively. Thereupon, all the three samples 01 are classified as sandy loam soil. Likewise, all of three soil samples extracted at point 02 also

have a high percentage of sand, namely, 93.68%, 90.68% and 92.68% at a depth of 0, 25, and 50 cm, respectively. Thus, all the three samples 02 are classified as sandy soil. Furthermore, all the three soil samples extracted at point 03 have a high percentage of sand; specifically, 45.76%, 78.68%, and 76.68% at a depth of 0, 25, and 50 cm. Thereupon, all the three samples 03 are classified as sandy loam soil.

On the other hand, according to the analyses carried out by X-ray diffraction in contaminated and uncontaminated samples: at a depth of 0 cm, zinc sulfide was found as a contaminant, followed by a small percentage of the vermiculite contaminant; at a depth of 25 cm, goethite was found to be a contaminant in a high percentage, followed by zinc sulfide; and at a depth of 50 cm, goethite was found as a contaminant in a high percentage, followed by zinc sulfide. Figure 2 shows the minerals phases found by X-ray diffraction for samples of contaminated soils having a depth of 0, 25 and 50 cm, respectively. In this figure, for the mineral names, we have used the terminology according to Whitney & Evans (2010). Therein, we realize the mineralogical phases exhibit characteristic peaks of ZnS oxihydroxide ($2\theta = 11.57^\circ$), vermiculite ($2\theta = 5.75^\circ$), quartz well defined and superimposed with illite and montmorillonite ($2\theta = 26.44^\circ$), and pure quartz ($2\theta = 20.79^\circ$), goethite ($2\theta = 34.92^\circ$). Illite and montmorillonite are clayey mineral and goethite is an amorphous mineral. Also, calcite appears overlapped with quartz and zinc sulfide.

In the figure 2 (a), we show the superposition of the diffractograms of the samples extracted from surface and a depth of 0.5 cm, respectively; the presence of vermiculite is high; the presence of ZnS Oxihydroxide ($2\theta = 11.57^\circ$) is very high. The intensity of ZnS Oxihydroxide at the surface is greater than that at 25 cm depth and the intensity at 25 cm depth is greater than that at 50 cm depth. The Cuajone mine exploits Zn. So, the particles having micrometric dimensions can be transported by the air as well as other weathering factors over long distances. These particles were oxidized by air and arrive at the Ite Bay. The natural concentrations of Zn in air, water and soils increase due to human activities how mining between other. This metal may form hydroxides or carbonates, in condition many contaminated and when it is present in very high concentrations, Zinc can precipitate easy as ZnS and co-precipitate with oxides of Fe or Mn (Evanko & Dzombak, 1997). In Figures 2b and 2c, we show the sample at a depth of 0.25 cm and 0.50 cm, respectively. Therein, we observe the picks of illite overlapped with montmorillonite in $2\theta = 8.82^\circ$, which maintain their absolute intensity comparable to those from the surface.

Table 2. Determination of the texture class by the hydrometer method

| | Point 1 (depth) | | | Point 2 (depth) | | | Point 3 (depth) | | |
|--------------------------|-----------------|------------|------------|-----------------|------------|------------|-----------------|------------|------------|
| | 0 cm | 25 cm | 50 cm | 0 cm | 25 cm | 50 cm | 0 cm | 25 cm | 50 cm |
| m (g) | 50.00 | 50.00 | 50.00 | 50.00 | 50.00 | 50.00 | 50.00 | 50.00 | 50.00 |
| T _{40s} (°C) | 26 | 26 | 26 | 26 | 26 | 26 | 24.5 | 26 | 26 |
| FC _{40s} (g/L) | 2.16 | 2.16 | 2.16 | 2.16 | 2.16 | 2.16 | 1.62 | 2.16 | 2.16 |
| L _{40s} (g/L) | 5 | 4 | 6 | 0.5 | 2 | 1 | 25 | 8 | 9 |
| L _{40s-d} (g/L) | -0.5 | -0.5 | -0.5 | -0.5 | -0.5 | -0.5 | -0.5 | -0.5 | -0.5 |
| LC _{40s} (g/L) | 7.66 | 6.66 | 8.66 | 3.16 | 4.66 | 3.66 | 27.12 | 10.66 | 11.66 |
| T _{2h} (°C) | 26.5 | 26 | 26 | 26 | 26 | 26 | 26 | 26 | 26 |
| FC _{2h} (g/L) | 2.34 | 2.16 | 2.16 | 2.16 | 2.16 | 2.16 | 2.16 | 2.16 | 2.16 |
| L _{2h} (g/L) | -0.5 | 0.5 | 1 | -0.5 | 0 | -0.5 | 5 | 1.5 | 2 |
| L _{2h-d} (g/L) | -0.5 | -0.5 | -0.5 | -0.5 | -0.5 | -0.5 | -0.5 | -0.5 | -0.5 |
| LC _{2h} (g/L) | 2.34 | 3.16 | 3.66 | 2.16 | 2.66 | 2.16 | 7.66 | 4.16 | 4.66 |
| % sand | 84.68 | 86.68 | 82.68 | 93.68 | 90.68 | 92.68 | 45.76 | 78.68 | 76.68 |
| % silt | 10.64 | 7.00 | 10.00 | 2.00 | 4.00 | 3.00 | 38.92 | 13.00 | 14.00 |
| % clay | -- | --- | -- | -- | -- | -- | 15.32 | 8.32 | 9.32 |
| | Sandy loam | Sandy loam | Sandy loam | Sandy loam | Sandy loam | Sandy loam | Sandy loam | Sandy loam | Sandy loam |

Conclusions

The results of the texture testing indicate that the samples are from sandy loam, sandy and sandy loam soils, for samples 01, 02 and, 03, respectively. This is natural for an area near the seashore. From the results obtained by X-ray diffraction, we have found that zinc sulfide is a contaminant of the soils; this sulfide naturally is part of the minerals goslarite (heptahydrate) and bianchite (hexahydrate). Another less contaminant found was goethite, which is the mineral form of iron oxyhydroxide (III). In a small percentage, we found as contaminant vermiculite, which is a mineral formed by silicates of iron or magnesium.

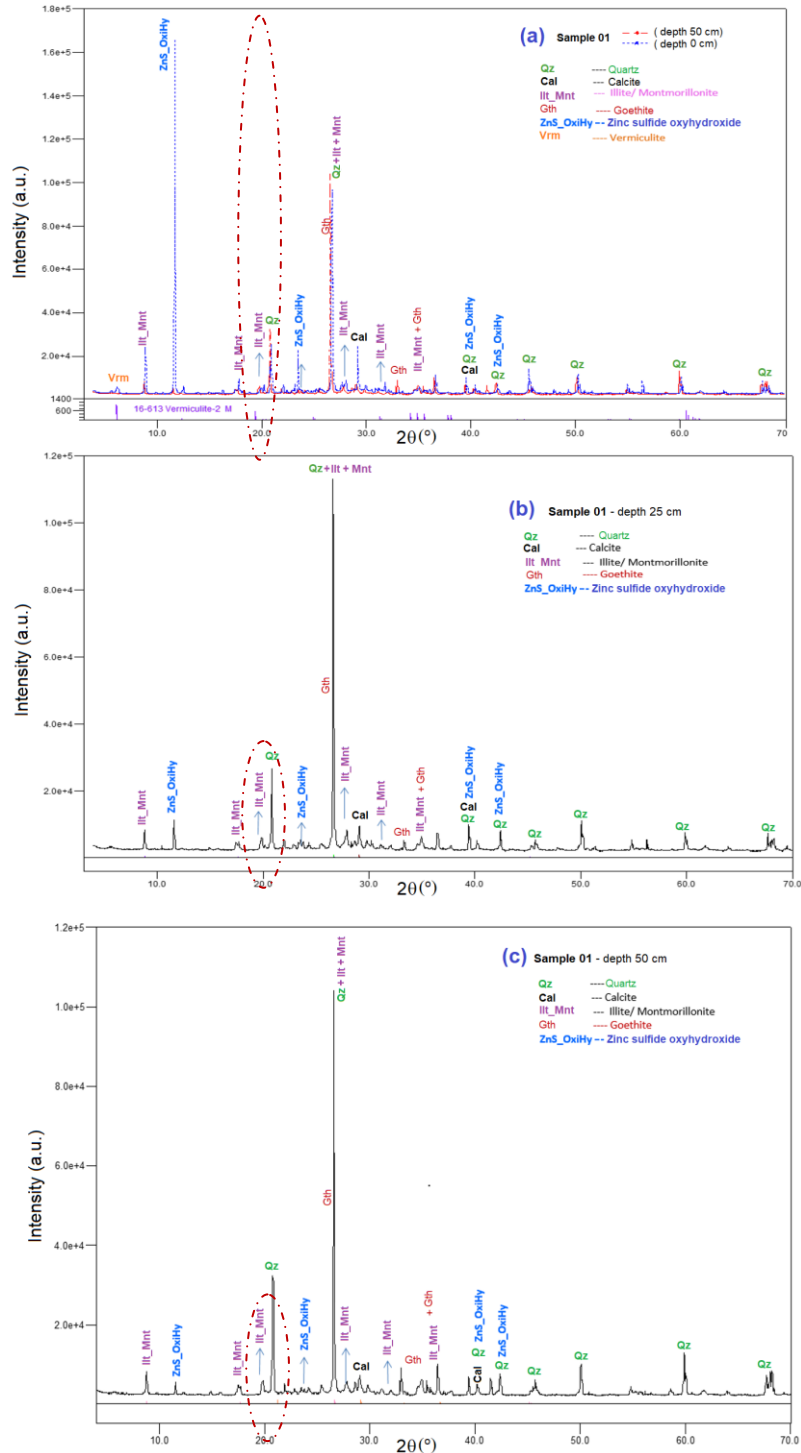


Figure 2. X-ray diffraction for samples 01 having contaminated soil and a depth of (a) 0 and 50 cm, (b) 25 cm, and (c) 50 cm, respectively.

Recommendations

We recommended to carry out an additional study to extract samples at a greater depth since the tailings have been dumped in this area for more than 30 years, so greater contamination should be found. We also recommended to carry out research in order to apply a method of removing contaminants to recover the contaminated soils. These additional studies will allow a complete analysis of the environmental impact in the Peruvian Ite Bay.

Scientific Ethics Declaration

The authors declare that the scientific ethical and legal responsibility of this article published in EPSTEM journal belongs to the authors.

Acknowledgments

This article was presented as a poster presentation at the International Conference on Basic Sciences, Engineering and Technology (www.icbaset.net) held in Istanbul/Turkey on August 25-28, 2022. We thank the staff of X-ray Diffraction Laboratory, Archaeometry Laboratory, and Soil Analysis Laboratory of the National University of San Marcos for providing the laboratories to carry out the measurements.

References

- Crompton, T. R. (2019). *Determination of toxic organic chemicals in natural waters, sediments and soils — Determination and Analysis*, Academic Press (Elsevier).
- Evanko, C.R., & Dzombak, D.A. (1997). Remediation of metals-contaminated soils and groundwater. Ground-Water Remediation Technologies Analysis Center (GWRTAC) “E” Series Report. 53 pp.
- Ibárcena Fernández, L. W. (2011). *Estudio de la contaminación por metales ecotóxicos en sedimentos en la bahía de Ite, Tacna (Study of contamination by ecotoxic metals in sediments in the Ite Bay, Tacna)*. *Revista de Ciencia y Desarrollo (Universidad Nacional Jorge Basadre Grohmann de Tacna)*, 13, 28-35.
- James, R. W. (1962). *The Optical Principles of the Diffraction of X-Rays*. London: George Bell & Sons Ltd.
- Santos Jallath, J. E. (2007). *Caracterización de suelos contaminados con hidrocarburos en una empresa minera y desarrollo de un método biológico para su remediación (Characterization of soils contaminated with hydrocarbons in a mining company and development of a biological method for their remediation)*. (Master's dissertation). Universidad Nacional Autónoma de México, México. Retrieved from <http://132.248.9.195/pd2007/0614897/Index.html>
- Whitney, D. L. & Evans, B. W. (2010). Abbreviations for names of rock-forming minerals. *American Mineralogist*, Vol. 95, 185-187. DOI: [10.2138/am.2010.3371](https://doi.org/10.2138/am.2010.3371)

Author Information

María Luisa Cerón Loayza

Laboratorio de Análisis de Suelos, Facultad de Ciencias Físicas, Universidad Nacional Mayor de San Marcos.

Av. Germán Amézaga 375, Cercado de Lima, Perú.

Corresponding author: mceronl@unmsm.edu.pe

Marlon Gastón Farfán-Córdova

Universidad César Vallejo.

Instituto de Investigación en Ciencia y Tecnología.

Av. Víctor Larco 1770, Trujillo, La libertad, Perú.

Jenny Aleida Montoya Burga

¹Universidad César Vallejo.

Av. Víctor Larco 1770, Trujillo, La libertad, Perú.

²Laboratorio de Análisis de Suelos, Facultad de Ciencias Físicas, Universidad Nacional Mayor de San Marcos.

Av. Germán Amézaga 375, Cercado de Lima, Perú.

Fanny Mori Escobar

Laboratorio de Análisis de Suelos, Facultad de Ciencias Físicas, Universidad Nacional Mayor de San Marcos.

Av. Germán Amézaga 375, Cercado de Lima, Perú.

Felipe Américo Reyes Navarro

Laboratorio de Análisis de Suelos, Facultad de Ciencias Físicas, Universidad Nacional Mayor de San Marcos.

Av. Germán Amézaga 375, Cercado de Lima, Perú.

Content Management of Time Bank Credit Website for the Elderly in Malaysia

Tan Swee Leng OLIVIA
Multimedia University

Ooi Shih YIN
Multimedia University

Rossanne Gale VERGARA
Multimedia University

Shereen KHAN
Multimedia University

Nasreen KHAN
Multimedia University

Abstract: Time banking is a value-based system for reciprocal service exchange that focuses on public contributions to address local community needs. The hours spent offering or receiving service are the unit of trade and account. In Malaysia, Time Bank content management is being used for the first time. Volunteer hours are "deposited" into a personal account for people who take care of the elderly who require assistance. When a volunteer reaches retirement age and needs assistance, he can use the time bank to have a volunteer allocated to him. The study proposed that, in addition to formal work, older people may contribute to society by volunteering as a method to stay active. The Time Bank website for the Activity Centre for the Elderly in Malaysia (PAWE) was created as a content management system for the PAWE committee, members, and users. The members may use this content management system to update their profiles and manage their time credits. With the addition of new business models, government agencies, and vendors, the website will continue evolve. Multimedia University, PAWE Putrajaya, and the Department of Social Welfare Malaysia collaborated on the website, which may be found at <https://pawetimebank.com>. The pilot project was initiated with the older persons community in Putrajaya, Malaysia, with the first activity as assisting PAWE Putrajaya members in registering for COVID-19 vaccine. As a result, PAWE Centre Putrajaya now has 237 members with 95 percent of the members vaccinated through this time-bank scheme. In the content management system, the effort put in to help the elderly get vaccinated has been noted.

Keywords: Timebank System, Elderly and Technology, Management Information Systems

Introduction

In society and associated commercial activities, knowledge management has piqued people's curiosity. In the case for the members of the Activity Centre for the Elderly in Putrajaya, Malaysia, they needed to better manage massive data and knowledge generated during different life cycle stages of recording time bank credit earned. Thus, the researchers developed an effective way to acquire, store, process, and share knowledge from and among different stakeholders to make appropriate decisions and continuously improve time bank operations. When dealing with rising amounts of data and expertise, such as Excel Sheet Planning, According to Naughton-Doe (2011), computerized Maintenance Management, and Product Life-cycle Management Systems is challenging to inter-operate and integrate with each other, which was what the researchers faced when trying to develop a solution for the PAWE members.

Therefore, the researchers developed a content management system (CMS). CMS is a tool for managing vast volumes of web-based data without having to manually code all data into each page in HTML (Seadle, 2006). Due to the sheer volume of public online presence has reached the point where upkeep is an issue, content management systems are critical to society and industry. Older members of the Activity Centre for the Elderly in Putrajaya, Malaysia, have continued to gain personal interest in online activities, especially for those who have explored new occupations or just retired. This made developing a CMS in the form of a website the sensible solution for PAWE Putrajaya.

- This is an Open Access article distributed under the terms of the Creative Commons Attribution-Noncommercial 4.0 Unported License, permitting all non-commercial use, distribution, and reproduction in any medium, provided the original work is properly cited.

- Selection and peer-review under responsibility of the Organizing Committee of the Conference

The Activity Centre for the Elderly in Malaysia (PAWE) used the Time Bank website as a content management system for its committee, members, and users. Members may update their profiles and manage their time credits using this content management system. The website will continually evolve as new business models, government organisations, and vendors are added. The website, which can be located at <https://pawetimebank.com/>, was created in collaboration between Multimedia University, PAWE Putrajaya, and the Department of Social Welfare Malaysia.

Time Bank System at Activity Centre for the Elderly, Malaysia

This research shows the importance of creating a CSM system to maintain data in the Time Bank for PAWE (*Pusat Aktiviti Warga Emas*, Activity Centre for the Elderly) developed website. The website content management typically enables the elderly to manage structured information sources such as excel sheet, document management systems, time credit management process and according to predefined business rules, processes and workflows.

When a supplementary information management system, such as e-mail archiving, is integrated with content management, users of the CMS may perform in-place retention management of unstructured data, such as email kept in traditional mode or in the archive. The goal of this time bank content management system is to allow older users to gather, capture, deliver, and develop information and knowledge in their chosen manner, all of which may be controlled through the time-bank chain. Laravel application is the Open Source Content Management System used for the time bank maintenance and service applications to manage information and knowledge during the operations' time credit process.

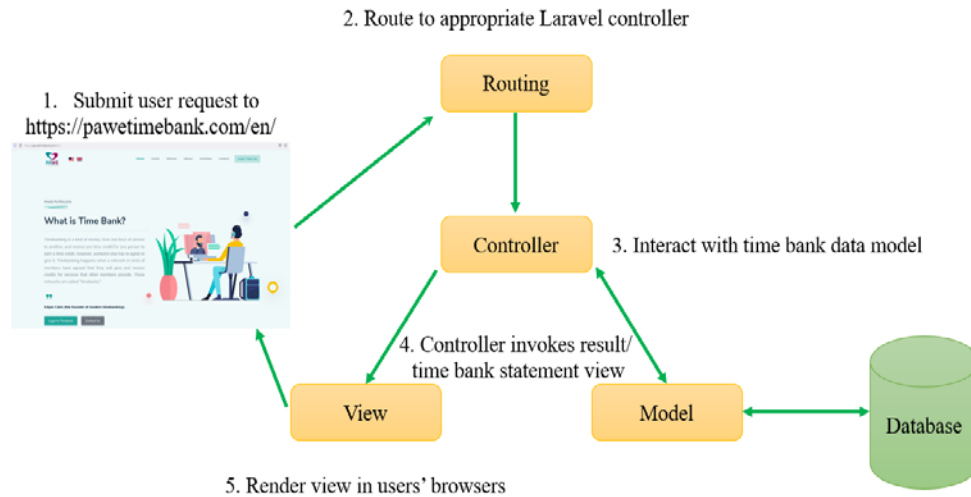


Figure 1. Work flow of the Open Source CMS for Time Bank system

Note. This figure shows the system architecture of the time-bank content management system, from submitting user request to render view in users' browsers.

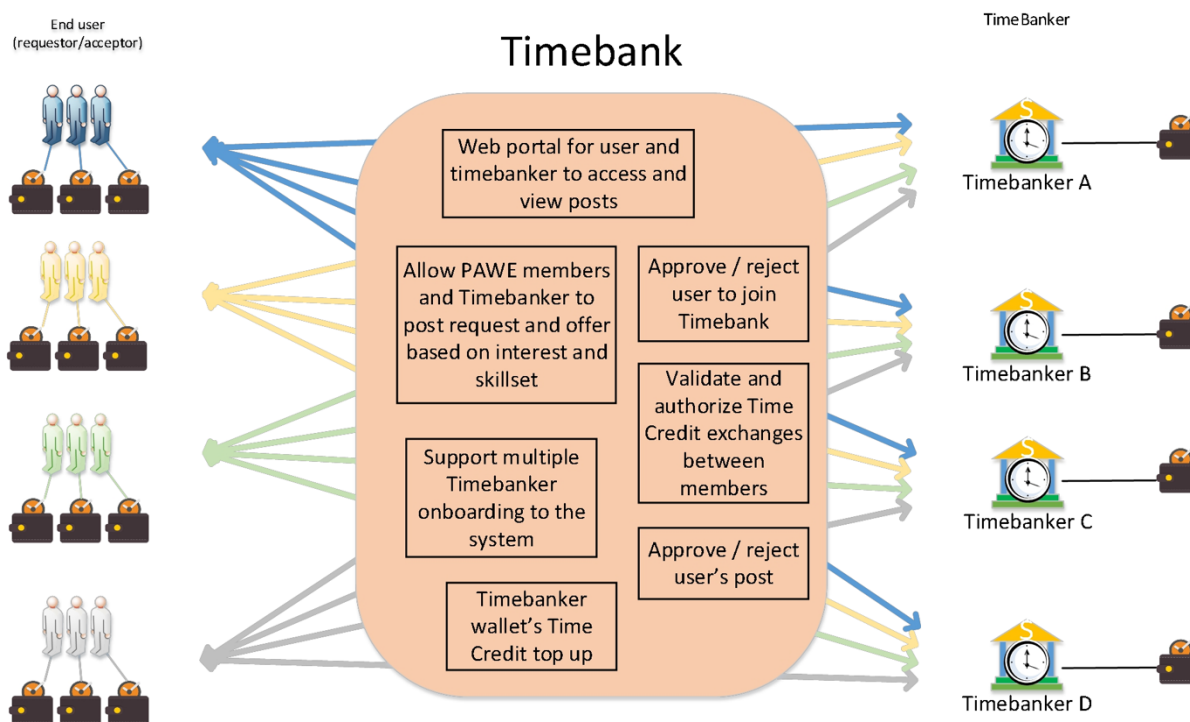


Figure 2 .High -Level diagram for Time Bank system

Note. Figure 2 is a high level diagram for Time Bank system (The workflow control by backend CMS module).

The content management system through the website allows the elderly to record the time credit collected for future redemption. The current endorsement of the credit hours collected is from the chairman of the Activity Centre for the Elderly in Malaysia.

Website : Pawetimebank.com

Timebank is a portal that brings organization / company and senior citizens / retirees together by offering time filler matters based on interest or skill set and using time credit as in exchange for service to build for a healthy community. The portal runs on social-based web application conceptually that allows everyone to join as a PAWE member and uses time to trade for services.

The system consists of 3 types of users, namely:

(a) End user

This can be any user who is registered and joined as a PAWE group member to post their skill and request.

(b) Sub admin (Time-banker)

This type of user is normally under the third party (labour banks) who are allowed to post for a skill set request or to post available job offers to everyone in the PAWE. They manage their own time bank wallet as a middleman to approve for the time credit transactions. For example, Time banker A offering a job for 2 hours gardening and member B takes the offer and completes the job within 2 hours. Time banker will approve and send the credits to member B based on their own timebank wallet balance.

(c) Admin

This user has full access and control to the system.

This will be similar to social-media group page where there will be a dedicated page managed by a sub-admin user as below:

- Setting up community (name, location, privacy setting, community status).

- Approve / Reject / Suspend user from joining the community
- Managing user post request / skill set offer (approve / reject post)
- Posting offer, request on its own
- Setting up own user profile.
- Managing own Timebank wallet to top-up the time credit when it is running low
- Approve / Reject to send credit hour to members upon job done.

The system supports multiple Timebank group creations and there is no limitation on geographic location or organization. End user can join multiple Timebank groups as long as getting the credential's approval from sub_admin who manage the Timebank group.

All users (end user, sub-admin, admin) are allowed to post their skill to offer. If the user joined more than 1 Timebank community, he can choose which Timebank to post. All users are also allowed to post their request to look for the skills offered by the members within the Timebank. User can specify maximum acceptance count and upon maximum, the post will close.

Timebank application's trading using time credit allocations whereby all users will have their own Time Credit Wallet to earn their credit. Only sub-admin can top up Time Credit to its wallet to maintain sufficient Time Credit circulating within the Timebank ecosystem. There are 3 types of time credit allocations for Timebank management:

1. Member that offered their help to others will be given time credit from timebank, i.e.: 1 hour = 1 credit.
2. Member that request for help, their time credit will be deducted from timebank.
3. Member with 0 credit are only allowed once usage on credit terms with a maximum limit time allocation.

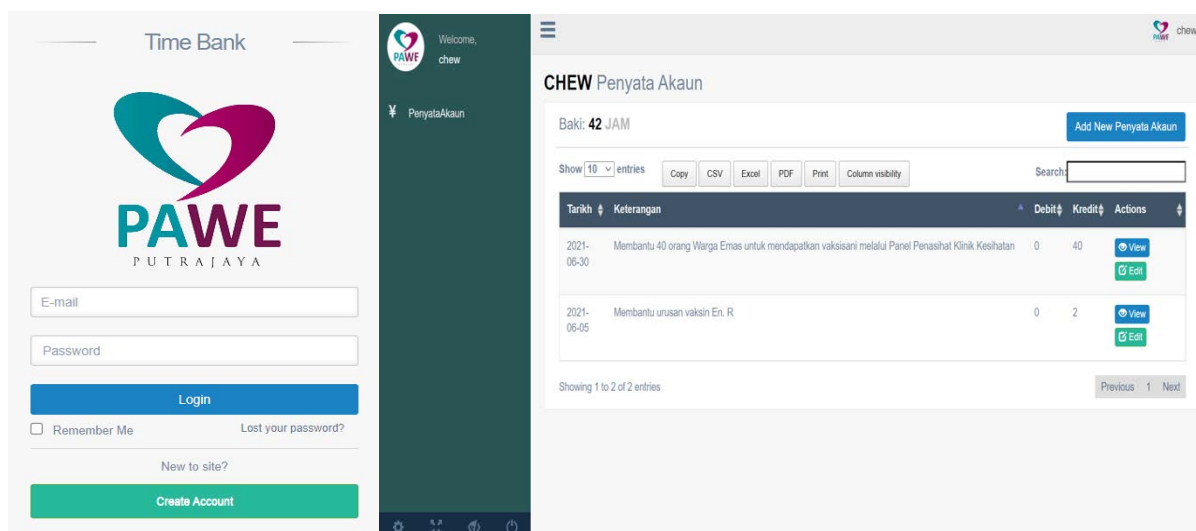


Figure 3. Time bank sign in page and account statement

Note. Figure 3 shows the sign in and create account page on the left. On the right is the member time bank account statement where the user can view/edit or submit activity and time credit earned for the PAWE committee to approve.

Results and Discussion

This pilot project greatly improved the older persons community in Putrajaya, Malaysia. The first activity undertaken by the older people at PAWE, Putrajaya was to assist each member in registering for the COVID-19 vaccine. PAWE Centre Putrajaya has 237 members, and as a result of the timebank scheme, 95 percent have been vaccinated. In the content management system, the effort put in to help the elderly get vaccinated has been noted.

The project has been expanded to elderly helping the recent flash flood victims in Malaysia and the time credit for the volunteering process has been recorded through the pawetimebank website. Currently there are 116 members registered under the pawetimebank.com system since its soft launch on Dec 2021

Conclusion

Time bank content management system is the first system to be used among the elderly in Malaysia and this system helps to promote volunteerism among the people and elderly in Malaysia. The time bank movement has given a fresh lease on life to a wide range of activities that yield intrinsic benefits. It provides a framework for creating wealth that isn't based on money and for recognising important work that isn't valued by money-based marketplaces. Despite the fact that time banking has grown internationally, the majority of time banks are local or regional organisations that operate as self-contained membership organisations. They occur in many kinds and sizes, from tiny, unstructured gatherings to enormous, formalised organisations. Some time banks are only available for a limited period of time. Others have been in existence for decades. People have also utilised time banking to achieve a range of societal objectives.

Recommendations

The time bank content management system via website will be used eventually by the other 143 activity centres for the elderly in Malaysia in due course. In general, time banks assist people in drawing on the resources of their society to address both old and new difficulties. Three advantages of the time bank approach should be highlighted. To begin with, time banking allows each individual to define himself or herself as a worker who contributes in a measurable way to the advancement of the public good or the solution of a pressing societal issue. Second, time banking allows a community to assess its social capacity and mobilise resources in order to meet unmet social demands. Third, time banking provides a framework for involving service beneficiaries as active partners in obtaining objectives in large-scale social welfare systems. Beneficiaries may obtain new skills, make new relationships, and learn new things instead of being passive recipients of those services. Hence this research encourages and recommends the society through the world to own its time- bank system and eventually improve on the social welfare system of their respective countries.

Scientific Ethics Declaration

The authors declare that the scientific ethical and legal responsibility of this article published in EPSTEM journal belongs to the authors.

Acknowledgements or Notes

This article was presented as an oral presentation at the International Conference on Basic Sciences, Engineering and Technology (www.icbaset.net) conference held in Istanbul/Turkey on August 25-28, 2022.

This research is funded by the Malaysian Ministry of Education (MOE) through the Fundamental Research Grant Scheme (FRGS) FRGS/1/2019/SSI10/MMU/02/1. The authors alone are responsible for the views expressed in this article, which does not necessarily represent the views, decisions, or policies of MOE or the institutions with which the authors are affiliated. The funder had no role in study design, data collection and analysis, or preparation of the manuscript.

References

- Naughton-Doe, R. (2011). Time banking in social housing: A toolkit for co-production in public services. *International Journal of Community Currency Research*, 15D(1), 73-76. <https://ijccr.files.wordpress.com/2012/05/ijccr-2011-special-issue-14-naughton-doe.pdf>
- Seadle, M. (2006), Content management systems. *Library Hi Tech*, 24(1), 5-7. <https://doi.org/10.1108/07378830610652068>

Author Information

Tan Swee Leng Olivia

Multimedia University
Persiaran Multimedia , Cyberjaya 63100, Selangor, Malaysia
oliviatan@mmu.edu.my

Shih Yin Ooi

Multimedia University
Jalan Ayer Keroh Lama, 75450 Bukit Beruang, Melaka,
Malaysia

Rossanne Gale Vergara

Multimedia University
Persiaran Multimedia , Cyberjaya 63100, Selangor, Malaysia

Shereen Khan

Multimedia University
Persiaran Multimedia , Cyberjaya 63100, Selangor, Malaysia

Nasreen Khan

Multimedia University
Persiaran Multimedia , Cyberjaya 63100, Selangor, Malaysia

Off-center Supported Beam with Additional Elastic Supports located at the Height of the Beam and Asymmetrical Cross Section

Albena DOICHEVA

University of Architecture, Civil Engineering and Geodesy (UACEG) - Sofia

Abstract: The study of structural elements is most often carried out under the premise of their center support and center connection at the transmission of forces. In practice, however, building structures abound with examples of off-center support (crane beams, bridge girders) and off-center connection (frame structures with different beam heights). This type of support can be attributed also to the connection of beams from frame structures subjected to high loads and suffered large deformations, leading to local destruction of a part of the supporting edge. Accurate modeling of the response of beam both from the point of view of the stress and strain state, as well as in the analysis of beam-column cross section in the frames, leads to interesting conclusions worthy of attention. A prismatic Bernoulli-Euler beam with asymmetrical cross-section of linearly elastic material is considered in the paper. The supports of the beams are symmetrical in regard to the middle section. The beam is located on two vertical off-center supports. In addition, there are two horizontal linear springs, which change their position along the height of the beam. The stiffness of spring is a function of the beam stiffness of tension (compression). Two pairs of additional horizontal supports with linear springs and variable stiffness are introduced. The springs are located on both sides of the longitudinal axis of the beam, asymmetrically. A concentrated vertical force in the middle section loads the beam. The beam is statically indeterminate and it is in the conditions of special bending. The formulas for the horizontal support reactions are deduced. Comparisons of their values, which are calculated as a function of the different positions of the supports in regard to the longitudinal axis and varying springs stiffness are made. The derived formulas can be used to study the shear force in the beam-column connection.

Keywords: Beam, Off-center supports, Additional horizontal elastic supports, Asymmetrical beam, Shear force in the beam-column joint

Introduction

The centric connection of the structural elements in the transmission of forces, as well as the centric arrangement of the support devices, is the most often accepted premise in the study of the structural elements. In fact, construction practice abounds with examples about off-center supports (crane beams, bridge beams) and off-center connection (frame structures with different beam heights). For this type of off-center supports can also include the connection of beams from frame structures, subjected to high loads and underwent large deformations, causing local destruction on a part of the supporting edge. Accurate modeling of the response of a beam-type bodies, both from the point of view of the stressed and deformed state, as well as in the analysis of the beam to column joints adjacent to the beams, leads to interesting conclusions worthy of attention.

In the monograph (*Park & Paulay, 1974*), a detailed analysis of a plane frame structures and their component elements is made. Studies of the stressed and strained state are based on specimen tests and have led to a large number of empirical formulas.

The main element in frame constructions is the beam-column joint. Compromise of this connection often leads to results in irreversible damage to the entire building structure. The distribution of forces and the response of beam-column joints has occupied scientists for the past few decades (*Park & Keong, 1979; Paulay, 1989; Park 2002; Lowes & Altoontash, 2003; Altoontash, 2004; Celik & Ellingwood, 2008*). While the moment resistance frame response can now to be considered as known, the effect of shear forces in the beam-column joint continues to concern researchers in this field (*Shiohara, 2001; Sharma et al., 2009; Shafaei et al., 2014*). Their research in recent years is reduced to search for procedures which will allow more accurate determination of the shear force in the beam-column joint. Analyzes of the experimental results of internal and external beam-column joints and the built models often take into account in the smallest detail like the cracks that occur in the concrete front and around the joint, the adhesion and slip of the reinforcement, as well as a number of other factors such as the strength of the materials and the working conditions. These detailed analyses, however, do not take into account the emerging off-centricity in the beam elements and columns occurring as a result of the

- This is an Open Access article distributed under the terms of the Creative Commons Attribution-NonCommercial 4.0 Unported License, permitting all non-commercial use, distribution, and reproduction in any medium, provided the original work is properly cited.

- Selection and peer-review under responsibility of the Organizing Committee of the Conference

local destructions, nor do they take into account the linear deformations causing the appearance of axial forces in the beams and the subsequent redistribution of the forces in them.

The purpose of the present work is to reveal the influence of eccentricity on the stressed and deformed state on the beam. Moreover, the serious size of the axial forces, which in most cases exceed the magnitude of the vertical transverse load, as well as the sensitivity of the normal forces from considering the deformations along the axis of the beam is demonstrated.

Method

Problem

In the present work, a statically indeterminate, prismatic and asymmetric beam under the conditions of special bending, elastic material and Bernoulli-Euler hypothesis is considered. It is located on two off-center supports that change their position along the height of the beam and they are equipped with horizontal linear springs (H_1) with linearly changing spring constants set as functions of the beam's own stiffness in centric tension (compressure). Two pairs of additional horizontal supports with linear springs and variable stiffness are introduced, which are located on both sides of the beam axis (H_2, H_3). The beam is loaded with a concentrated transverse load at the mid-section. In other publications with participation of the author, the results about off-center supported beams with supports located only below (or above) the axis of the beam and the appearance of significant axial forces were demonstrated (Doicheva 2011; Mladenov & Doicheva, 2009). Approximate solutions by first-order theory have indicated that the magnitude of the normal force from a vertical load depends strongly on the contribution to the expression for the potential energy of the linear deformation caused by the normal force (Doicheva & Mladenov, 2009). In this situation, the question arises about the magnitudes and changes of the horizontal reactions and the normal force under the new support conditions, when varying the spring constants and the position of the supports, as well as about the nature of the stressed state of the beam.

Math model

In this article we considered the beam from Figure 1. The special bending due to the action of the force $P [kN]$ in the mid-section, will cause stretching of the lower threads of the beam, and contracting the threads near its upper edge. The supports of the beam hindered this tendency to deform. This leads to the occurrence of the compressive support reactions ($H_1 [kN]$ and $H_2 [kN]$) in the area below the zero line of the beam, and tensile support reactions above it ($H_3 [kN]$). If we consider a moment of the load, when large deformations have been realized, and a part of the vertical edges of the beam has been destroyed, then its support will take place in the undestroyed zone with length $2b [cm]$. The reaction $H_1 [kN]$, which is symmetrically located with respect to the intact lateral edge, moves along the height of the beam as the crack length increases. For convenience, it has transferred $H_1 [kN]$ to the support along the lower edge (support one), after applying Poinso's theorem concerning the transfer of forces in parallel to their directrix. This necessitated the introduction of compensating moments $H_1 b [kN.cm]$. In supports two and three support reactions $H_2 [kN]$ and $H_3 [kN]$ occurs. Support two is located on the underside of the beam axis at a distance $a [cm]$ from it, which means it is offset from the bottom edge of the beam by a distance of $c [cm]$. Respectively, support three is on the upper side of the axis of the beam, at a distance $d [cm]$ from it and at a distance $e [cm]$ from the upper edge of the beam. The beam has length $L [cm]$ and height $h [cm]$. The beam has a modulus of elasticity $E [kN / cm^2]$ and characteristics of the cross-section - Area $A [cm^2]$ and moment of inertia $I [cm^4]$.

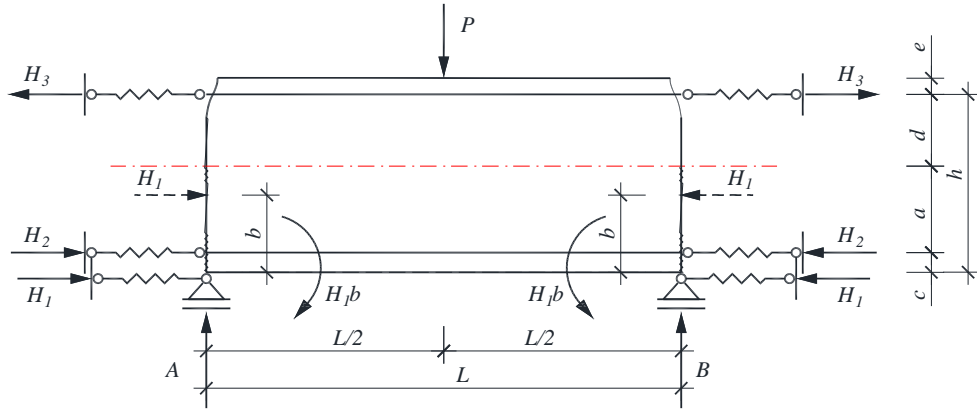


Figure 1. Off-center supported beam with additional elastic supports located at the height of the beam

Support reactions

Due to the symmetry of the beam, with respect to the mid-section, the horizontal forces on the left side are equal to those on the right side. The beam is three times statically indeterminate.

The solution is based on Menabria's theorem about statically indeterminate systems in first-order theory.

The potential energy of deformation in special bending, combined with tension (compression) and with the effect of linear springs taken into account, will be:

$$\Pi = \frac{1}{2} \int_0^{L/2} \frac{M^2(x)}{EI} dx + \frac{1}{2} \int_0^{L/2} \frac{N^2(x)}{EA} dx + \frac{H_1^2}{k_1} + \frac{H_2^2}{k_2} + \frac{H_3^2}{k_3} \quad (1)$$

It is a well-known fact that, according to Menabria's theorem, the desired hyperstatic unknown is determined by the minimum potential energy condition with respect to it or will be:

$$\frac{\partial \Pi}{\partial H_1} = 0; \quad \frac{\partial \Pi}{\partial H_2} = 0; \quad \frac{\partial \Pi}{\partial H_3} = 0. \quad (2)$$

The vertical support reactions are:

$$A = \frac{P}{2} \quad \text{and} \quad B = \frac{P}{2}. \quad (3)$$

The bending moments for both part of the beam will be:

$$M_1 = \frac{P}{2} x - H_3 d - H_2 a - H_1 (c + a - b); \quad (4)$$

$$M_2 = \frac{P}{2} \left(\frac{L}{2} - x \right) - H_3 d - H_2 a - H_1 (c + a - b); \quad (5)$$

and the normal force respectively:

$$N = -H_1 - H_2 + H_3. \quad (6)$$

Substitute them in (1).

$$\Pi = \frac{1}{2} \int_0^{L/2} \frac{M_1^2(x)}{EI} dx + \frac{1}{2} \int_0^{L/2} \frac{M_2^2(x)}{EI} dx + \frac{1}{2} \int_0^{L/2} \frac{N^2(x)}{EA} dx + \frac{H_1^2}{k_1} + \frac{H_2^2}{k_2} + \frac{H_3^2}{k_3}; \quad (7)$$

$$\Pi = \frac{1}{2EI} \left(\int_0^{L/2} M_1^2(x) dx + \int_0^{L/2} M_2^2(x) dx + i^2 \int_0^L N^2(x) dx \right) + \frac{H_1^2}{k_1} + \frac{H_2^2}{k_2} + \frac{H_3^2}{k_3}. \quad (8)$$

It follows from here

$$\begin{aligned} 2EI \frac{\partial \Pi}{\partial H_1} &= 2 \int_0^{L/2} \left(\frac{P}{2} x - H_3 d - H_2 a - H_1 (c + a - b) \right) (- (c + a - b)) dx + \\ &+ 2 \int_0^{L/2} \left(\frac{P}{2} \left(\frac{L}{2} - x \right) - H_3 d - H_2 a - H_1 (c + a - b) \right) (- (c + a - b)) dx + \\ &+ 2 (H_3 - H_1 - H_2) (-1) Li^2 + 4 \frac{EI}{k_1} H_1; \end{aligned} \quad (9)$$

$$\begin{aligned} 2EI \frac{\partial \Pi}{\partial H_2} &= 2 \int_0^{L/2} \left(\frac{P}{2} x - H_3 d - H_2 a - H_1 (c + a - b) \right) (-a) dx + \\ &+ 2 \int_0^{L/2} \left(\frac{P}{2} \left(\frac{L}{2} - x \right) - H_3 d - H_2 a - H_1 (c + a - b) \right) (-a) dx + \\ &+ 2 (H_3 - H_1 - H_2) (-1) Li^2 + 4 \frac{EI}{k_2} H_2; \end{aligned} \quad (10)$$

$$\begin{aligned} 2EI \frac{\partial \Pi}{\partial H_3} &= 2 \int_0^{L/2} \left(\frac{P}{2} x - H_3 d - H_2 a - H_1 (c + a - b) \right) (-d) dx + \\ &+ 2 \int_0^{L/2} \left(\frac{P}{2} \left(\frac{L}{2} - x \right) - H_3 d - H_2 a - H_1 (c + a - b) \right) (-d) dx + \\ &+ 2 (H_3 - H_1 - H_2) Li^2 + 4 \frac{EI}{k_3} H_3. \end{aligned} \quad (11)$$

After equating the left side to zero, taking into account the minimum potential energy condition, a system of three linear equations with respect to the three unknowns, is obtained. The solutions give the formulas of the horizontal support reactions below:

$$H_1 = \frac{PL^2 k_1 [2AE(a+c-b) + Lk_3(a+c-b+d) + Lk_2(c-b)]}{8 \left\{ 2EA [2EI + Lk_2 a^2 + Lk_3 d^2 + Lk_1(a+c-b)^2] + 2EIL(k_1 + k_2 + k_3) + L^2 [k_1 k_2 (c-b)^2 + k_1 k_3 (a+c-b+d)^2 + k_2 k_3 (a+d)^2] \right\}} \quad (12)$$

$$H_2 = \frac{PL^2 k_2 [2AEa + Lk_1(b-c) + Lk_3(a+d)]}{8 \left\{ 2EA [2EI + Lk_2 a^2 + Lk_3 d^2 + Lk_1(a+c-b)^2] + 2EIL(k_1 + k_2 + k_3) + L^2 [k_1 k_2 (c-b)^2 + k_1 k_3 (a+c-b+d)^2 + k_2 k_3 (a+d)^2] \right\}} \quad (13)$$

$$H_3 = \frac{PL^2 k_3 [2AEd + Lk_1(a+c-b+d) + Lk_2(a+d)]}{8 \left\{ 2EA [2EI + Lk_2 a^2 + Lk_3 d^2 + Lk_1(a+c-b)^2] + 2EIL(k_1 + k_2 + k_3) + L^2 [k_1 k_2 (c-b)^2 + k_1 k_3 (a+c-b+d)^2 + k_2 k_3 (a+d)^2] \right\}} \quad (14)$$

When a cross section is symmetric, where $a = d$, $e = c$, $k_2 = k_3$ we get the expressions obtained in (Doicheva, 2021):

$$H_1 = \frac{(-PL^2k_1)(Lk_2 + AE)(2b - h)}{(Lk_2 + AE)[32(EI + Lk_2a^2) + 4Lk_1(2b - h)^2] + 16Lk_1(EI + Lk_2a^2)} \quad (15)$$

$$H_2 = \frac{(PL^2k_2)[4a(Lk_2 + AE) + Lk_1(2a + 2b - h)]}{(Lk_2 + AE)[64(EI + Lk_2a^2) + 8Lk_1(2b - h)^2] + 32Lk_1(EI + Lk_2a^2)} \quad (16)$$

$$H_3 = \frac{(PL^2k_2)[4a(Lk_2 + AE) + Lk_1(2a - 2b + h)]}{(Lk_2 + AE)[64(EI + Lk_2a^2) + 8Lk_1(2b - h)^2] + 32Lk_1(EI + Lk_2a^2)} \quad (17)$$

If the participation of supports two and three is zeroed out, keeping only the linear springs, and off-center support at the base of the beam (support one), then the horizontal force will acquire a value:

$$H_1 = \frac{PL^2a}{8 \left[L(a^2 + i^2) + 2 \frac{EI}{k_1} \right]} \quad (18)$$

When the spring is one, only on the left or right of the beam, the force is as determined in a previous publication with the author's participation (Doicheva & Mladenov, 2009):

$$H_1 = \frac{PL^2a}{8 \left[L(a^2 + i^2) + \frac{EI}{k_1} \right]} \quad (19)$$

In (Doicheva & Mladenov, 2009), attention was paid to two points in the interpretation of the obtained result. The first result is that, while the stiffness of the spring increases, the horizontal reaction increases significantly, and with it the normal force in the beam also increases. The second moment refers to the contribution of the normal force, which in many cases is commensurate with that of the bending moment in the potential energy expression.

The major focus of the research, regards the redistribution of the forces, from the three support reactions when the supports are moved and when varying the stiffness of the springs, in the respective supports occurred. And the second problem regards that, what is the effect onto the magnitudes of the three support reactions from the contribution of the normal force in the potential energy expression.

Results and Discussion

The numerical results are calculated for beams with a trapezoidal cross-section shown in Figure 2. The short base has a size equal to the altitude $h[cm]$ of the trapezoid, and the long base has a size of $\left(2\frac{1}{5}+1\right)h$. The beam is composed of two elastic materials. The first material, with modulus of elasticity $E_1[kN/cm^2]$, forms the main section of the beam, and the second material, with modulus of elasticity $E_2[kN/cm^2]$, is the material of two threads of the beam at the level of the second and third supports. The length of the considered beam is $L = 1000\text{ cm}$. The force remain constant and unchanged for all reported numerical results. The position of the supports on the second and third support reactions is at a distance $c = 3\text{ cm}$ from the lower edge and $e = 3\text{ cm}$ from the upper edge of the beam, respectively. The position of the support, in which the support reaction H_1 occurs, vary in the interval $\left[b = y_c = \frac{19}{36}h; 0\right)$ measured from the bottom edge of the beam. The stiffness of the first spring is k_1 and it is reduced to the stiffness of centric tension (compression) of the beam E_1A_1 . The

stiffness of the second and third springs are k_2 and k_3 , and are reduced to the stiffness of the threads at the level of supports two and three E_2A_2 . The modulus of elasticity of the beam is adjusted with two accepted Young's moduli for the two materials E_1 and E_2 , in accordance with their area participation in the general area of the beam cross section.

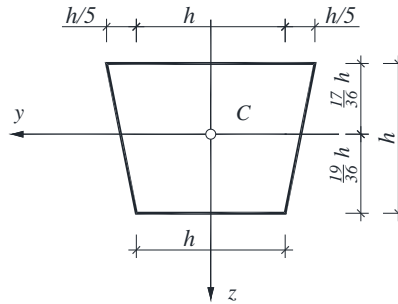


Figure 2. Cross section of the beam

The solutions were performed for different sizes of the beam cross section. The results, shown here in the article, are related for beams with dimensions $h = 75 \text{ cm}$, $h = 50 \text{ cm}$, and $h = 25 \text{ cm}$.

Figure 3 reveals the change in the parameters of the three support reactions when position of the first support changes along the height of the cross-section of the beam. The position of the first support is defined with the change in the value of variable h/b . When the first support is in the axis of the beam, then $b = 19/36h$, and the ratio $h/b = 1,9(1,89474)$, while when the first support is located on the lower edge of the beam, $b = 0$, then $h/b = \infty$.

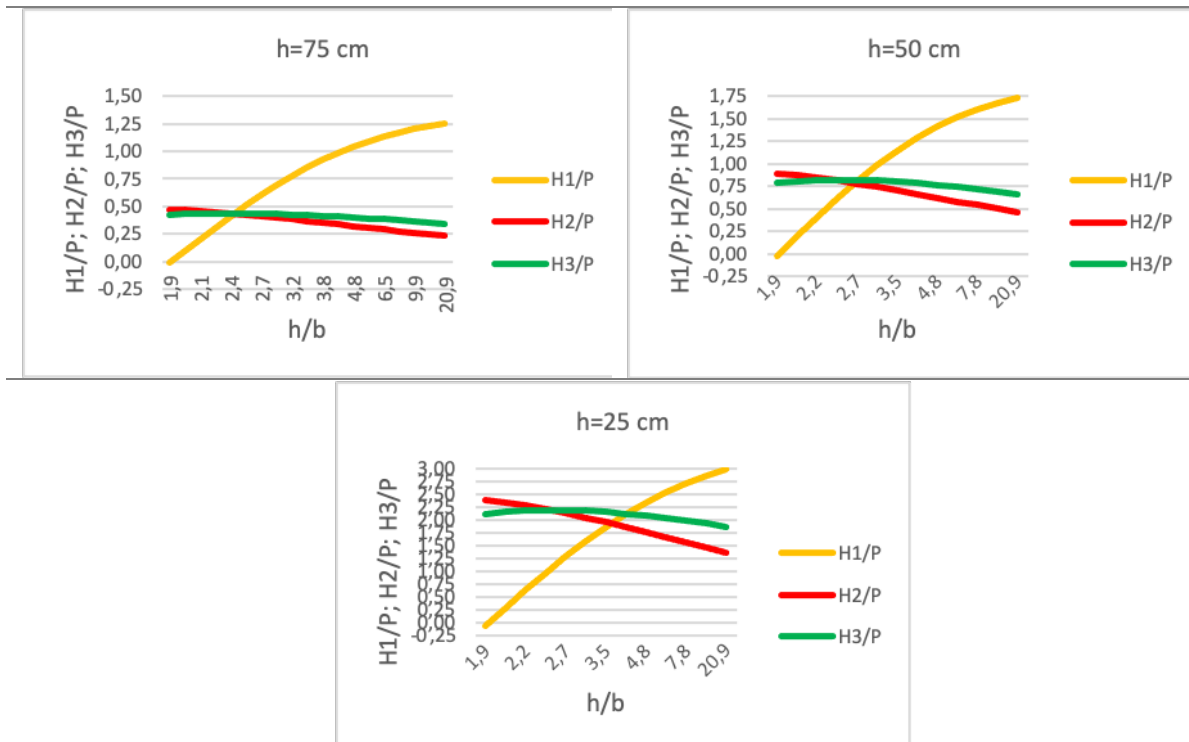


Figure 3. Changing the parameters of the three support reactions, when the first support moves

Figure 3 shows an increase in the magnitudes of the three support reactions with the beam cross-section decreases. The magnitude of the support reaction H_1 approaches to zero, when first support is located at the center of cross-section of the beam (ie $h/b = 1,9$). At the same position of the first support, the reaction H_2 is

greater than reaction H_3 , as in the case of beam $h=75\text{ cm}$ - $H_2=0,47P$ and $H_3=0,42P$, in the case of a beam $h=50\text{ cm}$ their values are $H_2=0,89P$ and $H_3=0,79P$, and in the case of beam $h=25\text{ cm}$ their values are $H_2=2,39P$ and $H_3=2,12P$.

The reaction H_1 equalizes in magnitude with the load at a first support position set as $h/b=4,3$ for a beam $h=75\text{ cm}$. For a beam $h=50\text{ cm}$, the equalization of the magnitudes of the forces comes at $h/b=3,1$, and for a beam $h=25\text{ cm}$ it is correspondingly at $h/b=2,5$.

For the three beams with the three cross-sections, support reaction H_2 decreases constantly, as first support moves along to the bottom edge of the beam, while support reaction H_3 first increases its value for $h=75\text{ cm}$ at $h/b=2,2-2,5 \rightarrow H_3=0,44P$, for $h=50\text{ cm}$ at $h/b=2,2-2,7 \rightarrow H_3=0,82P$, and for $h=25\text{ cm}$ at $h/b=2,5 \rightarrow H_3=2,2P$, respectively, and then decreases until first support reaching to the bottom edge on the beam.

The values of the three support reactions as part of the loading force P at $h/b=20,9$ for the three beams are shown in Table 1. It can be seen that H_1 increases for all beams. Reducing the size of the cross-section of the beam, leads to an increase in H_1 up to 3 times. Support reaction H_2 decreases to half of its initial value (at $h/b=1,9$), while reaction H_3 retains about 4/5 from its initial value.

Table 1. The values of the three support reactions at $h/b=20,9$

| h | H_1 | H_2 | H_3 |
|-----|---------|---------|---------|
| 75 | $1,25P$ | $0,23P$ | $0,34P$ |
| 50 | $1,74P$ | $0,46P$ | $0,66P$ |
| 25 | $2,99P$ | $1,37P$ | $1,87P$ |

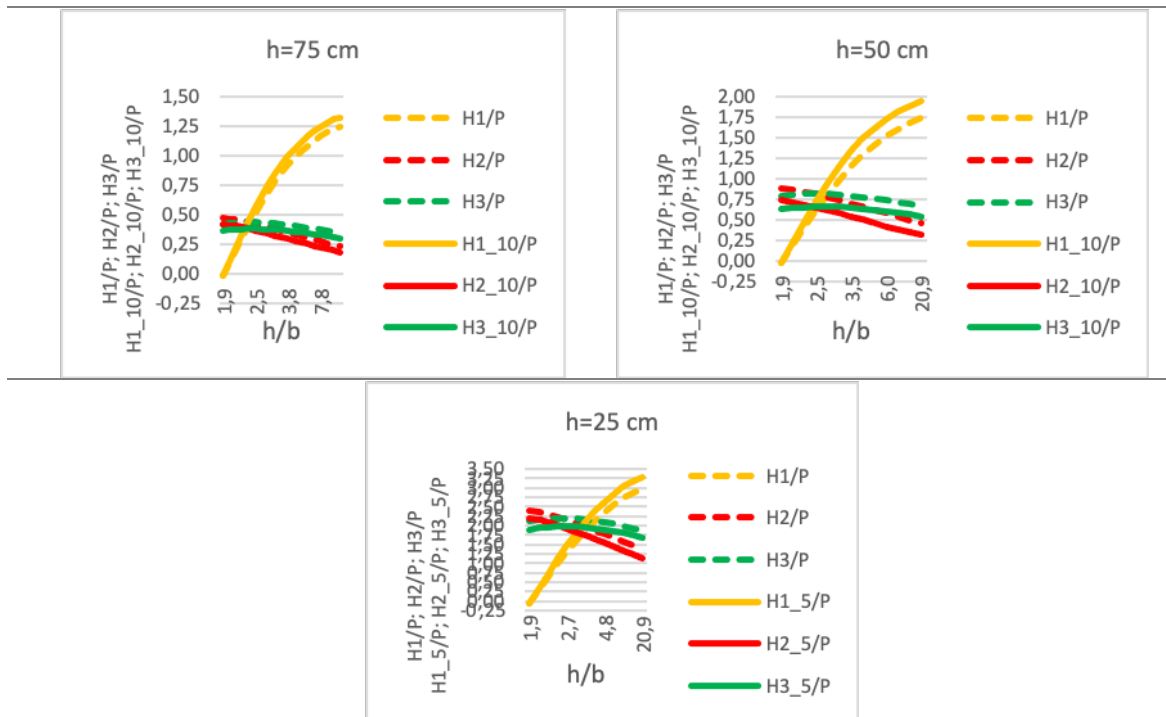


Figure 4. Comparison of the parameters of the support reactions at $c = e = 3\text{ cm}$ for the three beams and at $c = e = 10\text{ cm}$ for beams with $h = 75\text{ cm}$, $h = 50\text{ cm}$ and $c = e = 5\text{ cm}$ for beam with $h = 25\text{ cm}$

Figure 4 shows a comparison of the parameters of the three support reactions when the first support moves from the center of the cross section to the bottom edge of the beam, and the other two supports are fixed. The curves already considered in Figure 3 are shown with a dotted line. The solid line shows the values of the support

reactions at $c = e = 10 \text{ cm}$ for beams with $h = 75 \text{ cm}$ and $h = 50 \text{ cm}$ and $c = e = 5 \text{ cm}$ for beam with $h = 25 \text{ cm}$, i.e. supports two and three approach to the axis of the beam. For all considered sizes of the cross section of the beam, observed an increase in support reaction H_1 and a decrease in H_2 and H_3 . It can be seen that H_2 decreases significantly also at the end of the graphs, when $h/b = \infty$ it approaches values commensurate with zero.

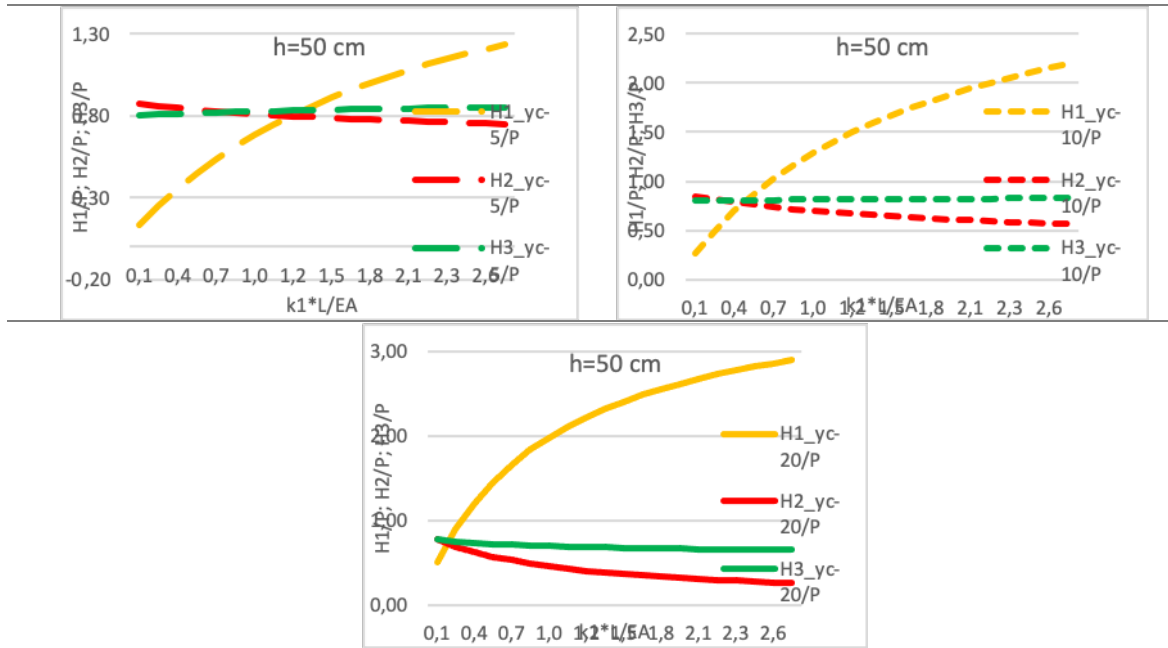


Figure 5. Changing the parameters of the support reactions when the stiffness of the first spring changes

Figure 5 shows the parameter of the support reactions for the case of a beam with $h = 50 \text{ cm}$ and three positions of the first support. The first support is at a distances of 5, 10 and 20 cm from the axis of the beam. The position of the second and third support is unchanged and is set by the distance $c = e = 3 \text{ cm}$, measured from the edges of the beam. Stiffness of the first spring is variable, increasing. In addition to the fast and significant increasing of H_1 , it is obvious that H_3 also increases when first support is close to the axis of the beam. When first support is at a distance of 20 cm from the axis of the beam H_3 decreases with the increase of k_1 . Reaction H_2 does not change its decreasing trend.

The support conditions for Figure 6 are the same as those of Figure 5, but now the stiffness of the second and the third springs are variable. The stiffness of the first spring is constant.

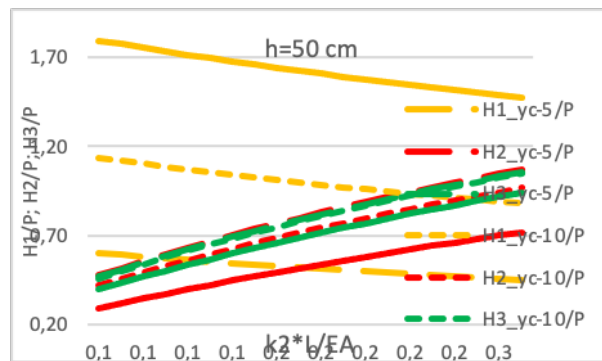


Figure 6. Changing the parameters of the support reactions when the stiffness k_2 and k_3 increases

The increase in the stiffness of the second and third springs leads to an increase in the support reactions corresponding to those two springs. The support reaction H_1 decreases.

Figure 7 shows the reflection of the normal force contribution in the potential energy expression. The position of the first support is variable and is monitored by the relation h/b . The position of the second and third support is set with the distance $c = e = 3 \text{ cm}$ measured from the edges of the beam. The stiffness of the springs does not change.

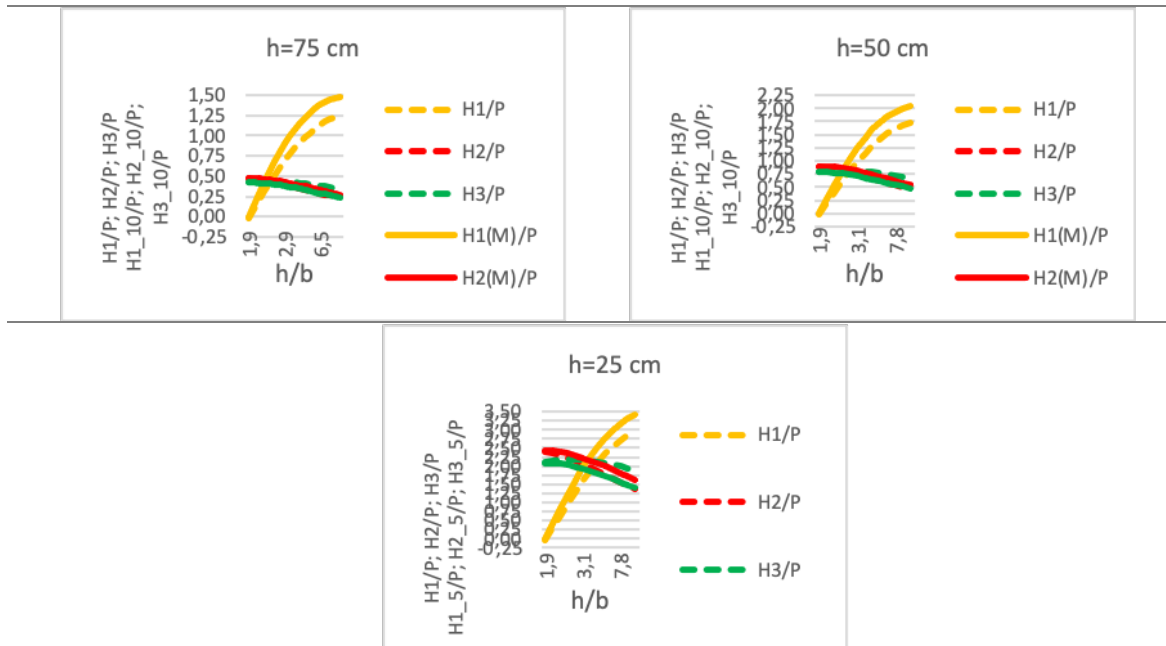


Figure 7. Comparison of support reaction parameters with and without considering the axial force N

Figure 7 shows values of the parameters to the three support reactions without considering N - solid lines and with its consideration - dashed lines. It is observed that the inclusion of N in the expression for the potential energy leads to smaller values of H_1 . The same refers to H_2 . While at H_3 observe an increase if the linear deformations of the beam are taken into account.

Conclusion

A solution of an Off-center Supported Beam with Additional Elastic Supports located at the Height of the Beam and Asymmetrical Cross Section was carried out. The beam is loaded with a transverse force at the mid-section.

- The expressions for the horizontal support reactions in the elastic supports are derived. The obtained results illustrate the distribution of horizontal forces along the height of the beam.
- The effect of moving the first support from the center of cross section to the bottom edge of the beam is considered.
- The results of changing the position of the second and third supports (moving them towards the axis of the beam) are demonstrated.
- The influence of the change in the stiffness of the first (k_1) spring has been reported. The stiffness of the second and third spring (k_2, k_3) was varied separately.
- The influence of the normal (axial) force in the potential energy expression is shown.

The obtained results may be interesting both for researchers and for engineers from practice. Research from this paper can help in the interpretation of results obtained from construct analyses.

Scientific Ethics Declaration

The author declares that the scientific ethical and legal responsibility of this article published in EPSTEM journal belongs to the author.

Notes

This article was presented as an oral presentation at the International Conference on Basic Sciences, Engineering and Technology (www.icbasnet.net) conference held in Istanbul/Turkey on August 25-28, 2022.

References

- Park, R. & Paulay T. (1974). Reinforced Concrete Structures. *Christ church*, New Zealand.
- Park R. & Keong Y. S. (1979). Test on structural concrete beam-column joints with intermediate column bars, *Bulletin of the New Zealand national society for earthquake engineering*, 12, No 3.
- Paulay T. (1989). Equilibrium criteria for reinforced-concrete beam-column joints. *ACI Struct Journal*, 86, 635–643.
- Park, R. (2002). A Summary of results of simulated seismic load tests on reinforced concrete beam-column joints, beams and columns with substandard reinforcing details. *Journal of Earthquake Engineering*, 6 (2), 1-27.
- Lowes L. & Altoontash A. (2003). Modeling reinforced-concrete beam-column joints subjected to cyclic loading. *Journal Structural Engineering*, 129, 1686–97.
- Altoontash, A. (2004). Simulation and damage models for performance assessment of reinforced concrete beam-column joints, (PhD Dissertation), *Department of Civil and Environment Engineering, Stanford University*, Stanford, California.
- Celik, O.C. & Ellingwood, E.R. (2008). Modelling beam-column joints in fragility assessment of gravity load designed reinforced concrete frames. *Journal of Earthquake Engineering*, 12:357–381.
- Shiohara, H. (2001). New model for shear failure of RC interior beam-column connection. *Journal of Structural Engineering*, 127 (2), 152-160
- Sharma, A., Reddy G.R., Vaze K.K., Ghosh A.K., Kushwaha H.S. & Eligehausen R. (2009). Joint model to simulate inelastic shear behavior of poorly detailed exterior and interior beam-column connections reinforced with deformed bars under seismic excitations. *Bhabha atomic research centre*, Mumbai, India
- Shafaei, J., Zareian M. S., Hosseini A. & Marefat M. S. (2014). E Effects of joint flexibility on lateral response of reinforced concrete frames. *Engineering Structures*, 81, 412-413.
- Mladenov, K. & Doicheva A. (2009). Flexural-torsional buckling of an off-centre supported beam, *Annual of University of Architecture, Civil Engineering and Geodezy*, Sofia, XLIV (V), 103-114. ISSN 1310-814X (in bulgarian)
- Doicheva A. (2011). Exact solution for a beam on off-center spring supports. *Journal of theoretical and Applied Mechanics*, 2, 69-82, ISSN 0861-6663
- Doicheva A. & Mladenov K. (2009). A problem of an off-centre supported beam with an elastic link. *Third Symposium on bridges "Design and construction of bridges" UACEG - Sofia, Civil Engineering - Bulgaria*, 4, (2009), 11-16, ISSN 0562-1852 (in bulgarian)
- Doicheva A. (2021). Off-center supported beam with additional elastic supports located at the height of the beam. *X-th International Scientific Conference on Architecture and Civil Engineering ArCivE 2021*, 29 May, Varna, Bulgaria (in bulgarian)

Author Information

Albena Doicheva

University of Architecture, Civil Engineering and Geodesy (UACEG)

Bulgaria, Sofia 1164, 1 Hristo Smirnenski Blvd.

Contact e-mail: doicheva_fhe@uacg.bg

Estimation SNR of CCD camera for OD medium

Miranda KHAJISHVILI

Batumi Shota Rustaveli State University

Nugzar GOMIDZE

Batumi Shota Rustaveli State University

Jaba SHAINIDZE

Batumi Shota Rustaveli State University

Abstract: Common methods of analysing the chemical composition of a substance includes many existing optical methods. Selecting an effective and optimal method from numerous optical methods and adapting it to the properties of the investigated substance is one of the most urgent tasks of modernity. Modern fluorescent spectrometers are economical, portable devices and they are easy to use in the outside conditions for investigation of biological structure, environment and clinical studies. But to obtain high-throughput spectra expensive stationary equipment is still needed. In addition, its operation requires properly trained staff. One of the main parameters is the signal-to-noise ratio (SNR) for a CCD camera when incident light partially absorbed via optically dense media.

Keywords: Spectroscopy, Optical Density, Signal-Noise Relation

Introduction

Today, the growing interest in laser fluorescence spectroscopy is due to its practical application in laser communication, ecology, and medicine. Medical imaging, for example, is one of the major problems in medicine.

Under conditions of weak and strong turbulence, an analytical image of the partially spatial coherence beam intensity correlation function was obtained in the paper (Leader 1979), (Mandel 1995), (Joseph & Lakowic Z 2006) paper investigates the scintillation effect for a partially temporal coherence wave.

Within grant project №FR-152-9-240-14 (Gomidze et al., 2013), (Gomidze et al., 2016), (Gomidze et al., 2011), was taken spectra using spectrometer StellarNet Black-Comet (190-900 nm) which captures of laser beams scattered from an optically dense random phase screen.

The difficulty is otherwise - to evaluate the statistical characteristics of the signal detected through a heterogeneous environment and to visualize the spectral image. These difficulties are caused by environmental statistics. For example, the detection of fluorescence signals in complex environments and the visualization of spectral images are associated with significant difficulties, because the complex composition of the environment (petroleum, petroleum products, organic compounds, etc.) determines the overlap of spectra and reduces the ability to decipher useful information. It becomes important to increase the quality of the signal registered on the detector and to determine the factors that are responsible for this quality.

Optical density (OD), also referred to as absorbance, is a property that describes a material's ability to absorb the part of energy an incident light (called "radiant power") that is passed through that material. It is defined as a ratio between the incident radiant power and the transmitted radiant power. In other words, optical density is the ability of a material to block a light with particular frequencies. The optical density itself is dimensionless. The optical density represented in the logarithmic dimension $\lg\left(\frac{P_{in}}{P_{out}}\right)$ better reflects the absorption properties of the environment. For example, seawater with an optical density of 1 means that seawater absorbs 90% of the power of incident light. This means that in the case when optical density is more than 3, only 1 photon can be detected of 1000 light photons via the detector. Even with the most sophisticated tools, detecting these small amounts of detected photons in the electronic noise condition is a very complex task. It is therefore always recommended to dilute the samples when the optical density more than 3. Then calculate the dilution coefficient before the final measurement. It turns out that the relationship between the power of light falling at low optical density and the concentration of the solution is almost linear, but at high optical density this relationship is nonlinear.

- This is an Open Access article distributed under the terms of the Creative Commons Attribution-Noncommercial 4.0 Unported License, permitting all non-commercial use, distribution, and reproduction in any medium, provided the original work is properly cited.

- Selection and peer-review under responsibility of the Organizing Committee of the Conference

Spectroscopy, the study of the interaction of light with a matter, can be used for qualitative and quantitative analysis of a substance. It is important to select a light wavelength sample for hypothetical solution analysis based on the supporting sample (distillate or hexane). However, the effect of solution concentration on the optical density (absorption) of the sample can be investigated by Berry's law: $OD = \epsilon L c$, where ϵ is the absorption coefficient, L is the thickness of the sample (in this case the thickness of the cuvette is 2.5 cm), and c is the concentration of the solution (Fig. 1). The absorption spectrum allows the analysis of atomic, molecular and nuclear energy transitions.

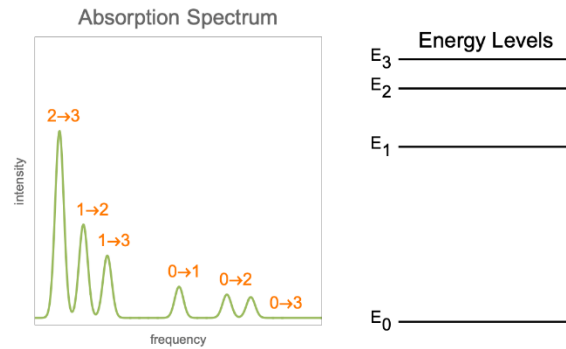


Fig. 1. Determination of energy transitions according to the absorption spectrum

The part of the photon energy absorbed by the system as light is lost and the photon radiated by the system has less energy, consequently, it has longer wavelength. The relaxation processes cause the creation of the background of strong “electronic noise”, which overlays to fluorescence signal, though, it is possible to suppress using spectral filter.

Theoretical part

The quantum theory of radiation pictures atoms with quantized energy levels interacting with an assembly of photons of varying frequencies. When the energy difference between two atomic states fulfills a resonance condition $\hbar\omega = E_1 - E_0$, three possible transition processes can occur: absorption, stimulated emission, and spontaneous emission. In the electric-dipole approximation, the transition rates for absorption and stimulated emission are given by (Blinder 2004):

$$W_{abs} = W_{stim\ em} = \frac{4\pi^2}{3\hbar^2} \rho(\omega) |\langle 0|\mu|1\rangle|^2,$$

where μ is the electric dipole operator and $\rho(\omega)$ is the spectral density of the radiation field at frequency ω . The corresponding rate of spontaneous emission is:

$$W_{spont\ em} = \frac{4\omega^2}{3\hbar c^3} |\langle 0|\mu|1\rangle|^2.$$

All three radiative processes depend on the matrix element $\langle 0|\mu|1\rangle$ and therefore obey the same selection rules. A convenient measure of the intensity of a transition is the oscillator strength:

$$f_{0,1} = \frac{2m_e\omega}{3\hbar e} |\langle 0|\mu|1\rangle|^2,$$

which generally lies in the range from 0 to 1. The dependence on ω^3 makes spontaneous emission significant only for higher-energy transitions—in practice, only for optical frequencies and higher. The Figure 1 shows considers the transition-energy range of 0.1 to 10 eV, corresponding to radiation wavelengths of 12000 to 120 nm, which includes the visible region 380–750 nm, as well as parts of the infrared and ultraviolet (fig.2).

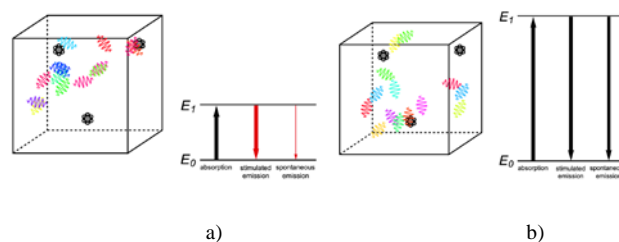


Fig.2. Demonstration of transition processes: a) transition in the infrared region $E_1 - E_0 = 0,2$ eV, $\lambda = 6200$ nm, $f_{0,1} = 0,5$; b) transition in the ultraviolet region $E_1 - E_0 = 10$ eV, $\lambda = 120$ nm, $f_{0,1} = 0,5$

The electromagnetic field is governed by the same equations as the quantum harmonic oscillator. The probabilities for annihilation and creation of a photon of frequency ω are given by:

$$|\langle n_\omega - 1 | a_\omega | n_\omega \rangle|^2 = n_\omega,$$

and

$$|\langle n_\omega + 1 | a_\omega^+ | n_\omega \rangle|^2 = n_\omega + 1,$$

respectively. The photon numbers n_ω are proportional to the spectral density $\rho(\omega)$, while the additional term +1 in the creation formula accounts for the phenomenon of spontaneous emission.

When tissue is penetrated, the dominant effects are scattering and absorption by polarizable bio-particles. The most important parameter in the interaction is the power density, $s(r, z)$ (mW/mm^2). This is a function of power source delivered from an optical radiation source to the biological tissue, where input power is (W), and the spot has a radius $R(mm)$. The propagation of the scattered radiation is described by the photon transport equation (Hoppe et al.,1983):

$$(s\nabla)L(r, s) = \frac{dL}{ds} = -\mu_s L(s, s') + \mu_s \int_{4\pi} P(s, s') L(s, s') ds.$$

We can expand the plane waves in terms of Legendre polynomials to find an expression from the scattering amplitude and the differential cross section:

$$f(\theta, \varphi) = \frac{1}{4\pi} \int e^{i(\vec{k}\vec{r})} U(\vec{r}) d\vec{r},$$

$$\frac{d\sigma}{d\Omega} = \frac{1}{k^2} \left| \sum_{l=0}^{\infty} (2l+1) e^{i\delta} \sin\delta P_l(\cos\theta) \right|^2.$$

where $U(\vec{r})$ is the potential energy. The amplitude $f(\theta, \varphi)$ depends on the potential, the scattering angle θ , and the target area φ . The total cross section is:

$$\sigma_T = \frac{4\pi}{k^2} \left| \sum_{l=0}^{\infty} (2l+1) e^{i\delta} \sin^2\delta \right|^2,$$

We verify directly that:

$$\sigma_T = \frac{4\pi}{k^2} \text{Im}f(0).$$

which is called the optical theorem. So, we can find power factor on optical radiation penetration in tissue depth and analyze depends power factor on wavelength for different scattering and absorption factor:

$$s(\lambda, P, \delta, d) = \frac{55P}{4\pi\delta^2 0.01} \exp \left[-0.1 \left(\frac{\sin(0.5)}{\lambda} \right)^2 + \frac{d}{\delta} \right].$$

Fig.3 show that changing the wavelength from shorter to longer slightly increases the power factor in the volume of bioparticles (measured in mW/mm^2). This means that shorter wavelengths generate heat more than longer wavelengths. Longer wavelengths remain constant with changes in tissue depth due to the penetration of photon radiation d , as well as due to the properties of the optical thickness of the tissue δ . Other factors include a change in the source of the radiation power P and a change in the wavelength λ , as well as the angle of incidence of the radiation photons θ . Since heat generation is caused by the radiation beam propagation through highly water-absorbing tissue, the intensity is exponentially attenuated due to the low scattering factor.

This model includes several assumptions: 1) Scattering process is elastic, which means that the frequencies of incident and scattered radiation are the same. 2) Any interaction between the scattering bio-particles is neglected, therefore, we don't take into account the process of multiple scattering. 3) The width of the incident beam is much larger than the width of the scattered beam, hence the bioparticle will have a well-defined momentum.

When a diatomic molecule undergoes a transition to an excited electronic state higher by ΔE_{elec} , it generally changes its vibrational and rotational quantum numbers as well. In the liquid state, the individual rotational levels are not generally resolved and the resulting process is characterized as a *vibronic transition*. Both the ground and excited electronic states are represented by potential energy curves, shown in blue and red, respectively, on the figures 3. The probability densities of the first few ground state and excited-state vibrational

levels, $|U_{\nu_1}^{(0)}|^2$ and $|U_{\nu_2}^{(1)}|^2$, are shown, superposed on the vibrational energy-level diagrams, with $\nu = 0, 1, 2 \dots$. Here the superscripts refer to the electronic state, while the subscripts label the vibrational level.

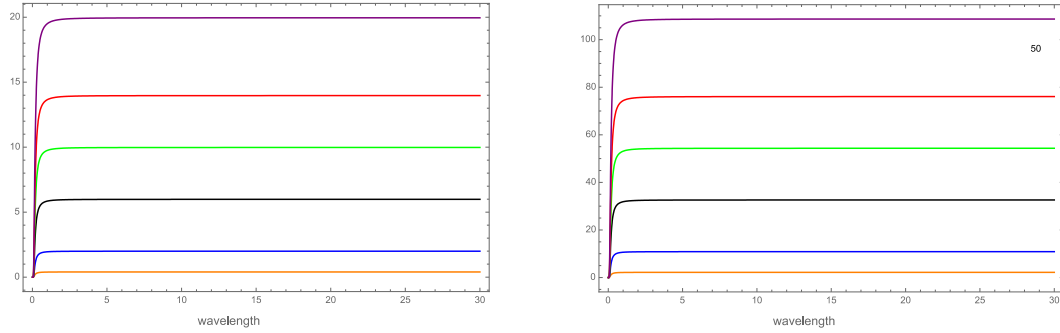
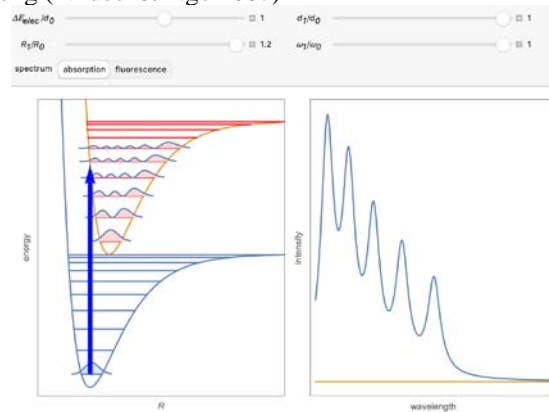


Fig. 3. Power factor on optical radiation penetration in optical and tissue depth for analysis of scattering and absorption factor a) $d = 7 \text{ mm}, \delta = 1 \text{ mm}$, b) $d = 7 \text{ mm}, \delta = 10 \text{ mm}$

At normal temperatures, only the $\nu = 0$ vibrational level of the ground state is occupied. When a molecule absorbs a photon in an electronic transition, the electrons can rearrange themselves much more rapidly than the much heavier nuclei (consistent with the Born–Oppenheimer approximation). Thus, electronic transition can be approximated by the vertical blue arrow to internuclear distances R in the excited state very close to its maximum value in the ground state. This leads to a mixture of several excited-state vibrational levels, predominated by the level that completely overlaps with the $U_0^{(0)}$ wavefunction. According to the Franck–Condon principle, the relative intensities of the individual vibrational peaks are proportional to the factors $|\langle U_{\nu_2}^{(1)} U_0^{(0)} \rangle|^2$. This gives rise to an absorption spectrum shown in blue. The relative intensity of the vibrational components depends on the molecular parameters of the two electronic states, but most sensitively on the difference between equilibrium internuclear distances, R_0 and R_1 .

A molecule excited in an electronically allowed transition will generally return to its ground electronic state, a process called *fluorescence*, within the order of a few nanoseconds. Before it does so, most of the excited molecules will decay to the lowest vibrational state $U_0^{(1)}$ by radiationless transition processes, such as internal collisional processes between molecules. These are represented in the upper curve by a series of black arrows. Fluorescence will then produce a series of peaks corresponding to different vibrational levels of the ground state, with intensities proportional to the Franck–Condon factors $|\langle U_{\nu_1}^{(0)} U_0^{(1)} \rangle|^2$. Because of the geometry of the energy curves, the fluorescent spectrum is very nearly a mirror image of the absorption spectrum, with the transitions $\nu_1 = 0 \leftrightarrow \nu_2 = 0$, meaning that this same transition occurs in both the absorption and fluorescence spectra. Figure 4 shows the Franck–Condon factors and spectral intensities are simulated since explicit computation would take too long (Videen& Ngo 2007)



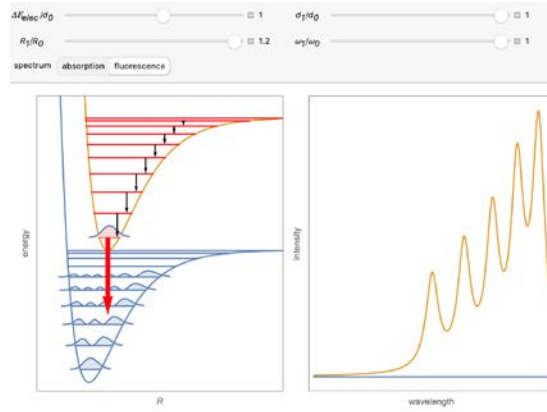


Fig. 4. $\frac{\Delta E_{elec}}{d_0} = 1$, $\frac{R_1}{R_0} = 1.2$, $\frac{d_1}{d_0} = 1$, $\frac{\omega_1}{\omega_0} = 1$ a) the vibrational peaks in the absorption spectrum are notated, right to left. The peak is dominant here since R_0 , and R_1 differ only slightly. b) corresponding fluorescence spectrum; the peaks are notated, left to right

Discussion and Analysis

Suppose (x_1, z_1) the coordinates of a beam of light for an optical system are known. After passing through the phase screen, the coordinates of the beam are transformed by the matrix equation (Gomidze et al., 2021), Thorlabs (2021):

$$\begin{bmatrix} z_2 \\ x_2 \end{bmatrix} = \begin{bmatrix} A & B \\ C & D \end{bmatrix} \begin{bmatrix} z_1 \\ x_1 \end{bmatrix}$$

where $x_1 = \varepsilon\theta$, ε - is the refractive index of the media at the point where the beam falls, θ is the angle between the direction of propagation of the beam and the optical axis. The determinant of the beam transmission matrix is the ratio of the refractive index to the input and output of the optical system.

Such an approach allows us to study dependence of scintillation index σ a random phase screen on the correlation radius of the diffuser and the distance from the diffuser. Capturing and then visualizing the detected signal spectrum is one of the most important tasks in medical physics. The realization of visualization is carried out using appropriate mathematical methods. The object of study can be considered as a linear system that determines the transformation of the primary signal. Important part is the computation of the matrix of this transformation by mathematical methods. In principle, formation of the visual image involves receiving a medical signal, forming it using reconstruction techniques, then analyzing and evaluating the medical image.

As can be seen from the diagram, five components are important: the patient, the image formation system, the operator system, the image, and the observer. According to the task, we currently have different systems, such as: X-ray radiology, radioisotope radiation formation systems, magnetic resonance, ultrasound systems. In each method it is possible to control different physical parameters by the operator, for example: change of potential in the X-ray tube, controls of the concentration and type of radioisotopes, control of the magnetic field gradient and characteristic times, etc.

There are different methods for creating or registering a medical image. For example: photographic plate coverage, gamma camera, digital detectors and others. In the end, the image is analyzed by the observer to obtain structural (anatomical) or in some cases functional (physiological) information. Of course, it is up to the observer to detect a number of pathologies, however the latter depends on three factors at the same time: the quality of the image, the condition of the observation, the physical characteristics of the observation. The image itself depends on 5 factors: contrast, resolution (spatial resolution), background noise, artifacts and distortions. It is these factors that contribute to the high quality of the image in the process of its formation.

Different radiations have different scales of resolution, for example: the range of vision for gamma radiation is in the range of 10-3 mm, 5-2 mm for ultrasound, 3-1 mm for magnetic resonance, 2-0.8 mm for tomography, fluoroscopy 1-0.4 mm, conventional radiography 0.5-0.1 mm, mammography below 0.05 mm.

Suppose experimental measurements are carried out on the object under examination by the selected method. Assume that some physical characteristic parameters were taken into account when performing N independent measurements:

$$x_1, x_2, x_3, \dots, x_i, \dots, x_N,$$

to each x_i measured value Corresponds only integer number. The main characteristics of these data are their sum and average size:

$$\Sigma \equiv \sum_{i=1}^N x_i, \quad \bar{x}_e \equiv \frac{\Sigma}{N}.$$

The distribution of sets x_i can be represented by the distribution function $F(x)$, which is the relative frequency at which x takes values from the database described above. Frequency allocation is automatically normalized to 1:

$$\sum_{x=0}^{\infty} F(x) = 1.$$

Let us considered that process of detection is binary. We can have only two outcomes: "success" or "failure". The probability of success can be conditionally denoted by P , which we consider to be constant for all experimental trials. The number of experiments can usually be denoted by N .

Under certain conditions we might predict a distribution function that describes a process. Let us distinguish three well-known statistical models: 1. Binomial distribution - one of the most general and usable in computational calculations; 2. Poisson distribution - a relatively simplified model when P is small and N is large; 3. Gaussian or Normal Distribution - an even more simplified model when the average probability of success is relatively high.

By binomial distribution the probability of x success in N experiments can be expressed by the formula:

$$P(x) = \frac{N!}{(N-x)!x!} p^x (1-p)^{N-x}$$

where:

$$\begin{aligned} \sum_{x=0}^N P(x) &= 1, \\ \bar{x} &= \sum_{x=0}^N xP(x) = pN, \\ \sigma^2 &\equiv \sum_{x=0}^n (x - \bar{x})^2 P(x) = pn(1-p) = \bar{x}(1-p) \end{aligned}$$

σ is a dispersion. When $\bar{x} \gg 1$, the Poisson distribution can then be approximated by the Gaussian (normal) distribution:

$$P(x) = \frac{1}{\sqrt{2\pi}\sigma} e^{-\frac{(x-\bar{x})^2}{2\sigma^2}}.$$

where $\sigma^2 = \bar{x}$ is practically a boundary condition. The Gaussian or normal distribution is most often found in the continuous distribution of probabilities of true random x . In our case the photons fall on the detector. Suppose v is the average speed of photon detection. rdt is the differential probability that an event will occur in dt time, assuming that the photon occurred at time $t = 0$. The differential probability that the following photon will occur in dt time can be calculated by the formula:

$$I_1(t)dt = P(0)rdt,$$

$P(0)$ is the probability of no photon being generated between 0 and t . It can be expressed by the Poisson distribution:

$$P(0) = \frac{(rt)^0 e^{-rt}}{0!} = e^{-rt}.$$

The differential probability that the following photon will occur in the detector dt time will be:

$$I_1(t)dt = re^{-rt} dt.$$

Probability of time interval distribution between two subsequent detected photons for different average velocities is shown in Fig. 5.

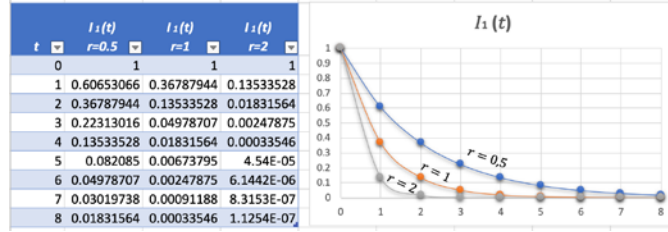


Fig. 5. probability of time interval distribution between two subsequent detected photons for different average velocities

Noise in a camera image is the aggregate spatial and temporal variation in the measured signal, assuming constant, uniform illumination (Reinaudi et al., 2007). There are several components of noise: σ_D - Dark Shot Noise. Dark current is a current that flows even when no photons are incident on the camera. It is a thermal phenomenon resulting from electrons spontaneously generated within the silicon chip (valence electrons are thermally excited into the conduction band); σ_R - Read Noise. This is the noise generated in producing the electronic signal. This results from the sensor design but can also be impacted by the design of the camera electronics. It is independent of signal level and temperature of the sensor, and is larger for faster CCD pixel clock rates; σ_S - Photon Shot Noise. This is the statistical noise associated with the arrival of photons at the pixel. Since photon measurement obeys Poisson statistics, the photon shot noise is dependent on the signal level measured. It is independent of sensor temperature; Fixed Pattern Noise. σ_F - This is caused by spatial non-uniformities of the pixels and is independent of signal level and temperature of the sensor. Note that fixed pattern noise will be ignored in the discussion below; this is a valid assumption for the CCD cameras sold here but may need to be included for other non-scientific-grade sensors.

The total effective noise per pixel is the quadrature sum of each of the noise sources listed above:

$$\sigma_{eff} = \sqrt{\sigma_D^2 + \sigma_R^2 + \sigma_S^2 + \sigma_F^2}$$

The formula for calculating the optical density (OD) is [14]:

$$OD(x, y) = n_{col}(x, y)\sigma_0^2 = \log\left(\frac{C_{in}(x, y) - C_{bg}(x, y)}{C_{out}(x, y) - C_{bg}(x, y)}\right) + \frac{C_{in}(x, y) - C_{bg}(x, y)}{C_{sat}^{eff}}$$

where:

$$C(x, y) = I(x, y) \frac{A_{pix}}{M^2} \frac{\lambda}{hc} TQE_T \times \frac{1}{ADC}$$

$I(x, y)$ - is the intensity distribution of light on the atom, A_{pix} - is the pixel size of the CCD camera, $\frac{A_{pix}}{M^2}$ - is the real pixel size including the magnification of the image system, λ - is the wavelength of the probe light, T - is the transmission rate of the image system, QE - is the camera quantum efficiency, ADC - is the analog-to-digital conversion efficiency of the camera, τ - is the exposure time, $C_{in}(x, y)$ - the input light distribution on the atom, $C_{out}(x, y)$ - the output light (after absorption), $C_{bg}(x, y)$ - the background.

Then, the SNR is:

$$SNR = \frac{OD(x, y)}{\sqrt{\sigma_{eff}^2}} = \frac{\log\left(\frac{C_{in} - C_{bg}}{C_{out} - C_{bg}}\right) - \frac{C_{in} - C_{out}}{C_{sat}^{eff}}}{\sqrt{\left(\frac{1}{C_{sat}^{eff}} + \frac{1}{C_{in} - C_{bg}}\right)^2 \sigma_{C_{in}}^2 + \left(\frac{1}{C_{sat}^{eff}} + \frac{1}{C_{out} - C_{bg}}\right)^2 \sigma_{C_{out}}^2 + \left(\frac{1}{C_{in} - C_{bg}} - \frac{1}{C_{out} - C_{bg}}\right)^2 \sigma_{C_{bg}}^2}}$$

But at the same time, it is necessary to determine the signal-to-noise ratio (SNR) to estimate the absorption spectrum. To do this, we need to obtain an optical density image OD (x, y), which is a function of laser intensity, CCD detector pixel function, wavelength function, quantum efficacy function of CCD detector, incident (on the sample) light distribution function and output light (from sample) distribution function (Fig. 6).

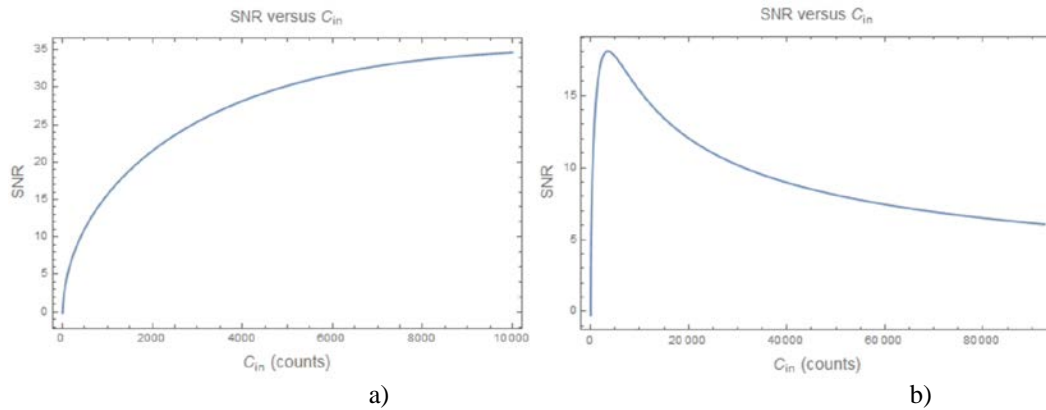


Fig.6. Signal-noise relation vs concentration for optically dense media: Optical Density: $OD = 1$, Readout noise $\sigma_R = 2.3$, Dark current $I_D = 0.001$, Clock noise: 0, Noise factor: 1, gain of electron multiplying: 1, exposure time: $\tau = 50 \mu s$. a) saturated count rate per pixel 200, plot range of $C_{in} = 10000$, b) saturated count rate per pixel 53.42, plot range of $C_{in} = 92600$

So, the two-dimensional analytical image $OD(x,y)$ of the optical density is a function of the laser intensity, the pixel function of the CCD detector, the function of the wavelength, the function of the quantum efficiency of the CCD detector, function incident light distribution and function of distribution Background (noise). via OD can be evaluated signal-to-noise ratio (SNR) of CCD-detector.

Acknowledgement

The work was supported by the 2022 Higher Education Support Program of Ministry of Education, Culture and Sport of Autonomous Republic of Adjara; Project implementer - PhD of Physics Miranda Khajishvili

References

- Leader, J. C. (1979). Intensity fluctuations resulting from a spatially partially coherent light propagating through atmospheric turbulence, *J. Opt. Soc. Am. A*, Vol.69, 1, 73 – 84.
- Mandel, L., Wolf, E. (1995). *Optical Coherence and Quantum Optics*. Cambridge University Press, Cambridge
- Joseph, R., Lakowic Z., (2006). *Principles of Fluorescence Spectroscopy*. N.Y.: Springer Science, 960.
- Gomidze, N.Kh., Shashikadze, Z.Kh., Makharadze, K.A., & Khajishvili, M.R. (2013) September 9-13). About fluorescence excitation spectrums. *6th International Conference on Advanced Optoelectronics and Lasers*. Conference Proceedings. Sudak, Ukraine, 317-319.
- Gomidze, N.Kh., Khajishvili, M.R., Makharadze, K.A., Jabnidze, I.N., & Surmanidze Z.J. (2016). About Statistical Moments of Scattered Laser Radiation from Random Phase Screen. *International Journal of Emerging Technology and Advanced Engineering*. ISSN 2250-2459 (ISO 9001:2008 Certified), Vol. 6, Issue 4, 237-245.
- Gomidze, N.Kh., Makharadze, K.A., Khajishvili, M.R., & Shashikadze, Z.Kh. (2011) About Numerical Analyses of Sea Water with Laser Spectroscopy Method. XXXth URSI General Assembly and Scientific Symposium, (5 VOLS), pp.1620- 1624, ISBN 978-1-4244-5117-3.
- Blinder, S.M. (2004). *Introduction to Quantum Mechanics*, Amsterdam: Elsevier, 68–71.
- Hoppe, W., Lohmann, W., Markl, H., & Ziegler, H. (1983). *Biophysics*, New York: Springer-Verlag.
- Videen, G., & Ngo, D. (2007). "Light Scattering from a Cell," in *Optics of Biological Particles*, *NATO Science Series, Series II: Mathematics, Physics and Chemistry*, Vol. 238, New York: Springer.
- Gomidze, N., Shainidze, J., Khajishvili, M., Jabnidze, I., Makharadze, K., Kalandadze, L., Nakashidze, O., Surmanidze, Z., Mskhaladze, E., & Gomidze, L. (2021, November 24-26). 3D fluorescence spectroscopy to study the distribution of bioparticles. *International Scientific Conference on Modern Research Methods of Bio-Nano-Agents*, Batumi.
- Thorlabs (2021). "Camera Noise and Temperature Tutorial." www.thorlabs.com/newgrouppage_cfm?objectgroup_id=10773.

Reinaudi, G., Lahaye, T., Wang, Z., & Guéry-Odelin, D., (2007).
Strong Saturation Absorption Imaging of Dense Clouds of Ultracold Atoms,
Optics Letters, 32(21), 3143–3145. doi:10.1364/ol.32.003143.

Author Information

Miranda Khajishvili

Batumi Shota Rustaveli State University
35, Ninoshvili street, Batumi, Georgia, 6010
Contact e-mail: miranda.khajishvili@bsu.edu.ge

Nugzar Gomidze

Batumi Shota Rustaveli State University
35, Ninoshvili street, Batumi, Georgia, 6010
Contact e-mail: gomidze@bsu.edu.ge

Jaba Shainidze

Batumi Shota Rustaveli State University
35, Ninoshvili street, Batumi, Georgia, 6010
Contact e-mail: jabashainidze@gmail.com

Extraction of Frequent Itemset Mining on Spark

Youssef FAKIR

Sultan Moulay Slimane University

Mohamed FAKIR

Sultan Moulay Slimane University

Rachid ELAYACHI

Sultan Moulay Slimane University.

Abstract: In last years, data generated by machines and devices, production-planning systems where the quality and inventory management systems have reached a volume of over a thousand Exabyte's per year and are expected to increase over the next few years. Growing capacities recent applications to produce and store huge amounts of information, called "Big Data", have radically changed the importance of smart analytics data that originally referred to the huge flow data, expanded the scope of technological capability to store, manage, process, interpret and visualize the quantity of data. Data mining is considered one of the fundamental tools on which Big Data analysis is based. In both academic and industrial fields, interest in data mining, which focuses on mining effective and usable knowledge from large data collections, has increased. The need for efficient and highly scalable data mining tools increases with the size of data sets, as well as their value to companies and researchers aiming to extract meaningful information increases. In this work, we are interested in the extraction of frequent itemsets from databases. Extracting sets of frequent itemset is one of the most complex exploration techniques in data mining. It is used to discover frequently co-occurring elements according to a user-supplied frequency threshold, called minimal support. For this reason, we use parallel approaches and distributed, generally based on Spark frameworks. The algorithms implemented are DFPS, RAPRIORI, PFP and YAFIM. Experimental results show that the PFP is more efficient than the others algorithms in memory space and time consuming.

Keywords: Spark, Data mining, frequent itemset, Big Data.

Introduction

Extracting data from large datasets has always been considered a major topic in data mining. One of the most popular methods for this purpose is the extraction of frequent itemsets. This is because this type of extraction searches for frequent combinations of items. Many frequent item mining algorithms exist (X. Jin et al, 2015) (Chung, H. et al, 1999) (Fakir Y. et al, 2020) (Al-Jarrah O.Y. , et al, 2015) (Zaharia M. et al, 2012) (Fakir Y. , et al, 2020) but they are not suited for the massive amount of data we have today. Therefore, to explore endlessly increasing volumes of data, there is a need for a pattern-mining algorithm that can handle large volumes of data while still performing well. For this type of parallel/distributed applications, MapReduce (Sourav S. et al, 2013) is one of the best solutions to guarantee fault tolerance. Hadoop is one of the most popular frameworks based on the MapReduce programming model. The latter is known for distributed storage and processing large data sets using stand-alone clusters. However, disk input-output operations are considered cumbersome in the case of an iterative algorithm. This makes Hadoop inefficient. In recent years, several platforms based on distributed architectures have emerged. Spark (Zaharia M., et al, 2012) is one of the solutions that has gained a lot of attention due to its native support for distributed computing.

Spark (Sourav S et al, 2003) is a framework developed at the Berkeley AMPLab. It offers a number of features to speed up big data processing. The fundamental feature is its parallel in-memory execution model in which all data will be loaded into memory. Spark's programming model is based on a new distributed memory abstraction called Resilient Distributed Datasets (RDD), offered for in-memory computations on a large cluster (Qiu, H. et al, 2014).

An RDD is a collection of data records. It can provide a variety of built-in operations to turn one RDD into another RDD. Spark will cache the contents of RDDs in memory on worker nodes, which will greatly speed up data reuse.

- This is an Open Access article distributed under the terms of the Creative Commons Attribution-Noncommercial 4.0 Unported License, permitting all non-commercial use, distribution, and reproduction in any medium, provided the original work is properly cited.

- Selection and peer-review under responsibility of the Organizing Committee of the Conference

In this paper, a comparative study between four algorithms are done using the Spark data processing framework, and the results of the association rules method to determine the most interesting relationships between items in a large database. These algorithms are the following:

- Parallel Frequent Itemset Mining with Spark (YAFIM)
- An Efficient APRIORI based algorithm on Spark (RAPRIORI)
- Distributed FP-Growth based on Spark (DFPS)
- Parallel FP-Growth (PFP).

This paper organized as follows. The second section describes the proposed frequent itemset mining algorithms. The third section deals with the experimental results. Section four concludes the paper.

Frequent itemset mining algorithms

There are several algorithms for frequent items mining. In this section, we introduce four algorithms, which are DFPS, YAFIM, PFP and RApriori.

Parallel Frequent Itemset Mining Algorithm with Spark (YAFIM)

YAFIM is a parallel Apriori (Qiu, H. et al, 2014) algorithm based on the Spark Resilient Distributed Datasets (RDD) model. It contains two phases of workflow processing (Han, Jiawei et al, 2009). First, YAFIM is an APRIORI implementation on Spark significantly outperforms APRIORI implementation. The transactional datasets are loaded from HDFS into Spark RDD, which are memory-based data objects in Spark, to make good use of available cluster memory in two steps.

An Efficient Apriori based Algorithm on Spark (RAPRIORI)

RAPRIORI is a parallel APRIORI (HAN, Jiawei et al, 2009) algorithm based on the Spark RDD model. It contains three phases of workflow processing. RAPRIORI is an improvement of YAFIM in the third phase.

Distributed FP-Growth Algorithm Based on Spark (DFPS)

FP-Growth (Wang Li, H., et al, 2012) (Fakir Y. et al 2022) uses a depth-first strategy and does not use the generate and verify paradigm as in APRIORI. It uses the tree to symbolize the dataset in a compact form, called FP-tree. DFPS is a parallel FP-Growth algorithm (Shi, X., et al, 2017) based on the Spark model RDD. DFPS loads the transaction dataset from HDFS into Spark as RDD and counts the support of each element.

Parallel FP-Growth (PFP)

FP-Growth is composed of two stages (Wang Li, H., et al, 2012) . In the first stage, the data is scanned for the first time to calculate the frequency of each element, and the elements are sorted in descending order of frequency. Then, the data is scanned in a second step to eliminate the elements whose frequencies are lower than a threshold and to sort each transaction according to the frequencies. In the second step, an FP-Tree is built based on sorted transactions and retrieved recursively to generate the set of frequent items. PFP is based on a new computational distribution scheme. This is because it distributes the work across a cluster of nodes using the Spark model. Thus, it is more scalable and faster than its traditional implementation based on a single machine. The Spark MLlib library (spark.ml) provides an in-memory implementation of the PFP algorithm that facilitates the use of association rules techniques, and the extraction of frequent patterns in a distributed environment. With the defaults of conventional parallel FP-Growth (minimum support) and minimum confidence thresholds (to define association rules), the spark.ml package also takes the numPartitions parameter which specifies the number of partitions used to divide the work.

Experimental results

In this section, we present in-depth experiments to evaluate the performance of different algorithms implemented in Spark. All the algorithms used in the experiments are implemented in the java and Scala languages. The version of Spark used is 3.0.2. The code of the programs was created and compiled via IntelliJ IDEA which provides Scala (version 2.12.13) which represents a native programming language of Spark Framework.

The experimental part were carried out to show the performance of the algorithms to extract the frequent itemset in a data set in terms of execution time, the number of “itemset” patterns extracted, and the memory space compared to the different values of support used. The datasets we used include Mushroom (a dataset describing poisonous and edible fungi by different attributes) and Connect (a dataset of 67,557 transactions and 150 items).

Runtime performance

In this section, the “connect” and “mushroom” datasets are used for our experiments. The purpose of the first comparison is to estimate the speed performance by analyzing the execution time of the algorithms in (Spark 3.0.2). Table 1 and Table 2 shows the specific run time (in seconds) of RAPRIORI, YAFIM, PFP and DFPS for the “mushroom”, and “connect” datasets respectively.

Table 1. Execution time (in seconds) in Mushroom dataset

| Minsup | DFPS | YAFIM | RAPRIORI | PFP |
|--------|-------|-------|----------|-------|
| 0.25 | 23.31 | 57.36 | 54.14 | 14.01 |
| 0.35 | 15.94 | 25.74 | 22.13 | 12.25 |
| 0.4 | 14.74 | 15.96 | 15.18 | 12.06 |
| 0.65 | 11.19 | 13.96 | 12.57 | 10.1 |
| 0.8 | 9.74 | 10.86 | 9.54 | 9.29 |

In order to assess the performance of the algorithms, the minimum support (minsup) ranging from 0.25 to 0.8 for “mushroom” and “connect” data set. We can see from both tables that the quarterly algorithms tend to be more efficient when the minsup is set at a higher level. We take the two datasets “mushroom” and “connect”. Let us start with the “mushroom” dataset (Table 1), we notice that the execution time of YAFIM and RAPRIORI is always greater than DFPS, when the minsup is 0.4; the execution times of YAFIM and RAPRIORI are respectively 15.96s and 15.85s. However, this time we notice that the execution time of PFP is changed if we vary the minsup for the connect dataset.

Table 2. Execution time (in seconds) in Connect dataset

| Minsup | DFPS | YAFIM | RAPRIORI | PFP |
|--------|------|-------|----------|-----|
| 0.25 | 949 | 3700 | 2040 | 53 |
| 0.4 | 486 | 2100 | 1380 | 42 |
| 0.65 | 256 | 1260 | 900 | 36 |
| 0.8 | 120 | 789 | 520 | 29 |

The run times with varying min-support for the “mushroom” and “connect” dataset are shown in Figure 1 and Figure 2 respectively. The x-axis indicates the min support and the y-axis represents the execution time. As the level of support, increases from 0.25 to 0.8 for both “mushroom” and “connect” data sets. We notice in figure 1 that we can confirm the remark in the previous section concerning the PFP algorithm (the execution time values almost the same each time if we change the minsup).

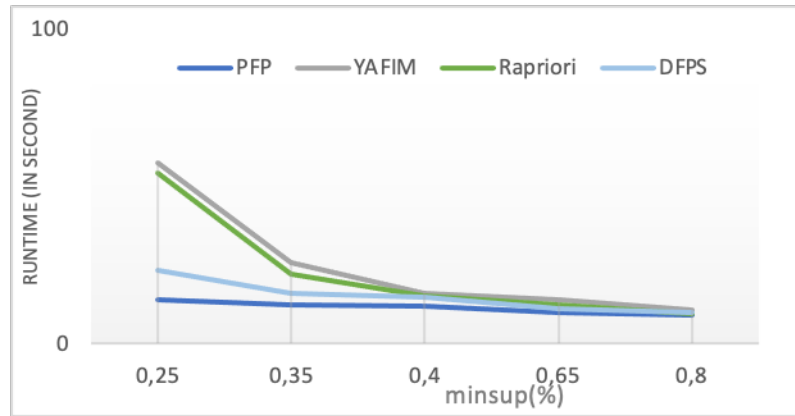


Figure 1. Execution time as a function of minsup (%) in the "mushroom" dataset

We notice in Figure 2 and in Figure 3 that the execution time value for YAFIM, RAPRIORI and DFPS is consistently higher than the same minimum support value for PFP. When the minsup is 0.4 the execution times of DFPS (486 s), RAPRIORI (1380 s), YAFIM (2100 s), this time with a value of 42s for PFP, we can see that the difference between the four algorithms is larger compared to that noticed in Figure 3. Figure 2 shows as the superiority of PFP in terms of metric time remaining is clearer when using the larger datasets (connect).

Figure 3 illustrates the execution time for different numbers of the extracted itemset. For example, for the extraction of 5545 itemset in the same data set, YAFIM spends 57.36 s to find the frequent itemset, RAPRIORI spends 54.14s, and DFPS spends 23.31s while PFP spends only needs 14.01s to extract the same number of itemset (5545 itemset). The results of the experiments expressed in this section show that the performances (execution time) of the PFPs are much better than those of the DFPS, YAFIM and RAPRIORI algorithms. In fact, other algorithms need more time to generate a set of frequent items.

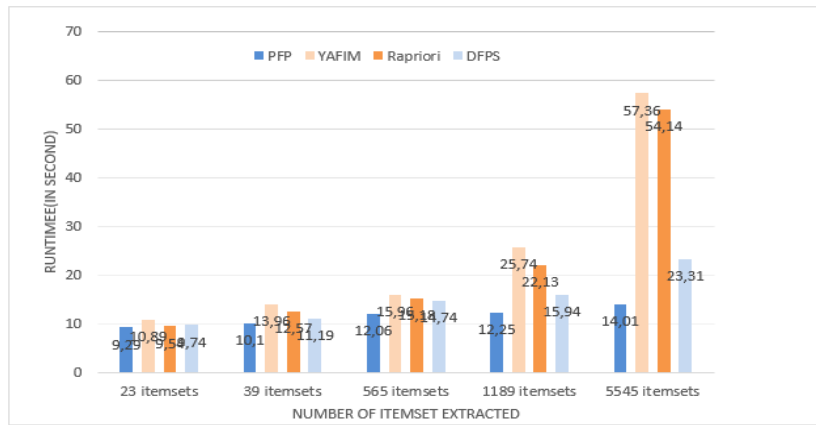


Figure 2. Runtime as a function of minsup (%) in the “connect” database

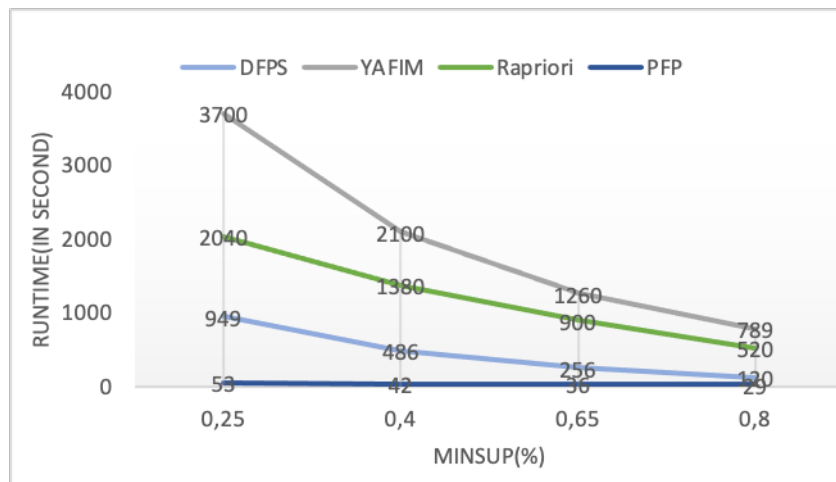


Figure 3. Runtime in function of the number of itemset extracted in the “mushroom” dataset

Memory space performance

In this section, the connect and mushroom datasets are used for our experiments. The aim of this second comparison is to estimate the speed performance by analyzing the memory space of the algorithms. Table 3 and Table 4 show the specific memory space (in MB) in each dataset for RAPRIORI, YAFIM, DFPS and PFP.

The experiments were carried out to evaluate the memory consumption of the algorithms already studied in the previous section using the parameters described in Table 3 and Table 4. The results are illustrated in Figure 4 and Figure 5. In Figure 5 when the minsup is 0.4, the consumed memory spaces of PFP, DFPS, YAFIM and RAPRIORI are respectively 163MB, 199MB, 324MB and (316MB). In Figure 4, the memory spaces consumed for the same minsup are respectively 492 MB, 691 MB, 862 MB and 732 MB for PFP, DFPS, YAFIM and RAPRIORI.

Table 4. Memory space (Mega Bytes) in the Connect dataset

| Minsup | DFPS | YAFIM | RAPRIORI | PFP |
|--------|------|-------|----------|-----|
| 0.25 | 831 | 864 | 860 | 511 |
| 0.4 | 691 | 862 | 732 | 492 |
| 0.65 | 575 | 861 | 480 | 291 |
| 0.8 | 344 | 538 | 410 | 376 |

Table 5. Memory space (Mega Bytes) in the Mushroom dataset

| Minsup | DFPS | YAFIM | RAPRIORI | PFP |
|--------|------|-------|----------|-----|
| 0.25 | 214 | 426 | 410 | 178 |

| | | | | |
|------|-----|-----|-----|-----|
| 0.4 | 199 | 324 | 316 | 163 |
| 0.65 | 151 | 216 | 177 | 109 |
| 0.8 | 123 | 156 | 143 | 98 |

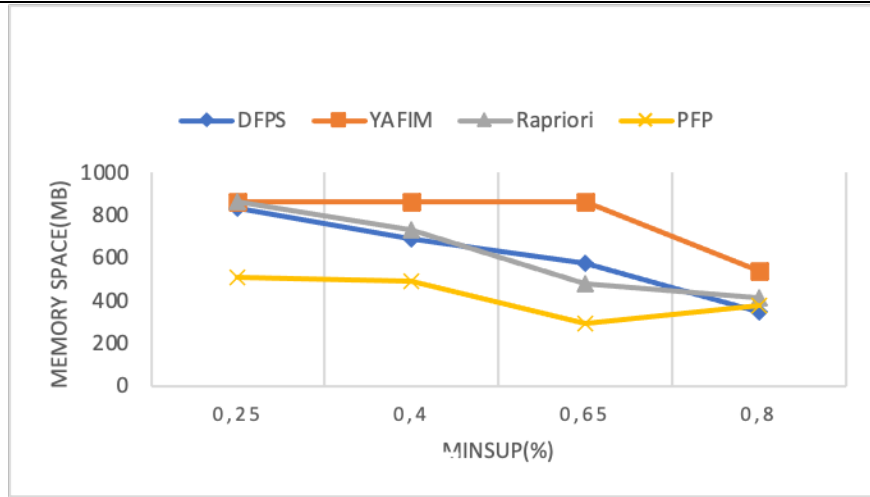


Figure 4. Memory space as a function of minsup in the “connect” dataset

It can be seen that the three algorithms (DFPS, YAFIM, RAPRIORI) always require more memory than the PFP algorithm two sets of data illustrated in Figure 4 and Figure 5. In particular, the PFP algorithm requires almost constant memory under various min-support for both sets of data. The YAFIM algorithm requires the most memory among the four algorithms. From the experimental results, in the two previous sections (Time performance of and memory space performance) show that PFP has a low execution time value compared to other algorithms, and consumed less memory compared to other algorithms, and the less efficient YAFIM algorithm.

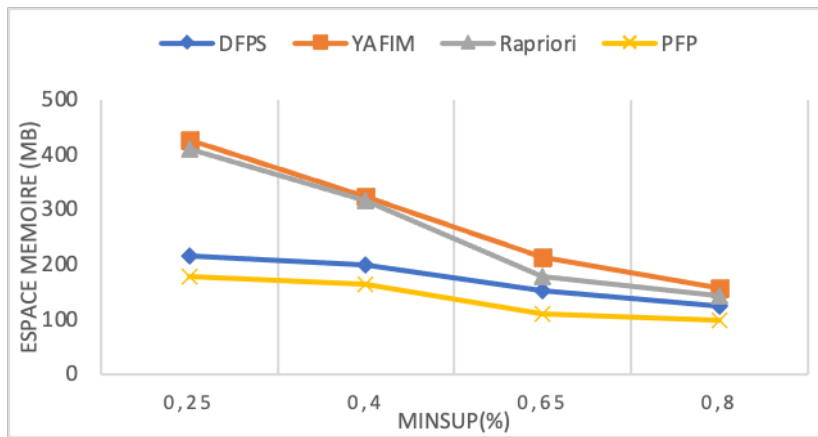


Figure 5. Memory space as a function of minsup in the “mushroom” dataset

Conclusion

The objective of our research project is to compare the different algorithms for extracting frequent patterns (frequent items and mining) in order to discover the most efficient algorithm using Spark, which is a unified analysis framework for the distributed processing of Big Data. To set up this work, the DFPS, YAFIM, RAPRIORI and PFP algorithms chosen and evaluated according to the best performance in terms of execution time and size of memory consumed by each algorithm. We implemented the algorithms with the Scala language in Spark 3.0.2. To test the performance of these algorithms, we went through two levels. The first is runtime performance using different datasets of different sizes, which contain a number of different items and transactions. Each time we vary the minimum support, we visualize the result. These results express that if the degree of support increases the execution time decreases for all the algorithms, and for all the data sets used we notice that the YAFIM algorithm takes the highest value of execution time on the other hand the PFP algorithm is very efficient compared to DFPS, YAFIM, RAPRIORI. The second level is that of the performance of the

memory space, this factor has confirmed the result obtained in the first comparison (execution time). This experimental result indicates that the PFP algorithm reduces the execution time and gives better result compared to other algorithms (YAFIM, RAPRIORI and DFPS); therefore, a result line drawn from this experiment is that PFP has better efficiency than the YAFIM, RAPRIORI and DFPS algorithms. Our analysis of the topic allowed us to gain insight into Big Data and how we can make it more powerful by using frequent item set extraction techniques between variables in a dataset.

Acknowledgements or Notes

* This article was presented as an oral presentation at the International Conference on Basic Sciences, Engineering and Technology (www.icbasaset.net) conference held in Istanbul/Turkey on August 25-28, 2022.

References

- Al-Jarrah, O. Y. , Yoo, P. D., Muhaidat, S., Karagiannidis, G. K. & Taha, K. (2015). Efficient machine learning for big data: A review, *Big Data Research 2 (3)*. doi:10.1016/j.bdr.2015.04.001.
- Chung, H. M., & Gray, P. (1999). Data mining. *Journal of management information systems*, 16(1), 11-16.
- Han, Jiawei, PEI, Jian, & YIN, Yiwen. (.2009), Mining frequent patterns without candidate generation. *ACM sigmod record*, vol. 29, no 2, p. 1-12.
- Fakir Y., (2020). Mining frequent pattern by Titanic and FP-Tree algorithms, *International journal of scientific research in computer science, engineering and information technology*, 6 (5), 208-215.
- Fakir Y., Elmouhi M., Elayachi R., & Fakir M. (2020). A Comparative Study between Relim and SaM Algorithms, *International Journal of Computer Science and Information Security (IJCSIS)*, Vol. 18, No. 5, May 2020
- Fakir Y. , Maarouf A. & El Ayachi R., Mining frequents itemsets and association rules in diabetic dataset, *Lecture Notes in Business Information Processing*, vol.449, 2022.
- Jin X., B. W. Wah, X. Cheng, Y. Wang, (2015). Significance and challenges of big data research, *Big Data Research 2 (2) pp: 59 – 64*. Doi: <http://dx.doi.org/10.1016/j.bdr.2015.01.006>.
- Qiu, H., Gu, R., Yuan, C., & Huang, Y. (2014). YAFIM: A Parallel frequent itemset mining algorithm with spark. *IEEE International Parallel & Distributed Processing Symposium Workshops*. doi:10.1109/ipdpsw.185.
- Shi, X., Chen, S., & Yang H. (2017). DFPS: Distributed FP-growth algorithm based on Spark. *Second Advanced Information Technology, Electronic and Automation Control Conference (IAEAC)* (pp. 1725-1731), IEEE
- Sourav S. Bhowmick Qiankun Zhao, (2003). "Association rule mining: a survey," Nanyang Technological University, Singapore.
- Wang, Y., Zhang, D., Zhang, M., & Chang, E. Y. (2008). PFP: Parallel FP-growth for query recommendation, *Proceedings of the ACM Conference on Recommender Systems - RecSys '08*. doi:10.1145/1454008.1454027,
- Zaharia M., Chowdhury M, DT. , Dave A., Ma J., McCauley M., Franklin M. J., Shenker M. J., & Stoica I., (2012), Resilient distributed datasets: A fault tolerant abstraction for in-memory cluster computing, in: *NSDI'12*.

Author Information

Youssef Fakir

Sultan Moulay Slimane University
Contact e-mail: info.dec07@yahoo.fr

Mohamed Fakir

Sultan Moulay Slimane University
Faculty of Sciences and Technics, BP:523, Beni Mellal,
Morocco

Rachid El Ayachi

Sultan Moulay Slimane University
Faculty of Sciences and Technics, BP:523, Beni Mellal,
Morocco

The Monte Carlo Solution of Nonlinear Problems in Engineering

A.S. RASULOV

University of World Economy and Diplomacy, Uzbekistan

G.M. RAIMOVA

University of World Economy and Diplomacy, Uzbekistan

D. HASANOVA

University of World Economy and Diplomacy, Uzbekistan

Abstract: In this work, we study the approach connected with branching Markov processes. Branching Markov random processes are created to solve boundary-value problems (BVP) with polynomial nonlinearities. The realization of these processes creates so called “trees”. Unbiased estimators of the solution of the nonlinear problem are constructed on these random trees. We also obtain expressions for the minimal variance (statistical error) of the constructed unbiased estimators. We offer computational algorithms for solving some nonlinear diffusion problems which frequently appears in engineering. The case of a quadratic nonlinearity for the boundary BVP is considered in detail. Algorithms, for diffusion BVPs with nonlinear boundary conditions, differ from those algorithms presented in papers (Haji-Sheikh & Sparrow, 1967, p.18, and Haji-Sheikh & Sparrow 1966, p. 370) and we compare their efficiencies. The described algorithms to applied computationally to problem of thermal engineering in the presence of a nonlinear boundary condition. Also, this problem is solved as a conductive boundary value problem of heat transfer.

Keywords: branching Markov process, boundary-value problems, polynomial nonlinearities, unbiased estimators, conductive boundary.

Introduction

The application of Monte Carlo methods in various fields is constantly growing due to increases in computer capabilities. Increasing speed and memory, and the wide availability of multiprocessor computers, allows us to solve many problems using the “method of statistical sampling”, better known as the Monte Carlo method.

Monte Carlo methods are known to have particular strengths. These include:

1. Algorithmic simplicity with a strong analogy to the underlying physical processes.
2. The ability to solve complex realistic problems that include sophisticated geometry and many physical processes.
3. The ability to solve problems set in very high dimensions.
4. The ability to obtain point solutions or a linear functional of the solution.
5. Error estimates can be empirically obtained for all types of problems.
6. Ease of efficient parallel implementation.

In the current time three approaches are connected with solving nonlinear problems of engineering using method of Monte Carlo. The first approach implies the linearization of the problem (sequential solution of the series of linear problems). The second approach is connected with branching Markov processes. The third one is connected with optimal random search.

In this work, we study the approach connected with branching Markov processes. Branching Markov random processes are created to solve boundary-value problems (BVP) with polynomial nonlinearities. The realization of these processes creates so called “trees”. Unbiased estimators of the solution of the nonlinear problem are constructed on these random trees. We also obtain expressions for the minimal variance (statistical error) of the constructed unbiased estimators.

We offer computational algorithms for solving some nonlinear diffusion problems which frequently appears in engineering. The case of a quadratic nonlinearity for the boundary BVP is considered in detail.

Results

At every move of the particle to the next sphere, its weight increases by w where i is step index. Also, equation (5) can be interpreted in the following way. When the particle reaches x_i at t_i with probability P , the particle gives birth to two new equivalent particles and with probability Q one new particle. Also, with probability R , the random walk is absorbed and the weight becomes w . The particle continues its random walk analogous to the origin.

For each transition from point (x_i, t_i) to point (x_{i+1}, t_{i+1}) the random time step Δt is sampled according to densities as described in papers (Ermakov at al. 1989, p. 282 and Elepov at al., 1980, p.174, in Russian). The time is expressed in the form of $t_i + \Delta t$, where Δt , and t_i . The random walk process is terminated when either it is absorbed on the boundary, or the following condition holds

$$w > W_{max} \tag{6}$$

In the last case, the particle gets a weight, equal to initial condition w_0 .

When the initial particle gives birth at the k -th step, the current value of t is given to each of the new particles and we store these time values. After the next particle is absorbed, other particles (indexed by coordinates x_i and time t_i), which have been saved earlier, are taken from memory for processing. This "memorized" particle continues its random walk. The process finishes when the branching Markov process is completely finished.

The validate of the method, we applied it to problem (1)-(3) with the following data:

| | | | | | |
|--------|------------|-------------------|----------|------------|------------|
| Z, m | $l, 10-2m$ | $\epsilon, 10-3m$ | σ | Δt | Δx |
| 0.57 | 0.1 | 0.3 | 86.71 | 2.15 | |
| 0.57 | 0.1 | 0.1 | 89.34 | 2.77 | |
| 0.3 | 0.06 | 0.1 | 87.14 | 2.14 | |
| 0.3 | 0.1 | 0.3 | 86.32 | 2.93 | |

A point estimator of the temperature was used at locating equidistant from the cylindrical surfaces and moving along the cylindrical axis. The origin of coordinates is the base of the cylinder. Results of the computation with a 97% confidence interval for a various value of σ and l , using 10000 experiments in each series are given below:

| Z, m | $l, 10-2m$ | $\epsilon, 10-3m$ | σ | Δt | Δx |
|--------|------------|-------------------|----------|------------|------------|
| 0.57 | 0.1 | 0.3 | 86.71 | 2.15 | |
| 0.57 | 0.1 | 0.1 | 89.34 | 2.77 | |
| 0.3 | 0.06 | 0.1 | 87.14 | 2.14 | |
| 0.3 | 0.1 | 0.3 | 86.32 | 2.93 | |

Table 1: Numerical results of solution the problem (1)-(2)-(3).

Here σ is standard deviation. The time dynamics the temperature of the point (0.0285m, 0.015 m, 0.3 m) is given in table 2. The CPU time for calculating the temperature was about 45 sec. on our PC.

| t | σ | Δt |
|-----|----------|------------|
| 5 | 17.26 | 3.21 |
| 10 | 53.61 | 9.86 |
| 15 | 75.34 | 12.72 |
| 20 | 86.93 | 17.12 |

Table 2. Dynamics of changing of temperature at the point (0.0285, 0.015, 0.3).

Conclusions and Contributions

In our work, the probabilistic representation of the solutions of boundary-value problems were used with discrete (grid) approximations the original stochastic process. These discrete processes are easy for computing, don't require large amounts of memory of computer, but at the same time are comparatively complex because of the need to simulate "long" random trajectories.

It is known for solving nonlinear boundary problems by simulating branching processes, there are currently two practical Monte Carlo schemes which are thoroughly developed. The first is based on random walks on the grids with branching and the second is based on random walks on spheres with branching.

When we use the random walks on the grid with branching or random walks on spheres with branching, we note that when solving problem at an isolated point, we do not have to determine the solution at all the points on the grid. This is one of the fundamental advantages of using the Monte Carlo method to solve nonlinear boundary value problems. We should construct an efficient statistical algorithm.

Sometimes in constructing algorithms mostly used mean value theorems for parabolic equations and applied the analogy of algorithms like "random walk on spheres" and "random walk on spheroids" with branching. These results can be used for further studying and constructing Monte Carlo algorithms for the solution more general diffusion BVP with polynomial nonlinearities. In the future we want to apply these results for the solution to the most complicated practical engineering problems.

Scientific Ethics Declaration

The authors declare that the scientific ethical and legal responsibility of this article published in EPSTEM journal belongs to the authors.

References

- Ermakov S.M., (1975). Monte-Carlo method and adjacent matters, Nauka, Moscow, p. 472, (in Russian).
Ermakov S.M., Nekrutkin V. V. & Sipin A.S. (1989). Random Processes for Classical Equations of Mathematical Physics, Kluwer Acad. Publ., p. 282.
Elepov B.S., Kronberg A.A., Mihaylov G.A., Sabelfeld K.K., (1980). p.174, (in Russian).
Haji-Sheikh A. & Sparrow E.M. (1967). "Proc. Amer. Assoc. Engen. and Mechan", v. 2, *Monte-Carlo method for solving the thermal equations*.1-18.
Haji-Sheikh A. & Sparrow E.M. (1966). J. SIAM Appl. Math., V.14, 2, *The floating random walk and its application to Monte-Carlo solution of heat equations*, 370-389. doi:10.1137/0114031

Author Information

Abdujabar Rasulov

Department System Analysis and Mathematical Modelling,
University of World Economy and Diplomacy, 54,
Mustqillik avenue,
Tashkent, Uzbekistan, 100007
E mail: asrasulov@gmail.com

Gulnora Raimova

Department System Analysis and Mathematical Modelling,
University of World Economy and Diplomacy, 54,
Mustqillik avenue,
Tashkent, Uzbekistan, 100007
E mail: raimova27@gmail.com

Dilfuza Hasanova

Department System Analysis and Mathematical Modelling,
University of World Economy and Diplomacy, 54,
Mustqillik avenue,
Tashkent, Uzbekistan, 100007
E mail: dhasanova@uwed.uz

